Disease Markers

Microvessel Structure and Microvascular Alterations in Chronic Diseases

Lead Guest Editor: Yi Shao
Guest Editors: Jin Yuan, Ting Su, Qi-Cheng Yang, Wensi Tao, and Nan Jiang

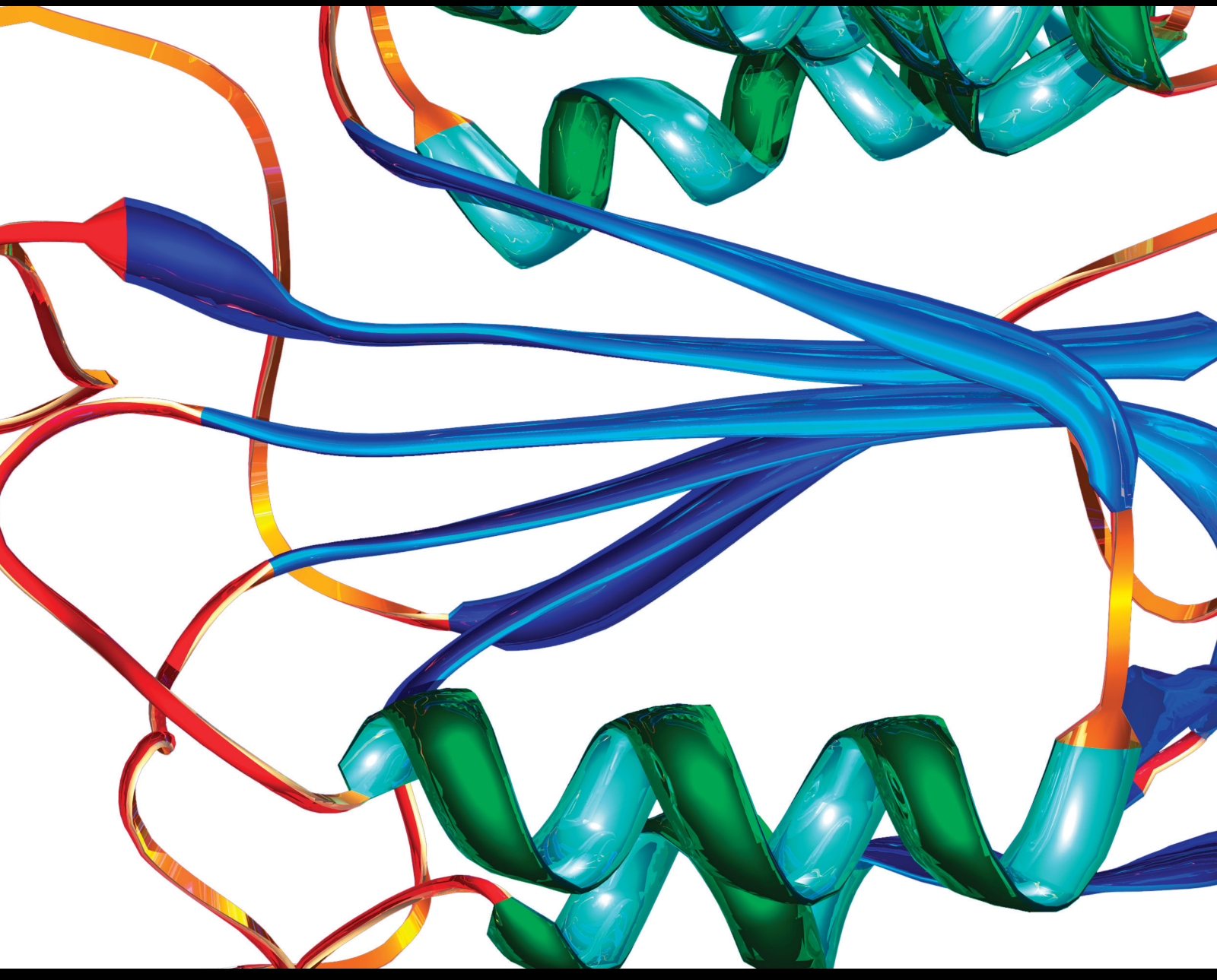

Microvessel Structure and Microvascular Alterations in Chronic Diseases

Disease Markers

Microvessel Structure and Microvascular Alterations in Chronic Diseases

Lead Guest Editor: Yi Shao
Guest Editors: Jin Yuan, Ting Su, Qi-Cheng Yang, Wensi Tao, and Nan Jiang

Chief Editor

Paola Gazzaniga, Italy

Associate Editors

Donald H. Chace, USA
Mariann Harangi, Hungary
Hubertus Himmerich, United Kingdom
Yi-Chia Huang, Taiwan
Giuseppe Murdaca, Italy
Irene Rebelo, Portugal

Academic Editors

Muhammad Abdel Ghafar, Egypt
George Agrogiannis, Greece
Mojgan Alaeddini, Iran
Atif Ali Hashmi, Pakistan
Cornelia Amalinei, Romania
Pasquale Ambrosino, Italy
Paul Ashwood, USA
Faryal Mehwish Awan, Pakistan
Atif Baig, Malaysia
Valeria Barresi, Italy
Lalit Batra, USA
Francesca Belardinilli, Italy
Elisa Belluzzi, Italy
Laura Bergantini, Italy
Sourav Bhattacharya, USA
Anna Birková, Slovakia
Giulia Bivona, Italy
Luisella Bocchio-Chiavetto, Italy
Francesco Paolo Busardó, Italy
Andrea Cabrera-Pastor, Spain
Paolo Cameli, Italy
Chiara Caselli, Italy
Jin Chai, China
Qixing Chen, China
Shaoqiu Chen, USA
Xiangmei Chen, China
Carlo Chiarla, Italy
Marcello Ciaccio, Italy
Luciano Colangelo, Italy
Alexandru Corlateanu, Moldova
Miriana D'Alessandro, Saint Vincent and the Grenadines
Waaqo B. Daddacha, USA
Xi-jian Dai, China
Maria Dalamaga, Greece
Serena Del Turco, Italy
Jiang Du, USA
Xing Du, China
Benoit Dugue, France
Paulina Dumnicka, Poland
Nashwa El-Khazragy, Egypt
Zhe Fan, China
Rudy Foddis, Italy
Serena Fragiotta, Italy
Helge Frieling, Germany
Alain J. Gelibter, Italy
Matteo Giulietti, Italy
Damjan Glavač, Slovenia
Alvaro González, Spain
Rohit Gundamaraju, USA
Emilia Hadziyannis, Greece
Michael Hawkes, Canada
Shih-Ping Hsu, Taiwan
Menghao Huang, USA
Shu-Hong Huang, China
Xuan Huang, China
Ding-Sheng Jiang, China
Esteban Jorge Galarza, Mexico
Mohamed Gomaa Kamel, Japan
Michalis V. Karamouzis, Greece
Muhammad Babar Khawar, Pakistan
Young-Kug Kim, Republic of Korea
Mallikarjuna Korivi, China
Arun Kumar, India
Jinan Li, USA
Peng-fei Li, China
Yiping Li, China
Michael Lichtenauer, Austria
Daniela Ligi, Italy
Hui Liu, China
Jin-Hui Liu, China
Ying Liu, USA
Zhengwen Liu, China
César López-Camarillo, Mexico
Xin Luo, USA
Zhiwen Luo, China
Valentina Magri, Italy
Michele Malaguarnera, Italy
Erminia Manfrin, Italy
Upender Manne, USA

Contents

Grey Matter Hypertrophy and Atrophy in Early-Blind Adolescents: A Surface-Based Morphometric Study
Fen Hou, Hengguo Li, Ping Li, Hongrong Shen, Yu Yang, Bo Li, Long Qian, Yang Fan, Hai Li, Gangqiang Hou, Wentao Jiang, Zhifeng Zhou, and Xia Liu
Research Article (8 pages), Article ID 8550714, Volume 2022 (2022)

Altered White Matter Integrity in Patients with Retinal Vein Occlusion: A Diffusion Tensor Imaging and Tract-Based Spatial Statistics Study
Mou-Xin Zhang, Min-Jie Chen, Li-Ying Tang, Chen-Yu Yu, Yu-Ling Xu, San-Hua Xu, Ping Ying, Min Kang, Li-Juan Zhang, and Yi Shao
Research Article (9 pages), Article ID 9647706, Volume 2022 (2022)

IDH1 Mutation Induces HIF-1α and Confers Angiogenic Properties in Chondrosarcoma JJ012 Cells
Xiaoyu Hu, Luyuan Li, Josiane E. Eid, Chao Liu, Jinming Yu, Jinbo Yue, and Jonathan C. Trent
Research Article (11 pages), Article ID 7729968, Volume 2022 (2022)

Sequential and Dynamic Variations of IL-6, CD18, ICAM, TNF-α, and Microstructure in the Early Stage of Diabetic Retinopathy
Ang Xiao, HuiFeng Zhong, Lei Xiong, Lin Yang, YunFang Xu, SiMin Wen, Yi Shao, and Qiong Zhou
Research Article (14 pages), Article ID 1946104, Volume 2022 (2022)

Cinnamaldehyde Downregulation of Sept9 Inhibits Glioma Progression through Suppressing Hif-1α via the Pi3k/Akt Signaling Pathway
Zhiwen Wang, Changfeng Wang, Jieping Fu, Ruen Liu, and Xinhui Zhou
Research Article (13 pages), Article ID 6530934, Volume 2022 (2022)

Analysis of Macular Retinal Thickness and Microvascular System Changes in Children with Monocular Hyperopic Anisometropia and Severe Amblyopia
Lin-Lin Liu, Yu-Chuan Wang, Miao Cao, Fang Liu, Shuang Zhang, Jing Liu, Jin-Chang Liu, Lian-Feng Xie, and Hui Wang
Research Article (7 pages), Article ID 9431044, Volume 2022 (2022)

Association of Iris Structural Measurements with Corneal Biomechanics in Myopic Eyes
Lin Fu, Yufeng Ye, Xu Jia, Yunjie Zhang, Xiaoyu Chen, Hengli Lian, Weihua Yang, and Qi Dai
Research Article (6 pages), Article ID 2080962, Volume 2021 (2021)

Transneuronal Degeneration in the Visual Pathway of Rats following Acute Retinal Ischemia/Reperfusion
Yanyan Fu, Tu Hu, Qianyue Zhang, Shuhan Meng, Ying Lu, Aiqun Xiang, Yewei Yin, Yuanjun Li, Jiayu Song, and Dan Wen
Research Article (15 pages), Article ID 2629150, Volume 2021 (2021)

The Role of Conjunctival Microvasculation Combined with Echocardiography in Evaluating Pulmonary Arterial Hypertension in Systemic Lupus Erythematosus
Jiangbiao Xiong, Shujiao Yu, Ren Liu, Xia Fang, and Rui Wu
Research Article (6 pages), Article ID 2135942, Volume 2021 (2021)

Machine Learning Classification of Mild Traumatic Brain Injury Using Whole-Brain Functional Activity: A Radiomics Analysis
Xiaoping Luo, Dezhao Lin, Shengwei Xia, Dongyu Wang, Xinmang Weng, Wenming Huang, and Hongda Ye
Research Article (7 pages), Article ID 3015238, Volume 2021 (2021)

Association between Iris Biological Features and Corneal Biomechanics in Myopic Eyes
Lin Fu, Qi Dai, Pengzhi Zhu, Xu Jia, Fangjun Bao, Xiaoyu Chen, Yana Fu, Hengli Lian, Weihua Yang, and Yufeng Ye
Research Article (6 pages), Article ID 5866267, Volume 2021 (2021)

Cyclophosphamide Attenuates Fibrosis in Lupus Nephritis by Regulating Mesangial Cell Cycle Progression
Yuehong Ma, Ling Fang, Rui Zhang, Peng Zhao, Yafeng Li, and Rongshan Li
Research Article (9 pages), Article ID 3803601, Volume 2021 (2021)

Pericytes of Indirect Contact Coculture Decrease Integrity of Inner Blood-Retina Barrier Model *In Vitro* by Upgrading MMP-2/9 Activity
Tianye Yang, Liang Guo, Yuan Fang, Mingli Liang, Yongzheng Zheng, Mingdong Pan, Chun Meng, and Guanghui Liu
Research Article (10 pages), Article ID 7124835, Volume 2021 (2021)

EAD-Net: A Novel Lesion Segmentation Method in Diabetic Retinopathy Using Neural Networks
Cheng Wan, Yingsi Chen, Han Li, Bo Zheng, Nan Chen, Weihua Yang, Chenghu Wang, and Yan Li
Research Article (13 pages), Article ID 6482665, Volume 2021 (2021)

Cysteine-Rich Intestinal Protein 1 Served as an Epithelial Ovarian Cancer Marker via Promoting Wnt/β-Catenin-Mediated EMT and Tumour Metastasis
Yujuan Liu, Wenyu Li, Ji Luo, Yiguo Wu, Yuanyuan Xu, Tingtao Chen, Wei Zhang, and Fen Fu
Research Article (12 pages), Article ID 3566749, Volume 2021 (2021)

Hindawi
Disease Markers
Volume 2022, Article ID 8550714, 8 pages
https://doi.org/10.1155/2022/8550714

Research Article

Grey Matter Hypertrophy and Atrophy in Early-Blind Adolescents: A Surface-Based Morphometric Study

Fen Hou,[1] Hengguo Li,[2] Ping Li,[1] Hongrong Shen,[1] Yu Yang,[1] Bo Li,[1] Long Qian,[3] Yang Fan,[4] Hai Li,[4] Gangqiang Hou,[5] Wentao Jiang,[5] Zhifeng Zhou,[5] and Xia Liu[5]

[1]*Department of Radiology, First Affiliated Hospital of Hunan University of Chinese Medicine, 95 Shaoshan Middle Road, Yuhua District, Changsha 410007, China*
[2]*Medical Imaging Center, The First Affiliated Hospital of Jinan University, Guangzhou 510632, China*
[3]*3GE Healthcare, Beijing, China*
[4]*Beijing Intelligent Brain Cloud, Inc, Beijing, China*
[5]*Neuropsychiatric Imaging Center, Shenzhen Kangning Hospital, Shenzhen Mental Health Center, Shenzhen 518000, China*

Correspondence should be addressed to Zhifeng Zhou; z_zf1015@163.com and Xia Liu; lauraliu0061@126.com

Received 5 August 2021; Accepted 9 April 2022; Published 3 May 2022

Academic Editor: Yi Shao

Objective. This study is aimed at exploring the regional changes in brain cortical morphology (thickness, volume, and surface area) in the early-blind adolescents (EBAs) by using the surface-based morphometric (SBM) method. *Methods*. High-resolution structural T1-weighted images (T1WI) of 23 early-blind adolescents (EBAs) and 21 age- and gender-matched normal-sighted controls (NSCs) were acquired. Structural indices, including cortical thickness (CT), cortical volume (CV), and surface area (SA), were analyzed by using FreeSurfer software, and the correlations between structural indices and the blindness duration were computed by Pearson correlation analysis. *Results*. Compared to controls, EBAs had significantly reduced CV and SA mainly in the primary visual cortex (V1) and decreased CV in the left vision-related cortices (r-MFC). There were no regions that EBAs had a significantly larger CV or SA than NSCs. EBAs had significantly increased CT in the V1 and strongly involved the visual cortex (right lateral occipital gyrus, LOG.R) and the left superior temporal gyrus (STG.L), while it had decreased CT in the left superior parietal lobule (SPL.L) and the right lingual gyrus (LING.R). Additionally, no correlation was found between cortical morphometric measures and clinical variables in the EBA group. *Conclusions*. SBM is a useful method for detecting human brain structural abnormalities in blindness. The results showed that these structural abnormalities in the visual cortex and visual-related areas outside the occipital cortex in the EBAs not only may be influenced by neurodevelopment, degeneration, plasticity, and so on but also involved the interaction of these factors after the early visual deprivation.

1. Introduction

Blindness provides a rare model to explore the impacts of visual experience on the structural and functional organization of the human brain [1–5]. A number of studies have investigated brain structural abnormalities in early-blind people. These findings include changes of the local brain structures, such as significantly volumetric atrophy of gray matter [6–11], decreased SA [12, 13], increased CT [12–19], and impaired white matter integrity [20], as well as alterations of the brain structural networks, such as decreased network efficiency in the blind individuals [21].

However, most of them were based on volumetric measures, using voxel-based morphology (VBM) or deformation-based morphometry (DBM), which may conceal fine anatomic details in other features. Several VBM [6–8] and DBM [10] studies have observed significant volumetric atrophy of gray matter (GM) throughout the visual cortex in early-blind (EB) subjects [6–8, 10]. A more effective morphometry analysis tool than VBM and DBM is the SBM method which provides fine

anatomic details in other features, such as CT and SA, and profoundly probe determining factors of CV approximated by multiplying CT by SA [22]. Previous SBM studies of blindness have shown decreased CV and SA [12, 13] and increased CT [12–19] in the occipital lobe. These changes may be accountable for following factors: neurodevelopment, degeneration, and plasticity [23, 24]. Previous research [25] indicated that degeneration and neurodevelopment may cause axonal damage and synapses interruption, which could lead to the reduced CV, SA, and CT of the visual cortex in the blind. However, other researches [26–28] concluded that plasticity and neurodevelopment may cause strengthened subcortical and corticocortical connections and reduced synaptic pruning, which could lead to the increased CV, SA, and CT in the visual cortex. From these previous results, we learned that these major factors, namely, neurodevelopment, degeneration, and plasticity, may influence differently on determining measures such as CV, SA, and CT. Therefore, these measures may change in even opposite directions (like a decreased CV or SA and an increased CT) under the interactions of these factors. However, the interactions of these factors remain to be not clearly understood.

In addition, these early blindness studies focused on the structural reorganization of the visual cortex, but the visual-related areas outside the occipital cortex in the blind have few been reported. Previous MRI studies of blindness reported reduced cortical thickness in the visual-related areas outside the occipital cortex (anterior STG and SPL) and increased cortical thickness in the visual cortex [12, 17]. Thus, whether the alteration mechanism in the thickness of the nonvisual cortex is as same as the visual cortex remains to be determined. Furthermore, it is interesting to explore the impact of the critical developmental period on the structural reorganization of these regions and the correlation between these structural indices and the blindness duration.

To elucidate these questions, in this study, we investigated cortical morphology (CT, CV, and SA) alterations in the visual cortex and visual-related areas outside the occipital cortex in the EBAs using a surface-based morphometric method [29]. We aimed to investigate the major factor(s) (neurodevelopment and/or degeneration and/or plasticity) how to play an interactive role in structural reorganization and possible neurological mechanism of structural reorganization in the blind.

2. Materials and Methods

2.1. Participants. Twenty-three EBAs (loss of sight at birth or within 1 year, 8 female, range = 11-18 years, mean age ± S.D.: 14.80 ± 2.07 years) were recruited from the Guangdong Province Blind School. Twenty-one NSCs (normal-sighted controls, NSCs) of volunteers (10 female, range = 11-19 years, mean age ± S.D.: 14.56 ± 2.59 years) participated in the study. Analysis of two-sample T-test did not indicate any significant difference in age ($t = 0.33$, $P = 0.74$), and a chi-squared test did not reveal a gender effect ($X^2 = 0.75$, $P = 0.39$) between the EBA and NSC groups. Causes of blindness included retinopathy of prematurity, congenital retinal lesions, congenital glaucoma, and congenital cataracts. All participants met the following inclusion criteria: (1) right-handedness, (2) no history of neurological or psychiatric diseases and identifiable MRI normal structural brain, and (3) normal hearing. The study was approved by the Ethics Committee of the First Affiliated Hospital of Jinan University, and all subjects and their guardians signed a written informed consent form before undergoing the MRI examinations.

2.2. Data Acquisition. High-resolution 3D T1-weighted BRAVO images were obtained on a 3.0-Tesla MR scanner (Discovery MR750 System; General Electric, Milwaukee, WI, USA), fitted with an 8-channel head coil. The parameters were as follows: flip angle = 12°, TR = 8.2 ms, TE = 3.2 ms, FOV = 256 × 256 mm^2, 256 × 256 matrix, slice gap = 0 mm, slice thickness = 1 mm, and 172 slices in the axial plane. Total scan time was 3 min 17 sec. During this MR scan, the subject's head was fixed using several foam cushions to minimize head motion.

2.3. Image Analysis. 3D T1-weighted MRI data were processed and analyzed using FreeSurfer V6.0 [30, 31] (http://surfer.nmr.mgh.harvard.edu/) with a standard cross-sectional pipeline. Starting from nonuniform intensity normalization, removal of nonbrain tissue, transformation to Talairach space, skull stripping, segmentation into white-matter (WM) and gray-matter (GM), and tessellation into the WM and GM boundary, an initial surface was constructed. This surface was used to reconstruct the final cortical surface after smoothed, inflated, and automated topology correction. The cortical thickness measurements were produced by calculating the distance between these surfaces at each point across the cortical mantle [32]. The cortical thickness was compared node by node, and the statistical results were visualized by creating an average template and registering the cortical surface for each subject to it by a surface-based registration method [30, 31]. The cortex was parcellated, and the means of CT, CV, and SA were obtained at each point on the reconstructed surface. Finally, a heat kernel (10 mm width) was used to smooth the data of CT, CV, and SA to improve the normality of the data.

2.4. Statistical Analysis. Firstly, the obtained structural indicators were compared between groups based on vertices. For each hemisphere, the General Linear Model (GLM) with vertex-wise analyses of surface morphometric measurements, including CT, CV, and SA, was performed in EBA and NSC groups. Statistical maps were generated using FreeSurfer's Query, Design, Estimate, Contrast (QDEC) interface. Age and gender were introduced in the model as nuisance factors. Finally, multiple comparisons were corrected with Monte Carlo Simulation using a vertex-level P value set at <0.01, and cluster-level threshold $P < 0.05$. In addition, the Statistical Package for the Social Sciences (SPSS) software (version 23.0; IBM Corporation, NY, USA) was applied in all demographics analysis and the correlation analysis between cortical morphometric measures and subjects' age in both groups. Simultaneously, the correlation between cortical morphometric measures and blindness

duration in the EBA group was examined. A two-tailed value less than 0.05 was considered statistically significant.

3. Results

Compared to controls, EBAs had significantly increased CT in the left pericalcarine (pCAL.L), left cuneus (CUN.L), left superior temporal gyrus (STG.L), and right lateral occipital gyrus (LOG.R), while they had decreased CT in left superior parietal lobule (SPL.L) and right lingual gyrus (LING.R). In terms of the CV, EBAs had significant CV loss in bilateral pCAL and left rostral middle frontal gyrus when comparing with NSCs, and there were no CV increased regions found in EBAs. Regarding the SA, EBAs had significantly reduced SA in bilateral pCAL and LING and left cuneus (CUN.L) compared to NSCs. No larger SA was observed in EBAs in comparison to NSCs. The detailed data are summarized in Table 1 and illustrated in Figure 1. Additionally, no significant differences in the demographic characteristics were noted and no correlation was found between cortical morphometric measures and clinical variables in both groups ($P > 0.05$).

4. Discussion

4.1. Morphological Alteration in the Primary Visual Cortex (V1) and Vision-Related Cortices (Left Rostral Middle Frontal Gyrus, L-r MFC). Our findings revealed significantly decreased CV and SA and increased CT in the V1 in the EBA group, which are similar to previous studies [12, 13]. These findings demonstrated that the development of V1 is strongly dependent on early visual experience [21, 25, 33, 34]. The following factors may affect the morphological alteration of the V1 during the developmental period. First, axonal degeneration is a key factor causing a reduced SA of the V1 in the early blind [25]. However, our finding of SA loss in the V1 of EBAs cannot completely be explained by axonal degeneration, which may be associated, at least to some degree, with visual loss leading to neurodevelopmental retardation during the developmental stage since no significant negative correlation was found between SA and blindness duration within the EBA group [12, 13]. Second, the increase of CT in the V1of EBAs cannot be explained by disuse atrophy and crossmodal plasticity at the adolescence stage, since there was no significant correlation found between CT and blindness duration within the EBA group. However, the increase of CT in the V1 may be attributed to the loss of normal neurodevelopment, which induces the reduction of synaptic pruning [35]. In addition, a thicker V1 is not found in the subjects who became blind in adulthood, whose V1 CT showed no difference from the sighted controls [33]. According to the microscopic neuroanatomical studies, the synaptic density in the human V1 is largest in the first postnatal year and gradually drops to the adult level during adolescence [36]. The disruption of the normal pruning process in EB, however, might result in a higher synaptic density in the blindnessV1 and spare other sensory connections such as thalamocortical connections and corticocortical connections [26–28], which could lead to the increased CT in the visual cortex. Finally, the reduction of GMV in the V1 in early blindness is also consistent with our previous VBM result [37], which reflected axonal degeneration secondary to the impaired visual pathway in the early blindness [38–40].

Using this more effective method than VBM, we could further attribute the atrophy of GMV in these areas of the EBA group to the reduced SA despite the increased CT, since CV can be approximated by multiplying CT by SA, so we could infer that the reduction in SA is greater than the increase in CT. According to the study of the cortical development in early childhood, it was reported that CT is developed earlier than SA. At the age of two, CT can reach 97% of adult values, while SA only 69%. The authors concluded that cortical growth after age 1 is mainly induced by increases in SA [41]. The reduction of SA in V1 in the EBAs implied that the loss the light stimulation lagged the SA development after age 1, whereas the loss of light has little impact on the neuron development of CT. In the light of the radial unit hypothesis, SA is defined by the number of cortical columns, while CT is determined by the number of neurons within a column [41]. Although the number of cortical columns declined, the number of neurons in each column increased in V1 in the EBAs that might attribute to the other sensory connections of the crossmodal plasticity. A few literatures have reported that the V1 cortex played an important role in various sensory cognitions (such as auditory and tactile sensation) in blind people, although visual stimulation is lacking [2, 4, 5]. In short, the early-blind patients showed various changes in the CV, CT, and SA in the V1, which reflected the different influence factors like axonal degeneration, disuse atrophy, neurodevelopment, and plasticity that played a diverse effect on these indicators.

The left middle frontal lobe approximately overlaps the frontal eye field, which may be a heterogeneous component of multiple extrastriate visual areas in charge of eye movements like the intentional saccade trigger [42] and smooth pursuit, showing reduced CV in EB. It should also be a subsequent change caused by vision loss.

4.2. Cortical Thickness Alteration in the Visual Cortex (Right Lingual Gyrus, LING.R, and Right Lateral Occipital Gyrus, LOG.R) and Visual-Related Areas outside the Occipital Cortex (SPL.L and STG.L). In contrast to the previous report of [15, 17] the increased CT in the LING.L in the early-blind subjects, significantly decreased CT was found in the LING.R in this study. As is known, this cortical area related to visual object recognition function forms part of the ventral visual pathway [43, 44]. Kim and Zatorre [45] found that this cortical area of a right hemisphere advantage might be recruited and activated to process auditory spatial position tasks in the blind during identifying auditory objects. In addition, according to the studies by Park et al. and Anurova et al. [12, 17], the negative correlations were found between CT of the occipital cortex and functional activation during auditory localization task in EB. This might account for the decreased thickness of the LING.R in EB who have better crossmodal plasticity abilities to guide action related to auditory localization and spatial discrimination. Meanwhile, the

Table 1: The significant altered cortical morphometry regions in EBA when compared with the NSC group.

Cortical morphometrics	Brain regions	Max	VtxMax	Size (mm^2)	MNIX	MNIY	MNIZ	CWP	NVtxs
CT of left hemisphere	Superior parietal lobule	-5.693	19424	65.24	-26.9	-52.6	62.4	0.0002	131
	Cuneus	5.055	68981	64.45	-4.6	-70.3	13.7	0.0002	80
	Pericalcarine	3.454	112523	44.64	-8.6	-92.5	7.4	0.01157	44
	Lingual	3.635	56056	41.46	-16.7	-87.6	-8.3	0.01931	42
	Pericalcarine	4.816	28560	38.47	-23.8	-68.9	7.6	0.03332	97
	Superior temporal gyrus	4.332	84916	36.35	-60.4	-14.8	-3	0.04996	74
CT of right hemisphere	Lateral occipital gyrus	4.3	136992	50.41	13.2	-100.6	3.7	0.0042	68
	Lingual	-4.572	148749	39.79	25.8	-46.8	-6.4	0.02761	69
CV of left hemisphere	Pericalcarine	-5.638	75563	137.23	-14.8	-81.3	7.4	0.0002	264
	Pericalcarine	-3.068	29579	11.77	-13.3	-85.8	7.1	0.0014	21
	Rostral middle frontal gyrus	-3.424	4470	11.23	-32	31.7	34.9	0.0016	15
CV of right hemisphere	Pericalcarine	-4.575	86494	11.35	15.1	-75	6.4	0.0026	18
	Pericalcarine	-4.192	61382	8.49	7	-84.1	8.4	0.02997	11
SA of left hemisphere	Pericalcarine	-5.796	128114	155.1	-12.1	-77.7	3.7	0.0002	260
	Pericalcarine	-5.497	158064	146.1	-21.1	-71.3	7.8	0.0002	291
	Pericalcarine	-5.581	41148	70.84	-13.6	-90.8	3	0.0002	86
	Pericalcarine	-6.195	39176	52.31	-6.1	-91.9	7.8	0.0002	55
	Pericalcarine	-4.742	126455	41.71	-7.1	-85.4	11.1	0.0002	56
	Lingual	-5.064	162439	21.18	-26.3	-65.3	2.4	0.0002	56
	Cuneus	-5.263	158481	17.78	-4.9	-91.6	8.4	0.0002	19
	Lingual	-4.92	17525	16.56	-4.1	-83.3	-0.8	0.0002	23
	Cuneus	-3.621	135774	15.94	-3.7	-77.8	13	0.0002	23
	Cuneus	-3.461	39164	11.3	-4.7	-88.4	17.8	0.0016	13
	Cuneus	-4.573	68974	9.96	-7.1	-71.3	16	0.00519	14
	Lingual	-3.504	114632	9.52	-7.7	-84	-5.2	0.00878	7
	Lingual	-5.023	162465	8.44	-16.4	-64.3	0.4	0.02662	13
	Lingual	-3.355	139407	7.99	-21.6	-62.4	-0.1	0.04528	14
SA of right hemisphere	Pericalcarine	-4.964	25443	99.08	12.4	-88	1.3	0.0002	141
	Pericalcarine	-5.676	161917	90.23	6.7	-80.6	1.4	0.0002	112
	Lingual	-5.595	132374	68.78	16.4	-69.2	3.7	0.0002	104
	Pericalcarine	-6.278	86238	66.94	13.8	-85.9	8.1	0.0002	90
	Pericalcarine	-4.442	27615	23.38	8.8	-84	8.9	0.0002	30
	Pericalcarine	-5.256	135388	15.09	24.3	-66.1	7.6	0.0002	35
	Pericalcarine	-5.472	43531	13.78	19	-70.7	10.2	0.0004	26
	Lingual	-4.629	35860	12.7	5.3	-67.9	6.1	0.0006	23
	Lingual	-4.082	22548	9.47	18.6	-80.2	-12.1	0.01355	8
	Lingual	-3.719	90574	8.94	8.4	-77.4	-1.8	0.0199	8
	Pericalcarine	-4.312	156632	8.9	13.6	-91.7	7.1	0.0203	15
	Pericalcarine	-3.263	118284	8.65	16.1	-94.8	3.4	0.02642	10
	Lingual	-3.418	95382	8.63	8.3	-61.5	1.3	0.02662	16

Abbreviations: EBA: early-blind adolescents; NSC: normal-sighted controls; CT: cortical thickness; CV: cortical volume; SA: surface area; MNIX, Y, Z:the MNI coordinate of peak vertex; VtsMax: number of peak vertex of the significant cluster; CWP: cluster-wise probability and the nominal *P* value; NVtxs: number of vertices in cluster.

decrease of the CT in the LING.R is consistent with the theory mentioned above, in which the synaptic density is largest in the first postnatal year and gradually drops to the adult level by synaptic pruning during the activation and development.

Moreover, in line with this, many previous studies [15] have shown that increased CT was also located in the higher-level visual association areas (BA 19) such as extrastriate occipital cortex (LOG.R), which plays an important role in the attention, feature extracting, shape recognition, and multimodal integrating functions [46–52].

After visual deprivation, the alteration of the cortical thickness not only was found in the occipital cortex but also

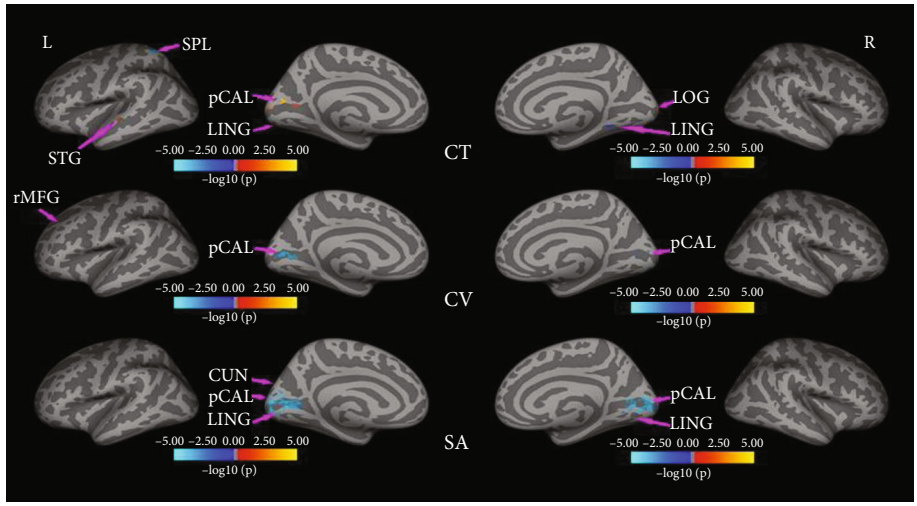

Figure 1: The significant altered cortical morphometry regions in EBAs when compared with the NSC group on CT, CV, and SA.

in the visual-related areas outside the occipital cortex, such as SPL.L and STG.L.

As a part of the dorsal attention network [53], the SPL is involved in spatial cognition [2, 54], sensorimotor, attention, and working memory [55–59]. There is a massive experience-related reorganization that blind people participate in the processing of spatial information from auditory [45, 60] and tactile [44] sense instead of visual input. According to a study by Park et al. and Anurova et al. [12, 17], areas with a thinner cortex should be associated with more effective function in EB. Therefore, the thin cortex of SPL may reveal that stronger plasticity of function in EB remaps the additional available sensory inputs (e.g., audition, touch) so that they could handle nonvisual tasks better in the absence of vision.

Our studies found that the increased CT in the left posterior STG (pSTG) is inconsistent with previous reports [12, 17] of the decreased CT in the anterior STG (aSTG). The STG is known to involve in the auditory comprehension process [61, 62]. Moreover, previous studies [63] have suggested that pSTG was more involved in the sound localization, while aSTG was related to auditory pattern processing, which may be explained by anterior-posterior functional dissociation in temporal areas. The increase of pSTG might correspond to the improvement of the ability of the sound localization in EBAs, which might indicate that cortical plasticity following visual deprivation enhances intramodal organization of auditory and tactile perception [64].

In summary, this study explored the structural characteristics of brain gray matter from different perspectives in early EBAs, including CV, SA, and CT. On the one hand, for V1, EBAs had significantly decreased CV and SA but increased CT; axonal degeneration is a key factor leading to a reduced SA of the V1, as well as neurodevelopmental retardation caused by visual loss, while the increase of CT results from the reduction of synaptic pruning due to neurodevelopmental retardation and crossmodal plasticity companying auditory and tactile perception; thus, the decrease of CV might indicate that the reduction of the SA was much more than the increase of the CT. On the other hand, visual-related areas outside the occipital cortex included the decrease of the CV in the left rostral middle frontal gyrus (r-MFC), the increase of the left superior temporal gyrus (STG.L), and the decrease of the CT in the left superior parietal lobule (SPL.L) and the right lingual gyrus (LING.R), which might mainly attribute to intramodal plasticity. Moreover, these cortical alterations were not correlated with the blindness duration. These structural findings might provide the certain basis to interpret the functions of brain regions in the blind. It has proved that the visual-related cortex does not shrink and degenerate and they are involved in various sensory cognitions to different degrees, which ignites a little light to achieve the possibility of cross-modal sensory substitution for blindness.

4.3. Limitation. The major limitation of this study is the limited small sample size, and further studies with larger cohorts are needed to explore different patterns between subgroups. Additionally, the results reveal structural changes, but the relationship between structural changes and functional activation has not been clearly understood and calls for further study for mutual interaction between structure and function.

5. Conclusion

Using the surface-based morphometric (SBM) method and combining different dimensions, such as CT, CV, and SA, to analyze the different morphological alterations of brain after visual deprivation, we investigated the cortical structural reorganization which occurs not only in the occipital cortex but also in the visual-related areas outside the occipital cortex. Our result demonstrated that structural reorganization of different brain regions in EBAs differently was influenced by the major factor(s) (neurodevelopment and/or degeneration and/or plasticity) and their interactions during development.

Data Availability

The processed data required to reproduce these findings cannot be shared at this time as the data also forms part of an ongoing study.

Conflicts of Interest

The authors declare that they have no conflicts of interest.

Authors' Contributions

Long Qian provided the guidance for the MRI scan parameter settings. Yang Fan guided us interpret the results of FreeSurfer. Hai Li helped us do picture processing. Gangqiang Hou provided the help for the subject collection. Wentao Jiang facilitated the MRI scan of the subjects. Fen Hou and Hengguo Li contributed equally to this work.

Acknowledgments

This work was supported by the Key Discipline Construction Project of Hunan University of Chinese Medicine (No. 4901-020000200806), the Shenzhen Science and Technology Plan Project (No. JCYJ20190809161011503), the Shenzhen Fund for Guangdong Provincial High-level Clinical Key Specialties (No. SZGSP013).

References

[1] S. Abboud, S. Maidenbaum, S. Dehaene, and A. Amedi, "A number-form area in the blind," *Nature Communications*, vol. 6, no. 1, p. 6026, 2015.

[2] O. Collignon, G. Dormal, G. Albouy et al., "Impact of blindness onset on the functional organization and the connectivity of the occipital cortex," *Brain*, vol. 136, no. 9, pp. 2769–2783, 2013.

[3] R. Kupers, D. R. Chebat, K. H. Madsen, O. B. Paulson, and M. Ptito, "Neural correlates of virtual route recognition in congenital blindness," *Proceedings of the National Academy of Sciences of the United States of America*, vol. 107, no. 28, pp. 12716–12721, 2010.

[4] R. Kupers and M. Ptito, "Compensatory plasticity and cross-modal reorganization following early visual deprivation," *Neuroscience and Biobehavioral Reviews*, vol. 41, pp. 36–52, 2014.

[5] R. Araneda, S. Silva Moura, L. Dricot, and A. G. de Volder, "Beat detection recruits the visual cortex in early blind subjects," *Life*, vol. 11, no. 4, p. 296, 2021.

[6] U. Noppeney, K. J. Friston, J. Ashburner, R. Frackowiak, and C. J. Price, "Early visual deprivation induces structural plasticity in gray and white matter," *Current Biology*, vol. 15, no. 13, pp. R488–R490, 2005.

[7] W. J. Pan, G. Wu, C. X. Li, F. Lin, J. Sun, and H. Lei, "Progressive atrophy in the optic pathway and visual cortex of early blind Chinese adults: a voxel-based morphometry magnetic resonance imaging study," *NeuroImage*, vol. 37, no. 1, pp. 212–220, 2007.

[8] M. Ptito, F. C. Schneider, O. B. Paulson, and R. Kupers, "Alterations of the visual pathways in congenital blindness," *Experimental Brain Research*, vol. 187, no. 1, pp. 41–49, 2008.

[9] N. Lepore, P. Voss, F. Lepore et al., "Brain structure changes visualized in early- and late-onset blind subjects," *NeuroImage*, vol. 49, no. 1, pp. 134–140, 2010.

[10] C. Yang, S. Wu, W. Lu, Y. Bai, and H. Gao, "Anatomic differences in early blindness: a deformation-based morphometry MRI study," *Journal of Neuroimaging*, vol. 24, no. 1, pp. 68–73, 2014.

[11] A. Jiang, J. Tian, R. Li et al., "Alterations of regional spontaneous brain activity and gray matter volume in the blind," *Neural Plasticity*, vol. 2015, Article ID 141950, 12 pages, 2015.

[12] H. J. Park, J. D. Lee, E. Y. Kim et al., "Morphological alterations in the congenital blind based on the analysis of cortical thickness and surface area," *NeuroImage*, vol. 47, no. 1, pp. 98–106, 2009.

[13] J. Jiang, W. Zhu, F. Shi et al., "Thick visual cortex in the early blind," *The Journal of Neuroscience*, vol. 29, no. 7, pp. 2205–2211, 2009.

[14] H. Bridge, A. Cowey, N. Ragge, and K. Watkins, "Imaging studies in congenital anophthalmia reveal preservation of brain architecture in 'visual' cortex," *Brain*, vol. 132, no. 12, pp. 3467–3480, 2009.

[15] P. Voss and R. J. Zatorre, "Occipital cortical thickness predicts performance on pitch and musical tasks in blind individuals," *Cerebral Cortex*, vol. 22, no. 11, pp. 2455–2465, 2012.

[16] W. Qin, Y. Liu, T. Jiang, and C. Yu, "The development of visual areas depends differently on visual experience," *PLoS One*, vol. 8, no. 1, article e53784, 2013.

[17] I. Anurova, L. A. Renier, A. G. De Volder, S. Carlson, and J. P. Rauschecker, "Relationship between cortical thickness and functional activation in the early blind," *Cerebral Cortex*, vol. 25, no. 8, pp. 2035–2048, 2015.

[18] M. J. Guerreiro, M. V. Erfort, J. Henssler, L. Putzar, and B. Roder, "Increased visual cortical thickness in sight-recovery individuals," *Human Brain Mapping*, vol. 36, no. 12, pp. 5265–5274, 2015.

[19] C. Mateus, O. C. d'Almeida, A. Reis, E. Silva, and M. Castelo-Branco, "Genetically induced impairment of retinal ganglion cells at the axonal level is linked to extrastriate cortical plasticity," *Brain Structure & Function*, vol. 221, no. 3, pp. 1767–1780, 2016.

[20] Z. Zhou, J. Xu, L. Shi et al., "Alterations of the brain microstructure and corresponding functional connectivity in early-blind adolescents," *Neural Plasticity*, vol. 2019, Article ID 2747460, 2019.

[21] J. Li, Y. Liu, W. Qin et al., "Age of onset of blindness affects brain anatomical networks constructed using diffusion tensor tractography," *Cerebral Cortex*, vol. 23, no. 3, pp. 542–551, 2013.

[22] A. Raznahan, P. Shaw, F. Lalonde et al., "How does your cortex grow?," *Journal of Neuroscience*, vol. 31, no. 19, pp. 7174–7177, 2011.

[23] J. S. Shimony, H. Burton, A. A. Epstein, D. G. McLaren, S. W. Sun, and A. Z. Snyder, "Diffusion tensor imaging reveals white matter reorganization in early blind humans," *Cerebral Cortex*, vol. 16, no. 11, pp. 1653–1661, 2006.

[24] N. Shu, J. Li, K. Li, C. Yu, and T. Jiang, "Abnormal diffusion of cerebral white matter in early blindness," *Human Brain Mapping*, vol. 30, no. 1, pp. 220–227, 2009.

[25] A. K. Andelin, J. F. Olavarria, I. Fine et al., "The effect of onset age of visual deprivation on visual cortex surface area across-species," *Cerebral Cortex*, vol. 29, no. 10, pp. 4321–4333, 2019.

[26] S. J. Karlen, D. M. Kahn, and L. Krubitzer, "Early blindness results in abnormal corticocortical and thalamocortical connections," *Neuroscience*, vol. 142, no. 3, pp. 843–858, 2006.

[27] M. A. Kingsbury, N. A. Lettman, and B. L. Finlay, "Reduction of early thalamic input alters adult corticocortical connectivity," *Brain Research. Developmental Brain Research*, vol. 138, no. 1, pp. 35–43, 2002.

[28] M. Sur and C. A. Leamey, "Development and plasticity of cortical areas and networks," *Nature Reviews. Neuroscience*, vol. 2, no. 4, pp. 251–262, 2001.

[29] Z. F. Zhou, X. Liu, L. Qian et al., "Grey matter hypertrophy and atrophy in early-blind adolescents: a surface-based morphometric study," in *ISMRM 28th Annual Meeting & Exhibition*, Paris, France, August 2020.

[30] B. Fischl, M. I. Sereno, and A. M. Dale, "Cortical surface-based analysis: II: inflation, flattening, and a surface- based coordinate system," *NeuroImage*, vol. 9, no. 2, pp. 195–207, 1999.

[31] A. M. Dale, B. Fischl, and M. I. Sereno, "Cortical surface-based analysis: I. Segmentation and surface reconstruction," *Neuroimage*, vol. 9, no. 2, pp. 179–194, 1999.

[32] B. Fischl and A. M. Dale, "Measuring the thickness of the human cerebral cortex from magnetic resonance images," *Proceedings of the National Academy of Sciences of the United States of America*, vol. 97, no. 20, pp. 11050–11055, 2000.

[33] B. M. Hooks and C. Chen, "Critical periods in the visual system: changing views for a model of experience-dependent plasticity," *Neuron*, vol. 56, no. 2, pp. 312–326, 2007.

[34] Q. Li, M. Song, J. Xu, W. Qin, C. Yu, and T. Jiang, "Cortical thickness development of human primary visual cortex related to the age of blindness onset," *Brain Imaging and Behavior*, vol. 11, no. 4, pp. 1029–1036, 2017.

[35] J. P. Bourgeois, P. J. Jastreboff, and P. Rakic, "Synaptogenesis in visual cortex of normal and preterm monkeys: evidence for intrinsic regulation of synaptic overproduction," *Proceedings of the National Academy of Sciences of the United States of America*, vol. 86, no. 11, pp. 4297–4301, 1989.

[36] P. R. Huttenlocher, C. de Courten, L. J. Garey, and H. Van der Loos, "Synaptogenesis in human visual cortex — evidence for synapse elimination during normal development," *Neuroscience Letters*, vol. 33, no. 3, pp. 247–252, 1982.

[37] F. Hou, X. Liu, Z. Zhou, J. Zhou, and H. Li, "Reduction of interhemispheric functional brain connectivity in early blindness: a resting-state fMRI study," *BioMed Research International*, vol. 2017, Article ID 6756927, 2017.

[38] N. L. Reislev, T. B. Dyrby, H. R. Siebner, R. Kupers, and M. Ptito, "Simultaneous assessment of white matter changes in microstructure and connectedness in the blind brain," *Neural Plasticity*, vol. 2016, Article ID 6029241, 2016.

[39] G. K. Aguirre, R. Datta, N. C. Benson et al., "Patterns of individual variation in visual pathway structure and function in the sighted and blind," *PLoS One*, vol. 11, no. 11, article e0164677, 2016.

[40] N. H. Reislev, T. B. Dyrby, H. R. Siebner, H. Lundell, M. Ptito, and R. Kupers, "Thalamocortical connectivity and microstructural changes in congenital and late blindness," *Neural Plasticity*, vol. 2017, Article ID 9807512, 2017.

[41] R. Buechler, D. Wotruba, L. Michels et al., "Cortical volume differences in subjects at risk for psychosis are driven by surface area," *Schizophrenia Bulletin*, vol. 46, no. 6, pp. 1511–1519, 2020.

[42] C. Pierrot-Deseilligny, R. M. Muri, C. J. Ploner, B. Gaymard, and S. Rivaud-Pechoux, "Cortical control of ocular saccades in humans: a model for motricity," *Progress in Brain Research*, vol. 142, pp. 3–17, 2003.

[43] D. J. Kravitz, K. S. Saleem, C. I. Baker, L. G. Ungerleider, and M. Mishkin, "The ventral visual pathway: an expanded neural framework for the processing of object quality," *Trends in Cognitive Sciences*, vol. 17, no. 1, pp. 26–49, 2013.

[44] M. Ptito, I. Matteau, A. Zhi Wang, O. B. Paulson, H. R. Siebner, and R. Kupers, "Crossmodal recruitment of the ventral visual stream in congenital blindness," *Neural Plasticity*, vol. 2012, Article ID 304045, 9 pages, 2012.

[45] J. K. Kim and R. J. Zatorre, "Tactile-auditory shape learning engages the lateral occipital complex," *The Journal of Neuroscience*, vol. 31, no. 21, pp. 7848–7856, 2011.

[46] K. S. Rockland and H. Ojima, "Multisensory convergence in calcarine visual areas in macaque monkey," *International Journal of Psychophysiology*, vol. 50, no. 1-2, pp. 19–26, 2003.

[47] D. Bonino, E. Ricciardi, L. Sani et al., "Tactile spatial working memory activates the dorsal extrastriate cortical pathway in congenitally blind individuals," *Archives Italiennes de Biologie*, vol. 146, no. 3-4, pp. 133–146, 2008.

[48] O. Collignon, M. Davare, E. Olivier, and A. G. De Volder, "Reorganisation of the right occipito-parietal stream for auditory spatial processing in early blind humans. A transcranial magnetic stimulation study," *Brain Topography*, vol. 21, no. 3-4, pp. 232–240, 2009.

[49] O. Collignon, M. Lassonde, F. Lepore, D. Bastien, and C. Veraart, "Functional cerebral reorganization for auditory spatial processing and auditory substitution of vision in early blind subjects," *Cerebral Cortex*, vol. 17, no. 2, pp. 457–465, 2007.

[50] C. Lane, S. Kanjlia, A. Omaki, and M. Bedny, ""Visual" cortex of congenitally blind adults responds to syntactic movement," *The Journal of Neuroscience*, vol. 35, no. 37, pp. 12859–12868, 2015.

[51] G. Cappagli, S. Finocchietti, E. Cocchi, and M. Gori, "The impact of early visual deprivation on spatial hearing: a comparison between totally and partially visually deprived children," *Frontiers in Psychology*, vol. 8, p. 467, 2017.

[52] M. Guggenmos, V. Thoma, R. M. Cichy, J. D. Haynes, P. Sterzer, and A. Richardson-Klavehn, "Non-holistic coding of objects in lateral occipital complex with and without attention," *NeuroImage*, vol. 107, pp. 356–363, 2015.

[53] Y. Wang, F. Deng, Y. Jia et al., "Disrupted rich club organization and structural brain connectome in unmedicated bipolar disorder," *Psychological Medicine*, vol. 49, no. 3, pp. 510–518, 2019.

[54] O. Collignon, G. Vandewalle, P. Voss et al., "Functional specialization for auditory-spatial processing in the occipital cortex of congenitally blind humans," *Proceedings of the National Academy of Sciences of the United States of America*, vol. 108, no. 11, pp. 4435–4440, 2011.

[55] H. Burton, R. J. Sinclair, and S. Dixit, "Working memory for vibrotactile frequencies: comparison of cortical activity in blind and sighted individuals," *Human Brain Mapping*, vol. 31, no. 11, pp. 1686–1701, 2010.

[56] E. Bueicheku, N. Ventura-Campos, M. A. Palomar-Garcia, A. Miro-Padilla, M. A. Parcet, and C. Avila, "Functional connectivity between superior parietal lobule and primary visual cortex "at rest" predicts visual search efficiency," *Brain Connectivity*, vol. 5, no. 8, pp. 517–526, 2015.

[57] K. M. Shafritz, J. C. Gore, and R. Marois, "The role of the parietal cortex in visual feature binding," *Proceedings of the*

National Academy of Sciences of the United States of America, vol. 99, no. 16, pp. 10917–10922, 2002.

[58] M. Koenigs, A. K. Barbey, B. R. Postle, and J. Grafman, "Superior parietal cortex is critical for the manipulation of information in working memory," *The Journal of Neuroscience*, vol. 29, no. 47, pp. 14980–14986, 2009.

[59] D. M. Wolpert, S. J. Goodbody, and M. Husain, "Maintaining internal representations: the role of the human superior parietal lobe," *Nature Neuroscience*, vol. 1, no. 6, pp. 529–533, 1998.

[60] M. Gori, G. Sandini, C. Martinoli, and D. C. Burr, "Impairment of auditory spatial localization in congenitally blind human subjects," *Brain*, vol. 137, no. 1, pp. 288–293, 2014.

[61] I. DeWitt and J. P. Rauschecker, "Convergent evidence for the causal involvement of anterior superior temporal gyrus in auditory single-word comprehension," *Cortex*, vol. 77, pp. 164–166, 2016.

[62] T. Wolbers, P. Zahorik, and N. A. Giudice, "Decoding the direction of auditory motion in blind humans," *NeuroImage*, vol. 56, no. 2, pp. 681–687, 2011.

[63] W. Chen, B. Liu, J. Zheng, X. Li, P. Wang, and B. Wang, "What and where in the auditory systems of sighted and early blind individuals: evidence from representational similarity analysis," *Journal of the Neurological Sciences*, vol. 413, article 116805, 2020.

[64] A. W. de Borst and B. de Gelder, "Mental imagery follows similar cortical reorganization as perception: intra-modal and cross-modal plasticity in congenitally blind," *Cerebral Cortex*, vol. 29, no. 7, pp. 2859–2875, 2019.

Hindawi
Disease Markers
Volume 2022, Article ID 9647706, 9 pages
https://doi.org/10.1155/2022/9647706

Research Article

Altered White Matter Integrity in Patients with Retinal Vein Occlusion: A Diffusion Tensor Imaging and Tract-Based Spatial Statistics Study

Mou-Xin Zhang,[1,2] **Min-Jie Chen**,[3] **Li-Ying Tang**,[4] **Chen-Yu Yu**,[1] **Yu-Ling Xu**,[1] **San-Hua Xu**,[1] **Ping Ying**,[1] **Min Kang**,[1] **Li-Juan Zhang**,[1] **and Yi Shao**[1]

[1]*Department of Ophthalmology, The First Affiliated Hospital of Nanchang University, Jiangxi Province Ocular Disease Clinical Research Center, Nanchang, China*
[2]*Affiliated Xiamen Eye Center of Xiamen University, School of Medicine, Xiamen University, Xiamen, China*
[3]*Department of Clinical Medicine, Queen Mary School, Nanchang University, Nanchang, China*
[4]*Department of Ophthalmology, Zhongshan Hospital of Xiamen University, School of Medicine, Xiamen University, Xiamen, China*

Correspondence should be addressed to Yi Shao; freebee99@163.com

Mou-Xin Zhang, Min-Jie Chen, and Li-Ying Tang contributed equally to this work.

Received 17 July 2021; Revised 8 December 2021; Accepted 4 February 2022; Published 24 February 2022

Academic Editor: Dai Xi-jian

Background. To investigate microstructural alterations of white matter in retinal vein occlusion (RVO) patients by tract-based spatial statistics (TBSS) and diffusion tensor imaging (DTI). *Material/Methods*. DTI was performed on 14 RVO patients and 14 normal controls (HCs). We measured and recorded fractional anisotropy (FA) and radial diffusivity (RD) of white matter fibers and classified them through the receiver operating characteristic (ROC) curve and correlation analysis, respectively. *Results*. The mean FA value of white matter in RVO patients is lower than the HCs, and the mean RD value in RVO patients increased, especially in the bilateral posterior thalamic, bilateral sagittal stratum, body of corpus callosum, cingulum, and fornix. The ROC curve of different brain regions showed high accuracy. Moreover, the mean FA and RD values were significantly correlated with visual and psychological disorders. *Conclusion*. TBSS could be regarded as an important method to reveal the alterations of white matter in RVO patients, indicating the underlying neurological mechanism of the RVO.

1. Background

The retinal vein occlusion (RVO) is a kind of second major retinal vascular disorder, which is characterized by the expansion and dilation of retinal veins [1]. Meanwhile, RVO is considered to be an important cause of visual loss, including central (CRVO) and branch retinal vein occlusions (BRVO) [2, 3]. According to the previous epidemiological studies of world population, about 16 million adults have RVO, and the estimated prevalence rate of RVO is 5.2% [4]. RVO is closely related to the advancing age, which leads to its worldwide increase occurrence because of the increasing longevity of people [5]. RVO generally occurs in the case of thrombosis in the vascular system or some arterial diseases, which leads to intraluminal stenosis, venous congestion, and increased venous pressure [6]. This intravascular alteration potentially causes some secondary conditions including macular edema and neovascularization, which are the leading causes of vision loss in RVO [4, 6, 7]. Until now, there is still no complete and effective cure for RVO. A DTI study based on white matter suggests that retinal vascular pathology is related to poorer microstructure of cerebral white matter [8]. Thus, we speculate that some functional and microstructural changes may happen in the brain of patient with RVO. Currently, fundus fluorescein angiography (FFA) [1] and optical coherence tomography

(OCT) [9] are often used for imaging diagnosis of the retinal and choroidal vasculature, but the neuroimaging examination is still rare. We believe that neuroimaging method may provide a new direction for revealing RVO-related brain processes and the potential neuropathological mechanisms.

DTI is a special form of functional magnetic resonance imaging (MRI) and is a new way to describe the structure of the brain in recent years. As a new imaging method based on diffusion weighted imaging (DWI), DTI can analyze the dispersion motion of water molecules in the tissue in three-dimensional space, providing an insight into living human brain noninvasively, especially white matter anatomy. Additionally, it gives quantitative parameters related to the microstructure of white matter [10, 11]. A number of measures calculated using DTI measures can provide quantitative information, including FA, RD, axial diffusivity (AD), and mean diffusivity (MD) [12, 13]. Many studies successfully used DTI to demonstrate intrinsic neural alterations in patients with visual-related diseases. Li et al. [14] found that FA of optic nerve and optic nerve radiation decreased significantly, while MD of bundle increased significantly, suggesting that indicative degeneration and remodeling may occur in patients with glaucoma. Besides, Li et al. [15] applied voxel-wise statistical analysis and reported that there is a significant decrease FAs in several white matter tracts and reduced grey matter volume in children with amblyopia compare to HCs, which revealed that visual impairment of amblyopia affects normal development of brain structure. However, the intrinsic changes of white matter in RVO patients remain unclear. RVO could cause vision loss, which in turn may lead to mental illness such as anxiety and depression. Thus, we suspected that the average FA and RD might be related to anxiety, depression, and vision.

Because of the advantages of voxel and trajectory analysis, trajectory-based spatial statistics (TBSS) is not only widely used in various neurological system diseases but also has become a popular tool to evaluate DTI data. TBSS projects volumetric data onto a WM skeleton without data smoothing, resolving the defect caused by alignment inaccuracies [16, 17]. Previous studies have applied TBSS to assess the neural alterations in patients with visual-related diseases. A TBSS analysis of patients with concomitant exotropia showed that FA increased and RD decreased in the relevant areas [18]. TBSS was applied to investigate the white matter integrity of patients with congenital and terminal blind and monocular blindness and found the different mechanisms of structural changes in white matter [19, 20]. Therefore, our purpose here is to use TBSS analysis to research the alterations and to explore the diffusivities of fiber bundles in RVO patients.

2. Methods

2.1. Subjects. We recruited 14 RVO patients from the First Affiliated Hospital of Nanchang University Hospital. The inclusion criteria for this study included the following: [1] ophthalmoscopy showed RVO signs; [2] OCT revealed macular oedema; and [3] FFA showed occlusion of retinal vein (Figure 1 and Table 1). The exclusion criteria for RVO were as follows: [1] a history of intraocular or extraocular surgery; [2] combined with other ocular diseases; and [3] mental disease, cardiovascular diseases, and other systematic diseases.

At the same time, 14 healthy controls (HCs) were included with the following inclusion criteria: [1] no history of ocular disease; [2] no brain abnormalities; [3] no mental and cardiovascular diseases; [4] no drugs or alcohol abuse; and [5] have MRI examination ability. The age and gender background of all HCs and RVO were matched. This study was conducted in strict accordance with the guidelines and regulations of the Human Research Ethics Committee of the First Affiliated Hospital of Nanchang University on the basis of approval. All patients included in this study were informed and signed a consent form.

2.2. Data Acquisition and Preprocessing. The data in this study was collected by 3.0 T MRI scanner (Siemens, Erlangen, Germany). The parameters of these sequences are referenced in previous studies [18]. FMRIB Software Library (FSL) was used for all MRI data. We performed these data as previously described [18]. All original data were extracted, corrected eddy current distortion and head motion artifacts, and then a brain mask was made.

2.3. TBSS Procedures. Similar to the previous TBSS method [16], we used the following analytical methods to explore the characteristics of white matter diffusion. All FA images were aligned with the standard space of a Montreal Neurological Institute 152 (MNI152) through nonlinear registration. Firstly, the mean FA maps of all participants were projected onto the fMRIB 58 skeleton. Then, after maximum alignment of the common skeleton, the data was presented as a four-dimensional image. We used the FSL view and FSL cluster tool to visualize and select the statistically significant FA and RD voxel clusters, respectively, and simplified the visualization of the actual analytical representation through the script TBSS_fill.

2.4. Evaluation of Anxiety, Depression, and Visual quality. The Hospital Anxiety and Depression Scale (HADS) designed in 1983 was used to investigate anxiety and depression [21]. The Chinese version of National Eye Institute 25-Item Visual Function Questionnaire (NEI-VFQ25) was used to measure the quality score of life [22].

2.5. Receiver Operating Characteristic Curve (ROC). We analyzed the average values of FA and RD through the ROC methods as previously described [20]. The area under the curve (AUC) represented the diagnostic rate. The AUC value of 0.7~0.9 and 0.5~0.7 represented lower and higher accuracy, respectively.

2.6. Statistical Analysis. The clinical and demographic variables were analyzed by two-independent-sample t-tests of SPSS 23.0 (IBM Corp., USA). Threshold-free cluster enhancement option in the FSL randomize tool was used to synchronously implement the nonparametric method based on permutation. $P < 0.05$ indicated that the results

(a) (b)

Figure 1: Example of RVO seen on FC and FFA. (a) RVO observed using a FC which was characterized by massive flame-like hemorrhage (red arrow) in the retina. (b) RVO seen on FFA which was characterized by petal-shaped fluorescein leakage (red arrow) in the retina. RV: retinal vein occlusion. FC: fundus camera. FFA: fluorescence fundus angiography.

Table 1: Demographics and clinical measurements of RVO and HC groups.

Characteristic	RVO	HC
Male/female	8/6	8/6
Age (years)	52.22 ± 5.95	52.12 ± 5.01
Weight (kg)	51.23 ± 9.11	52.35 ± 10.09
Handedness	14R	14R

RVO: retinal vein occlusion. HC: healthy control. N/A: not applicable. R: right. L: left.

were statistically significant through multiple complete corrected comparisons.

3. Results

The demographic and clinicopathological factors of patients are shown in Table 1. The average ages of RVO patients and HCs were 52.22 ± 5.95 and 52.12 ± 5.01, respectively. The average weights of RVO patients and HCs were 51.23 ± 9.11 and 52.35 ± 10.09, respectively.

The comparison of voxel clusters between two groups in FA and RD presented a notably difference. The declining mean FA value of total cerebrum in RVO group was detected (Table 2). Additionally, the mean RD value of total cerebrum in RVO patients was higher than that in HCs (Table 3). The patients showed significantly lower FA values and higher RD values in five clusters: the bilateral posterior thalamic radiation, bilateral sagittal stratum, body of corpus callosum, cingulum, and fornix (Figures 2 and 3).

3.1. ROC Curve. The areas under the ROC curve for the FA values were as follows: the body of corpus callosum (CC), 0.862 ($p < 0.001$; 95% CI: 0.719–1.000); the right posterior thalamic radiation (RPTR), 0.883 ($p < 0.001$; 95% CI: 0.759–1.000); the left posterior thalamic radiation (LPTR), 0.959 ($p < 0.001$; 95% CI: 0.896–1.000); the right sagittal stratum (RSS), 0.770 ($p < 0.001$; 95% CI: 0.595–0.946); the left sagittal stratum (LSS), 0.837 ($p < 0.001$; 95% CI: 0.667–1.000); the right cingulum (RC), 0.893 ($p < 0.001$; 95% CI: 0.773–1.000); and the left fornix/stria terminalis (LF/ST), 0.796 ($p < 0.001$; 95% CI: 0.620–0.971) (Figure 4(a)).

Table 2: Clusters showing significant differences in FA between RVO patients and HCs.

Variable	Comparison	TFCE corrected p	Cluster number	MNI coordinates			T values
	RVO<HCs			X	Y	Z	
FA	BCC	<0.01	1	81	96	96	−6.254
	RPTR		2	58	83	89	−5.185
	LPTR		3	119	62	90	−6.025
	RSS		4	53	71	67	−4.187
	LSS		5	130	89	61	−5.029
	RC		6	79	79	97	−5.162
	LF		7	116	96	68	−4.587

RVO: retinal vein occlusion. HC: healthy control. BCC: body of corpus callosum. RPCR: right posterior corona radiata. LPTR: left posterior thalamic radiation. RSS: right sagittal stratum. LSS: left sagittal stratum. RC: right cingulum. LF: left fornix.

The areas under the ROC curve for the RD values were as follows: the body of CC, 0.923 ($p < 0.001$; 95% CI: 0.816–1.000); the RPTR, 0.918 ($p < 0.001$; 95% CI: 0.817–1.000); the LPTR, 0.969 ($p < 0.001$; 95% CI: 0.917–1.000); the RSS, 0.959 ($p < 0.001$; 95% CI: 0.896–1.000); the LSS, 0.908 ($p < 0.001$; 95% CI: 0.792–1.000); the RC, 0.847 ($p < 0.001$; 95% CI: 0.685–1.000); the LF/ST, 0.908 ($p < 0.001$; 95% CI: 0.792–1.000) (Figure 4(b)).

3.2. Correlation Analysis. The average FA value of the whole brain was positively correlated with the NEI-VFQ25 score ($r = 0.769$, $p = 0.001$) and negatively correlated with the HADS score ($r = -0.863$, $p < 0.0001$) in RVO patients. The mean RD value of the total cerebrum negatively correlated with the NEI-VFQ25 score ($r = -0.866$, $p < 0.0001$) and positively correlated with the HADS score ($r = 0.898$, $p < 0.0001$) (Figure 5).

4. Discussion

This study is the first TBSS analysis of RVO patients. We adopted DTI scanning and TBSS analysis to probe the fiber bundle architecture differences between the objective group and the HCs. To be brief, our findings were that there were

Table 3: Clusters showing significant differences in RD between RVO patients and HCs.

Variable	Comparison Patients > HCs	TFCE corrected p	Cluster number	MNI coordinates			T values
				X	Y	Z	
RD	BCC	<0.01	1	80	96	96	5.256
	RPTR		2	58	65	72	4.298
	LPTR		3	117	63	87	6.248
	RSS		4	51	91	68	3.284
	LSS		5	130	89	61	4.096
	RC		6	82	96	103	5.267
	LF		7	121	100	66	5.019

RVO: retinal vein occlusion. HC: healthy control. BCC: body of corpus callosum. RPCR: right posterior corona radiata. LPTR: left posterior thalamic radiation. RSS: right sagittal stratum. LSS: left sagittal stratum. RC: right cingulum. LF: left fornix.

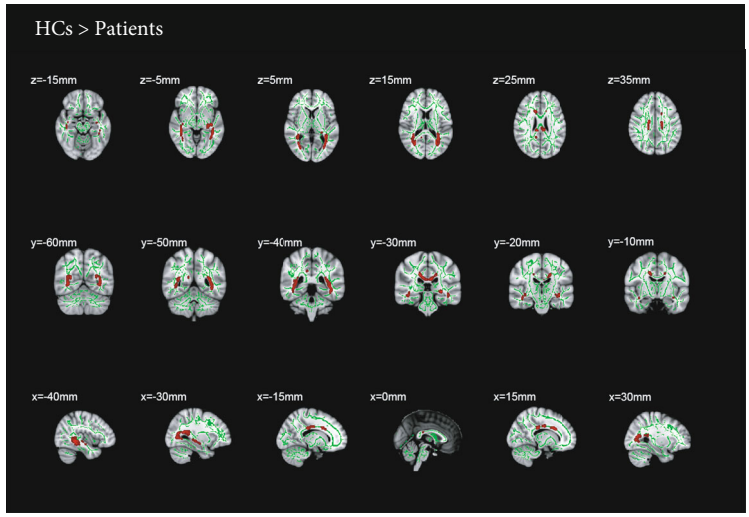

Figure 2: Results of whole-brain tract-based spatial statistics analysis comparing fractional anisotropy between RVO patients and HCss. The skeleton image (green = RD > 0.2) was overlaid by the mean fractional anisotropy image. And the red areas indicate all tracts with significantly decreased RD values in the RVO patients, which may reflect abnormal white matter integrity ($p < 0.05$). Significantly lower fractional anisotropy values were shown in the body of corpus callosum, right posterior thalamic radiation, left posterior thalamic radiation, right sagittal stratum, left sagittal stratum, right cingulum, left fornix/stria terminalis. RVO: retinal vein occlusion. HCs: healthy controls.

significant differences in voxel clusters, and RVO patients showed lower FA values than the other group, whereas higher RD values were presented.

Until now, the TBSS approach for DTI analysis has been widely used in neuroimaging studies. Compared to the statistical parametric mapping–based approach, TBSS averts the insufficiency about registration and smoothing of diffusion data. Furthermore, in TBSS, we can investigate the brain globally rather than specified certain tracts [16, 23].

In this study, DTI and TBSS were applied in RVO patients and we found reduced FA and increased RD in the B.PTR (involve the optic radiation) which is relevant for the connection between the thalamus and the visual cortex [24]. Previous voxel-based morphometry showed that reduced gray matter density in the occipital lobe has been demonstrated in patients with diabetic retinopathy [25]. Malania et al. [26] have found significant diffusion abnormalities along the visual pathways in patients with macular degeneration. Additionally, low FA in optic tract was especially detected in patients with retinitis pigmentosa in a previous study [27]. As the transmission of visual information involves the whole visual system. It is assumed that the damage at retina could trigger microstructural changes in brain. FA value is influenced by various neurostructural factors and a decrease in FA was interpreted as structural damage in nerve bundle [28]. Consistent with the above results, the decreased FA in our study indicated that the integrity of tracts was impaired in RVO patients. An increase in RD indicated the destruction of cell structure and myelin damage [29, 30]. We further infer that an increase in RD suggests that some pathologic alterations in PTR, representing the underlying neuropathologic mechanism. Consequently, we further deduce that this alteration might lead to visual damage in RVO patients.

The sagittal stratum, a large sagittal structure, consists of inferior longitudinal fasciculus (ILF), inferior fronto-occipital fasciculus (IFO), and other projection fibers [24, 31]. ILF and IFO are closely related to visual information

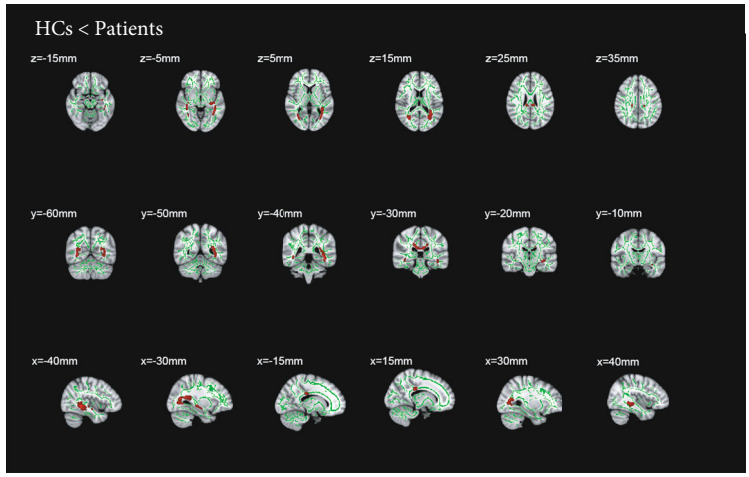

Figure 3: Comparison of radial diffusivity in RVO patients and HCs. The skeleton image (green = RD > 0.2) was overlaid by the mean fractional anisotropy image. And the red areas indicate all tracts with significantly increased RD values in the RVO patients, which may reflect abnormal white matter integrity ($p < 0.05$). The statistically significant clusters are presented at different coordinates in these six parts. These clusters include body of corpus callosum, right posterior thalamic radiation, left posterior thalamic radiation, right sagittal stratum, left sagittal stratum, right cingulum, left fornix/stria terminalis. RVO: retinal vein occlusion. HCs: healthy controls.

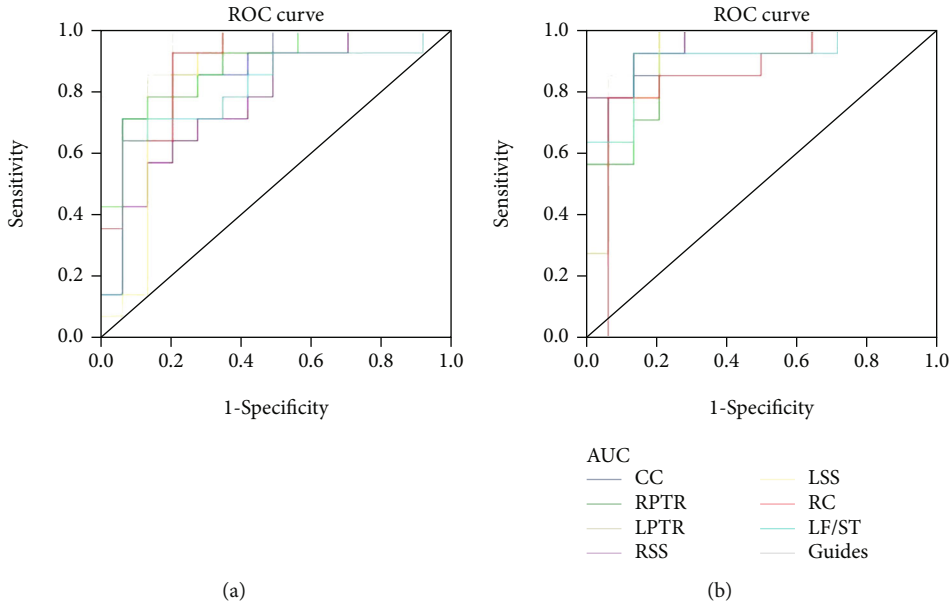

Figure 4: ROC curve analysis of the mean FA and RD values for altered brain regions. (a) The areas under the ROC curve for the FA values were as follows: the body of corpus callosum (CC), 0.862 ($p < 0.001$; 95% CI: 0.719–1.000); the right posterior thalamic radiation (RPTR), 0.883 ($p < 0.001$; 95% CI: 0.759–1.000); the left posterior thalamic radiation (LPTR), 0.959 ($p < 0.001$; 95% CI: 0.896–1.000); the right sagittal stratum (RSS), 0.770 ($p < 0.001$; 95% CI: 0.595–0.946); the left sagittal stratum (LSS), 0.837 ($p < 0.001$; 95% CI: 0.667–1.000); the right cingulum (RC), 0.893 ($p < 0.001$; 95% CI: 0.773–1.000); the left fornix/stria terminalis (LF/ST), 0.796 ($p < 0.001$; 95% CI: 0.620–0.971). (b) The areas under the ROC curve for the RD values were as follows: the body of CC, 0.923 ($p < 0.001$; 95% CI: 0.816–1.000); the RPTR, 0.918 ($p < 0.001$; 95% CI: 0.817–1.000); the LPTR, 0.969 ($p < 0.001$; 95% CI: 0.917–1.000); the RSS, 0.959 ($p < 0.001$; 95% CI: 0.896–1.000); the LSS, 0.908 ($p < 0.001$; 95% CI: 0.792–1.000); the RC, 0.847 ($p < 0.001$; 95% CI: 0.685–1.000); the LF/ST, 0.908 ($p < 0.001$; 95% CI: 0.792–1.000). AUC: area under the curve, FA: fractional anisotropy, RD: radial diffusivity, ROC: receiver operating characteristic, CC: corpus callosum, RPTR: right posterior thalamic radiation, LPTR: left posterior thalamic radiation, RSS: right sagittal stratum, LSS: left sagittal stratum, RC: right cingulum, LF/ST: left fornix/stria terminalis.

processing. The ILF provides pivotal connections between occipital and anterior temporal regions and also is closely associated with the optic radiations. A study focusing on functional anatomy of the ILF suggested that it mediated process of visual memory and recognition of visual information [32, 33]. The IFO was considered to connect with different cortical regions within the frontal, occipital, and temporal lobes. Study have once showed that IFO have a

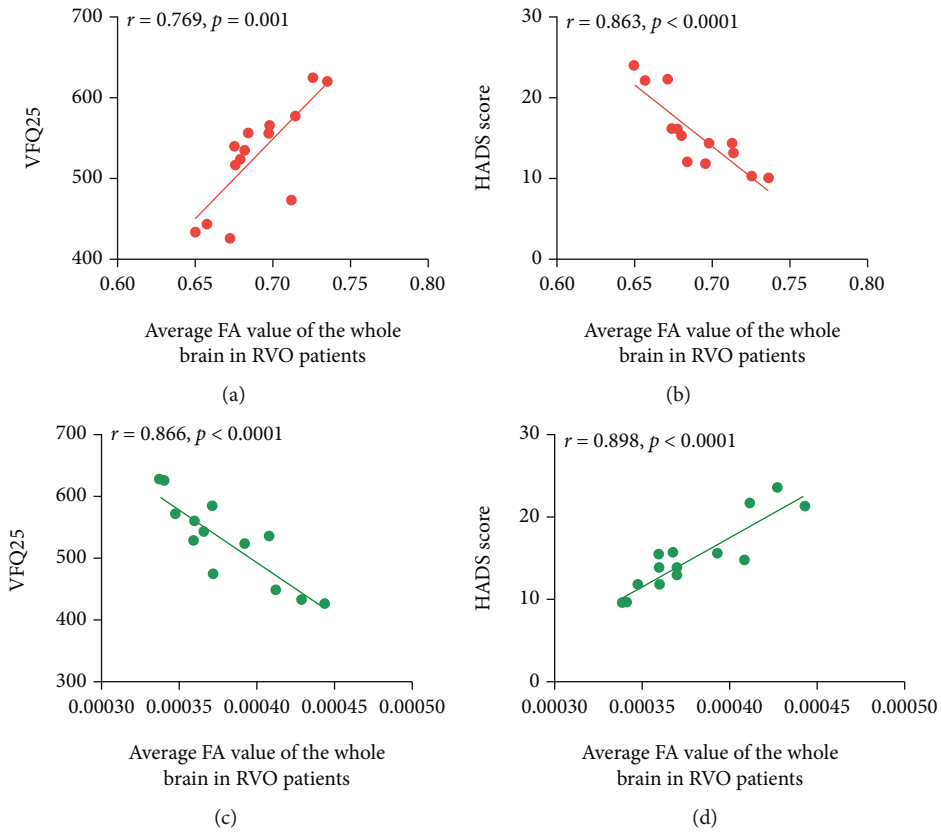

Figure 5: Correlation between the average FA and RD values of the whole brain in RVO patients and anxiety, depression and NEI-VFQ25 scores. (a) The average FA value of the whole brain was positively correlated with the NEI-VFQ25 score ($r = 0.769$, $p = 0.001$). (b) The average FA value of the whole brain was negatively correlations with the HADS score ($r = -0.863$, $p < 0.0001$). (c) The average RD value of the whole brain displayed negatively correlated with the NEI-VFQ25 score ($r = -0.866$, $p < 0.0001$). (d) The average RD value of the whole brain displayed positively correlations with the HADS score ($r = 0.898$, $p < 0.0001$). RVO: retinal vein occlusion. FA: fractional anisotropy. RD: radial diffusivity.

critical meaning in visual processing and reading [34, 35]. In similar visual neuroscience studies, Li et al. [15] used DTI method and indicated significant decreases in FA values in left ILF/IFO in children with anisometropic amblyopia. Li D. et al. [18] found an increased FA values in ILF and IFO in patients with comitant exotropia. Furthermore, Cheng et al. [36] reported that dyslexia may related to visual perception deficits. In current study, changed FA and RD values of SS suggested that relevant nerve tract was damaged in RVO patients, indicating visual information processing disorder and visual dysfunction. On the other hand, it was affirmed that the higher order visual processing systems of normal individuals is hierarchically organized into two functionally systems, the dorsal and ventral visual pathway [37]. The ventral stream consists of the IFO and the ILF principally, which is relevant to object recognition [38]. A DTI study has shown that the microstructure of the ventral stream changed in blind patients [39]. Therefore, the alterations in FA and RD values of sagittal stratum might clarify the visual impairment in RVO patients.

The corpus callosum is located at the base of the longitudinal fissure of the cerebral hemisphere. As the largest bundle of connective fibers in the human brain, it connects cortical regions of both hemispheres [40]. The major function of CC is to integrate information such as motor sensation and cognitive activity between two cerebral hemispheres [41]. Reports in the literature indicated that the CC has an intimate connection to the visual cortex. The well connectivity of the callosal fibers is influenced by alterations of visual input [42]. Kwinta et al. detected low FA values of the CC in premature infants with abnormal stereoscopic vision and visual perception [43]. Consistent with previous researches, we speculated that the decrease of FA and increase of RD indicated the integrity of inner structure of the CC was damaged and potential pathologic changes or degeneration may occur in the callosal fibers in RVO patients, which may leads to inability to integrate visual information and further cause visual deprivation.

Interestingly, in addition to vision-related regions, we also found changed FA and RD values in extravisual-related regions including cingulum and fornix. As one of the most distinctive fiber tracts in the brain, cingulum connects frontal, parietal, and temporal sites. The largest efferent pathway in the hippocampus is the fornix, which is the critical component of the limbic system of brain [44, 45]. According to previous studies, significantly decreased FA value of cingulum was discovered in depression patients [44]. McCarthy-Jones et al. [46] found reduced integrity of

fornix in the process of childhood adversity. Therefore, the limbic system plays an important role in regulating sensory information in the central nervous system. Previous studies have confirmed that patients with visual field and acuity loss have psychological and emotional disorders [47, 48]. On the basis of the above studies, the decrease of FA value in RVO patients may reflect the injury of nerve tracts related to emotion management. Moreover, Schafer et al. [48] have discovered that the autistic neurons grow faster and have more complex branches. We speculate that the increased RD values in correlative tracts may clarify the neuropathologic mechanism of RVO, which tries to repair nerve tract damage by enhancing neuronal branching to improve their function. Hence, visual impairment defects increase the psychological disorders of RVO patients. Our findings may contribute to illustrate the causes of negative emotions in RVO patients. In addition to treatment at the disease itself, focusing more on the psychotherapy may improve the prognosis of RVO patients.

Our current research has some boundedness. First, the sample capacity of RVO subjects is relatively small. We need larger samples for further study. Secondly, there are many aetiological causes of RVO, which may cause individual differences and lead to imprecise results of TBSS measurements. Additionally, we merely analyze the diffusivities separately and we believe it is necessary to investigate the interaction between FA and RD values.

5. Conclusion

It was shown that some structural alterations of correlative tracts developed, which may reveal the neuropathologic mechanism and may be responsible for the visual impairment in RVO patients. Overall, DTI with the TBSS method is an available tool to indicate the potential intracephalic tract involvement in RVO patients.

Abbreviations

RVO: Retinal vein occlusion
FC: Fundus camera
FFA: Fluorescence fundus angiography
HCs: Healthy controls
AUC: Area under the curve
FA: Fractional anisotropy
RD: Radial diffusivity
ROC: Receiver operating characteristic
CC: Corpus callosum
RPTR: Right posterior thalamic radiation
LPTR: Left posterior thalamic radiation
RSS: Right sagittal stratum
LSS: Left sagittal stratum
RC: Right cingulum
LF/ST: Left fornix/stria terminalis.

Data Availability

The data used to support the findings of this study are available from the corresponding author upon request.

Ethical Approval

This study was performed under the approval of the medical research ethics committee of the First Affiliated Hospital of Nanchang University. The methods in this study were conducted under relevant guidelines and regulations. All participants involved were offered the whole study design and signed the informed consent.

Consent

Each participant provided written informed consent. The ethical committee of the First Affiliated Hospital of Nanchang University has approved this study. Informed consent was obtained from all the patients included in this study.

Conflicts of Interest

The authors report no conflicts of interest in this work.

Acknowledgments

The Central Government Guides Local Science and Technology Development Foundation (No: 20211ZDG02003); Key Research Foundation of Jiangxi Province (No:20181BBG70004 and 20203BBG73059); Excellent Talents Development Project of Jiangxi Province (No: 20192BCBL23020); Natural Science Foundation of Jiangxi Province (No: 20181BAB205034); Grassroots Health Appropriate Technology "Spark Promotion Plan" Project of Jiangxi Province (No: 20188003); Health Development Planning Commission Science Foundation of Jiangxi Province (No: 20201032 and 202130210); Health Development Planning Commission Science TCM Foundation of Jiangxi Province (No: 2018A060 and 2020A0087); and Education Department Foundation of Jiangxi Province (No: GJJ200157, GJJ200159, and GJJ200169) funded this study.

References

[1] G. Coscas, A. Loewenstein, A. Augustin et al., "Management of retinal vein occlusion-consensus document," *Ophthalmologica*, vol. 226, no. 1, pp. 4–28, 2011.

[2] M. Rehak and P. Wiedemann, "Retinal vein thrombosis: pathogenesis and management," *Journal of Thrombosis and Haemostasis*, vol. 8, no. 9, pp. 1886–1894, 2010.

[3] N. Karia, "Retinal vein occlusion: pathophysiology and treatment options," *Clinical Ophthalmology*, vol. 4, pp. 809–816, 2010.

[4] M. Ho, D. T. Liu, D. S. Lam, and J. B. Jonas, "Retinal vein occlusions, from basics to the latest treatment," *Retina*, vol. 36, no. 3, pp. 432–448, 2016.

[5] A. Jaulim, B. Ahmed, T. Khanam, and I. P. Chatziralli, "Branch retinal vein OCCLUSION," *Retina (Philadelphia, Pa)*, vol. 33, no. 5, pp. 901–910, 2013.

[6] J. B. Jonas, J. Monés, A. Glacet-Bernard, and G. Coscas, "Retinal vein occlusions," *Developments in Ophthalmology*, vol. 58, pp. 139–167, 2017.

[7] H. Iijima, "Mechanisms of vision loss in eyes with macular edema associated with retinal vein occlusion," *Japanese Journal of Ophthalmology*, vol. 62, no. 3, pp. 265–273, 2018.

[8] U. Mutlu, L. G. Cremers, M. de Groot et al., "Retinal microvasculature and white matter microstructure," *Neurology*, vol. 87, pp. 1003–1010, 2016.

[9] E. A. Novais and N. K. Waheed, "Optical coherence tomography angiography of retinal vein occlusion," *Developments in Ophthalmology*, vol. 56, pp. 132–138, 2016.

[10] E. H. de Figueiredo, A. F. Borgonovi, and T. M. Doring, "Basic concepts of MR imaging, diffusion MR imaging, and diffusion tensor imaging," *Magnetic Resonance Imaging Clinics of North America*, vol. 19, no. 1, pp. 1-2, 2011.

[11] S. Shaikh, A. Kumar, and A. Bansal, "Diffusion tensor imaging: an overview," *Neurology India*, vol. 66, no. 6, pp. 1603–1611, 2018 Nov-Dec.

[12] L. R. Ranzenberger and T. Snyder, *Diffusion Tensor Imaging*, Stat Pearls Publishing, Treasure Island (FL), 2018.

[13] D. Qiu, L. H. Tan, K. Zhou, and P. L. Khong, "Diffusion tensor imaging of normal white matter maturation from late childhood to young adulthood: voxel-wise evaluation of mean diffusivity, fractional anisotropy, radial and axial diffusivities, and correlation with reading development," *NeuroImage*, vol. 41, no. 2, pp. 223–232, 2008.

[14] K. Li, C. Lu, Y. Huang, L. Yuan, D. Zeng, and K. Wu, "Alteration of fractional anisotropy and mean diffusivity in glaucoma: novel results of a meta-analysis of diffusion tensor imaging studies," *PLoS One*, vol. 9, no. 5, article e97445, 2014.

[15] Q. Li, L. Zhai, Q. Jiang et al., "Tract-based spatial statistics analysis of white matter changes in children with anisometropic amblyopia," *Neuroscience Letters*, vol. 597, pp. 7–12, 2015.

[16] S. M. Smith, M. Jenkinson, H. Johansen-Berg et al., "Tract-based spatial statistics: voxelwise analysis of multi-subject diffusion data," *NeuroImage*, vol. 31, no. 4, pp. 1487–1505, 2006.

[17] S. M. Smith, H. Johansen-Berg, M. Jenkinson et al., "Acquisition and voxelwise analysis of multi-subject diffusion data with tract-based spatial statistics," *Nature Protocols*, vol. 2, no. 3, pp. 499–503, 2007.

[18] D. Li, S. Li, and X. Zeng, "Analysis of alterations in white matter integrity of adult patients with comitant exotropia," *The Journal of International Medical Research*, vol. 46, no. 5, pp. 1963–1972, 2018.

[19] D. W. Wang, W. Qin, Y. Liu, Y. Zhang, T. Jiang, and C. Yu, "Altered white matter integrity in the congenital and late blind people," *Neural Plasticity*, vol. 2013, Article ID 128236, 8 pages, 2013.

[20] Y. X. Liu, B. Li, K. R. Wu et al., "Altered white matter integrity in patients with monocular blindness: a diffusion tensor imaging and tract-based spatial statistics study," *Brain and Behavior: A Cognitive Neuroscience Perspective*, vol. 10, no. 8, article e01720, 2020.

[21] A. S. Zigmond and R. P. Snaith, "The hospital anxiety and depression scale," *Acta Psychiatrica Scandinavica*, vol. 67, no. 6, pp. 361–370, 1983.

[22] C. M. Mangione, P. P. Lee, P. R. Gutierrez, K. Spritzer, S. Berry, and R. D. Hays, "Development of the 25-list-item National Eye Institute Visual Function questionnaire," *Archives of Ophthalmology*, vol. 119, no. 7, pp. 1050–1058, 2001.

[23] O. Abe, H. Takao, W. Gonoi et al., "Voxel-based analysis of the diffusion tensor," *Neuroradiology*, vol. 52, no. 8, pp. 699–710, 2010.

[24] A. Aralasmak, J. L. Ulmer, M. Kocak, C. V. Salvan, A. E. Hillis, and D. M. Yousem, "Association, commissural, and projection pathways and their functional deficit reported in literature," *Journal of Computer Assisted Tomography*, vol. 30, no. 5, pp. 695–715, 2006.

[25] A. M. Wessels, S. Simsek, P. L. Remijnse et al., "Voxel-based morphometry demonstrates reduced grey matter density on brain MRI in patients with diabetic retinopathy," *Diabetologia*, vol. 49, no. 10, pp. 2474–2480, 2006.

[26] N. Ohno, H. Murai, Y. Suzuki et al., "Alteration of the optic radiations using diffusion-tensor MRI in patients with retinitis pigmentosa," *The British Journal of Ophthalmology*, vol. 99, no. 8, pp. 1051–1054, 2015.

[27] M. Malania, J. Konrad, H. Jägle, J. S. Werner, and M. W. Greenlee, "Compromised integrity of central visual pathways in patients with macular degeneration," *Investigative Ophthalmology & Visual Science*, vol. 58, no. 7, pp. 2939–2947, 2017.

[28] R. Wang, Z. Tang, X. Sun et al., "White matter abnormalities and correlation with severity in Normal tension glaucoma: a whole brain atlas-based diffusion tensor study," *Investigative Ophthalmology & Visual Science*, vol. 59, no. 3, pp. 1313–1322, 2018.

[29] S. K. Song, S. W. Sun, M. J. Ramsbottom, C. Chang, J. Russell, and A. H. Cross, "Dysmyelination revealed through MRI as increased radial (but unchanged axial) diffusion of water," *NeuroImage*, vol. 17, no. 3, pp. 1429–1436, 2002.

[30] S. K. Song, J. Yoshino, L. S. J. Le TQ, S. W. Sun, A. H. Cross, and R. C. Armstrong, "Demyelination increases radial diffusivity in corpus callosum of mouse brain," *NeuroImage*, vol. 26, no. 1, pp. 132–140, 2005.

[31] S. Mori, K. Oishi, H. Jiang et al., "Stereotaxic white matter atlas based on diffusion tensor imaging in an ICBM template," *NeuroImage*, vol. 40, no. 2, pp. 570–582, 2008.

[32] G. Herbet, I. Zemmoura, and H. Duffau, "Functional anatomy of the inferior longitudinal fasciculus: from historical reports to current hypotheses," *Frontiers in Neuroanatomy*, vol. 12, p. 77, 2018.

[33] F. Latini, J. Mårtensson, E. M. Larsson et al., "Segmentation of the inferior longitudinal fasciculus in the human brain: a white matter dissection and diffusion tensor tractography study," *Brain Research*, vol. 1675, pp. 102–115, 2017.

[34] J. Martino, C. Brogna, S. G. Robles, F. Vergani, and H. Duffau, "Anatomic dissection of the inferior fronto-occipital fasciculus revisited in the lights of brain stimulation data," *Cortex*, vol. 46, no. 5, pp. 691–699, 2010.

[35] C. Rollans, K. Cheema, G. K. Georgiou, and J. Cummine, "Pathways of the inferior frontal occipital fasciculus in overt speech and reading," *Neuroscience*, vol. 364, pp. 93–106, 2017.

[36] D. Cheng, Q. Xiao, Q. Chen, J. Cui, and X. Zhou, "Dyslexia and dyscalculia are characterized by common visual perception deficits," *Developmental Neuropsychology*, vol. 43, no. 6, pp. 497–507, 2018.

[37] M. Mishkin, L. G. Ungerleider, and K. A. Macko, "Object vision and spatial vision: two cortical pathways," *Trends in Neurosciences*, vol. 6, pp. 414–417, 1983.

[38] D. Kravitz, K. S. Saleem, C. I. Baker, L. G. Ungerleider, and M. Mishkin, "The ventral visual pathway: an expanded neural framework for the processing of object quality," *Trends in Cognitive Sciences*, vol. 17, no. 1, pp. 26–49, 2013.

[39] N. L. Reislev, R. Kupers, H. R. Siebner, M. Ptito, and T. B. Dyrby, "Blindness alters the microstructure of the ventral but

not the dorsal visual stream," *Brain Structure & Function*, vol. 221, no. 6, pp. 2891–2903, 2016.

[40] B. A. Georgy, J. R. Hesselink, and T. L. Jernigan, "MR imaging of the corpus callosum," *MR imaging of the corpus callosum AJR Am J Roentgenol.*, vol. 160, no. 5, pp. 949–955, 1993.

[41] T. J. Herron, K. Xiaojian, and D. L. Woods, "Automated measurement of the human corpus callosum using MRI," *Frontiers in Neuroinformatics*, vol. 6, 2012.

[42] M. Pietrasanta, L. Restani, and M. Caleo, "The corpus callosum and the visual cortex: plasticity is a game for two," *Neural Plasticity*, vol. 2012, Article ID 838672, 10 pages, 2012.

[43] P. Kwinta, I. Herman-Sucharska, A. Leśniak et al., "Relationship between stereoscopic vision, visual perception, and microstructure changes of corpus callosum and occipital white matter in the 4-year-old very low birth weight children," *BioMed Research International*, vol. 2015, 842149 pages, 2015.

[44] E. J. Bubb, C. Metzler-Baddeley, and J. P. Aggleton, "The cingulum bundle: anatomy, function, and dysfunction," *Neuroscience and Biobehavioral Reviews*, vol. 92, pp. 104–127, 2018.

[45] D. Vanessa and C. Linda, "Fornix as an imaging marker for episodic memory deficits in healthy aging and in various neurological disorders," *Frontiers in Aging Neuroscience*, vol. 6, 2015.

[46] K. D. Bhatia, L. A. Henderson, E. Hsu, and M. Yim, "Reduced integrity of the uncinate fasciculus and cingulum in depression: a stem-by-stem analysis," *Journal of Affective Disorders*, vol. 235, pp. 220–228, 2018.

[47] L. Azoulay, P. Chaumet-Riffaud, S. Jaron et al., "Threshold levels of visual field and acuity loss related to significant decreases in the quality of life and emotional states of patients with retinitis pigmentosa," *Ophthalmic Research*, vol. 54, no. 2, pp. 78–84, 2015.

[48] E. K. Fenwick, P. G. Ong, R. E. K. Man et al., "Vision impairment and major eye diseases reduce vision-specific emotional well-being in a Chinese population," *The British Journal of Ophthalmology*, vol. 101, no. 5, pp. 686–690, 2017.

Hindawi
Disease Markers
Volume 2022, Article ID 7729968, 11 pages
https://doi.org/10.1155/2022/7729968

Research Article

IDH1 Mutation Induces HIF-1α and Confers Angiogenic Properties in Chondrosarcoma JJ012 Cells

Xiaoyu Hu,[1,2] Luyuan Li,[3,4] Josiane E. Eid,[3,4] Chao Liu,[2] Jinming Yu,[1,2] Jinbo Yue,[2] and Jonathan C. Trent[3,4]

[1]*Department of Oncology, Renmin Hospital of Wuhan University, Wuhan, China*
[2]*Department of Radiation Oncology, Shandong Cancer Hospital and Institute, Shandong First Medical University and Shandong Academy of Medical Sciences, Jinan, Shandong, China*
[3]*Department of Medicine, Division of Medical Oncology, University of Miami Miller School of Medicine, Miami, USA*
[4]*Sylvester Comprehensive Cancer Center, University of Miami Miller School of Medicine, Miami, USA*

Correspondence should be addressed to Jinming Yu; sdyujinming@163.com, Jinbo Yue; jbyue@sdfmu.edu.cn, and Jonathan C. Trent; jtrent@med.miami.edu

Xiaoyu Hu and Luyuan Li contributed equally to this work.

Received 12 September 2021; Accepted 15 December 2021; Published 14 February 2022

Academic Editor: Ting Su

Chondrosarcoma is a group of primary bone cancers that arise from transformed cells of chondrocytic lineage. Tumor recurrence and metastasis are devastating for patients with chondrosarcoma since there are no effective treatment options. IDH mutations occur in over 50% of tumors from patients with conventional or dedifferentiated chondrosarcomas and represent an attractive target for therapy. However, their role in the pathogenesis of chondrosarcoma remains largely unknown. In this study, we sought to determine the association of IDH mutation and HIF-1α in chondrosarcoma. We used the chondrosarcoma JJ012 cell line and its derived CRISPR/Cas9 mutant IDH1 (IDH1^{mut}) knockout (KO) cells. RNA-Seq data analysis revealed downregulation of several HIF-1α target genes upon loss of IDH1^{mut}. This was associated with reduced HIF-1α levels in the IDH1^{mut} KO cells and tumors. Loss of IDH1^{mut} also attenuated the expression of angiogenic markers in tumor tissues and abrogated the angiogenic capacity of JJ012 cells. Moreover, we observed that exogenous expression of HIF-1α significantly promoted anchorage-independent colony-formation by IDH1^{mut} KO cells. These results suggest IDH1 mutation confers angiogenic and tumorigenic properties of JJ012 cells by inducing HIF-1α. Thus, the HIF pathway represents a promising candidate for combinatorial regimens to target IDH1 mutated chondrosarcomas.

1. Introduction

Chondrosarcomas constitute a heterogeneous group of primary bone cancers characterized by the formation of a hyaline cartilaginous matrix. Following osteosarcoma, chondrosarcoma is the second most common bone malignancy, accounting for 20% to 27% of primary bone tumors [1, 2]. Approximately 85% of chondrosarcomas are the conventional subtypes which can be further classified into central, peripheral, and periosteal lesions. The remaining 10–15% consist of rare subtypes including dedifferentiated, mesenchymal, clear cell, and myxoid chondrosarcoma. Chondrosarcomas are notoriously resistant to chemotherapy and radiotherapy, and surgery is the backbone treatment for most localized tumors [2, 3]. Chondrosarcomas tend to recur with more aggressive behavior than the original neoplasm following initial tumor resection. As a result, many patients develop metastatic disease which is nearly uniformly fatal. Due to lack of effective treatment strategies for recurrent or metastatic chondrosarcoma, high-grade conventional and dedifferentiated chondrosarcomas have poor prognosis [1, 4]. Current studies focus on clarifying the link between molecular events and pathogenesis of this malignancy and developing new molecularly targeted therapies for advanced diseases.

Isocitrate dehydrogenase (IDH) mutation is among one of the promising therapeutic targets. IDH1/2 mutations were found in 71% of conventional chondrosarcomas and 57% of dedifferentiated chondrosarcomas [4, 5], as well as in gliomas and acute myeloid leukemia [6, 7], suggesting a potential role for aberrant IDH function in the pathogenesis of these malignancies. IDHs normally convert isocitrate to α-ketoglutarate (α-KG). However, mutant IDHs lose the ability to catalyze this reaction but instead gain a neomorphic function of reducing α-KG to D-2-hydroxyglutarate (D-2HG), which has been reported to accumulate at high levels in IDH1/2-mutated tumors [8, 9]. D-2HG and α-KG are structurally similar. Thus, accumulated D-2HG is thought to act as an oncometabolite through the inhibition of various α-KG-dependent enzymes including the TET family of 5-methycytosine hydroxylases, JumonjiC domain-containing histone demethylases (JHDMs), and the Prolyl Hydroxylase Domain-Containing Proteins (PHDs) [9–11].

HIF-1α, a key hypoxia-inducible transcription factor, is associated with tumor development as it functions as a master regulator of genes involved in angiogenesis, glucose metabolism, and other cellular pathways [12]. HIF-1α overexpression is correlated with disease progression, chemoradio-resistance, and increased patient mortality in certain cancers [13–15]. The stability and transcriptional activity of HIF-1α are regulated by PHDs (PHD1, PHD2, and PHD3). Under normal oxygen conditions, PHDs utilize α-KG and O_2 to hydroxylate a conserved proline in HIF-1α, leading to Von Hippel-Lindau- (VHL-) mediated ubiquitination and subsequent proteasomal degradation of HIF-1α [16, 17]. In hypoxic conditions, however, these hydroxylation events cannot proceed efficiently, resulting in accumulation of HIF-1α [18]. Interestingly, studies examining the effects of D-2HG on PHDs and HIF-1α in IDH-mutant gliomas and leukemias have yielded conflicting results. It has been reported that D-2HG competitively inhibits the activity of PHDs as mentioned above and thus leads to increased levels of HIF-1α [18, 19]. Conversely, D-2HG was shown to act as an activator rather than an inhibitor of PHDs, ultimately leading to decreased levels of HIF-1α [20, 21]. In contrast to the emerging knowledge in gliomas and leukemias, little is known regarding the effect of IDH mutation or D-2HG on HIF-1α activity in chondrosarcoma. Understanding their relationship would have great clinical importance in terms of developing novel targeted therapies for advanced chondrosarcomas.

In this study, we sought to determine the potential association of IDH mutation and HIF-1α in chondrosarcoma. We employed the IDH1-mutant chondrosarcoma JJ012 cell line, CRSPR/Cas9 mutant IDH1 ($IDH1^{mut}$) knockout (KO) JJ012 clones, and their derived xenografts. We found that CRISPR/Cas9 knockout of $IDH1^{mut}$ reduced HIF-1α levels *in vitro* and *in vivo*, leading to downregulation of HIF-1α target genes. Loss of $IDH1^{mut}$ also decreased the expression of angiogenic markers in tumors and attenuated the angiogenic capacity of JJ012 cells. Moreover, we observed restoring HIF-1α levels with exogenous expression significantly enhanced the anchorage-independent growth of $IDH1^{mut}$ KO cells. These results suggest IDH1 mutation confers tumorigenic and angiogenic properties by inducing HIF-1α in a JJ012 chondrosarcoma model.

2. Materials and Methods

2.1. Cell Culture. The human chondrosarcoma JJ012 and human chondrocyte C28 cell lines were kindly provided by Dr. Joel Block and Dr. Karina Galoian, respectively. JJ012 harbors a monoallelic IDH1 R132G mutation while C28 carries wildtype IDH1 ($IDH1^{wt}$). JJ012 cells were cultured in RPMI-1640 medium (Lonza) supplemented with 10% fetal bovine serum (FBS) and 1% Penicillin/Streptomycin. C28 cells were grown in 1 : 1 DMEM/F12 medium (HyClone) supplemented with 10% FBS and 1% Penicillin/Streptomycin. Human umbilical vein endothelial cells (HUVECs) were obtained from Thermo Fisher Scientific and grown in Endothelial Cell Growth Medium 2 (EGM-2) (PromoCell) on 0.1% gelatin-coated plates. Cells were maintained at 37°C in a humidified air with 5% CO_2.

2.2. IDH1 Knockout by CRISPR/Cas9 Technology. Knockout of $IDH1^{mut}$ was achieved by the CRISPR/Cas9 system. The CRISPR/Cas9 plasmid products were purchased from Santa Cruz Biotechnology. Details of transfection, selection, and single-cell colonies propagation were previously described [22].

2.3. Measurement of D-2HG. Quantitative analyses of D-2HG were conducted by high-performance liquid chromatography–tandem mass spectrometry (HPLC-MS/MS) with single-reaction monitoring (SRM) scans. This was performed at MtoZ Biolabs (Boston, MA, USA).

2.4. Tumor Tissues. Tumor samples were obtained from mice-bearing chondrosarcoma xenografts which were derived from JJ012 parental and $IDH1^{mut}$ KO cells, as previously described. All animal experiments were performed in compliance with the University of Miami Institutional Animal Care and Use Committee (IACUC)-approved protocol (No. 19-079).

2.5. RNA-Seq and Ingenuity Pathway Analysis (IPA). RNA-Seq and IPA were described with details previously [22].

2.6. Quantitative Reverse Transcriptase Polymerase Chain Reaction (qRT-PCR). Total RNA was extracted using the miRNeasy Mini Kit (Qiagen) according to the manufacturer's protocol. cDNA was synthesized from 2 μg of total RNA using iScript a cDNA synthesis kit (Bio-Rad:1708891) in a 40 μl total volume. qRT-PCR was set up with 20x TaqMan probes, 2 μl of 1 : 5 diluted cDNA and TaqMan universal PCR Master Mix (Thermo Fisher Scientific) in 20 μl total volume. Samples were run in triplicate on a Bio Rad CFX-96 real time PCR system. Gene expression levels were calculated using the $2^{-\Delta\Delta Ct}$ method [23]. Gene-specific TaqMan primers/probe sets include GAPDH (internal normalization control), VEGFA, VEGFC, EDN1, and SLC2A3.

2.7. Western Blotting. Cells were lysed in a Laemmli sample buffer (Bio-Rad) supplemented with 2-mercaptoethanol (Sigma-Aldrich). The lysates were centrifuged at

14,000 rpm for 10 min at 4° C. The supernatants were collected and denatured at 95°C for 10 min. Equal protein lysates were separated on 4-20% Mini-PROTEIN TGX precast gels (Bio-Rad) and transferred to nitrocellulose membranes (Pall Corporation). The following antibodies were used: anti-IDH1 (1 : 1000, Abcam, ab172964), anti-HIF-1α (0.5 μg/ml, RD Systems, NB100-105), and anti-β-actin (1 : 5000, Cell Signaling).

2.8. Soft-Agar Colony Formation Assay. 5×10^3 cells were plated in a 0.3% top layer soft agar in RPMI-1640 with 10% FBS overlaid on a lower layer of a 0.5% basal agar. Cells were then maintained in regular incubator with 21% O_2, or in a hypoxia chamber with 1% O_2 at 37°C for 10-14 days. Colonies were stained with 2 mg/mL iodonitrotetrazolium chloride (Sigma-Aldrich), rinsed with PBS, and quantified with GelCount colony counter (Oxford Optronix).

2.9. Immunohistochemistry (IHC). Immunohistochemical analysis was performed on 5-μm sections cut from formalin-fixed, paraffin-embedded samples utilizing antibodies against CD31 (Servicebio, GB11063-2), HIF-1α (Bioworld, BS3514), VEGFA (Abcam, ab52917), and IDH1 (Abcam, ab172964) following a standard protocol. A semiquantitative evaluation method was applied as follows: the score obtained by the percentage of positive cells (0% = 0; 1 – 25% = 1, 26 – 50% = 2, 51 – 75% = 3, and >75% = 4) was multiplied by the score obtained by the staining intensity (no staining = 0, weak staining = 1, moderate staining = 2, and strong staining = 3). Scoring was evaluated by investigators who were blinded to the information of research subjects.

2.10. Vascular-Endothelial Tube Formation Assay. JJ012 parental and IDH1^{mut} KO cells were cultured with serum-supplemented RPMI-1640 overnight, followed by a 24 h starvation in serum-free medium. Secretome derived from the culture supernatant was then collected and centrifuged at 1200 rpm for 5 min to remove debris. The vascular-endothelial tube formation assay was performed with HUVEC cells in 24-well plates pre-coated with growth factor-reduced basal membrane Geltrex matrix (Thermo Fisher Scientific) and left to solidify for 30 min at 37°C. HUVEC cells were harvested with Trypsin/EDTA solution and the cell concentrations were determined in non-supplemented EGM-2. 2×10^5 cells were seeded in each well and incubated with 1 ml of cell supernatant secretome for 24 hr. After incubation, cells were stained with Calcein AM (2 μg/ml) for 30 min, rinsed with 1 mM $CaCl_2$ and 0.5 mM $MgCl_2$-supplemented PBS, and fixed with 4% paraformaldehyde in PBS for 25 min at room temperature. Capillary tubes were visualized with fluorescence microscopy. The total vascular-endothelial tube lengths were measured from randomly selected image fields per sample per group using NIH/Image J. At least five fields per well were examined, and each experimental condition was tested in triplicate. All HUVEC cells used in experiments underwent fewer than eight passages after resuscitation.

2.11. Statistical Analysis. GraphPad Prism 8 software was used for statistical analyses. p values were determined by unpaired, two-tailed t tests. $p < 0.05$ was considered statistically significant.

3. Results

3.1. Loss of IDH1^{mut} Leads to Downregulation of HIF-1α Target Genes in JJ012 Cells. In this study, we utilized the human chondrosarcoma JJ012 cell line which harbors an endogenous IDH mutation, and its derived two CRISPR/Cas9 IDH1^{mut} KO clones. Depletion of the IDH1 protein and reduced D-2HG levels in the two IDH1^{mut} KO clones are shown in Figures 1(a) and 1(b), respectively. To begin to understand the role of IDH mutation in chondrosarcoma tumorigenesis, we initially conducted an RNA-Seq analysis of JJ012 parental cells and its two IDH1^{mut} KO clones. The RNA-Seq analysis revealed an association between IDH mutation and aberrant activation of integrin signaling in chondrosarcoma [22]. Interestingly, in addition to mediators of cell adhesion and integrin-related pathways, we found in the transcriptome of JJ012 IDH1^{mut} KO cells many genes known to be involved in vasculogenesis. The downregulated HIF-1α target genes detected in both IDH1^{mut} KO clones are shown in Figure 1(c). These genes are implicated in glucose metabolism (SLC2A3, LDHA and LDHB) and angiogenesis (VEGFA and VEGFC). Downregulation of several well-established HIF-1α target genes including VEGFA, VEGFC, EDN1 and SLC2A3 in the IDH1^{mut} KO cells was further confirmed by qRT-PCR (Figure 1(d)). These results indicate that IDH mutation is associated with activation of the HIF-1α signaling pathway.

To be noted, both IDH1^{wt} and IDH1^{mut} were knocked out in our cell model. To confirm that it is the loss of IDH1-^{mut} allele rather than that of IDH1^{wt} is responsible for the downregulation of the HIF-1α target genes, we utilized C28 cells, an immortalized human chondrocyte cell line that expresses IDH1^{wt} only [24]. A pool of C28 IDH1^{wt} KO cells with markedly reduced IDH1 levels was created using the CRISPR/Cas9 technique (Figure 1(e)). qRT-PCR analysis revealed comparable expression of the aforementioned HIF-1α target genes between C28 parental and IDH1^{wt} KO cells (Figure 1(f)), suggesting that loss of the IDH1^{mut} rather than of the IDH1^{wt} allele caused the downregulation of the HIF-1α target genes in JJ012 cells.

3.2. Loss of IDH1^{mut} Reduces HIF-1α Levels in JJ012 Cells and Tumor Tissues. HIF-1α protein levels are regulated by PHDs which destabilize the angiogenic transcription factor by post-translational proline hydroxylation under normoxic conditions. It has been reported that D-2HG competitively inhibits PHDs due to its structural similarity to α-KG, thereby causing accumulation of HIF-1α in IDH1-mutant glioma cells [19]. In our model, D-2HG production was almost completely suppressed in JJ012 IDH1^{mut} KO clones [22]. Therefore, it is rational to inquire whether the down-regulation of HIF-1α target genes in the IDH1^{mut} KO cells is attributed to HIF-1α inhibition as a result of IDH1^{mut} loss and reduced D-2HG production. Indeed, HIF-1α expression appeared to be significantly decreased in the two IDH1^{mut} KO JJ012 cell lines compared to their parental control under

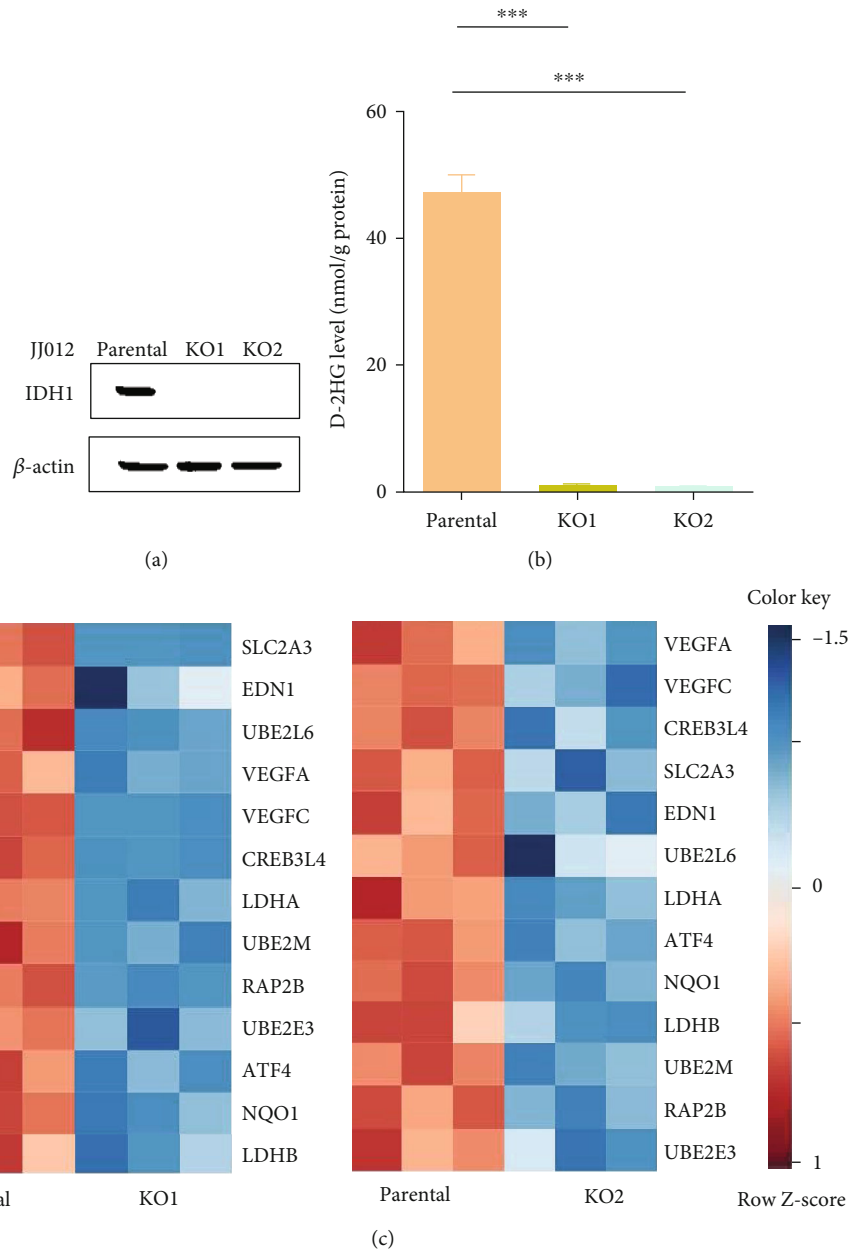

Figure 1: Continued.

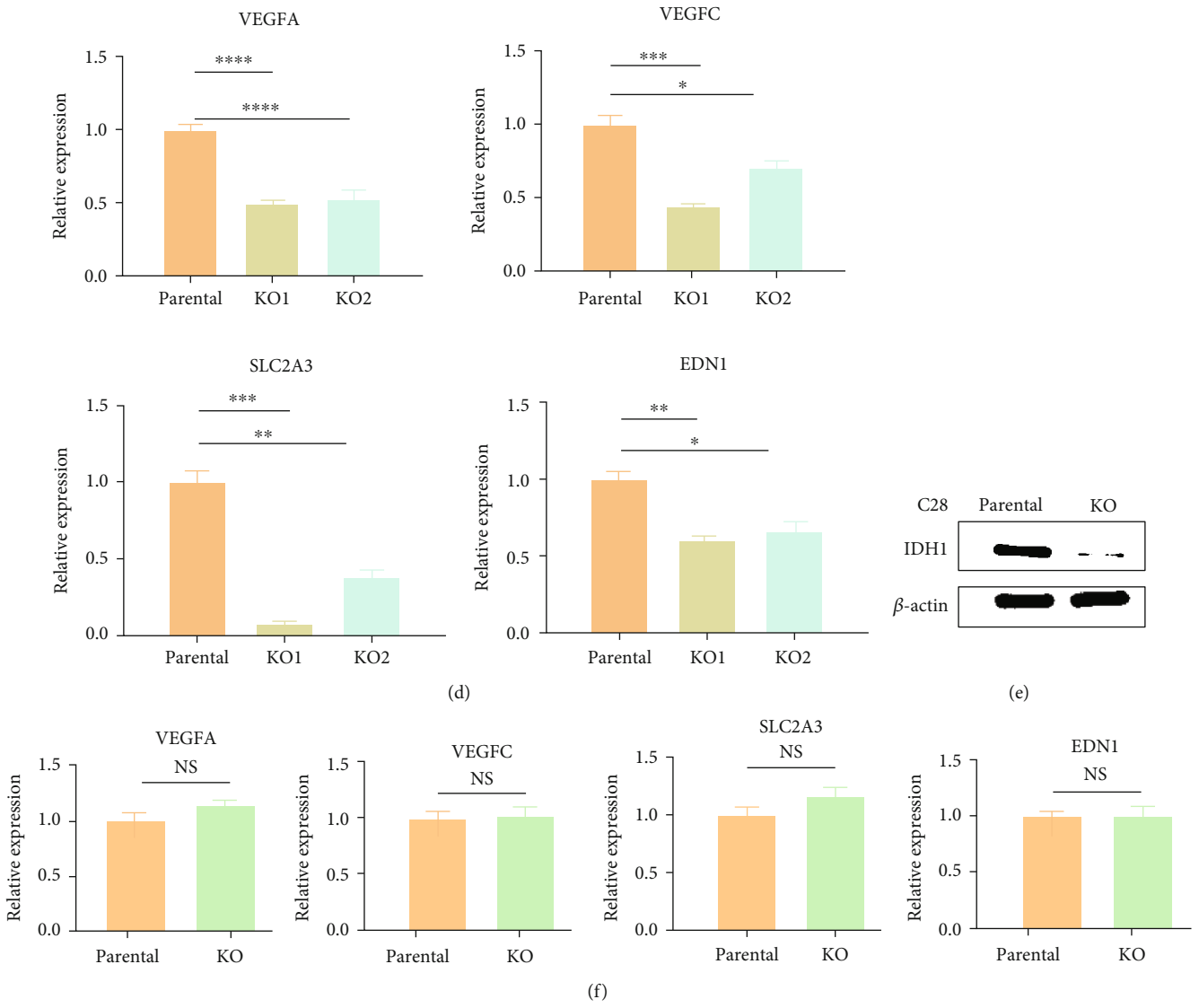

Figure 1: Downregulation of HIF-1α target genes upon loss of IDH1^{mut} in JJ012 cells. (a) Immunoblot shows depletion of IDH1 protein in two IDH1^{mut} KO clones of JJ012 cells. (b) HPLC-MS analysis indicates D-2HG production was nearly depleted in two IDH1^{mut} KO clones of JJ012 cells. (c) Heatmaps of HIF-1α target genes that are downregulated in both IDH1^{mut} KO clones compared to parental control of JJ012 cells. (d) mRNA expression of VEGFA, VEGFC, EDN1, and SLC2A3 in JJ012 cells was quantified by qRT-PCR. The amount of transcript was normalized to GAPDH, and the results are shown as fold-change relative to the parental control. Data are shown as mean $\pm$ SEM of triplicate values and are representative of three independent experiments. $*p < 0.05$, $**p < 0.01$, $***p < 0.001$. (e) Immunoblot shows levels of wildtype IDH1 in CRISPR/Cas9 KO C28 chondrocytes. (f) Bar graphs compare levels of VEGFA, VEGFC, EDN1, and SLC2A3 mRNA expression in parental and wildtype IDH1 KO C28 cells. NS: nonsignificant ($p > 0.05$).

normoxic conditions (Figure 2(a)). We then proceeded to ask whether HIF-1α was similarly regulated *in vivo*. For this we measured IDH1 expression in the chondrosarcoma xenografts derived from parental and IDH1^{mut} KO JJ012 cells that we have previously established (22). IHC analysis revealed significant reduction of IDH1 in the IDH1^{mut} KO tumors (Figure 2(b)). Importantly, HIF-1α levels were concomitantly reduced in the same tumors, thus confirming our *in vitro* findings. The staining score showed that HIF-1α expression was reduced by 70%-80% in the IDH1^{mut} KO tumors compared to parental controls (Figure 2(c)). These results demonstrate that knockout of IDH1^{mut} downregulates HIF-1α *in vitro* and *in vivo*, thus supporting the concept that IDH1 mutation promotes HIF-1α stabilization and its downstream signaling in our JJ012 chondrosarcoma model.

3.3. IDH1 Mutation Confers Angiogenic Properties in JJ012 Chondrosarcoma Cells. Angiogenesis represents an essential step in tumor proliferation, expansion, and metastasis, thus contributing to the pathology of virtually all human cancers. HIF-1α is a subunit of HIF-1, an oxygen-dependent transcriptional activator, which plays crucial roles in tumor angiogenesis and mammalian development [12]. HIF-1 activates transcription of genes encoding angiogenic growth factors which are secreted by hypoxic cells and promote

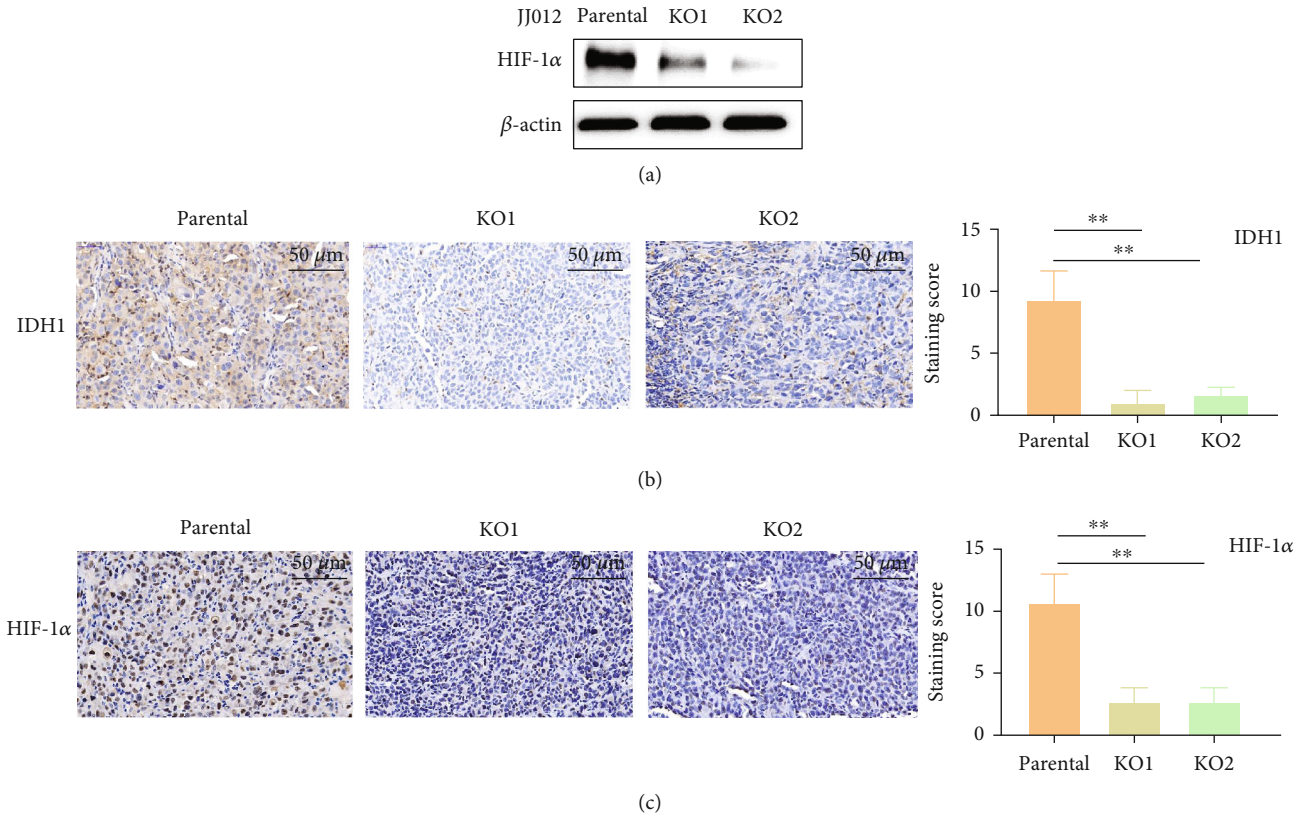

Figure 2: Loss of IDH1^{mut} suppresses HIF-1α in JJ012 cells and tumor tissues. (a) Immunoblots show HIF-1α expression in JJ012 parental and IDH1^{mut} KO cells; immunohistochemical (IHC) images show cytoplasmic IDH1 (b) and nuclear HIF-1α (c) expression in parental and IDH1^{mut} KO JJ012-derived xenografts. IHC staining was quantified with intensity scores as detailed in Materials and Methods. Scale bars are 50 μm. Data represent mean ± SEM of values from four random fields. $**p < 0.01$.

endothelial cell growth [25]. Given the apparent association of HIF-1α expression with IDH1 mutation, we asked whether such mutation confers angiogenic properties on the chondrosarcoma JJ012 cells. Interestingly, functional analysis of the transcriptome in JJ012 IDH1^{mut} KO cells identified angiogenesis as one of the most prominently regulated programs (adjusted $p = 1.02E - 06$) in chondrosarcoma. Upon further examination of angiogenic markers by IHC, we observed that CD31 and VEGFA expression in JJ012 IDH1^{mut} KO cell-derived tumors was markedly reduced when compared to parental cell-derived tumors (Figures 3(a) and 3(b)). These findings suggest a functional association of IDH1 mutation with the HIF-1α-driven angiogenic pathway. To further assess this functional link, we conducted vascular-endothelial tube formation assays using HUVECs incubated with the secretome of JJ012 parental or IDH1^{mut} KO cells. We found that culturing with the DH1^{mut} KO secretome significantly inhibited HUVECs ability to form vascular tubes and reduced capillary tube length by over 20% ($p < 0.05$) (Figure 3(c)). These findings indicate that IDH1-mutant JJ012 chondrosarcoma cells produce a secretome highly capable of stimulating angiogenesis and promoting tumor growth.

3.4. HIF-1α Contributes to Tumorigenicity of IDH1 Mutation in JJ012 Cells. HIF-1α regulates gene expression in critical pathways that drive tumorigenesis [25]. Thus, we endeavored to determine whether HIF-1α contributes to the oncogenic properties of IDH mutation in the JJ012 chondrosarcoma cells. One of the defining criteria of tumorigenicity is anchorage-independent cell growth [26]. In our previous study, we demonstrated that loss of IDH1^{mut} attenuated the tumorigenic potential of chondrosarcoma cells. In particular, depletion of IDH1^{mut} led to a marked reduction in JJ012 capacity for anchorage-independent growth in soft agar [22]. To verify whether HIF-1α contributes to the observed promotion of colony formation by IDH mutation, we performed this assay under conditions of hypoxia (1% O_2) and normoxia (21% O_2) using JJ012 parental and IDH1^{mut} KO cells. We observed that hypoxia caused a dramatic increase in colony numbers in the IDH1^{mut} KO groups (over 60%; $p < 0.05$), compared with those grown under normoxic conditions (Figure 4(a)). A similar pattern was also seen in the parental cells (Figure 4(a)). Notably, growth in hypoxia appeared to abolish the previously reported difference in colony formation between the parental and IDH1^{mut} KO JJ012 cells performed in a normoxic atmosphere (22). HIF-1α levels under both conditions were analyzed by immunoblotting. As expected, incubation with 1% O_2 stimulated HIF-1α expression to comparable levels in all three cell groups (Figure 4(b)). Together, these results suggest that IDH1 mutation contributes to JJ012 cells oncogenic functions, at least in part through HIF-1α activation.

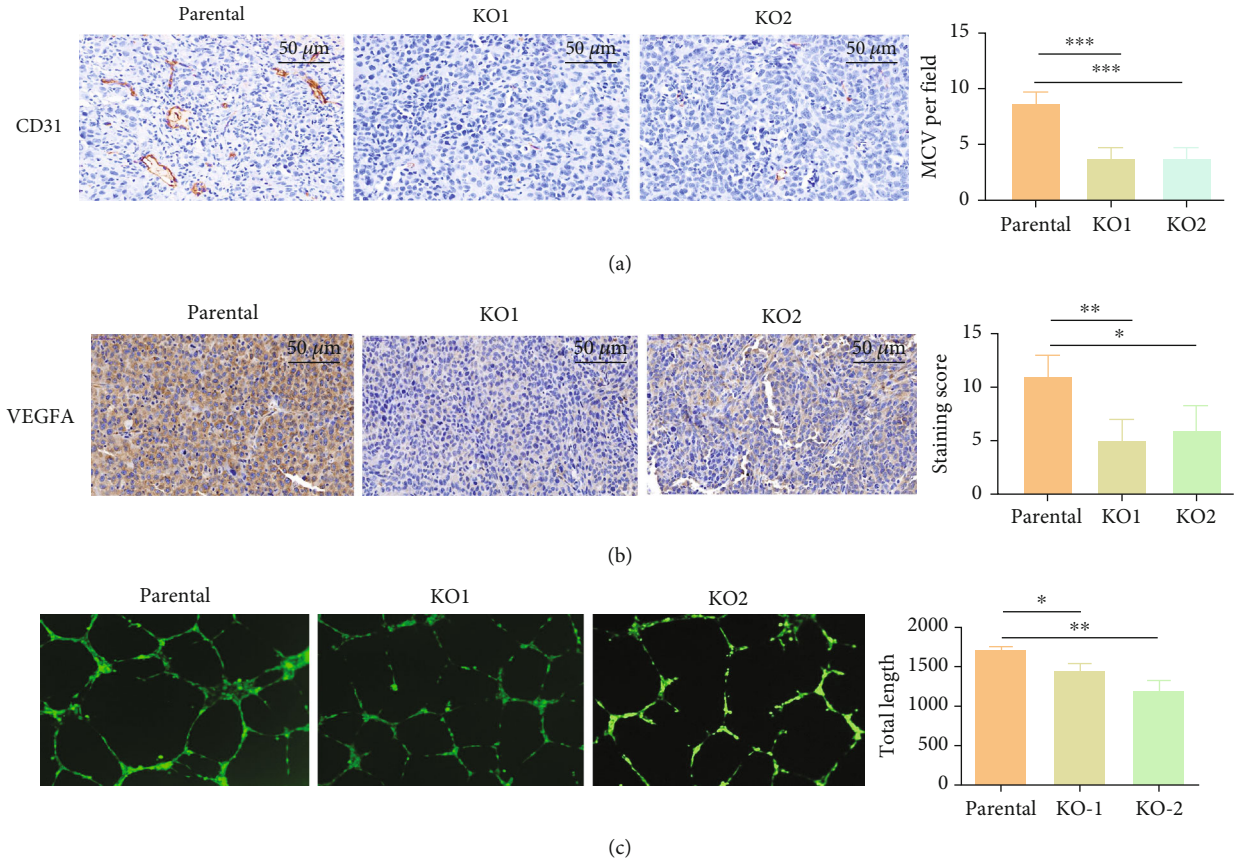

Figure 3: IDH1 mutation promotes angiogenic property of JJ012 cells. (a) IHC images show CD31 expression in JJ012 parental and IDH1^{mut} KO cell-derived xenografts. Right graph depicts number of CD31-positive microvessels (MCV) per field in each group. (b) IHC images show VEGFA expression in JJ012 parental and IDH1^{mut} KO cell-derived xenografts. VEGFA staining was quantified with intensity scores (right graph) as detailed in Materials and Methods. Scale bars are 50 μm. Data represent mean ± SEM of values from at least four random fields. (c) Representative images and quantification (right graph) of endothelial tube formation. HUVECs were cultured in secretome-derived media from JJ012 parental and IDH1^{mut} KO cells. The total capillary tube lengths were measured from 9 to 12 randomly selected image fields per sample per group using NIH/Image J. $*p < 0.05$, $**p < 0.01$, $***p < 0.001$.

4. Discussion

Tumor recurrence and metastasis are major challenges in the treatment of chondrosarcomas. Metastatic chondrosarcoma has a dismal prognosis due to lack of effective systemic therapies. IDH1/2 mutations have been frequently found in chondrosarcoma and have become an attractive target for IDH-mutant advanced chondrosarcomas. By means of drug inhibition and CRISPR/Cas9 knockout of IDH1^{mut}, our previous studies have implicated IDH mutation in chondrosarcoma tumorigenicity, *in vitro* and *in vivo* [22, 24]. However, the underlying mechanism remains largely unknown. It has been proposed that D-2HG at high levels acts as an oncometabolite and exerts some potential pro-tumorigenic effects by competitively inhibiting α-KG-dependent enzymes such as PHDs which regulate HIF-1α stability. Studies have shown IDH mutations compromise the activity of PhD and stabilize HIF-1α in glioma cells under normoxic conditions, leading to inappropriate activation of its target genes [18, 19]. Moreover, HIF-1α and its target genes such as Glut1, VEGF, and PGK1 are also upregulated in the brains of IDH1 R132H knock-in mice [27]. Consistently, in our study, RNA-Seq data analysis of chondrosarcoma JJ012 cells revealed downregulation of several HIF-1α target genes upon loss of IDH1^{mut}. This is correlated with reduced HIF-1α levels in these IDH1^{mut} KO cells and tumors compared with their parental controls. These findings are suggestive of a similar association between IDH mutation and HIF-1α induction in chondrosarcoma cells.

HIF1α is a key component of HIF1, a transcription factor that senses low cellular oxygen levels and regulates the expression of genes implicated in glucose metabolism, angiogenesis, and other signaling pathways that are critical to tumor growth. Increased expression of HIF-1α is closely associated with tumor progression in various cancers [28, 29]. Interestingly, two studies evaluated the expression of HIF-1α in cartilage tumors and suggested that HIF-1α expression was significantly correlated with shorter disease-free survival in chondrosarcoma [30, 31]. To determine whether HIF-1α is a contributor in IDH mutation-driven tumorigenesis of chondrosarcoma, we examined the capacity of JJ012 parental and IDH1^{mut} KO cells for anchorage-independent growth under normoxia and hypoxia conditions in a soft-agar colony formation assay. We observed

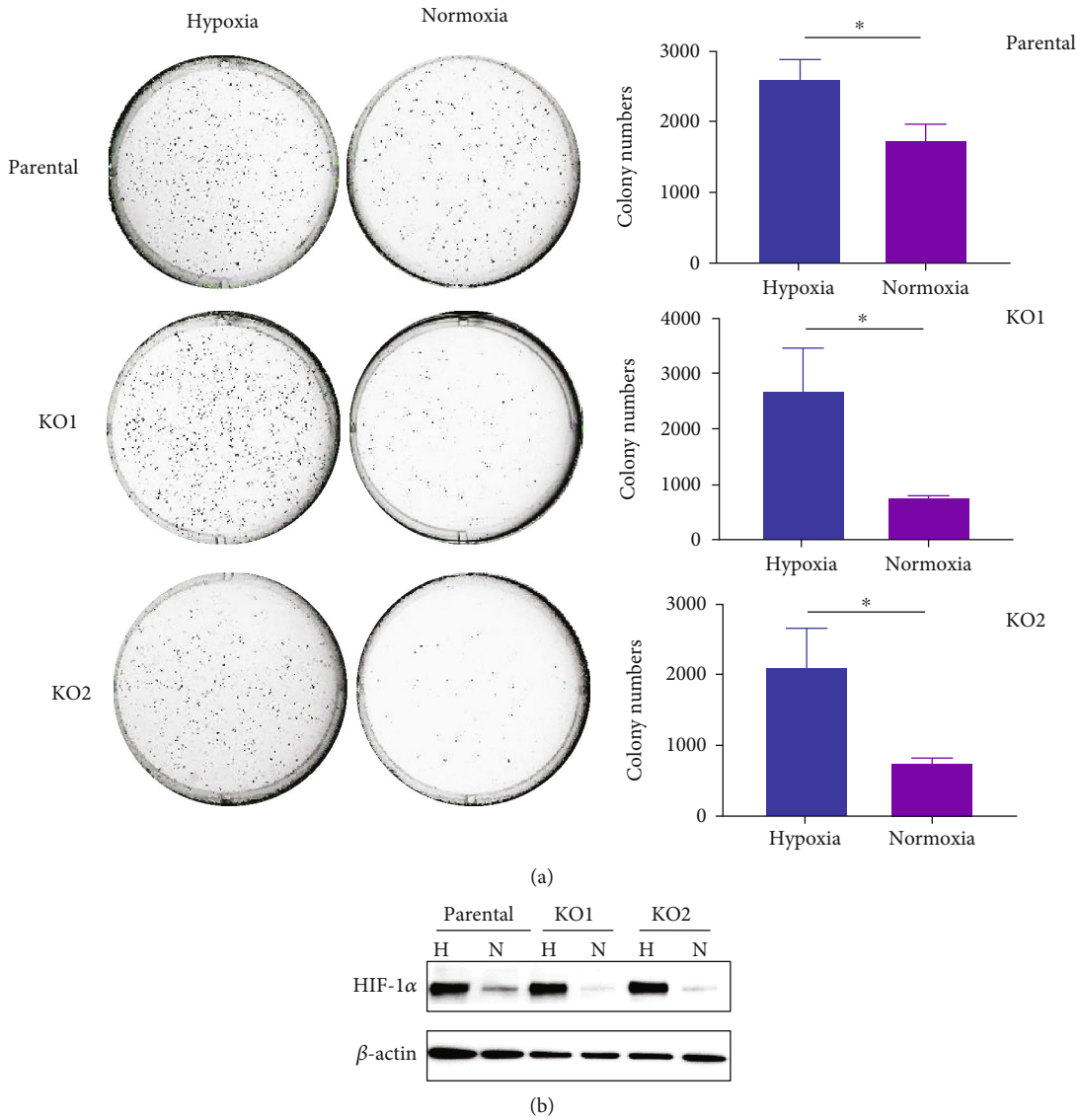

Figure 4: HIF-1α contributes to the tumorigenic function of IDH1 mutation in JJ012 cells. (a) Colony formation assay with JJ012 parental and IDH1^{mut} KO cells under hypoxic (1% O_2) and normoxic (21% O_2) conditions. 5×10^3 cells per well were seeded in 6-well plates and incubated for 10–14 days. Graphs compare effects of hypoxia and normoxia on the number of colonies in the parental, KO1, and KO2 groups. Data indicate mean ± SEM of triplicate cultures and are representative of 3 independent experiments. $*p < 0.05$. (b) Immunoblot shows HIF-1α levels in JJ012 parental and IDH1^{mut} KO cells under normoxia (N) and hypoxia (H) conditions.

that IDH1^{mut} knockout cells formed less colonies than parental cells under normoxia condition, but exogenous induction of HIF-1α significantly boosted the colony-forming capacity of these cells to a degree that is comparable with that of the parental cells. This suggests that activation of HIF-1α signaling is involved in the tumorigenic activity of IDH1^{mut}*in vitro*. Of note, our previous study has shown that loss of IDH1^{mut} led to a marked attenuation of chondrosarcoma tumor formation and D-2HG production in a xenograft model [22]. Since anchorage-independent growth is tightly correlated with tumorigenic potential *in vivo*, it is conceivable that the attenuated HIF-1α signaling caused by loss of IDH1^{mut} might contribute to the observed inhibition of chondrosarcoma formation in the xenograft model.

Angiogenesis is a key contributor to tumor progression and metastasis. HIF-1α and VEGF are known to play crucial roles in the tumor angiogenic process [12, 25, 32]. It is established that VEGF expression is mediated by HIF-1α during hypoxia. The VEGF gene contains a number of HIF-1α-binding sites at its regulatory region, and HIF-1α is able to activate the VEGF promoter [33, 34]. HIF-1α-induced VEGF expression is implicated in the angiogenic switch in chondrosarcoma [32]. Interestingly, studies have shown that IDH mutation is associated with elevated levels of HIF-1α and VEGF levels in IDH-mutant gliomas [18, 35]. Consistently, we found the expression of angiogenic markers, VEGFA and CD31, was significantly reduced in the IDH1^{mut} KO cell-derived tumors, suggesting that IDH1 mutation is associated with the angiogenic potential of chondrosarcoma

cells. This association was solidified by *in vitro* vascular tube formation assay, which shows that the secretome of $IDH1^{mut}$ KO cells substantially reduced HUVECs' ability to from primitive vascular tubes in comparison with the secretome of parental cells. To be noted, our previous study also showed an association between IDH mutation and aberrant activation of integrin signaling in chondrosarcoma cells [22]. A few integrins have been implicated in blood vessel formation and regulation of cell growth, survival, and migration during tumor angiogenesis and metastasis [36, 37]. Interestingly, although VEGF expression is induced by HIF-1α during hypoxia [38], its expression can also be modulated by tumor integrins, resulting in efficient tumor angiogenesis under normoxic conditions [39]. Therefore, integrin and HIF-1α signaling might intertwine with each other by shared mediators such as angiogenic factors in the tumor microenvironment, and thus both pathways contribute to the process of angiogenesis in IDH-mutant chondrosarcomas [12, 36]. In any case, the established association in this study renders antiangiogenic molecules appealing candidates for combinatorial regimens with $IDH1^{mut}$ inhibitors for advanced chondrosarcomas. The use of angiogenesis inhibitors has been used as an adjunct to other forms of therapy for preventing development of malignant neoplasms [40]. Preclinical studies have shown the benefits of targeting angiogenesis in chondrosarcomas [41]. Given the modest results with $IDH1^{mut}$ inhibitors in chondrosarcoma [42], future efforts to improve the efficacy of these compounds might benefit from emphasis on biology-driven therapeutic strategies to improve response rates in IDH-mutated chondrosarcomas.

The present study was limited by the use of only one conventional chondrosarcoma cell line. In fact, due to the rareness of this malignancy, very few chondrosarcoma cell lines are available worldwide. Thus, more chondrosarcoma cell lines, or patients' primary tumor cells, will be essential to further investigate and strengthen the concept explored in this study. Interestingly, we did not find a similar association between IDH mutation and HIF-1α in an IDH1-mutant fibrosarcoma cell line, HT1080, which was originally reported as a fibrosarcoma of bone, but is now considered to represent a dedifferentiated chondrosarcoma. We believe that the discrepancy is due to pathogenesis heterogeneity between the chondrosarcoma cell lines as conventional and dedifferentiated chondrosarcomas were shown to exhibit distinct biological behaviors and clinical characteristics. As described previously, differential biology was also observed within gliomas and leukemias with regards to the effects of IDH mutation on PHDs and HIF-1α activity [18–21]. Thus, much work remains to better understand the biology to fully clarify these discrepancies and identify the appropriate patient populations for specific targeted therapies. Nonetheless, herein, we identified a strong correlation between HIF-1α activation and IDH1 mutation status in chondrosarcoma cells. Furthermore, this study unravels one aspect of chondrosarcoma pathophysiology and provides insightful therapeutic possibilities such as combinatorial regimens of antiangiogenic agents with $IDH1^{mut}$ inhibitors for patients with advanced IDH mutated chondrosarcoma.

Data Availability

The experimental data used to support the findings of this study are included within the article.

Conflicts of Interest

The authors have declared that no conflict of interest exists.

Authors' Contributions

L.L., X.H., J.C.T., J.Y., and J.Y. conceived the experimental plan. X.H. and L.L. performed the experiments. All authors contributed to the data analysis. X.H., L.L., J.C.T., and J.E.E. wrote the manuscript. Xiaoyu Hu and Luyuan Li contributed equally to this work.

Acknowledgments

We thank Xiang-Xi Mike Xu' Laboratory, David Robbins' Laboratory, and Tan Ince's Laboratory for use of their equipment and technical support. We thank Fan Yang for the assistance in real-time PCR, Yuguang Ban for the assistance in RNA-Seq analysis, and Hongbiao Jing for the assistance with reviewing immunohistopathology of tumor samples. This work was supported by the Sylvester Comprehensive Cancer Center, University of Miami Miller School of Medicine. This work was supported by the following grants: NCI 1 P30 240139-01 CA grant, National Natural Science Foundation of China (Grant No. 81871895), Young Taishan Scholars and Academic Promotion Program of Shandong First Medical University (Grant No. 2019RC003).

References

[1] W. A. Chow, "Chondrosarcoma: biology, genetics, and epigenetics," *F1000Research*, vol. 7, p. 1826, 2018.

[2] J. C. Trent, A. E. Rosenberg, R. Pollock, and T. F. Delaney, *Sarcomas: evidence-based diagnosis and management*, Demos Medical Publishing, New York, NY, 2020.

[3] I. J. MacDonald, C. Y. Lin, S. J. Kuo, C. M. Su, and C. H. Tang, "An update on current and future treatment options for chondrosarcoma," *Expert Review of Anticancer Therapy*, vol. 19, no. 9, pp. 773–786, 2019.

[4] E. Nazeri, M. Gouran Savadkoohi, K. Majidzadeh-A, and R. Esmaeili, "Chondrosarcoma: An overview of clinical behavior, molecular mechanisms mediated drug resistance and potential therapeutic targets," *Critical Reviews in Oncology/Hematology*, vol. 131, pp. 102–109, 2018.

[5] M. F. Amary, K. Bacsi, F. Maggiani et al., "IDH1andIDH2mutations are frequent events in central chondrosarcoma and central and periosteal chondromas but not in other mesenchymal tumours," *The Journal of Pathology*, vol. 224, no. 3, pp. 334–343, 2011.

[6] F. G. Schaap, P. J. French, and J. V. Bovee, "Mutations in the isocitrate dehydrogenase genes IDH1 and IDH2 in tumors," *Advances in Anatomic Pathology*, vol. 20, no. 1, pp. 32–38, 2013.

[7] L. Dang, S. Jin, and S. M. Su, "IDH mutations in glioma and acute myeloid leukemia," *Trends in Molecular Medicine*, vol. 16, no. 9, pp. 387–397, 2010.

[8] L. Dang, D. W. White, S. Gross et al., "Cancer-associated IDH1 mutations produce 2-hydroxyglutarate," *Nature*, vol. 465, no. 7300, p. 966, 2010.

[9] P. S. Ward, J. Patel, D. R. Wise et al., "The Common Feature of Leukemia-Associated IDH1 and IDH2 Mutations Is a Neomorphic Enzyme Activity Converting α-Ketoglutarate to 2-Hydroxyglutarate," *Cancer Cell*, vol. 17, no. 3, pp. 225–234, 2010.

[10] L. Li, J. E. Eid, A. C. Paz, and J. C. Trent, "Metabolic enzymes in Sarcomagenesis: Progress toward biology and therapy," *BioDrugs*, vol. 31, no. 5, pp. 379–392, 2017.

[11] D. Ye, Y. Xiong, and K. L. Guan, "The mechanisms of IDH mutations in tumorigenesis," *Cell Research*, vol. 22, no. 7, pp. 1102–1104, 2012.

[12] J. W. Lee, S. H. Bae, J. W. Jeong, S. H. Kim, and K. W. Kim, "Hypoxia-inducible factor (HIF-1)α: its protein stability and biological functions," *Experimental & Molecular Medicine*, vol. 36, no. 1, pp. 1–12, 2004.

[13] H. Semukunzi, D. Roy, H. Li et al., "IDH mutations associated impact on related cancer epidemiology and subsequent effect toward HIF-1α," *Biomedicine & Pharmacotherapy*, vol. 89, pp. 805–811, 2017.

[14] P. Carmeliet, Y. Dor, J. M. Herbert et al., "Role of HIF-1α in hypoxia-mediated apoptosis, cell proliferation and tumour angiogenesis," *Nature*, vol. 394, no. 6692, pp. 485–490, 1998.

[15] B. Keith, R. S. Johnson, and M. C. Simon, "HIF1alpha and HIF2alpha: sibling rivalry in hypoxic tumour growth and progression," *Nature Reviews. Cancer*, vol. 12, no. 1, pp. 9–22, 2011.

[16] J. H. Marxsen, P. Stengel, K. Doege et al., "Hypoxia-inducible factor-1 (HIF-1) promotes its degradation by induction of HIF-α-prolyl-4-hydroxylases," *Biochemical Journal*, vol. 381, no. 3, pp. 761–767, 2004.

[17] S. Salceda and J. Caro, "Hypoxia-inducible factor 1 alpha (HIF-1 alpha) protein is rapidly degraded by the ubiquitin-proteasome system under normoxic conditions - its stabilization by hypoxia depends on redox-induced changes," *Journal of Biological Chemistry*, vol. 272, no. 36, pp. 22642–22647, 1997.

[18] S. Zhao, Y. Lin, W. Xu et al., "Glioma-derived mutations inIDH1Dominantly inhibit IDH1 catalytic activity and induce HIF-1α," *Science*, vol. 324, no. 5924, pp. 261–265, 2009.

[19] W. Xu, H. Yang, Y. Liu et al., "Oncometabolite 2-Hydroxyglutarate Is a Competitive Inhibitor of α-Ketoglutarate-Dependent Dioxygenases," *Cancer Cell*, vol. 19, no. 1, pp. 17–30, 2011.

[20] P. Koivunen, S. Lee, C. G. Duncan et al., "Transformation by the (_R_)-enantiomer of 2-hydroxyglutarate linked to EGLN activation," *Nature*, vol. 483, no. 7390, pp. 484–488, 2012.

[21] J. A. Losman, R. E. Looper, P. Koivunen et al., "(R)-2-hydroxyglutarate is sufficient to promote leukemogenesis and its effects are reversible," *Science*, vol. 339, no. 6127, pp. 1621–1625, 2013.

[22] L. Y. Li, X. Y. Hu, J. E. Eid et al., "Mutant IDH1 depletion downregulates Integrins and Impairs Chondrosarcoma Growth," *Cancers*, vol. 12, no. 1, p. 141, 2020.

[23] T. D. Schmittgen and K. J. Livak, "Analyzing real-time PCR data by the comparative C(T) method," *Nature Protocols*, vol. 3, no. 6, pp. 1101–1108, 2008.

[24] L. Li, A. C. Paz, B. A. Wilky et al., "Treatment with a small molecule mutant IDH1 inhibitor suppresses tumorigenic activity and decreases production of the Oncometabolite 2-Hydroxyglutarate in human chondrosarcoma cells," *PLoS One*, vol. 10, no. 9, article e0133813, 2015.

[25] Y. Z. Yang, M. J. Sun, L. H. Wang, and B. Jiao, "HIFs, angiogenesis, and cancer," *Journal of Cellular Biochemistry*, vol. 114, no. 5, pp. 967–974, 2013.

[26] S. M. Frisch and R. A. Screaton, "Anoikis mechanisms," *Current Opinion in Cell Biology*, vol. 13, no. 5, pp. 555–562, 2001.

[27] M. Sasaki, C. B. Knobbe, M. Itsumi et al., "D-2-hydroxyglutarate produced by mutant IDH1 perturbs collagen maturation and basement membrane function," *Genes & Development*, vol. 26, no. 18, pp. 2038–2049, 2012.

[28] M. Nepal, H. Jung Choi, B. Y. Choi et al., "Anti-angiogenic and anti-tumor activity of Bavachinin by targeting hypoxia- inducible factor-1α," *European Journal of Pharmacology*, vol. 691, no. 1-3, pp. 28–37, 2012.

[29] H. Zhong, A. M. de Marzo, E. Laughner et al., "Overexpression of hypoxia-inducible factor 1alpha in common human cancers and their metastases," *Cancer Research*, vol. 59, no. 22, pp. 5830–5835, 1999.

[30] D. Luo, H. Ren, W. Zhang, H. Xian, K. Lian, and H. Liu, "Clinicopathological and prognostic value of hypoxia-inducible factor-1α in patients with bone tumor: a systematic review and meta-analysis," *Journal of Orthopaedic Surgery and Research*, vol. 14, no. 1, p. 56, 2019.

[31] T. Kubo, T. Sugita, S. Shimose, T. Matsuo, K. Arihiro, and M. Ochi, "Expression of hypoxia-inducible factor-1alpha and its relationship to tumour angiogenesis and cell proliferation in cartilage tumours," *Journal of Bone and Joint Surgery. British Volume (London)*, vol. 90, no. 3, pp. 364–370, 2008.

[32] J. M. Fang, L. Yan, Y. Shing, and M. A. Moses, "HIF-1alpha-mediated up-regulation of vascular endothelial growth factor, independent of basic fibroblast growth factor, is important in the switch to the angiogenic phenotype during early tumorigenesis," *Cancer Research*, vol. 61, no. 15, pp. 5731–5735, 2001.

[33] D. T. Shima, M. Kuroki, U. Deutsch, Y. S. Ng, A. P. Adamis, and P. A. D'Amore, "The Mouse Gene for Vascular Endothelial Growth Factor:," *The Journal of Biological Chemistry*, vol. 271, no. 7, pp. 3877–3883, 1996.

[34] J. A. Forsythe, B. H. Jiang, N. V. Iyer et al., "Activation of vascular endothelial growth factor gene transcription by hypoxia-inducible factor 1," *Molecular and Cellular Biology*, vol. 16, no. 9, pp. 4604–4613, 1996.

[35] C. Yalaza, H. Ak, M. S. Cagli, E. Ozgiray, S. Atay, and H. H. Aydin, "R132H mutation in IDH1 gene is associated with increased tumor HIF1-alpha and serum VEGF levels in primary glioblastoma Multiforme," *Annals of Clinical and Laboratory Science*, vol. 47, no. 3, pp. 362–364, 2017.

[36] C. J. Avraamides, B. Garmy-Susini, and J. A. Varner, "Integrins in angiogenesis and lymphangiogenesis," *Nature Reviews. Cancer*, vol. 8, no. 8, pp. 604–617, 2008.

[37] G. Serini, D. Valdembri, and F. Bussolino, "Integrins and angiogenesis: a sticky business," *Experimental Cell Research*, vol. 312, no. 5, pp. 651–658, 2006.

[38] M. Kunz and S. M. Ibrahim, "Molecular responses to hypoxia in tumor cells," *Molecular Cancer*, vol. 2, p. 23, 2003.

[39] M. Lorger, J. S. Krueger, M. O'Neal, K. Staflin, and B. Felding-Habermann, "Activation of tumor cell integrin v 3 controls angiogenesis and metastatic growth in the brain," *Proceedings of the National Academy of Sciences of the United States of America*, vol. 106, no. 26, pp. 10666–10671, 2009.

[40] L. Yadav, N. Puri, V. Rastogi, P. Satpute, and V. Sharma, "Tumour angiogenesis and Angiogenic Inhibitors: A Review," *Journal of clinical and diagnostic research: JCDR*, vol. 9, no. 6, pp. XE01–XE05, 2015.

[41] S. Stacchiotti, S. Ferrari, A. Redondo et al., "Pazopanib for treatment of advanced extraskeletal myxoid chondrosarcoma: a multicentre, single-arm, phase 2 trial," *The Lancet Oncology*, vol. 20, no. 9, pp. 1252–1262, 2019.

[42] W. D. Tap, V. M. Villalobos, G. M. Cote et al., "Phase I study of the mutant IDH1 inhibitor Ivosidenib: safety and clinical activity in patients with advanced chondrosarcoma," *Journal of Clinical Oncology*, vol. 38, no. 15, pp. 1693–1701, 2020.

Hindawi
Disease Markers
Volume 2022, Article ID 1946104, 14 pages
https://doi.org/10.1155/2022/1946104

Research Article

Sequential and Dynamic Variations of IL-6, CD18, ICAM, TNF-α, and Microstructure in the Early Stage of Diabetic Retinopathy

Ang Xiao,[1] **HuiFeng Zhong**,[2] **Lei Xiong**,[3] **Lin Yang**,[1] **YunFang Xu**,[1] **SiMin Wen**,[1] **Yi Shao**,[1] **and Qiong Zhou**[1]

[1]*Department of Ophthalmology, The First Affiliated Hospital of Nanchang University, Jiangxi Province Ocular Disease Clinical Research Center, Nanchang, 330006 Jiangxi, China*
[2]*Departments of Intensive Care, The First Affiliated Hospital of Gannan Medical University, Ganzhou, 341000 Jiangxi, China*
[3]*Department of Pathology, The First Affiliated Hospital of Nanchang University, Nanchang, 330006 Jiangxi, China*

Correspondence should be addressed to Yi Shao; freebee99@163.com and Qiong Zhou; qiongzd06@126.com

Received 14 October 2021; Accepted 28 December 2021; Published 27 January 2022

Academic Editor: Alexander Berezin

Objective. The purpose of this project is to make sequential and indepth observation of the variations of retinal microvascular, microstructure, and inflammatory mediators at the early stage of diabetic retinopathy (DR) in streptozotocin-induced diabetes mellitus (DM) rats. *Methods*. DM was induced by a single intraperitoneal injection of 60 mg/kg body weight streptozotocin (STZ). The fluorescein fundus angiography, hematoxylin and eosin staining, periodic acid-Schiff staining, fluorescence imaging techniques, quantitative real-time PCR, and vascular endothelial growth factor- (VEGF-) A ELISA were performed on the 8th day, at the 4th week, 6th week, 8th week, and 10th week after DM induction, respectively. *Results*. In this study, we observed not only the decrease of retinal ganglion cells (RGCs) and the increase of endotheliocytes to pericytes (E/P) ratio, acellular capillaries, and type IV collagen-positive strands began to occur on the 8th day after induction but the vascular permeability and new vessel buds began to appear in the diabetes group at the 8th week, while the expression of VEGF-A, VEGF mRNA, IL-6 mRNA, ICAM mRNA, and TNF-α mRNA were significantly higher in the diabetes group compared with the normal group($P < 0.01$) on the 8th day after induction and maintained a high expression level throughout the 10-week observation period. However, the expression of CD18 mRNA began to increase significantly at the 4th week after induction and reached a peak at the 6th week. *Conclusion*. Our study indicated the abnormal alterations of microvessels, microstructure, and inflammatory mediators at the early stage of DR, which confirms and supplements the previous research, and also promotes an indepth understanding and exploration of the pathophysiology and underlying pathogenesis of DR.

1. Introduction

Diabetic retinopathy (DR) remains a leading cause of vision loss in the working age population of industrialized regions [1]. A third of the 463 million people with diabetes [2] have signs of diabetic retinopathy, and a third of these might suffer from severe retinopathy or macular edema [3]. DR is categorized as nonproliferative DR (NPDR) and proliferative DR (PDR). Due to the fact that the patients without typically asymptomatic, NPDR (especially the mild NPDR) usually represents the early stage of DR. Early diabetic retinopathy is mainly characterized by loss of pericytes and retinal ganglion cells (RGCs), overexpression of vascular endothelial growth factor (VEGF), and compensatory synthesis and deposition of extracellular proteins. In addition, a variety of inflammatory mediators on the retina can be upregulated in the early stage of diabetes, including intercellular adhesion molecule-1 (ICAM-1), VEGF, nuclear factor kappa B (NF-κB), inducible nitric oxide synthase (iNOS), tumor necrosis factor (TNF)-α, CD18, and local inflammatory response playing an important role in the occurrence and development of DR [4, 5].

Researchers have conducted some studies on early pathological changes, occurrence, and development of DR. One study [6] indicated that RGC apoptosis increased at the 4th week of the diabetes course, and that this early abnormality of neurons may be due to the loss of nerve cells. Moreover,

Kuwabara et al. [7] pointed out that microvascular pericytes were lost in the early stage of diabetic retinal tissue, and that the loss of pericytes in the vascular wall could lead to the formation of microhemangioma. Based on a study by Ayalasomayajula et al. [8], the vitreous VEGF expression of diabetic rats was significantly higher than that of normal control group on the 8th day after induction. In the 4-week observation period, the VEGF expression in vitreous of diabetic rats was the highest at the 4th week, which was significantly higher than that of the normal control group [9]. The overexpression of VEGF will transform or alter the occurrence of neovascularization and improve vascular permeability, leading to retinal structural and functional abnormalities [10].

Although the studies above have investigated the pathological changes of retinal structure in the early stage of DR, they have their own limitations, such as discontinuities in time and differences in results. The pathological changes of retinal structure in the early stage of DR at continuous time nodes remain unclear, and the theoretical basis for the early stage of DR needs further research. To further clarify the retinal microvascular injury, microstructure changes, and expression of interleukin-6 (IL-6), CD18, ICAM, TNF-α and VEGF in the early stage of DR (Figure 1), we conduct sequential and indepth observation of the occurrence and development at the early stage of DR in diabetic rats, especially using fluorescein fundus angiography (FFA) to examine the fundus of living organisms.

2. Material and Methods

2.1. Animals. A total of 50 eight-week-old male Sprague-Dawley (SD) rats (weight, 295 ± 15 g) were purchased from the Animal Center of Nanchang University (Nanchang, China). Rats were maintained under a condition of controlled temperature (23 ± 2°C), humidity (50%), and lighting (12-h light/dark cycle) and had ad libitum access to sterilized standard laboratory chow and water. Rats were treated in accordance with principles of animal ethics and were anesthetized with an intraperitoneal injection of pentobarbital (40 mg/kg body weight; Sigma-Aldrich; Merck Millipore, Darmstadt, Germany) for the subsequent experiments. All experiments were conducted in accordance with the Instruction and Administration of Experimental Animals and were approved by the Medical Ethics Committee of the First Affiliated Hospital of Nanchang University.

2.2. Diabetes Induction and Experimental Groups. Diabetes mellitus (DM) was induced by a single intraperitoneal injection of 60 mg/kg body weight streptozotocin(STZ) (Sigma-Aldrich; Merck Millipore). Rats with blood glucose levels ≥ 250 mg/dl 24 h after STZ injection and which remained hyperglycemic for four days were classified as diabetic. A total of 25 diabetic rats were treated as diabetes group, and 25 normal rats without any treatment were used as the normal group. The rats in each group were randomized (N=5) and sacrificed after FFA examination on the 8th day, at the 4th week, 6th week, 8th week, and 10th week after induction, respectively.

2.3. Animal Examination of Fluorescein Fundus Angiography (FFA). Fluorescein fundus angiography (FFA) is one of the common and main methods for diagnosing DR. The rats in each group were treated with FFA (Heidelberg Spectraalis HRA, Heidelberg, Germany) to examine the right eye of rats. The rats were given intraperitoneal injection of sodium pentobarbital (40 mg/kg) for anesthesia after being weighed, pupil dilation was performed with one drop of compound topicamide (Mydrin-P○R; Santen, Osaka, Japan) and local anesthesia with alcaine, and then the corneal surface was coated with methyl cellulose to keep moist. During FFA examination, SD rats were intraperitoneally injected with 10% sodium fluorescein injection (0.001 ml/g, International Medication Systems, Dunstable, United Kingdom) for quick examination.

2.4. Experimental Samples. In order to label all blood-circulating vessels, an intravascular perfusion of fluorescent tomato lectin was performed [11]. Anesthetized SD rats were intravenously injected with 100 μl fluorescein isothiocyanate-conjugated tomato lectin (1 mg/ml; Sigma-Aldrich; Merck Millipore) and 500 μl fluorescein isothiocyanate (1 mg/ml; Yuanye Bio-Technology; Shanghai; China). Tomato lectin bound uniformly to the luminal surface of endothelial cells [12] and labeled all blood vessels with adequate blood supply. At 15 mins after injection, rats were perfused with stroke-physiological saline solution for 5 mins through the left ventricle at pressures of 80-120 mmHg under anesthesia. The vitreous humor and retina were isolated from the eyes under an ×2.5 anatomic microscope. The vitreous humor was isolated for VEGF-A ELISA and the retina for hematoxylin and eosin (H&E) staining, periodic acid-Schiff (PAS) staining, fluorescence imaging techniques, and expression of proinflammatory proteins on the 8th day, at the 4th week, 6th week, 8th week, and 10th week after induction of DM, respectively.

2.5. Estimation of VEGF-A in Vitreous Humor. Isolated vitreous humor was homogenized in 185 μl sterile phosphate buffer saline (PBS) after being frozen at -80°C for 5 min. According to the manufacturer's instructions, a rat VEGF-A ELISA kit (RayBiotech Inc, Norcross, GA, USA) capable of detecting both VEGF-A isoforms (RayBiotech Inc, Norcross, GA, USA) was used to estimate the level of VEGF-A proteins in the vitreous homogenate. The antibodies in the kit have >95% crossreactivity with rat.

2.6. H&E-Stained Retinal Preparations. One-fourth of the retinal tissue in each sample was isolated from normal and diabetic rats and fixed in 4% paraformaldehyde solution at 20°C for 2 h. Samples were subsequently sectioned (5 μm), stained with H&E, and examined under a light microscope (magnification, ×400; Zeiss AG, Oberkochen, Germany) to determine the area and number of RGCs present in the samples.

2.7. Periodic Acid-Schiff Stain- (PAS-) Stained Retinal Preparations. One-fourth of the retinal tissue in each sample was isolated from each group and fixed in 4% paraformaldehyde solution for at 20°C for 24 h. Samples were subsequently placed into trypsin fluid for 40 mins at 37°C, stained with PAS, and examined under a light microscope (magnification, ×400;

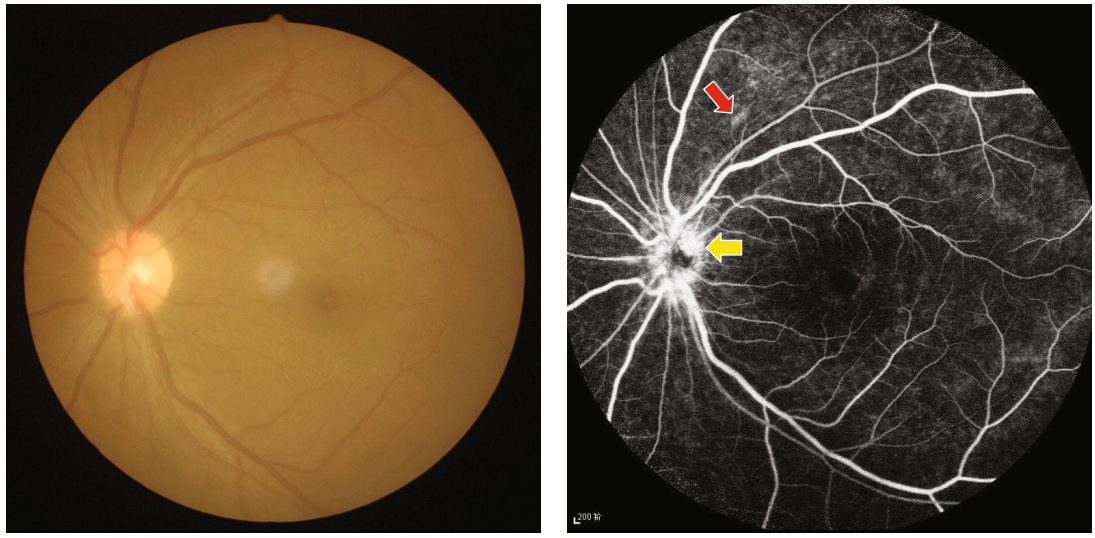

(a) (b)

Figure 1: Example of the early stage of DR patients was examined on fundus camera (a) and fluorescence fundus angiography (b). (a) Fundus photography showed no obvious abnormalities. (b) Optic disc capillaries showed dilation and leakage (yellow arrow) and hemangioma capillanisum (red arrow).

Zeiss AG) to calculate the number of acellular strands and the ratio of endotheliocytes to pericytes (E/P).

2.8. Fluorescence Imaging Techniques for Flat Retinal Preparations. Retinal flat mounts immersing in marker solutions were processed to visualize the vascular basement membrane. Prior to immersion staining, one-fourth of the retinal tissue in each sample was incubated for 45 mins at room temperature in 5% normal bovine serum in PBS containing 0.5% Triton-X-100 (0.5% T-PBS). Subsequently, the flat mounts were incubated overnight at 4°C in a marker solution containing rabbit polyclonal anti-type IV collagen antibody solution (1 : 300; ab19808; Abcam, Cambridge, UK) for basement membrane [9]. Fluorescent goat anti-rabbit immunoglobulin (Ig) G (1 : 45; BA1105; Wuhan Boster Biological Technology, Ltd., Wuhan, China) was treated as a secondary antibody. Subsequent to secondary incubation at 20°C for 5 mins, the retinal flat mounts were washed three times in 0.5% T-PBS, kept into DAPI for 5 mins, and washed another three times in 0.5% T-PBS. Then, the retinal flat mounts were prepared in a Vectashield (Wuhan Boster Biological Technology, Ltd.) and analyzed using a Zeiss LSM 710 confocal laser scanning microscope to determine the area and number of retinal neurocytes and the number of type-IV collagen strands.

2.9. Quantitative Real-Time PCR Analyses for VEGF and Various Inflammation-Related Molecules of Retina. In order to measure the mRNA expression levels of VEGF, IL-6, CD18, ICAM, and TNF-α in retinal tissue, total RNA was isolated from the one quarter of the retinal tissue remains using an extraction reagent (TRIzol; Invitrogen, Carlsbad, CA) and reverse-transcribed with a HiFiScript cDNA Synthesis Kit (First-Strand, CoWin Biosciences, china). PCR was performed using TaqDNA polymerase (Servicebio®, WuHan, China) in a thermal controller (Gene Amp PCR system; Applied Biosystems, Foster, CA). The primer sequences (Sangon Biotech, ShangHai, China) are as follows: 5′-GAGGCCGAAGTCTG TTTG-3′ (forward primer) and 5′-GGTTTGTCGTGTTT CTGGA-3′ (reverse primer) for VEGF, 5′-CACCAGGAA CGAAAGTCAA-3′ (forward primer) and 5′-CAACAACAT CAGTCCCAAGA-3′ (reverse primer) for IL-6, 5′-CAGC AGAAGGACGGAAAC-3′ (forward primer) and 5′-GGAG GAGGACACCAATCA-3′ (reverse primer) for CD-18, 5′-CCAGCCCCTAATCTGACCT-3′ (forward primer) and 5′-CTAAAGGCACGGCACTTGT-3′ (reverse primer) for ICAM, 5′-CAGCCAGGAGGGAGAAC-3′ (forward primer) and 5′-GTATGAGAGGGACGGAACC-3′ (reverse primer) for TNF-α, and 5′-AGCCATGTACGTAGCCATCC-3′ (forward primer) and 5′-ACCCTCATAGATGGGCACAG-3′ (reverse primer) for β-actin, respectively.

2.10. Image Processing and Statistical Analysis. IPP 6.0 and ImageJ 2.0 were used to process images, and IBM SPSS 19.0 (IBM Corporation, Armonk, NY, USA) statistical software was used for statistical analysis of the obtained data. Two-way ANOVA was conducted for multiple mean values, and independent sample t-test was conducted for data between groups. All data were treated with mean ± standard deviation. $P < 0.05$ was statistically significant.

3. Results

3.1. Metabolic Condition of Rats. The metabolism of rats was shown in Figure 2 after intraperitoneal injection of STZ. On the 4th day after DM induction, the body weight of SD rats in the diabetes group was reduced compared with the normal group ($P < 0.05$), and with the progress of disease, the body

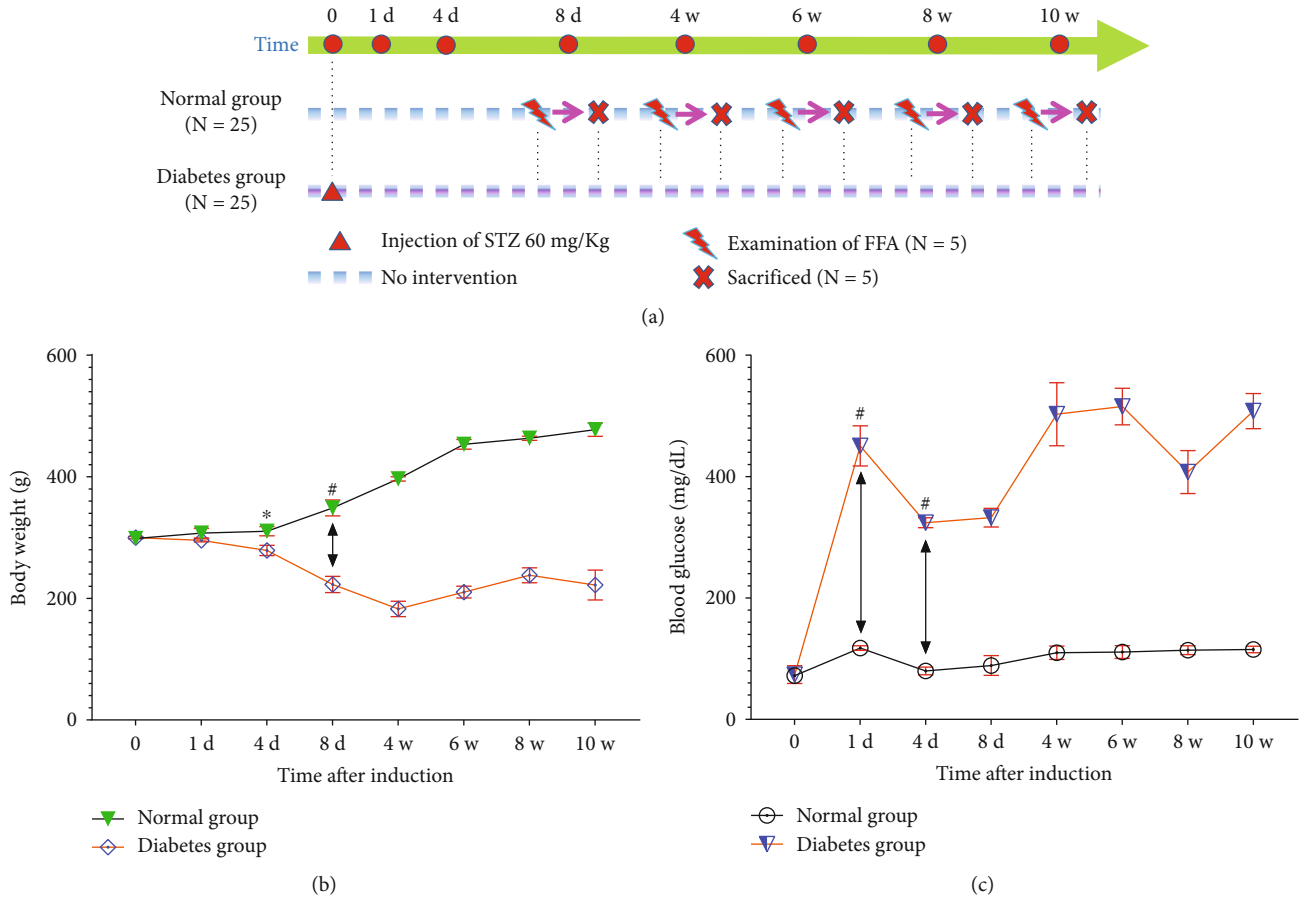

Figure 2: Changes in body weight and blood glucose levels of SD rats in this study. (a) Experimental design scheme. Twenty-five SD rats were intraperitoneally injected with 60 mg/kg STZ and treated as the diabetes group, and 25 normal SD rats were used as the normal group. Body weight (b) and blood glucose levels (c) of animals in this study. Data presented with mean ± standard deviation ($^{*}P < 0.05$, normal group vs. diabetes group on 4th day; $^{\#}P < 0.01$, normal group vs. diabetes group on 1th day, and 4th day, 8th day, respectively). Abbreviations: d: day; w: week; *N*: number; STZ: streptozotocin; FFA: fluorescein fundus angiography.

weight of SD rats in the diabetes group was significantly lower than that in the normal group ($P < 0.01$). In addition, the blood glucose level of SD rats in the diabetes group increased significantly 24 hours after intraperitoneal injection of STZ, which was significantly different from that in the normal group ($P < 0.01$), and the difference remained significant throughout the 10-week observation period after DM induction.

3.2. Animal Examination of FFA. In order to observe the changes of the retinal tissue vascular network system in diabetic SD rats during the 10-week observation period, FFA examination was performed (Figure 3). The optic disc of SD rats was located in the center of the retina, and the retinal blood vessels were radiated. After intraperitoneal injection of sodium fluorescein in SD rats for 3-5 s, retinal arteries began to fill, retinal vein laminar flow was observed for 5-7 s, and retinal vessel fluorescence decreased significantly for 3-6 mins until the fluorescence disappeared completely. The whole skin of SD rats was yellow at the end of examination. During the 10-week observation period after induction of DM, the SD rats in the diabetes group showed obvious vascular tortuosity and dilation at the 6th week, and the peripheral roughness and leakage began to appear at the 8th week, while the obvious vascular leakage and dilation appeared at the 10th week. However, no such phenomenon was observed in the normal group during the 10-week observation period after induction.

3.3. Retinal H&E Staining. In this study, the morphological changes between the retinal nerve fiber layer and the outer nuclear layer of rats were observed on the 8th day, at the 4th week, 6th week, 8th week, and 10th week after DM induction, respectively, and the number and area of RGCs were counted and measured in each group (Figure 4). The number of RGCs in SD rats in the diabetes group decreased significantly compared with that in the normal group ($P < 0.01$) on the 8th day after induction, and with the progression of the disease, the number of RGCs in the diabetes group decreased gradually. However, there was no significant difference in the number of RGCs in the diabetes group at the 8th week and 10th week ($P > 0.05$), and the number of RGCs tended to be stable. Furthermore, there was no significant difference in retinal ganglion cell area between the diabetes group and the normal group during the 10-weeek observation period after induction ($P > 0.05$). Microvascular dilatation was observed at the 6th week, and the formation of new vessel bud and obvious

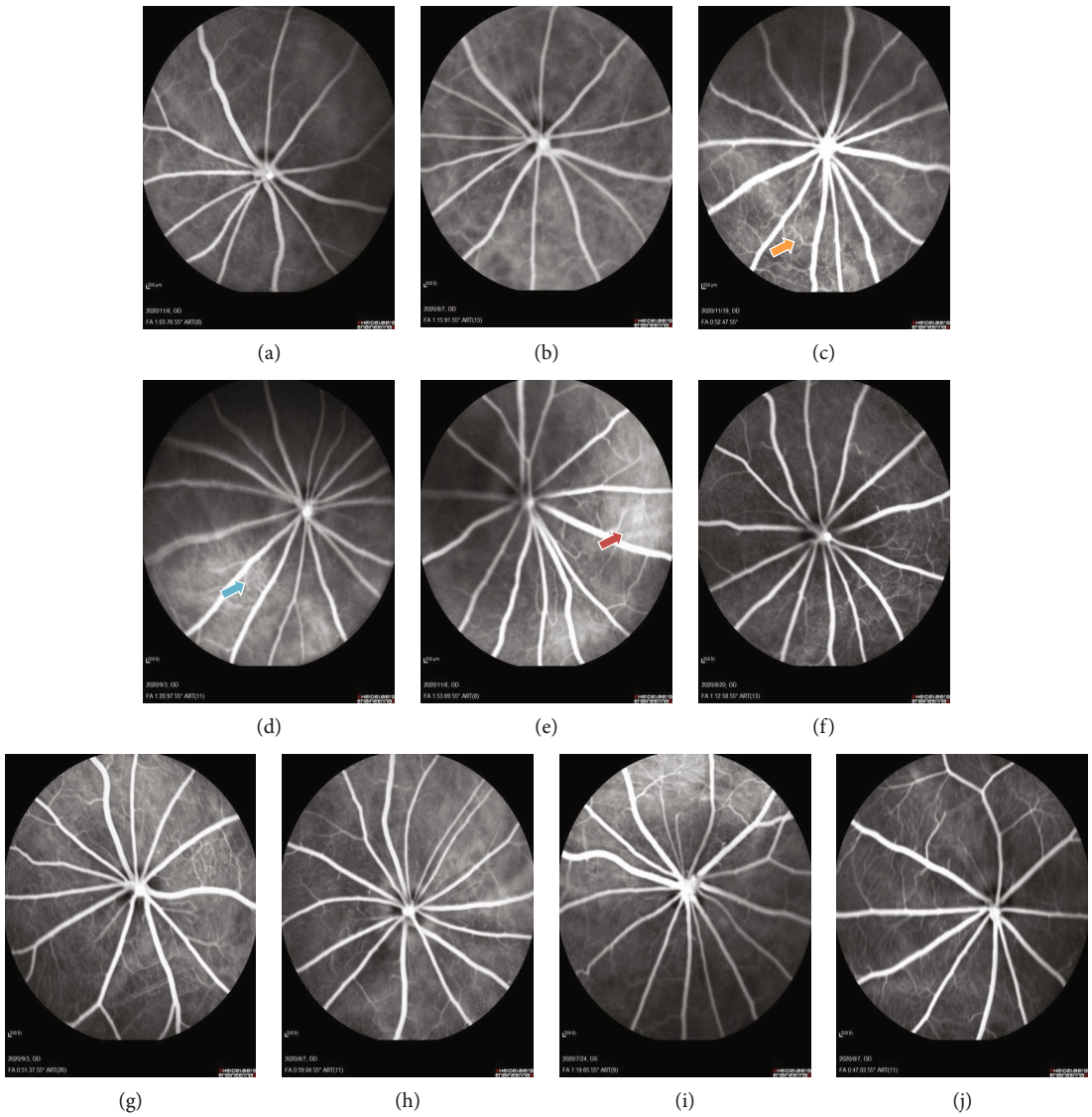

Figure 3: Morphological changes of retina in FFA. (a)–(e) were FFA examination images of diabetic rats on the 8th day, at the 4th week, 6th week, 8th week, and 10th week after induction in the diabetes group, respectively, while (f)–(j) represented FFA images in the normal group at corresponding time points. Yellow arrow indicated vascular tortuosity and dilation, blue arrow indicated rough and leakage of vascular, and red arrow indicated typical leaky vessels with vascular tortuosity and dilation. Scale bar: 200 μm.

microvascular dilatation was observed at the 8th week, while typical new vessel bud was observed between the ganglion cell layer and the inner nuclear layer at the 10th week.

3.4. Retinal PAS Staining. In the PAS staining, the nuclei of endotheliocytes were oval, and the dye was pale, while the nuclei of pericytes were circular and the dye was darker than the endotheliocytes (Figure 5). E/P ratio and acellular strands of retinal tissue vessels of SD rats in each group were counted on the 8th day, at the 4th week, 6th week, 8th week, and 10th week after DM induction, respectively. The E/P ratio in retinal tissue of SD rats in the diabetes group began to be significantly higher than that in the normal group at the 4th week ($P < 0.01$), and with the progress of disease, a significant difference was maintained between the two groups. The number of acellular capillaries was increased on the 8th day after induction in the diabetes group, and the trend of the increase was worse with the progress of the disease course. The significant difference began to appear at the 4th week after DM induction ($P < 0.01$). At 8th week, new vessel buds and a large number of acellular strands were observed, while typical new vessel buds and a large number of acellular filaments were also observed at the 10th week.

3.5. Estimation of VEGF-A in Vitreous Humor. In this study, VEGF-A ELISA kit was used to detect the concentration of VEGF-A in vitreous cavity of SD rats, and the changes in the concentration of VEGF-A in vitreous cavity of rats in each group were determined on the 8th day, at the 4th week, 6th week, 8th week, and 10th week after successful modeling (Figure 6), respectively. On the 8th day after DM induction, the concentration of VEGF-A in vitreous cavity of SD rats in the diabetes group became higher than that in the normal group at the same time point ($P < 0.01$) and remained at a

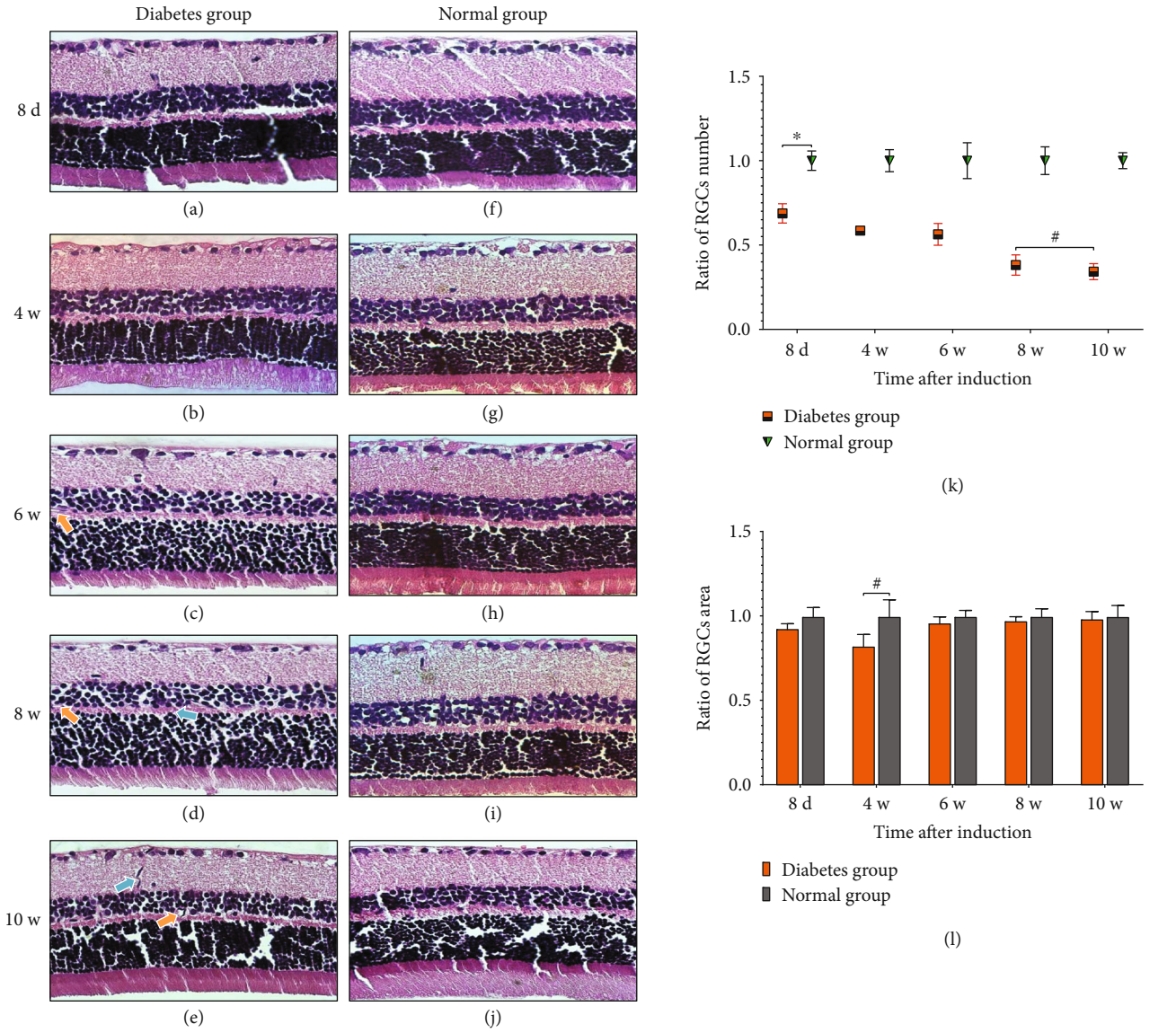

Figure 4: The number and area of RGCs and the morphological changes in two groups of retinal tissue HE staining, respectively (magnification, ×400). Retinal tissue looseness and edema and loosely arranged cells were observed in the diabetic group but not in the normal group. (a)–(e) were the HE staining of the diabetes group.(f)–(j) represented HE staining in the normal group at corresponding time points. (k, l) represented the ratio of RGCs and RGCs area between the two groups at each time, respectively ($^{*}P < 0.01$, $^{\#}P > 0.05$). Blue arrows indicated new vessel buds, and yellow arrows indicated abnormally dilated microvessels. Scale bar: 25 μm. Abbreviations: d: day; w: week; RGCs: retinal ganglion cells.

high concentration with the progression of the disease. However, the VEGF-A concentration in vitreous cavity of SD rats in diabetes group began to increase further at the 6th week after the successful modeling, reaching the peak at the 8th week.

3.6. Fluorescence Imaging Techniques for Retinal–Flat Preparations. In this study, the changes of microvessels and cells in the retinal tissue of SD rats were observed by fluorescein isothiocyanate (FITC)-tomato lectin, rabbit polyclonal anti-type IV collagen antibody, and DAPI-labeled retinal-flat (Figure 7). Compared with the normal group, the number of anti-IV$_+$ collagen strands crosslinked between retinal vessels in the diabetes group began to increase on the 8th day after induction of DM. It was higher than that in the normal group at the 4th week with statistical difference ($P < 0.05$), and with the progression of disease, there was a significant statistical difference ($P < 0.01$). The number of nerve cells in the retinal tissue decreased in the diabetes group compared with that in the normal group on the 8th day after induction ($P < 0.05$), but there was no statistical difference at the 4th week ($P > 0.05$). With the progress of the disease course, the number of nerve cells in retinal tissue decreased significantly in diabetes group at the 6th week ($P < 0.01$) and became worse at the 8th and 10th week, but the number of cells tended to be stable. In addition, the retinal tissue cell area of SD rats in the diabetes group

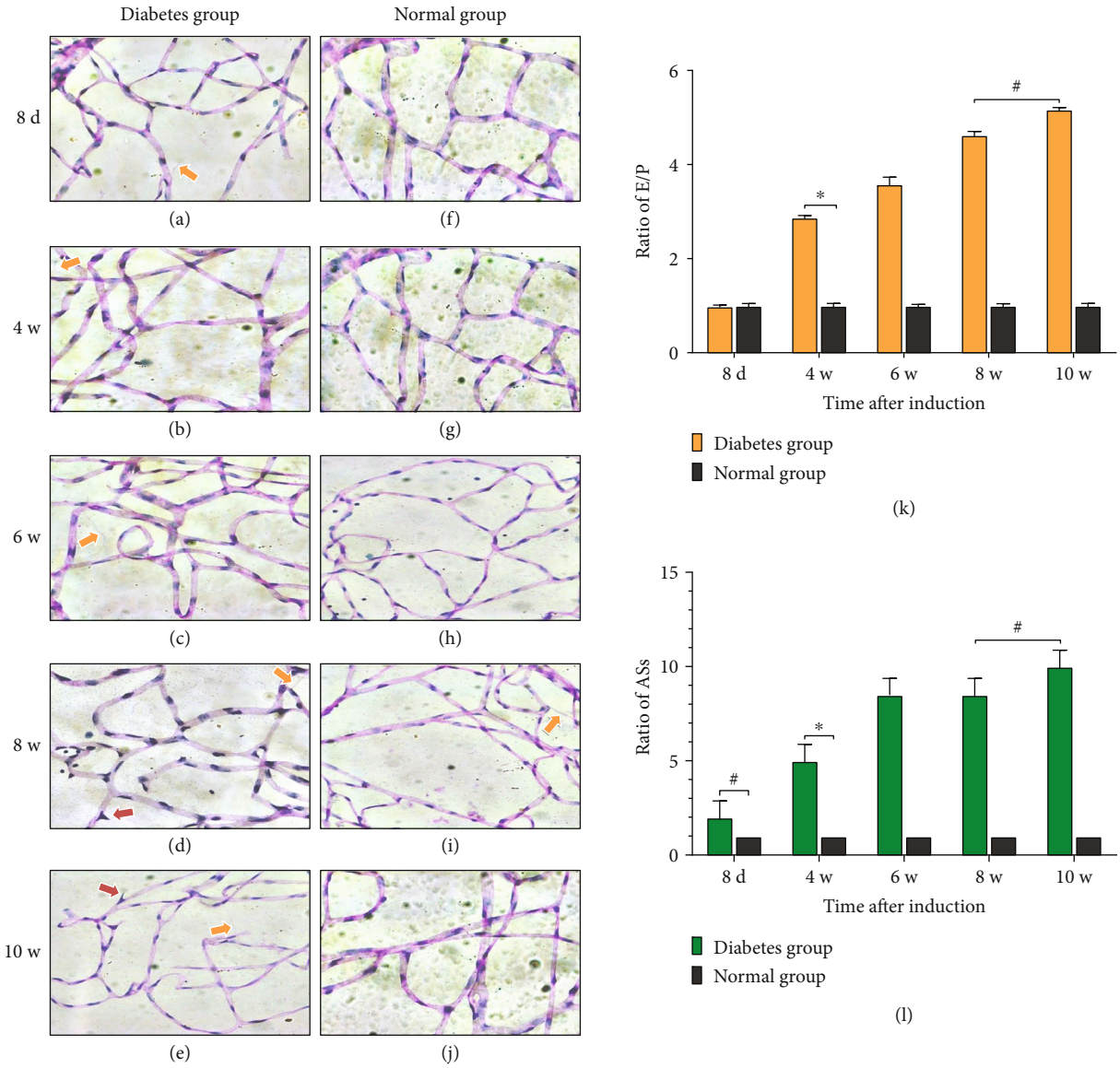

Figure 5: The ratio of E/P and number of acellular strands and the morphological changes between the two groups in PAS staining of retinal tissue (magnification, ×400). (a)–(e) were the PAS staining of the diabetes group. (f)–(j) represented PAS staining in the normal group at corresponding time points. (k, l) represented the ratio of E/P and acellular strands of rats in two groups at each time, respectively. ($^{*}P < 0.01$, $^{\#}P > 0.05$). Yellow arrows indicated acellular strands, and red arrows indicated new vessel buds. Scale bar: 25 μm. Abbreviations: d: day; w: week; E/P: endotheliocytes to pericytes; ASs: acellular strands.

was significantly higher than that in the normal group ($P < 0.01$) on the 8th day, but there was no statistical difference between the two groups with the progression of disease ($P > 0.05$). We observed that the retinal tissue vessels of SD rats in the diabetes group showed obvious tortuosity and local leakage at the 8th week, and the conditions were aggravated, and the formation of new vessel buds were observed at the 10th week.

3.7. The mRNA Expression Levels of VEGF, IL-6, CD18, ICAM, and TNF-α in Retinal Tissue. Many molecules with inflammatory characteristics were detected in the retina of diabetic animals (Figure 8). In this study, we found that the mRNA expression of VEGF in the retinal tissue of SD rats in the diabetes group began to increase on the 8th day after induction, which was higher than that in the normal group ($P < 0.05$), and reached the peak at the 8th week. During the 10-week observation period, the mRNA expression of VEGF in the retinal tissue maintained a state of high expression in the diabetes group. At the same time, the mRNA expression of IL-6, ICAM, and TNF-α in retinal tissue began to be highly expressed in the diabetes group on the 8th day after induction, and the difference was statistically significant compared with that in the normal group at the same time point ($P < 0.01$). With the progression of the disease, the mRNA expression levels of IL-6, ICAM, and TNF-α were in a high expression state in the diabetes group, and a new peak appeared at the 10th week. However, the CD18 mRNA expression in the

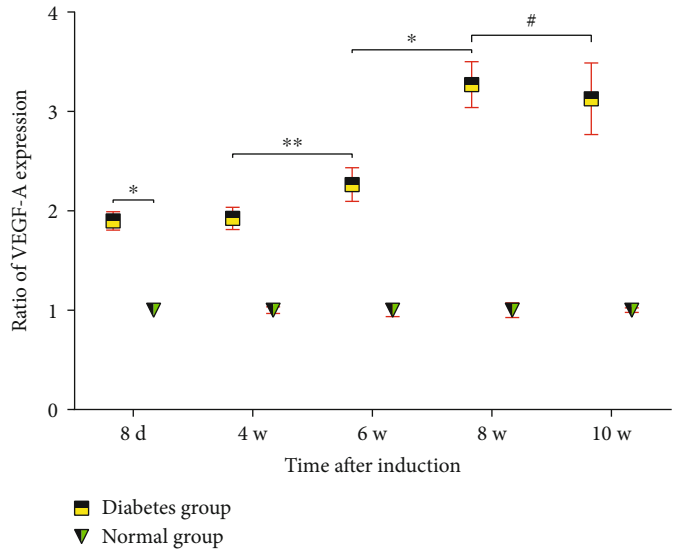

FIGURE 6: The ratio of the VEGF-A expression in vitreous cavity of SD rats in the diabetes group and normal group ($^{*}P < 0.01$, $^{**}P < 0.05$, $^{\#}P > 0.05$).

retinal tissue was significantly higher in the diabetes group than that in the normal group from the 4th week after model establishment ($P < 0.01$) and reached the peak at the 6th week after induction.

4. Discussion

Diabetic retinopathy affects up to 90% of patients with diabetes, with 5% progressing to legal blindness. It has become increasingly clear that diabetic retinopathy affects not only retinal vasculature and retinal neuronal and glial cells but also a variety of inflammatory mediators [4, 5, 13–17] (Figure 9). In our study, a series of RGC changes were observed during the 10-week observation period. The loss of RGCs could lead to a variety of degenerative diseases, including DR and glaucoma [18]. RGCs showed increased apoptosis during the fourth week of the diabetes course [6] and neuronal dysfunction across all retinal layers 12 weeks after STZ-induced diabetes in rats, which is consistent with a study [19] of the late functional loss [20]. As diabetes progresses, RGCs began to decrease at the 6th week [21, 22]. However, previous reports [23–25] suggested that the ganglion cells underwent apoptosis after 12 weeks of STZ-induced diabetes. Based on the observation of different nodes and interspecies difference between our study and previous reports [6, 20, 23–25], oxidative stress, and the high expression of inflammatory mediator precursors caused by hyperglycemia, the apoptosis of RGCs increased on the 8th day after induction. Although the molecular mechanisms of cell depletion or structural abnormalities are not clear, inflammation, oxidative stress, or advanced glycation end products have been suggested to be responsible for pathologic changes in the retina, including a decrease in the number of RGCs [22, 26–28]. Furthermore, a report suggested that the size of RGCs was unchanged compared with the control group during the three-month observation period [25], which is consistent with our observations, except on the 8th day after induction. We speculated that the oxidative stress and the release of inflammatory mediator might cause abnormal metabolism in the retinal neuronal cells in the early stage of diabetes, thereby leading to the increase of the area of the retinal neuronal cells on the 8th day after induction.

The morphological changes seen in retinal microvessels of DR include many pathological changes, such as early loss of pericytes, loss of endothelial cells, increased vascular permeability, and capillary dropout [29, 30]. Our study suggested that the ratio of E/P, acellular strands, and type IV collagen-positive strands in the diabetes group were significantly higher than those in the normal group at the 4th week after induction, while the vascular permeability and vessel buds were observed at the 8th week and 10th week after induction. These predict the abnormal structure of retinal vessels and the occurrence of new blood vessels, which will lead to retinal new vessels. The earliest identified lesion in the diabetic retina is pericyte loss [7, 31]. Pericyte loss progresses over time to endothelial cell loss, resulting in the formation of acellular capillaries [32]. However, the mechanism of pericyte loss in early DR is unclear. Akagi et al. [33] proposed that this mechanism was related to the sorbitol pathway, because they found that aldose reductase was present in human retinal capillary pericytes through immunohistochemical staining, but not in endothelial cells. A study [34] pointed out that hyperglycemia or galactosemia can cause abnormal secretion or function of platelet-derived growth factor B chain, which may selectively affect pericyte activity and lead to pericyte apoptosis. The loss of pericytes in the vascular wall can lead to the increase of E/P ratio, which will lead to the formation of microhemangioma.

In our study, we also found that the vitreous VEGF-A concentration and the expression level of VEGF RNA in the retinal tissue began to show high expression on the 8th day after induction in the diabetes group and reached the peak at the 8th week. Ayalasomayajula et al. [8] found that the concentration of VEGF and the VEGF mRNA expression in retinal tissue of diabetic rats were significantly higher than those in the normal

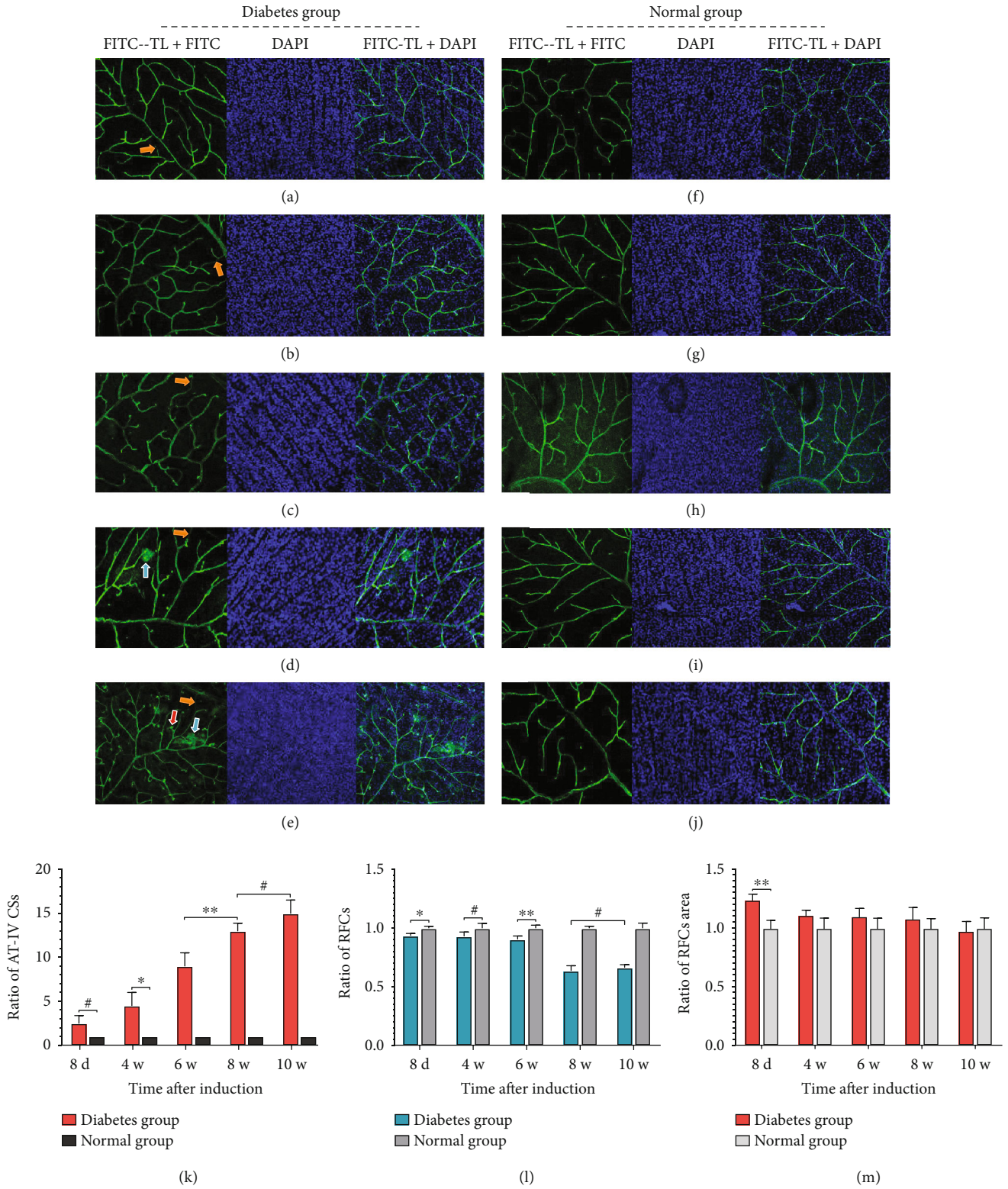

FIGURE 7: (a)–(e) were the immunohistochemical imaging of the diabetes group and (f)–(j) in the normal group, respectively (magnification, ×100). (k)–(m) represented the ratios of type IV collagen-positive strands, retinal cells, and the area of retinal cells in the diabetes group and the normal group at each time, respectively. Yellow arrows indicated type IV_+ collagen-positive strands, blue arrows indicated vascular permeability, and red arrows indicated new vessel buds. ($^*P < 0.05$, $^{**}P < 0.01$, $^{\#}P > 0.05$). Scale bar: 75 μm. Abbreviations: d: day; w: week; FITC: fluorescein isothiocyanate; TL: tomato lectin; AT-IV CSs: anti-type IV collagen strands; RFCs: retinal flat cells.

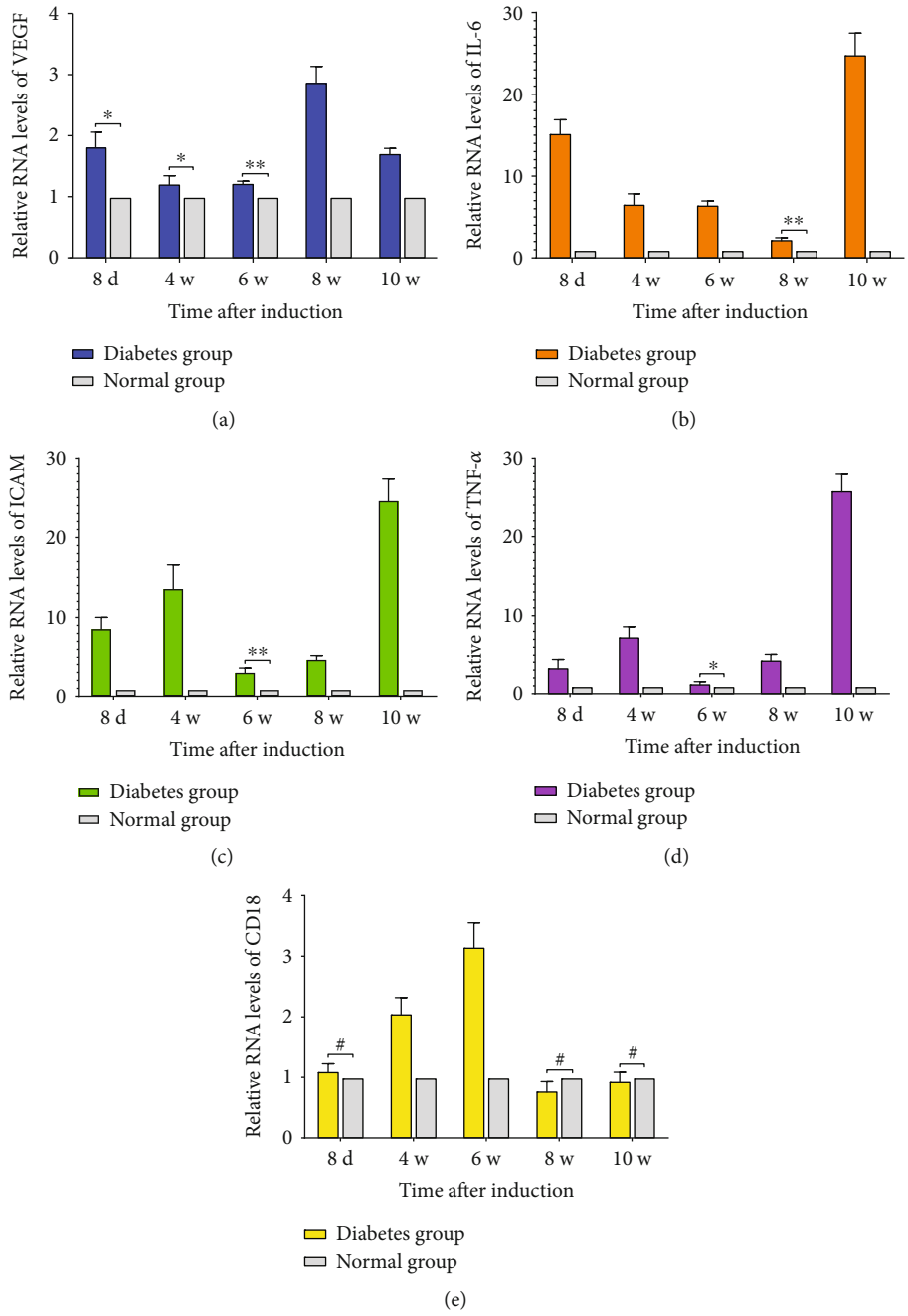

Figure 8: (a)–(e) represented the ratio of the VEGF RNA expression, the ratio of the IL-6 RNA expression, the ratio of the ICAM RNA expression, the ratio of the TNF-α RNA expression, and the ratio of the CD18 RNA expression in retinal tissues, respectively ($^{*}P < 0.05$, $^{**}P < 0.01$, $^{\#}P > 0.05$).

control group on the 8th day after induction, which was consistent with our results. In the 4-week or 12-week observation period, the VEGF concentration and the VEGF mRNA expression in retinal tissue of diabetic rats at the 4th week were the highest compared with the normal control group ($P < 0.01$) [9, 35]. However, the VEGF-A concentration in vitreous cavity and the VEGF mRNA expression level in retinal tissue at the 8th week in our study were different, which might be due to the sharp upregulation of the VEGF-A concentration and the VEGF mRNA expression level in diabetic rats caused by temporary acute high blood glucose concentration, ischemia, and hypoxia in the diabetic group. In addition, the overexpression of VEGF is related to altered angiogenesis and the increases of retinal vascular permeability, resulting in retinal dysfunction [10]. Based on the above studies, the occurrence of new vessel buds or new vessels may be inevitable, and the increasing vascular permeability seems to be a natural development of the DR progression. These new blood vessels may lead to retinal microaneurysms or pathological neovascularization. One study demonstrated that the number of type IV$_{+}$ collagen strands

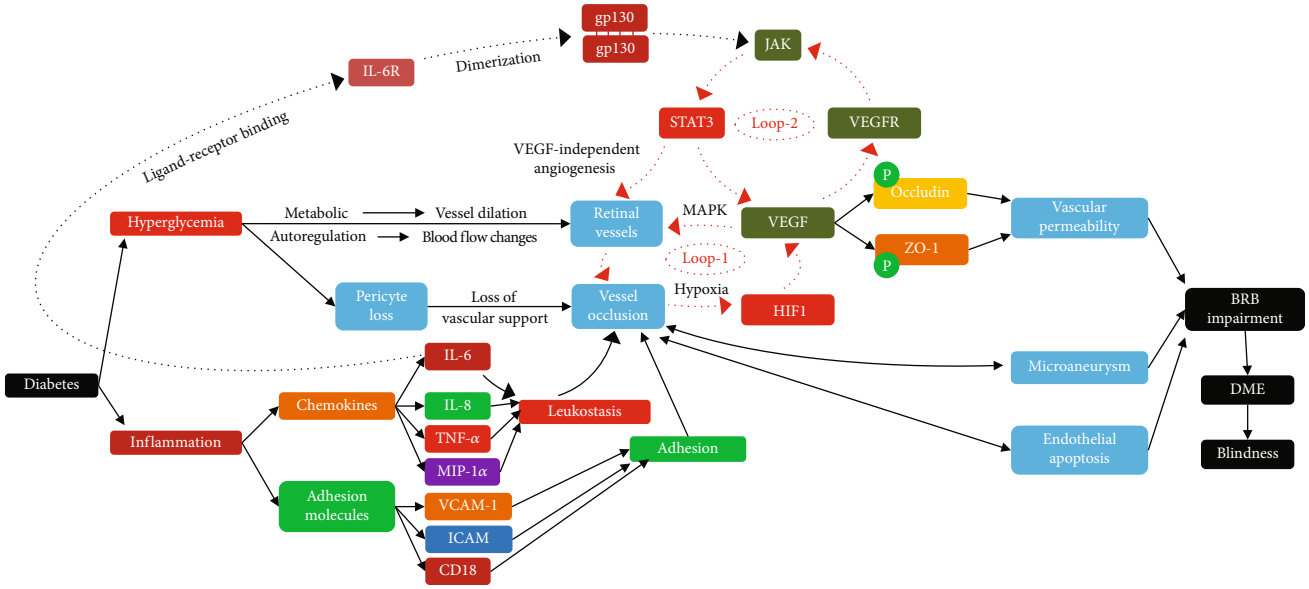

FIGURE 9: The pathogenetic process and molecular mechanism of the early occurrence and development of DR. There are two loops in the mechanism of DR: loop-1 (microcirculation obstruction-hypoxia-HIF1-VEGF-neovascularization-microcirculation obstruction) and loop-2 (VEGF-VEGFR-JAK-STAT3-VEGF).

without any evidences of endothelial proliferation and containing no cellular elements had been the earliest morphological changes at the 1th and 4th week after DM induction [9]. The type IV$_+$ strands indicate a potential relationship between the vascular degeneration and the very early stages of DM [36]. Meanwhile, the vascular regression maybe represent hollow vessels or structurally-collapsed without blood flow, resulting in "vascular ghosts" [37]. Thus, the presence of type IV$_+$ collagen strands in vascular degeneration is a residue of vascular basement membrane composition. These results suggest that endothelial cell degeneration and vascular basement membrane residue caused by diabetes are due to vascular degenerative changes.

Many reports have indicated that retinal microvascular injury is linked to upregulation of several cytokines such as IL-6, TNF-α, VEGF, and CD18 and the pathological overexpression of intercellular and vascular cell adhesion molecules (ICAM-1 and vascular cellular adhesion molecule-1) [38–41]. Our study finds that the mRNA expression levels of IL-6, ICAM, and TNF-α were always high in the diabetes group during the 10-week observation period, and the high expression levels began to appear on the 8th day after the DM induction, but the mRNA expression level of CD18 began to increase significantly at the 4th week after induction, and reached the peak at the 6th week. Increasing evidence suggests that the IL-6 signaling pathway plays a prominent role in the endothelial cell dysfunction and vascular inflammation of DR [42–45]. A report [46] has found that the levels of TNF-α and IL-6 in the diabetes group were significantly higher than those of the normal group at the 2th week after induction, while another study [47] has suggested that IL-6 and TNF-α became significantly elevated in diabetic retina after STZ injection as compared with normal rats at the 4th week after induction and continued to the 8th week. Our results are similar to what have been reported in the two reports. In addition, the expression of CD18 in retina became increased at the 1-week old diabetic rats [48]. Elevated levels of CD18 in neutrophils were present in each stage of DR: the more severe the disease, the higher the levels are [49]. The leukostasis is known to be increased in retinal blood vessels in diabetes, and this process is mediated via ICAM-1, while the retinal ICAM-1 levels were significantly increase when compared with the nondiabetic control group after 1 week of diabetes [50]. ICAM-1 is upregulated by several stimuli, including VEGF, poly (ADP-ribose) polymerase activation, oxidative stress, and dyslipidemia [51–53]. To our knowledge, the dynamics of these factors are attributable to metabolic disorders and the activation of inflammatory responses caused by hyperglycemia during diabetes. Our study is a continuation of the above studies and bears similarities. At the same time, it tries to offer an indepth and detailed understanding of the pathological changes in the early stage of DR.

In conclusion, our study indicated the abnormal alterations of microvessels, microstructure, and inflammatory mediators at the early stage of DR, which confirms and supplements the previous research, and also promotes an indepth understanding and exploration of the pathophysiology and underlying pathogenesis of DR. The results are sufficient to warrant further investigations, offer new insight into the pathogenesis of diabetic retinopathy, and offer novel targets to inhibit the ocular disease.

Data Availability

The datasets used and/or analyzed during this study are available from the corresponding author on reasonable request.

Ethical Approval

Procedure of animals was in accordance with the Association for Research in Vision and Ophthalmology's Resolution for the Use of Animals in Research, which were approved by the First Affiliated Hospital of Nanchang University.

Conflicts of Interest

All authors declare that they have no conflicts of interest.

Authors' Contributions

Ang Xiao, HuiFeng Zhong, and Lei Xiong contributed equally to this work.

Acknowledgments

All authors are equally participated in this study. Thanks are due to all the staffs in the department of The First Affiliated Hospital of Nanchang University, First Affiliated Hospital of Gannan Medical University for their technical support. The present study was supported by the Central Government Guides Local Science and Technology Development Foundation (No. 20211ZDG02003), Key Research Foundation of Jiangxi Province (Nos. 20181BBG70004, 20203BBG73059), Excellent Talents Development Project of Jiangxi Province (No. 20192BCBL23020), Natural Science Foundation of Jiangxi Province (No. 20181BAB205034), Grassroots Health Appropriate Technology "Spark Promotion Plan" Project of Jiangxi Province (No. 20188003), Health Development Planning Commission Science Foundation of Jiangxi Province (Nos. 20201032, 202130210), Health Development Planning Commission Science TCM Foundation of Jiangxi Province (Nos. 2018A060, 2020A0087), Education Department Foundation of Jiangxi Province (Nos. GJJ200157, GJJ200159, GJJ200169), and Key Research Foundation of Jiangxi Province (grant nos. 20203BBG73058, 20192BBGL70033).

References

[1] N. Cheung, P. Mitchell, and T. Y. Wong, "Diabetic retinopathy," *Lancet*, vol. 376, no. 9735, pp. 124–136, 2010.

[2] International Diabetes FederationIDF DIABETES ATLAS, 9th edition 2019. 2019: Assessed at: https://www.diabetesatlas.org/en/.

[3] J. B. Saaddine, A. A. Honeycutt, K. M. Narayan, X. Zhang, R. Klein, and J. P. Boyle, "Projection of diabetic retinopathy and other major eye diseases among people with diabetes mellitus: United States, 2005-2050," *Archives of ophthalmology (Chicago, Ill. : 1960)*, vol. 126, no. 12, pp. 1740–1747, 2008.

[4] T. S. Kern, "Contributions of inflammatory processes to the development of the early stages of diabetic retinopathy," *Experimental Diabetes Research*, vol. 2007, 14 pages, 2007.

[5] P. S. Chan, M. Kanwar, and R. A. Kowluru, "Resistance of retinal inflammatory mediators to suppress after reinstitution of good glycemic control: novel mechanism for metabolic memory," *Journal of Diabetes and its Complications*, vol. 24, no. 1, pp. 55–63, 2010.

[6] A. B. El-Remessy, M. Al-Shabrawey, Y. Khalifa, N. T. Tsai, R. B. Caldwell, and G. I. Liou, "Neuroprotective and blood-retinal barrier-preserving effects of cannabidiol in experimental diabetes," *The American Journal of Pathology*, vol. 168, no. 1, pp. 235–244, 2006.

[7] T. Kuwabara and D. G. Cogan, "Retinal vascular Patterns," *Archives of Ophthalmology*, vol. 69, no. 4, pp. 492–502, 1963.

[8] S. P. Ayalasomayajula and U. B. Kompella, "Celecoxib, a selective cyclooxygenase-2 inhibitor, inhibits retinal vascular endothelial growth factor expression and vascular leakage in a streptozotocin-induced diabetic rat model," *European Journal of Pharmacology*, vol. 458, no. 3, pp. 283–289, 2003.

[9] J. Mitsuhashi, S. Morikawa, K. Shimizu, T. Ezaki, Y. Yasuda, and S. Hori, "Intravitreal injection of erythropoietin protects against retinal vascular regression at the early stage of diabetic retinopathy in streptozotocin- induced diabetic rats," *Experimental Eye Research*, vol. 106, no. 16, pp. 64–73, 2013.

[10] L. Xu, K. Kanasaki, M. Kitada, and D. Koya, "Diabetic angiopathy and angiogenic defects," *Fibrogenesis & Tissue Repair*, vol. 5, no. 1, p. 13, 2012.

[11] T. Ezaki, P. Baluk, G. Thurston, A. L. Barbara, C. Woo, and D. M. Mcdonald, "Time course of endothelial cell proliferation and microvascular remodeling in chronic inflammation," *The American Journal of Pathology*, vol. 158, no. 6, pp. 2043–2055, 2001.

[12] G. Thurston, P. Baluk, A. Hirata, and D. M. McDonald, "Permeability-related changes revealed at endothelial cell borders in inflamed venules by lectin binding," *The American Journal of Physiology*, vol. 271, pp. H2547–H2562, 1996.

[13] V. Asnaghi, C. Gerhardinger, T. Hoehn, A. Adeboje, and M. Lorenzi, "A role for the polyol pathway in the early neuroretinal apoptosis and glial changes induced by diabetes in the rat," *Diabetes*, vol. 52, no. 2, p. 506, 2003.

[14] E. Lieth, T. W. Gardner, A. J. Barber, and D. A. Antonetti, "Retinal neurodegeneration: early pathology in diabetes," *Clinical & Experimental Ophthalmology*, vol. 28, no. 1, pp. 3–8, 2000.

[15] M. Lorenzi and C. Gerhardinger, "Early cellular and molecular changes induced by diabetes in the retina," *Diabetologia*, vol. 44, no. 7, pp. 791–804, 2001.

[16] T. W. Gardner, D. A. Antonetti, A. J. Barber, K. F. LaNoue, and S. W. Levison, "Diabetic retinopathy: more than meets the eye," *Survey of Ophthalmology*, vol. 47, pp. S253–S262, 2002.

[17] A. J. Barber, "A new view of diabetic retinopathy: a neurodegenerative disease of the eye," *Progress in Neuro-Psychopharmacology & Biological Psychiatry*, vol. 27, no. 2, pp. 283–290, 2003.

[18] Y. Koriyama, M. Ohno, T. Kimura, and S. Kato, "Neuroprotective effects of 5-S-GAD against oxidative stress-induced apoptosis in RGC-5 cells," *Brain Research*, vol. 1296, pp. 187–195, 2009.

[19] T. S. Kern and A. J. Barber, "Retinal ganglion cells in diabetes," *The Journal of Physiology*, vol. 586, no. 18, pp. 4401–4408, 2008.

[20] B. V. Bui, M. Loeliger, M. Thomas et al., "Investigating structural and biochemical correlates of ganglion cell dysfunction in streptozotocin-induced diabetic rats," *Experimental Eye Research*, vol. 88, no. 6, pp. 1076–1083, 2009.

[21] P. M. Martin, P. Roon, T. K. Van Ells, V. Ganapathy, and S. B. Smith, "Death of retinal neurons in streptozotocin-induced diabetic mice," *Investigative Ophthalmology & Visual Science*, vol. 45, no. 9, pp. 3330–3336, 2004.

[22] Y. Yang, D. Mao, X. Chen, L. Zhao, Q. Tian, C. Liu et al., "Decrease in retinal neuronal cells in streptozotocin-induced diabetic mice," *Molecular Vision*, vol. 18, pp. 1411–1420, 2012.

[23] A. J. Barber, E. Lieth, S. A. Khin, D. A. Antonetti, A. G. Buchanan, and T. W. Gardner, "Neural apoptosis in the retina during experimental and human diabetes. Early onset and effect of insulin," *The Journal of Clinical Investigation*, vol. 102, no. 4, pp. 783–791, 1998.

[24] A. Kanamori, M. Nakamura, H. Mukuno, H. Maeda, and A. Negi, "Diabetes has an additive effect on neural apoptosis in rat retina with chronically elevated intraocular pressure," *Current Eye Research*, vol. 28, no. 1, pp. 47–54, 2004.

[25] Y. Qin, G. Xu, and W. Wang, "Dendritic abnormalities in retinal ganglion cells of three-month diabetic rats," *Current Eye Research*, vol. 31, no. 11, pp. 967–974, 2006.

[26] I. Charles, A. Khalyfa, D. M. Kumar, R. R. Krishnamoorthy, R. S. Roque, N. Cooper et al., "Serum deprivation induces apoptotic cell death of transformed rat retinal ganglion cells via mitochondrial signaling pathways," *Investigative Ophthalmology & Visual Science*, vol. 46, no. 4, pp. 1330–1338, 2005.

[27] G. Tezel, "Oxidative stress in glaucomatous neurodegeneration: mechanisms and consequences," *Progress in Retinal & Eye Research*, vol. 25, no. 5, pp. 490–513, 2006.

[28] D. Galetović, L. Bojić, K. Bućan, D. Karlica, M. Lesin, and L. Znaor, "The role of oxidative stress after retinal laser photocoagulation in nonproliferative diabetic retinopathy," *Collegium Antropologicum*, vol. 35, no. 3, pp. 835–840, 2011.

[29] W. Wang and A. C. Y. Lo, "Diabetic retinopathy: pathophysiology and treatments," *International Journal of Molecular Sciences*, vol. 19, no. 6, 2018.

[30] T. Kern, D. Antonetti, and L. Smith, "Pathophysiology of diabetic retinopathy: contribution and limitations of laboratory research," *Ophthalmic Research*, vol. 62, no. 4, pp. 196–202, 2019.

[31] H. Hans-Peter, L. Jihong, R. Oliver, S. Moshe, L. Andrea, and B. Christer, "Pericytes and the pathogenesis of diabetic retinopathy," *Hormone & Metabolic Research*, vol. 37, no. S 1, pp. 39–43, 2005.

[32] A. P. Hall, "Review of the pericyte during angiogenesis and its role in cancer and diabetic retinopathy," *Toxicologic Pathology*, vol. 34, no. 6, pp. 763–775, 2006.

[33] Y. Akagi, P. F. Kador, T. Kuwabara, and J. H. Kinoshita, "Aldose reductase localization in human retinal mural cells," *Investigative Ophthalmology & Visual Science*, vol. 24, no. 11, pp. 1516–1519, 1983.

[34] M. Mizutani, T. S. Kern, and M. Lorenzi, "Accelerated death of retinal microvascular cells in human and experimental diabetic retinopathy," *The Journal of Clinical Investigation*, vol. 97, no. 12, pp. 2883–2890, 1996.

[35] T. L. Schrufer, D. A. Antonetti, N. Sonenberg, S. R. Kimball, T. W. Gardner, and L. S. Jefferson, "Ablation of 4E-BP1/2 prevents hyperglycemia-mediated induction of VEGF expression in the rodent retina and in Muller cells in culture," *Diabetes*, vol. 59, no. 9, pp. 2107–2116, 2010.

[36] J. Zhang, Y. Wu, Y. Jin, F. Ji, S. H. Sinclair, Y. Luo et al., "Intravitreal injection of erythropoietin protects both retinal vascular and neuronal cells in early diabetes," *Investigative Ophthalmology & Visual Science*, vol. 49, no. 2, pp. 732–742, 2008.

[37] T. Inai, M. Mancuso, H. Hashizume, F. Baffert, A. Haskell, P. Baluk et al., "Inhibition of vascular endothelial growth factor (VEGF) signaling in cancer causes loss of endothelial fenestrations, regression of tumor vessels, and appearance of basement membrane ghosts," *The American Journal of Pathology*, vol. 165, no. 1, pp. 35–52, 2004.

[38] C. Gustavsson, C. D. Agardh, A. V. Zetterqvist, J. Nilsson, E. Agardh, and M. F. Gomez, "Vascular cellular adhesion molecule-1 (VCAM-1) expression in mice retinal vessels is affected by both hyperglycemia and hyperlipidemia," *PLoS One*, vol. 5, no. 9, article e12699, 2010.

[39] S. S. Soedamah-Muthu, N. Chaturvedi, C. G. Schalkwijk, C. D. Stehouwer, P. Ebeling, and J. H. Fuller, "Soluble vascular cell adhesion molecule-1 and soluble E-selectin are associated with micro- and macrovascular complications in type 1 diabetic patients," *Journal of Diabetes and its Complications*, vol. 20, no. 3, pp. 188–195, 2006.

[40] V. Videm and M. Albrigtsen, "Soluble ICAM-1 and VCAM-1 as markers of endothelial activation," *Scandinavian Journal of Immunology*, vol. 67, no. 5, pp. 523–531, 2008.

[41] A. M. Joussen, V. Poulaki, M. L. le et al., "A central role for inflammation in the pathogenesis of diabetic retinopathy," *The FASEB Journal*, vol. 18, no. 12, pp. 1450–1452, 2004.

[42] C. Gabay, "Interleukin-6 and chronic inflammation," *Arthritis Research & Therapy*, p. S3, 2006.

[43] M. Rincon, "Interleukin-6: from an inflammatory marker to a target for inflammatory diseases," *Trends in Immunology*, vol. 33, no. 11, pp. 571–577, 2012.

[44] T. Barnes, M. Anderson, and R. Moots, "The many faces of interleukin-6: the role of IL-6 in inflammation, vasculopathy, and fibrosis in systemic sclerosis," *International Journal of Rheumatology*, vol. 2011, Article ID 721608, 6 pages, 2011.

[45] S. Rose-John, "IL-6 trans-signaling via the soluble IL-6 receptor: importance for the pro-inflammatory activities of IL-6," *International Journal of Biological Sciences*, vol. 8, no. 9, pp. 1237–1247, 2012.

[46] Y. Wang, W. L. Zhai, and Y. W. Yang, "Association between NDRG2/IL-6/STAT3 signaling pathway and diabetic retinopathy in rats," *European Review for Medical and Pharmacological Sciences*, vol. 24, no. 7, pp. 3476–3484, 2020.

[47] X. Gao, Y. Li, H. Wang, C. Li, and J. Ding, "Inhibition of HIF-1α decreases expression of pro-inflammatory IL-6 and TNF-α in diabetic retinopathy," *Acta Ophthalmologica*, vol. 95, no. 8, pp. e746–e750, 2017.

[48] F. C. Barouch, K. Miyamoto, J. R. Allport, K. Fujita, S. E. Bursell, L. P. Aiello et al., "Integrin-mediated neutrophil adhesion and retinal leukostasis in diabetes," *Investigative Ophthalmology & Visual Science*, vol. 41, no. 5, pp. 1153–1158, 2000.

[49] H. Song, L. Wang, and H. Yang, "Expression of CD18 on the neutrophils of patients with diabetic retinopathy," *Graefe's archive for clinical and experimental ophthalmology = Albrecht von Graefes Archiv für klinische und experimentelle Ophthalmologie*, vol. 245, no. 1, pp. 24–31, 2007.

[50] K. Miyamoto, S. Khosrof, S. E. Bursell, R. Rohan, T. Murata, A. C. Clermont et al., "Prevention of leukostasis and vascular leakage in streptozotocin-induced diabetic retinopathy via intercellular adhesion molecule-1 inhibition," *Proceedings of the National Academy of Sciences of the United States of America*, vol. 96, no. 19, pp. 10836–10841, 1999.

[51] L. Zheng, C. Szabó, and T. S. Kern, "Poly(ADP-ribose) polymerase is involved in the development of diabetic retinopathy via regulation of nuclear factor-kappaB," *Diabetes*, vol. 53, no. 11, pp. 2960–2967, 2004.

[52] M. Lu, V. L. Perez, N. Ma et al., "VEGF increases retinal vascular ICAM-1 expression in vivo," *Investigative Ophthalmology & Visual Science*, vol. 40, no. 8, pp. 1808–1812, 1999.

[53] W. Chen, D. B. Jump, M. B. Grant, W. J. Esselman, and J. V. Busik, "Dyslipidemia, but not hyperglycemia, induces inflammatory adhesion molecules in human retinal vascular endothelial cells," *Investigative Ophthalmology & Visual Science*, vol. 44, no. 11, pp. 5016–5022, 2003.

Hindawi
Disease Markers
Volume 2022, Article ID 6530934, 13 pages
https://doi.org/10.1155/2022/6530934

Research Article

Cinnamaldehyde Downregulation of Sept9 Inhibits Glioma Progression through Suppressing Hif-1α via the Pi3k/Akt Signaling Pathway

Zhiwen Wang,[1] **Changfeng Wang**,[1] **Jieping Fu**,[2] **Ruen Liu**,[1,3] **and Xinhui Zhou**[4]

[1]*Department of Neurosurgery, Jiangxi Provincial People's Hospital Affiliated to Nanchang University, Nanchang 330006, China*
[2]*Department of Neurosurgery, Yichun Second People's Hospital, Yichun 336000, China*
[3]*Department of Neurosurgery, Peking University People's Hospital, Beijing, 100044, China*
[4]*Department of Neurosurgery, The First Affiliated Hospital of Nanchang University, Nanchang 330006, China*

Correspondence should be addressed to Ruen Liu; liuruen@pku.edu.cn and Xinhui Zhou; zhouxinhui2013@163.com

Received 9 October 2021; Accepted 3 January 2022; Published 19 January 2022

Academic Editor: Liu Jinhui

Purpose. Cinnamaldehyde (CA) is the main ingredient in cinnamon, and it has been proven to have an inhibitory effect on many different tumor types. However, it lacks effect on glioma. This paper explores the effect CA has on glioma cells U87 and U251 at the cellular and molecular levels. *Methods*. The relationship between Hif-1α and Sept9 was found by CGGA. Cell Viability Assay (CCK8) was made to detect the proliferation ability. The scratch experiment and the transwell experiment were applied to the migration and invasion ability. Annexin V-FITC/PI were used to detect the cell apoptosis. Western blotting was used to determine the specified protein level. *Results*. Cell proliferation assay results revealed CA to inhibit the proliferation of glioma cells in a dose-dependent manner. It promoted apoptosis for upregulating the expression of Bax and downregulating the expression of Bcl-2. Wound Healing Assay and transwell test found CA to have anti-invasion ability and that it upregulated the expression of E-cadherin and downregulated the expressions of MMP-2 and MMP-9. The molecular mechanism was studied from a tumor microenvironment (TME) perspective. Pi3k inhibitor (LY294002) was used for interfering with cells, and the results found CA to demonstrate a similar effect. Hif-1α and Sept9 expressions were inhibited, and Akt and p-Akt were also inhibited. By using $CoCl_2$ to make hypoxia, CA was discovered to inhibit the high expression of Hif-1α and Sept9, demonstrating a correlation with the Pi3k/Akt pathway. It is suggested that the mechanism of Sept9 under hypoxia regulation can be realized through the Pi3k/Akt pathway. *Conclusions*. This study proves for the first time that CA is an effective drug for inhibiting the proliferation of glioma through Sept9 and reveals Sept9 to be related to the Pi3k/Akt pathway in terms of tumor microenvironment, providing a molecular basis for the further study of CA in glioma treatment.

1. Introduction

Glioma is the most common tumor that is found in the brain's nervous system. Treatments for it include chemotherapy, radiotherapy, surgery, targeted therapy, and stem cell therapy. However, it can easily relapse, it has a high mortality rate, and the prognosis is poor [1]. In recent years, the pharmacological effects of herbaceous plants have made significant progress, including tea polyphenols [2] and indirubin [3], which can effectively inhibit the progress of tumor cells. It has been proven that CA can inhibit colon cancer [4, 5], breast cancer [6], small cell lung cancer [7], and bone marrow-derived suppressor cells (MDSCs) [8] among others [9], but a lack of research has been conducted relating to the treatment of glioma with CA.

CA can inhibit expression of vascular endothelial growth factor (VEGF), reduce neovascularization and cancer cell proliferation, and promote cancer cell apoptosis through tumor hypoxia microenvironmental factor Hif-1α [10, 11]. Therefore, research on the target of Hif-1α has currently become a topic of great interest. It has been shown that Sept9 can bind and stabilize Hif-1α, promote its

transcriptional expression, and promote angiogenesis and tumor growth [12, 13]. By using Chinese Glioma Genome Atlas (CGGA) gene correlation analysis, it was discovered the significant positive correlation between Sept9 and Hif-1α. It has been proven that cinnamaldehyde can inhibit the growth and invasiveness of cancer cells through the Pi3k/Akt pathway. In this paper, experiments were conducted on this basis in order to confirm that CA can inhibit the expression of Sept9 and Hif-1α through the Pi3k/Akt pathway, inhibit the tumor microenvironment, and restrict tumor growth.

2. Materials and Methods

2.1. Chemicals, Reagents, and Antibodies. CA was purchased from MedChemExpress LLC China (purity 99%). This was dissolved in dimethylsulfoxide (DMSO) at a stock solution (200 μg/ml) and stored at -80°C. Dulbecco's modified Eagle's medium (DMEM) and fetal bovine serum (FBS) were purchased from Servicebio (Wuhan, China), and antibodies against Akt, p-Akt, Bax, MMP-2, MMP-9, Hif-1α, Sept9, and β-actin were purchased from Servicebio (Wuhan, China). LC3B was purchased from Bioss (Beijing China), Bcl-2 was purchased from Cell Signal Technology (Massachusetts, USA), rabbit anti-human antibody against Pi3k inhibitor LY 294002 was purchased from Cell Signal Technology (Massachusetts, USA), $CoCl_2$ was purchased from Aladdin (Shanghai, China), CCK8 kit was purchased from Biosharp Life Sciences (Beijing, China), and Annexin V conjugated to fluorescein-isothiocyanate (Annexin V-FITC) apoptosis detection kit was purchased from Beyotime (Beijing, China). All other chemicals that were used in the experiment were of the highest purity grade available.

2.2. Cell Culture. The glioma cell lines (U87, U251) were purchased from the Chinese Academy of Medical Sciences (Beijing, China) and cultured in DMEM that was supplemented with 10% fetal bovine serum (FBS) in an incubator that contained 5% CO_2 at 37°C.

2.3. Cell Viability Assay (CCK8 Analysis). 3×10^3 cells were uniformly cultured in 96-well plates for 12, 24, and 48 hours and were then treated with 0, 2, 4, 8, and 16 μg/ml of CA. 10 μl of CCK8 was added and incubation at 37°C continued for 30 minutes. The solution was then detected with a microplate reader, and the absorbance was checked at 490 nm.

2.4. Cell Apoptosis Assay. The Annexin V-FITC/PI apoptosis detection kit was used. Glioma cells were inoculated in a 6-well plate and treated with CA (0, 4, and 8 μg/ml) for 24 hours. The cells were harvested following trypsin digestion. After the cells were washed with cold phosphate buffer (PBS) twice, the cells were centrifuged for five minutes (1000g), and the supernatants were removed to allow for cell collection. PBS heavy suspension count: $5 \sim 10 \times 10^4$ cells were centrifuged for five minutes (1000g) and suspended in 195 μl binding buffer. Annexin V-FITC (5 μl) and 10 μl PI were added to the mix before incubation for 30~60 min in the dark at room temperature. The PBS was then washed twice, and the quenching solution was added before the film was observed under the fluorescence microscope.

2.5. Wound Healing Assay. U87 and U251 cells were cultured in 6-well plates. When they grew to approximately 85% confluence, they were scratched with a new 200 μl pipette tip and washed twice using PBS. The cells were then treated with 4 and 8 μg/ml of CA for 24 and 48 hours. Pictures were taken under a microscope. ImageJ software was used for the collection of images and to quantify the gap distance.

2.6. Invasion Assay. Transwell membrane filter inserts were used (pore size, 8 μm; Costar, Corning, NY, USA) in 24-well dishes. U87 and U251 cells were pretreated with 4 μg/ml and 8 μg/ml CA for 24 hours and then inoculated with approximately 1×10^4 cells in 200 μl of serum-free medium in the upper chamber and 600 μl medium containing 15% bovine serum in the lower chamber. They were incubated at 37°C with 5% CO_2 for 24 hours and then fixed in 4% paraformaldehyde for 30 minutes and stained in PBS with 0.05% crystal violet for 30 minutes. The cells were gently removed from the upper part of the filter using a cotton swab, the filter was allowed to dry naturally, and the cells from the lower part of the filter were checked and counted under a microscope.

2.7. Clinical Tissue Samples. Tumor tissue samples and adjacent normal brain tissue samples were obtained from eight patients who were undergoing glioma surgery, and the samples were rapidly preserved at Jiangxi Provincial People's Hospital Affiliated to Nanchang University (Jiangxi, China) from October 2019 to December 2020. None of the glioma patients received radiotherapy or chemotherapy prior to surgery while they were hospitalized. Each participant in this study provided written informed consent. The clinical characteristics of the patients were collected, including age, sex, and pathological findings (including WHO grade, immunohistochemical information, and genetic information). The study protocol was approved by the Ethics Committee of Jiangxi Provincial People's Hospital Affiliated to Nanchang University. The glioma and nonneoplastic brain tissue that were collected were fixed with formalin, embedded in paraffin, and cut into 5 μm thick sections for immunohistological analysis. The tissue was then frozen in liquid nitrogen and held at −80°C until calculation.

2.8. Western Blot Analysis. U87 and U251 cells were cultured and treated in 6-well plates. They were cleaved in an ice bath in the RIPA buffer for 30 minutes and centrifuged at 12,000g at 4°C for 15 minutes. The extracted supernatant was stored at -80°C until analysis. The protein concentration was determined using the BCA method (Beyotime). An equal volume of protein was loaded onto a 10% SDS-polyacrylamide gel for electrophoresis and was then transferred by electrophoresis to a polyvinylidene fluoride (PVDF) membrane (Millipore, Boston, MA, USA), which was blocked with 5% bovine serum albumin (BSA) at room temperature overnight at 4°C and then incubated with the primary antibodies against MMP-9 (1 : 1,000), MMP-2 (1 : 1,000), E-cadherin, Bax (1 : 1,000), Bcl-2 (1 : 1,000), Akt (1 : 1,000), Hif-1α

(1 : 1,000), β-actin (1 : 2,000), Sept9 (1 : 800), LC3B (1 : 1,000), and p-Akt (1 : 500). After being washed with a mixture of Tris-buffered saline and Tween-20 (TBST) three times (5 min/time), difluorescent antibody diluted at 1 : 2,000 was added at room temperature for 1 hour. SPECTRA MAX SoftMax Pro analysis software was used for the detection of the OD signal intensity of each band on the film. β-Actin was used as load control and normalization.

2.9. Statistical Analysis. All data are presented as means ± standard deviation (SD). The experiment was repeated a minimum of three times, and an independent t-test was used for making a comparison between the two groups. One-way analysis of variance was used for making comparative analysis between multiple groups with SPSS 26.0 software. $p < 0.05$ was considered to be statistically significant.

3. Results

3.1. There Was a High Expression and High Correlation of Sept9 and Hif-1α in Gliomas. The high expression of Sept9 and Hif-1α in CGGA datasets was detected, showing a positive correlation with WHO grade (Figures 1(a) and 1(b)). There was also a positive correlation between them and patient survival rate. It is suggested that glioma patients with low expressions of both have a better overall survival rate (Figures 1(c) and 1(d)). The correlation analysis of Sept9 and Hif-1α found there to be a high correlation between Sept9 and Hif-1α in both primary and recurrent tumors with WHO grade (Figure 1(e)). Western blotting analysis also confirmed high expressions of Sept9 and Hif-1α in glioma tissues and adjacent normal tissues in eight patients, conforming to WHO grade (Figures 1(f) and 1(g)). The above results demonstrate that a key role is played by Sept9 in the regulation of glioma progression and is closely related to Hif-1α.

3.2. CA Inhibited the Growth and Invasion of Glioma Cells (U87 and U251). This study examined whether CA can inhibit the proliferation of glioma cells in vitro. Following treatment with 0, 2, 4, 8, and 16 μg/ml of CA for 12, 24, and 48 hours, the effects of different concentrations of CA on cell viability were observed using the CCK8 method (Figures 2(a) and 2(b)). The cell survival rate following CA intervention was found to be significantly lower than in the control group in a dose-dependent manner ($p < 0.01$), and a certain time-dependent relationship was observed in the world group. In order to clarify the effect CA has on the migration of glioma cells, the inhibition of CA on the migration of U87 and U251 cells was demonstrated through wound healing experiments. Cells were treated with 0.4 and 8 μg/ml, and then, images of them were obtained under a microscope after 24 and 48 hours (Figures 2(c) and 2(d)). The results showed that CA inhibited cell migration in a dose-dependent manner ($p < 0.05$) (Figures 2(e) and 2(f)).

3.3. CA Promotes Apoptosis and Inhibits Cell Invasion. To confirm whether CA can induce apoptosis of glioma cells, the effect of CA on glioma cells was detected by Annexin V-FITC/PI double staining. Apoptosis was recorded using a fluorescence microscope and counted (Figures 3(a) and 3(b)). The results demonstrated that CA increased the rate of apoptosis in a dose-dependent manner, and the apoptosis rate of cells treated with 0, 4, and 8 μg/ml CA was significantly higher than the control group ($p < 0.01$). While conducting an exploration of the molecular mechanism of apoptosis induced by CA in human glioma cells, the expression of apoptosis-related proteins induced by 0 μg/ml, 4 μg/ml, and 8 μg/ml CA was detected by Western blotting. Analysis showed the expression of Bax to have increased significantly, whereas the expression of Bcl-2 decreased, which resulted in an increase in Bax/Bcl-2 ratio (Figures 3(c) and 3(d)).

3.4. Transwell Chamber Test Was Used for Detecting Whether CA Inhibits the Invasion of Glioma Cells (Figure 3(e)). The results showed that following treatment with CA (0, 4, and 8 μg/ml) for 24 hours, compared to the control group, the number of cells that invaded the lower chamber through holes with a diameter of 8 μm diameter decreased significantly, which indicates CA inhibited the invasion of glioma cells in a dose-dependent manner and that the inhibitory effect on cell invasion was enhanced as CA concentration increased (Figure 3(f)). The expression levels of MMP-2, MMP-9, and E-cadherin were analyzed using Western blotting (Figure 3(g)). CA significantly reduced the expressions of MMP-2 and MMP-9 in a concentration-dependent manner. The expression of E-cadherin was upregulated as the CA dose increased, which is potentially one of the mechanisms for reducing glioma cell invasiveness and adhesion.

3.5. CA Inhibited the Expressions of Hif-1α and Sept9, While Also Inhibiting the Expressions of Akt and p-Akt. Akt is the key factor of the classical signal path Pi3k/Akt. Western blotting was used for detecting the expression of related proteins in human glioma cells induced by 0, 4, and 8 μg/ml CA (Figures 4(a) and 4(f)). The results showed that CA significantly decreased the expressions of Hif-1α, Sept9, and LC3B in a concentration-dependent manner (Figures 4(b), 4(c), and 4(g)). At the same time, it also inhibited the expressions of Akt and p-Akt (Figures 4(d) and 4(e)). From the statistical results, it can be seen that when the concentration of CA is 8 μg/ml, the above proteins are statistically significant ($p < 0.05$).

3.6. The Effect of CA on the Pi3k/Akt Signal Pathway in Glioma Cells. The Pi3k/Akt signaling pathway is involved in the regulation of the biological behavior of cells. To provide further confirmation of the results, LY294002 (50 μM), a specific inhibitor of Pi3k [5], and CA 4 μg/ml were used as positive controls for 24 hours. Western blot analysis showed the effect of CA to be similar to that of LY294002, while it inhibited the expressions of Hif-1α, Sept9, Akt, and p-Akt protein (Figures 5(a)–5(c)). To determine whether CA can regulate glioma cell apoptosis through the Pi3k/Akt pathway under the condition of tumor anoxic microenvironment, the tumor anoxic microenvironment was pretreated with $CoCl_2$ (100 μM) for 24 hours, while the control group was treated with CA 8 μg/ml. Western

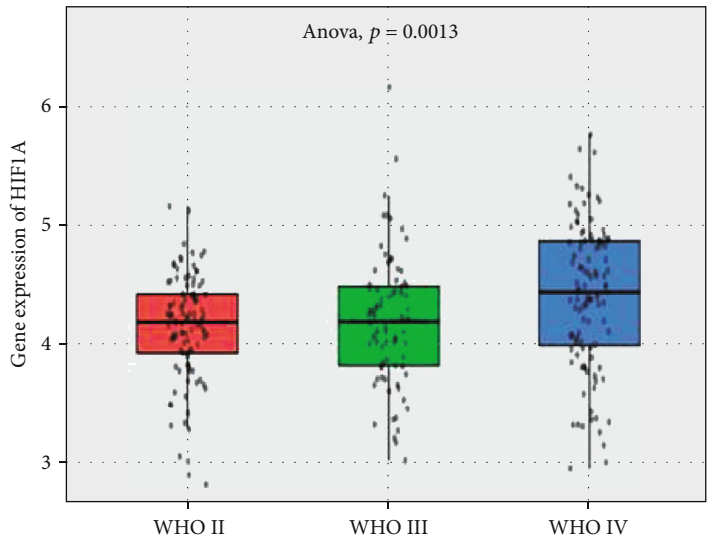

(a)

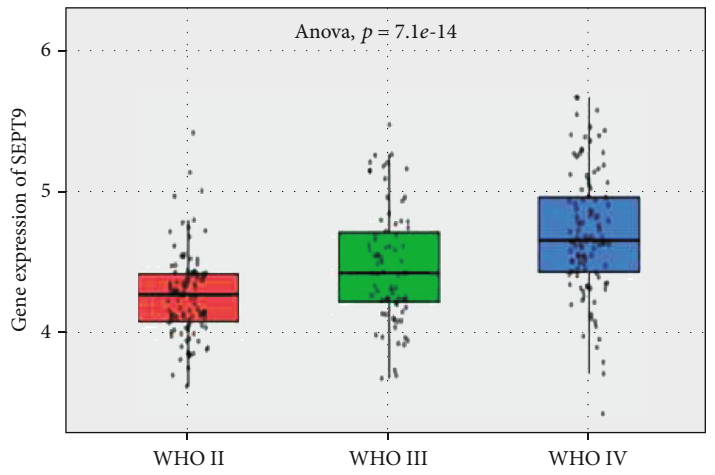

(b)

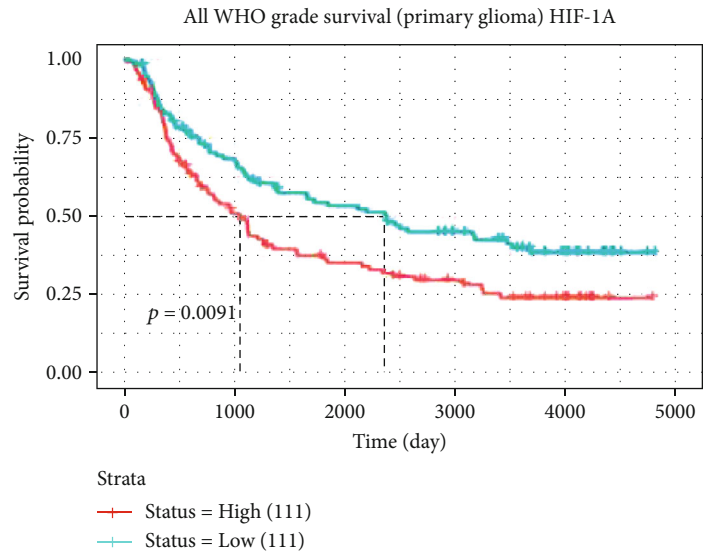

(c)

Figure 1: Continued.

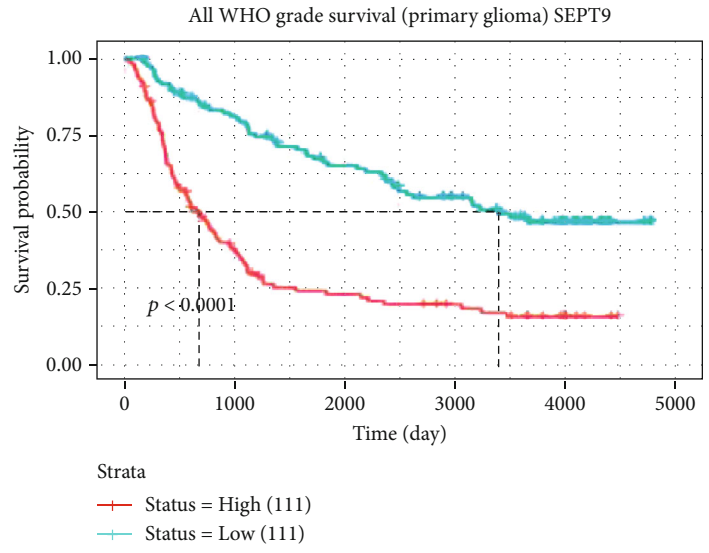

(d)

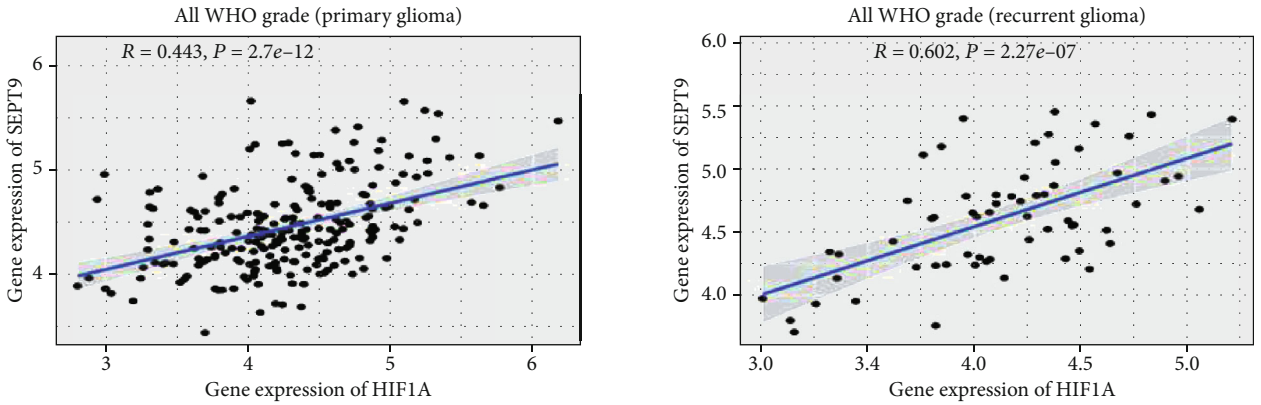

(e)

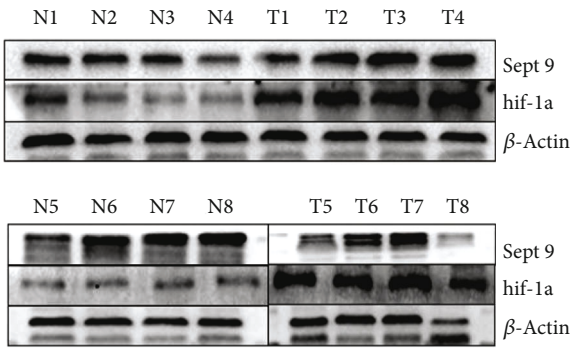

(f)

Figure 1: Continued.

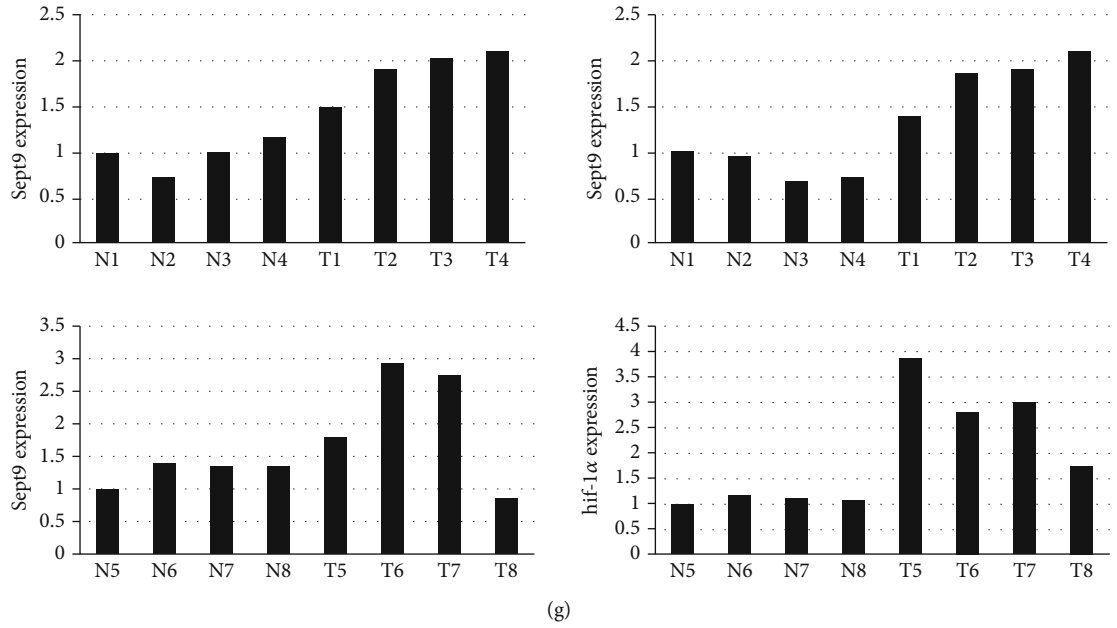

(g)

Figure 1: The expression of Hif-1α and Sept9 in tissues. CGGA database analysis shows the following: (a, b) the expression of Hif-1α and Sept9 in WHO grade of glioma (orange: WHO II, green: WHO III, and blue: WHO IV); (c, d) the relationship between Hif-1α and Sept9 survival rate in primary glioma patients; (e) the correlation between Hif-1α and Sept9 in primary and recurrent gliomas; (f, g) the expression of HIF-1α and Sept9 in tumor tissues and adjacent normal tissues of eight glioma patients.

blotting showed cobalt chloride to increase the expressions of Hif-1α, Sept9, Akt, and p-Akt (Figure 5(d)). Western blotting demonstrated that CA inhibited the expressions of Hif-1 α, Sept9, Akt, and p-Akt when 8 μg/ml CA acted on the cells that were treated with $CoCl_2$ ($p < 0.05$) (Figures 5(e)–5(h)).

4. Discussions

Malignant glioma has long been a problem that is difficult for clinicians. A high mortality rate and poor prognosis are a significant burden to both patients and society. Several methods are used for the treatment of glioma, but due to the characteristics of malignant proliferation, high recurrence, and easy migration, there is a worldwide consensus for studying the pathological mechanism of tumor cells and the way in which tumor progression can be curbed through molecular pathways. The study of tumor microenvironment is currently of great interest in terms of research. Under hypoxia, tumor angiogenesis increases, tumor cell proliferation and migration accelerate, and Hif-1α is the most important factor [14]. The Pi3k/Akt/Hif-1α pathway has been confirmed through experiments, but finding new target proteins remains the key point [15, 16]. The antitumor effect of many drugs is achieved by blocking this pathway. CA is the main component that can be extracted from traditional herbaceous plants [10]. Several studies on tumors have confirmed the inhibitory effect of CA on tumor growth and migration, but comparatively little glioma research has been conducted [9].

Using the CGGA database, it was discovered that the expression of Hif-1α in WHO grade increased as the malignant degree increased and had a positive correlation with patient survival rate. Hif-1α is the core factor of anoxic microenvironment and is highly expressed in several different tumors [7, 17]. The mechanism study is mainly reflected in the increase of reactive oxygen species (ROS) in cancer cells for the further promotion of apoptosis [18] and epithelial-mesenchymal transformation (EMT) [18, 19] and to promote the expression of vascular growth factor, including matrix-derived factor-1 (SDF-1), VEGF, and platelet-derived growth factor B (PDGFB), among others [20, 21]. Binding to PD-L1 in tumors limits T cell growth, increases apoptosis, and activates autophagy [19]. Hif-1α has many mechanisms that are worthy of deeper exploration.

The Sept9 gene is located on human chromosome 17q25.3, containing 17 exons and being approximately 240 $\times$ 103 bp in length. It encodes 15 types of peptide [22] and has the function of recruiting proteins to the cytoplasm [23]. It is also related to the morphological change and transformation of cells. Sept9 has direct involvement in actin dynamics, autophagy, angiogenesis, cell proliferation, cell motility, and microtubule regulation, and it has also been reported that Sept9 is involved in glioblastoma development [24, 25]. Some studies have found Sept9 to be a key factor for the binding and stabilization of Hif-1α and that it can increase the transcription of Hif-1α and activate Sept9-Hif-1α, thereby forming blood vessels and promoting tumor growth [26]. A high expression of Sept9 can effectively inhibit Hif-1α ubiquitination and degradation. CGGA gene analysis also found the expression to increase as the degree of malignancy defined by WHO grade increased, and that it had a positive correlation with patient survival rate. There was a correlation between Hif-1α and Sept9. Tumor samples and adjacent normal tissues from eight patients with different glioma types were detected by WB, and the expressions

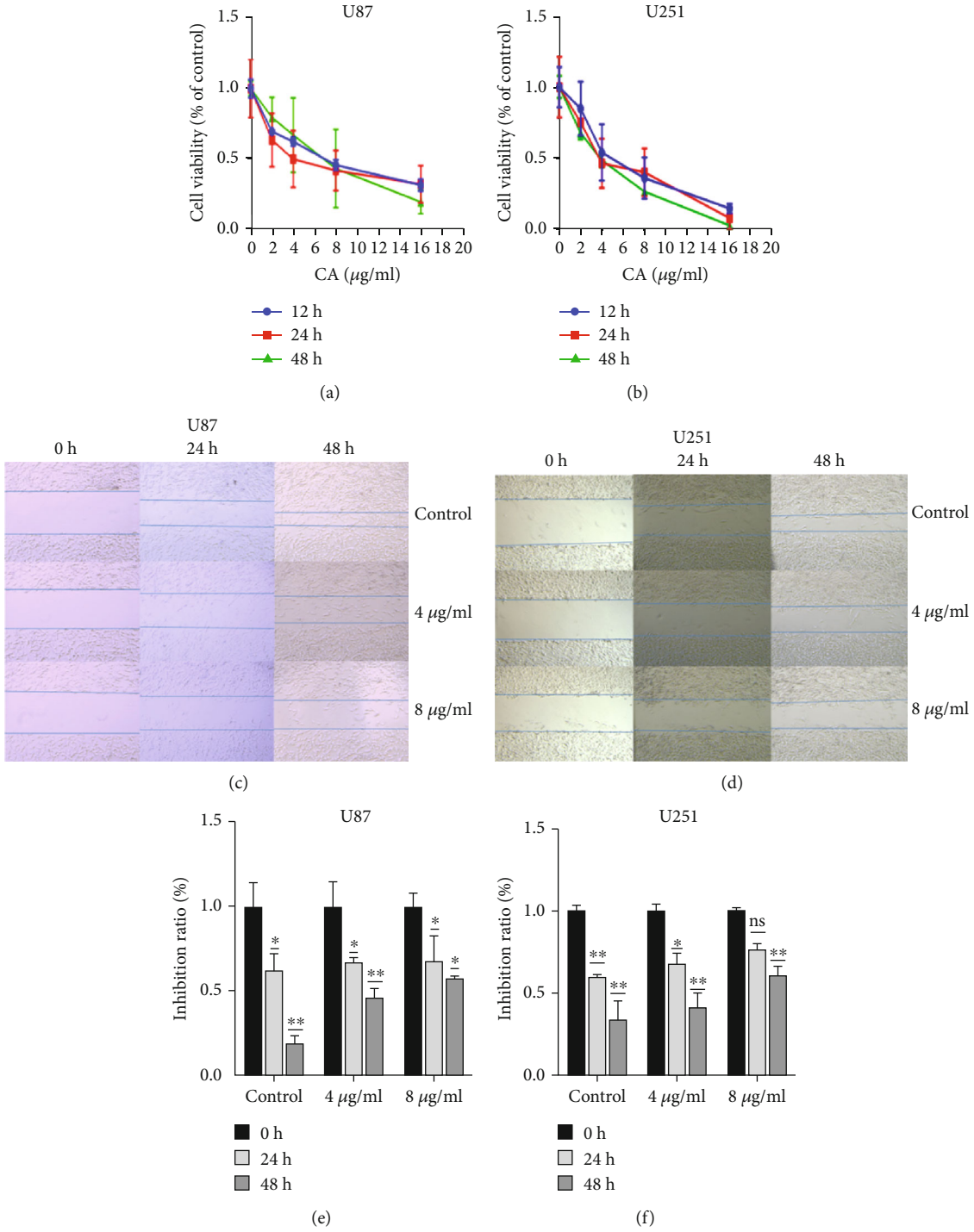

Figure 2: The effects of CA on the cell viability and migration of U87 and U251 cells. (a, b) U87 and U251 cells were treated with control, 2 μg/ml, 4 μg/ml, 8 μg/ml, and 16 μg/ml of CA for 12, 24, and 48 hours. Cell viability rate was measured using CCK8 assay. (c, d) Statistical analysis of scratches. Wound healing analysis was used for determining the migration of U87 and U251 cells for 24 and 48 hours. (e, f) The results of a minimum of three independent trials are presented as mean ± standard deviation (SD). $^{*}p < 0.05$ and $^{**}p < 0.01$ compared to the control group.

were found to be significantly high in WHO grades. This study has explored the changes of Sept9 in U87 and U251 cells treated with CA to become a potential therapeutic target. However, it is unknown which type of cellular signaling pathway it is related to.

CA was used to interfere with U87 and U251, the results showing that it could effectively inhibit proliferation and migration. Annexin V-FITC/PI double staining showed that CA can effectively promote the apoptosis of glioma cells at 4 μg/ml and 8 μg/ml. Western blot apoptotic protein analysis

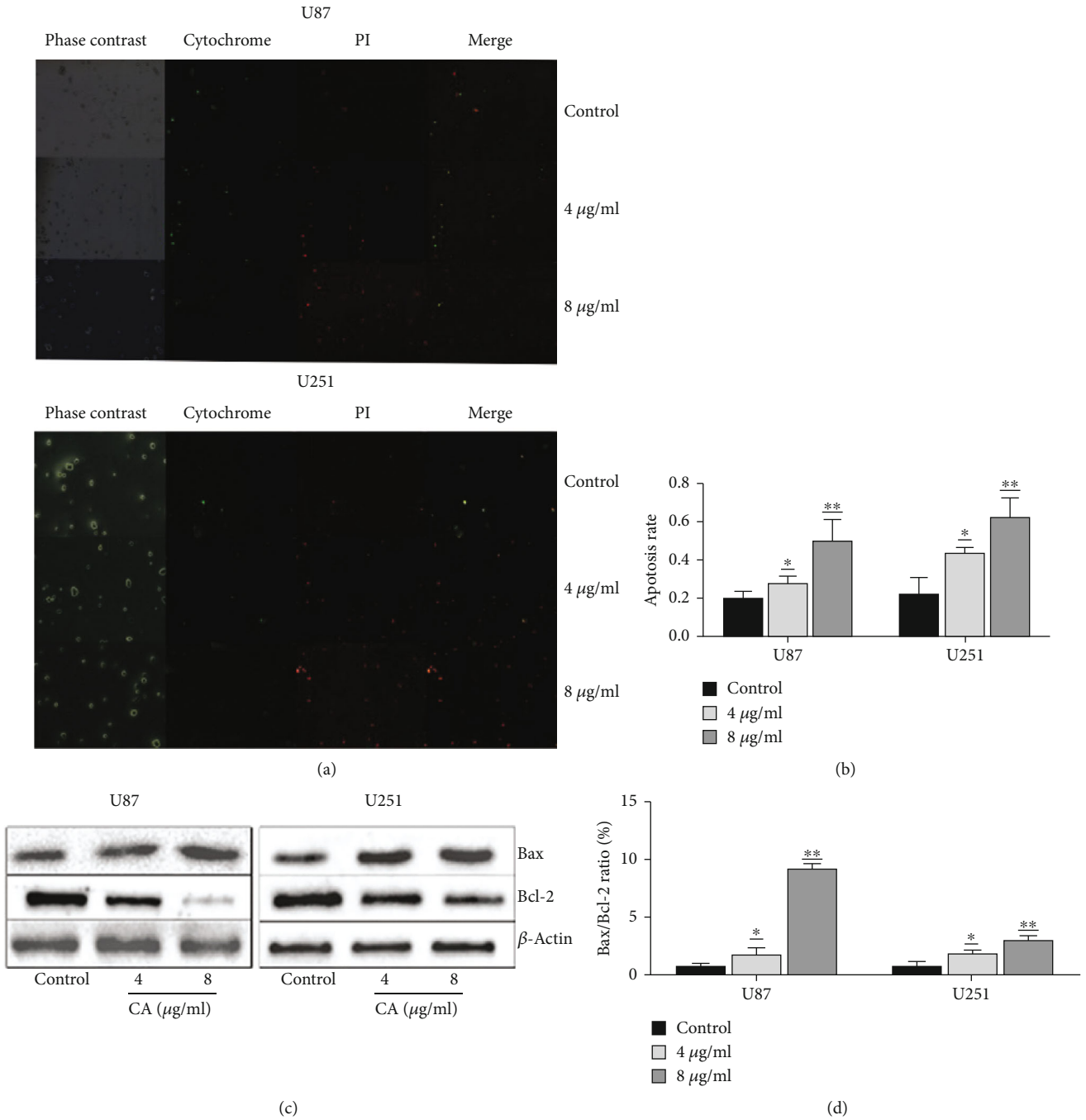

Figure 3: Continued.

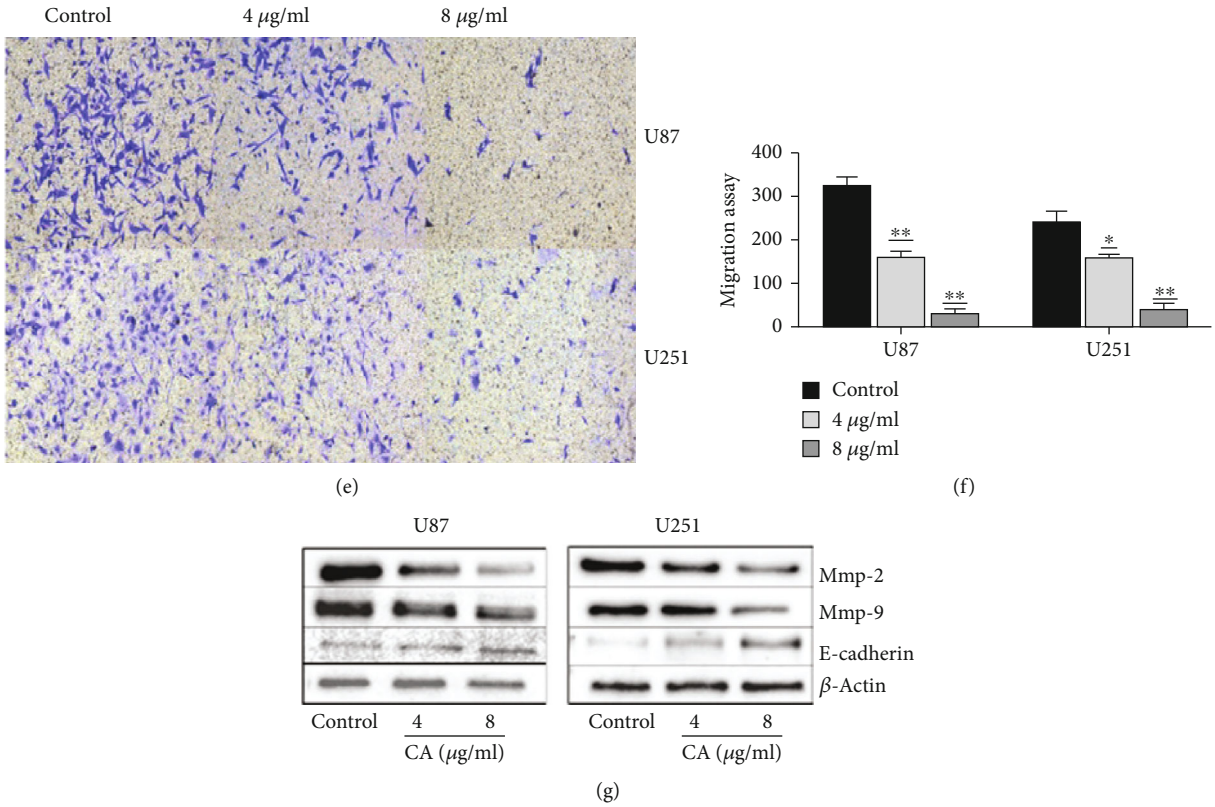

Figure 3: The effects of CA on cell apoptosis and invasive ability of U87 and U251 cells. (a) The cells were inoculated in 6-well plates and treated with CA (4 μg/ml and 8 μg/ml) for 24 hours. Annexin V-FITC/PI apoptosis was detected and photographed under a fluorescence microscope. (b) Statistical results of fluorescence microscope images from the apoptosis experiment. (c) CA induces apoptosis through the regulation of apoptosis-related genes. U87 and U251 cells were treated with 0, 4, and 8 μg/mL CA for 24 hours. Western blot was used for detecting the expressions of Bcl-2 and Bax, and β-actin was the control. (d) The expression levels of Bax and Bcl-2 were measured. The effect of CA was then evaluated using Bax/Bcl-2 ratio. (e) Following treatment with different concentrations (4 μg/ml and 8 μg/ml) of CA, the cells migrated through pores of 8 μm in diameter to the lower lumen within 24 hours, where images were captured using a light microscope (magnification 400x). The white dots are the 8 μm diameter pores of the transwell chamber. (f) Statistical results of invasion experiment. (g) CA suppresses the expressions of MMP-2 and MMP-9 while increasing the expression of E-cadherin. U87 and U251 cells were treated with CA (4 and 8 μg/ml) for 24 hours. The results of a minimum of three independent trials are presented as mean ± SD. $^{*}p < 0.05$ and $^{**}p < 0.01$ compared to the control group.

has shown that targeting Bcl-2 family proteins and Bax proteins are common factors of apoptosis induced by many anticancer drugs, and the proportion of Bax/Bcl-2 plays a key role [27]. As CA dose increased, WB showed a high expression of Bax, but a decreased expression of Bcl-2. Bax/Bcl-2 increased significantly as CA concentration increased, and the effect of CA 8 μg/ml was significant. The results of the invasion experiment showed CA could inhibit the invasion of cells. E-cadherin is a member of the cadherin superfamily, and matrix metalloproteinases (MMPs) can degrade extracellular matrix proteins, thereby affecting the invasion and differentiation of cells. With the aforementioned MMPs, the activities of MMP-2 and MMP-9 gelatinases have a close relationship with tumor metastasis [28]. Increasing the concentration of CA led to the expressions of MMP-2 and MMP-9 being inhibited, whereas the expression of E-cadherin was increased.

CA promotes apoptosis while inhibiting the proliferation of glioma cells, but is it related to Hif-1α and Sept9? Some literature has proven CA to reduce the expression of VEGF via the Pi3k/Akt pathway [29]. Therefore, an attempt was made to detect the expression of Akt and p-Akt in glioma cells that had been treated with CA. The results showed that the expressions of Hif-1α, Sept9, Akt, and p-Akt were inhibited as CA concentration increased. The effect is obvious when CA is 8 μg/ml. At the same time, the autophagy protein LC3B [30] was detected, and the results showed it to be significantly inhibited when CA was 8 μg/ml. Autophagy has a close relationship with anoxic microenvironment [31], but the further relationship requires further study in future experiments.

Further experiments verified the Pi3k/Akt pathway. The Pi3k/Akt pathway has been reported to inhibit apoptosis and facilitate the promotion of cell survival [16]. U87 and U251 cells were treated with LY249002 and CA, and the results showed CA to exhibit a similar effect to LY249002. The statistical results showed the synergistic effect of CA and LY 249003 to be significant. Many reports on the hypoxia model have been made by $CoCl_2$ [7, 32, 33]. Hypoxia can facilitate the promotion of the Pi3k/Akt pathway [34, 35].

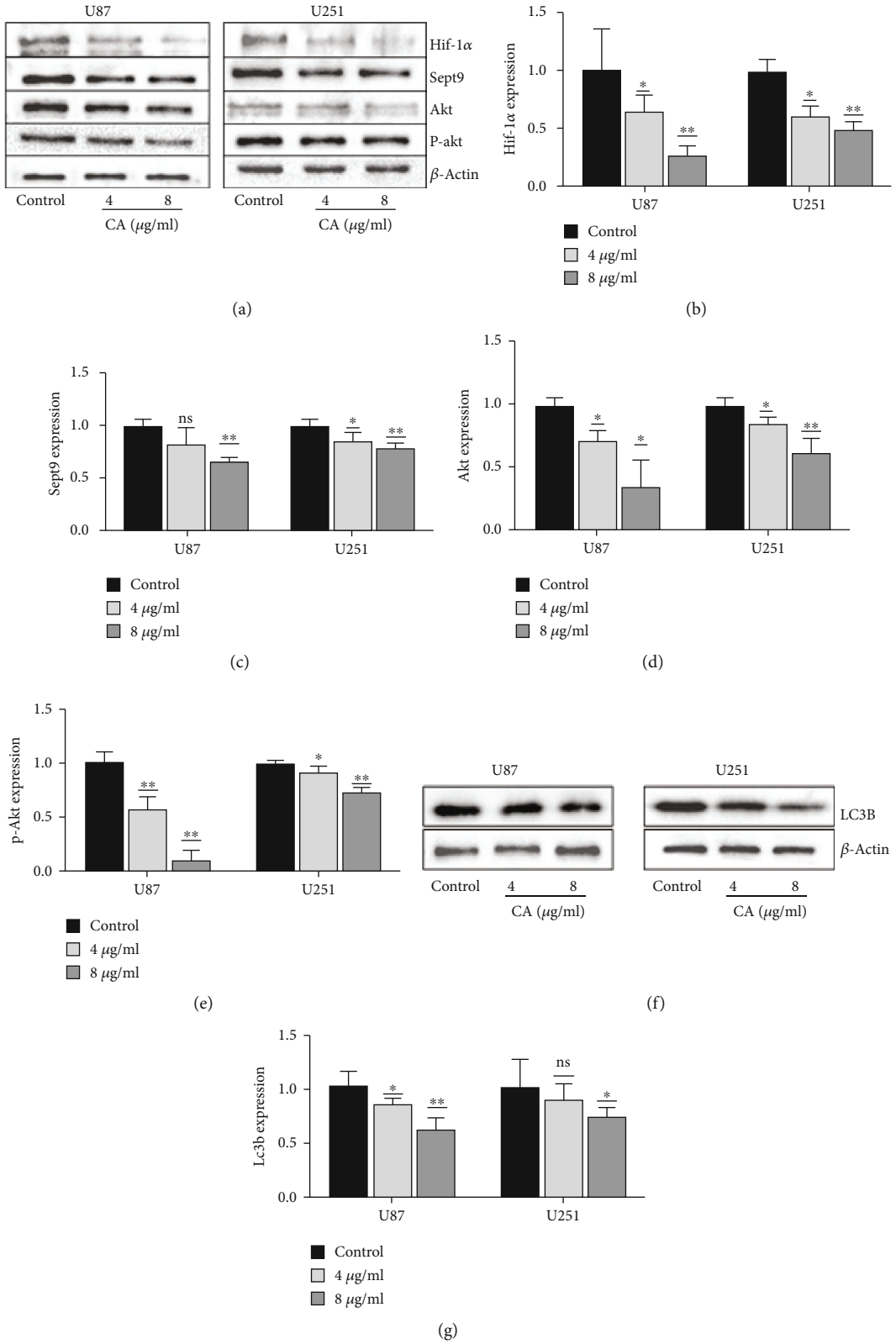

Figure 4: CA inhibits the expression of related proteins. (a) U87 and U251 cells were treated with CA (4 and 8 μg/ml) for 24 hours. The expression levels of Hif-1α, Sept9, Akt, and p-Akt were detected by Western blot analysis, and β-actin was used as a loading control. (b–e) Statistical results of the expressions of Hif-1α, Sept9, Akt, and p-Akt. (f) The expression levels of LC3B were detected using Western blot analysis, and β-actin was used as a loading control. The results of a minimum of three independent trials are presented as mean ± SD. $^{*}p < 0.05$ and $^{**}p < 0.01$ compared to the control group.

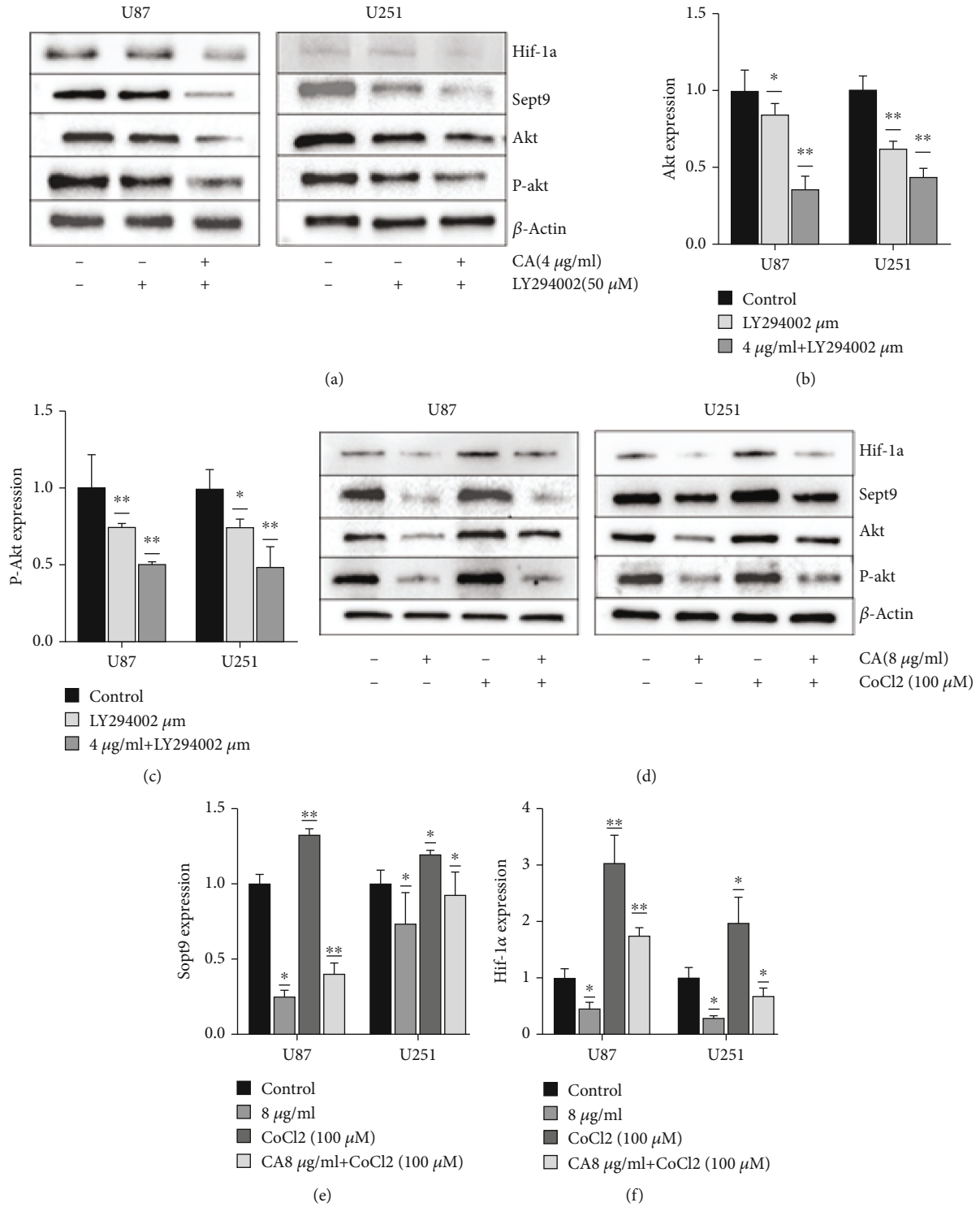

Figure 5: Continued.

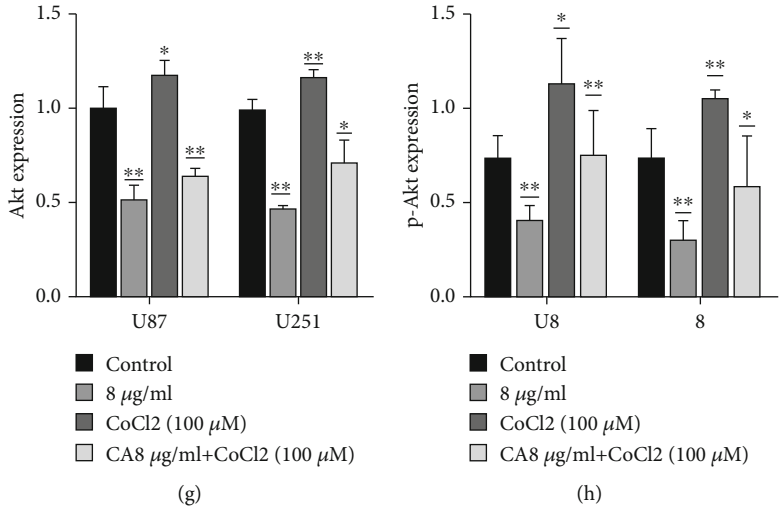

Figure 5: The effects of cinnamaldehyde (CA) on the Pi3k/Akt signaling pathway in U87 and U251 cells. (a) U87 and U251 cells were treated with CA (CA 4 μg/ml and CA 4 μg/ml) and LY294002 (50 μM) for 24 hours. The expression levels of Hif-1α, Sept9, Akt, and p-Akt were detected using Western blot analysis, and β-actin was used as a loading control. (b, c) The statistical results of the expressions of Akt and p-Akt. (d) U87 and U251 cells were treated with CA (CA 8 μg/ml) and CA 8 μg/ml+$CoCl_2$ (100 μM) for 24 hours. The expression levels of Hif-1α, Sept9, Akt, and p-Akt were detected using Western blot analysis, and β-actin as the control. (e–h) Statistical results of the expressions of Hif-1α, Sept9, Akt, and p-Akt. The results of a minimum of three independent trials are presented as mean $\pm$ SD. $^{*}p < 0.05$ and $^{**}p < 0.01$ compared to the control group.

Therefore, the control group was set up and CA 8 μg/ml and $CoCl_2$ (100 μM) were used for interfering with glioma cells in order to extract protein for WB detection. The statistical results showed $CoCl_2$ to promote the expressions of Akt and p-Akt, and the expressions of Hif-1α and Sept9 increased. However, when CA 8 μg/ml was added with cobalt chloride, CA's inhibitory effect improved, and the expressions of Akt and p-Akt increased slightly. Therefore, it can be speculated that CA inhibits glioma progression via the Pi3k/Akt pathway, and Hif-1α and Sept9 exhibit the same trend. However, it is unknown whether Hif-1α combines with Sept9 to produce such a synergistic effect, and this requires further confirmation through experiments.

5. Conclusions

The results of this study suggest that the high expression of Sept9 in gliomas is highly correlated with Hif-1α. This is consistent with previous CGGA statistical results, so the inhibitory effect CA has on glioma cells has a significant relationship with Hif-1α. It is also suggested that a decrease in Sept9 expression may be a new target for effectively inhibiting glioma progression. There were some limitations to this experiment, so further experiments are required for verification of the mechanism of CA inhibiting Sept9 in glioma.

Data Availability

My experimental data, including tables and pictures, were obtained from specific experiments, and the article included the analysis results and pictures of relevant data. The data used to support the findings of this study is available from the corresponding author upon request.

Conflicts of Interest

The authors declared that they have no conflicts of interest to this work.

Acknowledgments

This work was supported by a grant from the National Natural Science Foundation of China (Grant No. 2101000567).

References

[1] J. Li, J. Shen, Z. Wang et al., "ELTD1 facilitates glioma proliferation, migration and invasion by activating JAK/STAT3/HIF-1α signaling axis," *Scientific Reports*, vol. 9, no. 1, p. 13904, 2019.

[2] E. J. Mun, H. M. Babiker, U. Weinberg, E. D. Kirson, and D. D. Von Hoff, "Tumor-treating fields: a fourth modality in cancer treatment," *Clinical Cancer Research*, vol. 24, no. 2, pp. 266–275, 2018.

[3] L. Chen, J. Wang, J. Wu, Q. Zheng, and J. Hu, "Indirubin suppresses ovarian cancer cell viabilities through the STAT3 signaling pathway," *Drug Design, Development and Therapy*, vol. Volume 12, pp. 3335–3342, 2018.

[4] C. E. Wu, Y. W. Zhuang, J. Y. Zhou, S. L. Liu, R. P. Wang, and P. Shu, "Cinnamaldehyde enhances apoptotic effect of oxaliplatin and reverses epithelial-mesenchymal transition and stemnness in hypoxic colorectal cancer cells," *Experimental Cell Research*, vol. 383, no. 1, p. 111500, 2019.

[5] J. Li, Y. Teng, S. Liu et al., "Cinnamaldehyde affects the biological behavior of human colorectal cancer cells and induces apoptosis via inhibition of the PI3K/Akt signaling pathway," *Oncology Reports*, vol. 35, no. 3, pp. 1501–1510, 2016.

[6] Y. F. Chiang, H. Y. Chen, K. C. Huang, P. H. Lin, and S. M. Hsia, "Dietary antioxidant trans-cinnamaldehyde reduced

visfatin-induced breast cancer progression: in vivo and in vitro study," *Antioxidants*, vol. 8, no. 12, 2019.

[7] C. Wu, Y. Zhuang, S. Jiang et al., "Cinnamaldehyde induces apoptosis and reverses epithelial-mesenchymal transition through inhibition of Wnt/β-catenin pathway in non-small cell lung cancer," *The International Journal of Biochemistry & Cell Biology*, vol. 84, pp. 58–74, 2017.

[8] W. He, W. Zhang, Q. Zheng et al., "Cinnamaldehyde causes apoptosis of myeloid-derived suppressor cells through the activation of TLR4," *Oncology Letters*, vol. 18, no. 3, pp. 2420–2426, 2019.

[9] S. H. Hong, I. A. Ismail, S. M. Kang, D. C. Han, and B. M. Kwon, "Cinnamaldehydes in cancer chemotherapy," *Phytotherapy Research*, vol. 30, no. 5, pp. 754–767, 2016.

[10] K. Zhang, E. S. Han, T. H. Dellinger et al., "Cinnamon extract reduces VEGF expression via suppressing HIF-1α gene expression and inhibits tumor growth in mice," *Molecular Carcinogenesis*, vol. 56, no. 2, pp. 436–446, 2017.

[11] K. Patra, S. Jana, A. Sarkar, D. P. Mandal, and S. Bhattacharjee, "The inhibition of hypoxia-induced angiogenesis and metastasis by cinnamaldehyde is mediated by decreasing HIF-1α protein synthesis via PI3K/Akt pathway," *BioFactors*, vol. 45, no. 3, pp. 401–415, 2019.

[12] M. Golan and N. J. Mabjeesh, "SEPT9_i1 is required for the association between HIF-1α and importin-α to promote efficient nuclear translocation," *Cell Cycle*, vol. 12, no. 14, pp. 2297–2308, 2013.

[13] K. Tazat, S. Schindler, R. Depping, and N. J. Mabjeesh, "Septin 9 isoform 1 (SEPT9_i1) specifically interacts with importin-α7 to drive hypoxia-inducible factor (HIF)-1α nuclear translocation," *Cytoskeleton (Hoboken).*, vol. 76, no. 1, pp. 123–130, 2019.

[14] E. Ruoslahti, "Specialization of tumour vasculature," *Nature Reviews. Cancer*, vol. 2, no. 2, pp. 83–90, 2002.

[15] B. Xu, C. Jiang, H. Han et al., "Icaritin inhibits the invasion and epithelial-to-mesenchymal transition of glioblastoma cells by targeting EMMPRIN via PTEN/AKt/HIF-1αsignalling," *Clinical and Experimental Pharmacology & Physiology*, vol. 42, no. 12, pp. 1296–1307, 2015.

[16] W. Huang, X. Ding, H. Ye, J. Wang, J. Shao, and T. Huang, "Hypoxia enhances the migration and invasion of human glioblastoma U87 cells through PI3K/Akt/mTOR/HIF-1α pathway," *Neuroreport*, vol. 29, no. 18, pp. 1578–1585, 2018.

[17] X. Jing, F. Yang, C. Shao et al., "Role of hypoxia in cancer therapy by regulating the tumor microenvironment," *Molecular Cancer*, vol. 18, no. 1, p. 157, 2019.

[18] Y. Shen, J. Yang, J. Zhao, C. Xiao, C. Xu, and Y. Xiang, "The switch from ER stress-induced apoptosis to autophagy via ROS-mediated JNK/p62 signals: a survival mechanism in methotrexate-resistant choriocarcinoma cells," *Experimental Cell Research*, vol. 334, no. 2, pp. 207–218, 2015.

[19] M. Z. Noman, M. Hasmim, A. Lequeux et al., "Improving cancer immunotherapy by targeting the hypoxic tumor microenvironment: new opportunities and challenges," *Cells*, vol. 8, no. 9, 2019.

[20] M. A. Akanji, D. Rotimi, and O. S. Adeyemi, "Hypoxia-inducible factors as an alternative source of treatment strategy for cancer," *Oxidative Medicine and Cellular Longevity*, vol. 2019, 2019.

[21] G. L. Semenza, "Hypoxia-inducible factors: mediators of cancer progression and targets for cancer therapy," *Trends in Pharmacological Sciences*, vol. 33, no. 4, pp. 207–214, 2012.

[22] A. D. Chacko, S. S. McDade, S. Chanduloy et al., "Expression of the SEPT9_i4 isoform confers resistance to microtubule-interacting drugs," *Cellular Oncology (Dordrecht)*, vol. 35, no. 2, pp. 85–93, 2012.

[23] M. E. Sellin, S. Stenmark, and M. Gullberg, "Mammalian SEPT9 isoforms direct microtubule-dependent arrangements of septin core heteromers," *Molecular Biology of the Cell*, vol. 23, no. 21, pp. 4242–4255, 2012.

[24] G. Zhang, W. Feng, and J. Wu, "Down-regulation of SEPT9 inhibits glioma progression through suppressing TGF- β-induced epithelial-mesenchymal transition (EMT)," *Biomedicine & Pharmacotherapy*, vol. 125, p. 109768, 2020.

[25] D. Xu, A. Liu, X. Wang et al., "Repression of Septin9 and Septin2 suppresses tumor growth of human glioblastoma cells," *Cell Death & Disease*, vol. 9, no. 5, p. 514, 2018.

[26] S. Amir, M. Golan, and N. J. Mabjeesh, "Targeted knockdown of SEPT9_v1 inhibits tumor growth and angiogenesis of human prostate cancer cells concomitant with disruption of hypoxia-inducible factor-1 pathway," *Molecular Cancer Research*, vol. 8, no. 5, pp. 643–652, 2010.

[27] G. Y. Bae, S. J. Choi, J. S. Lee et al., "Loss of E-cadherin activates EGFR-MEK/ERK signaling, which promotes invasion via the ZEB1/MMP2 axis in non-small cell lung cancer," *Oncotarget*, vol. 4, no. 12, pp. 2512–2522, 2013.

[28] Z. Cavdar, A. E. Canda, C. Terzi, S. Sarioglu, M. Fuzun, and G. Oktay, "Role of gelatinases (matrix metalloproteinases 2 and 9), vascular endothelial growth factor and endostatin on clinicopathological behaviour of rectal cancer," *Colorectal Disease*, vol. 13, no. 2, pp. 154–160, 2011.

[29] W. Y. Bae, J. S. Choi, J. E. Kim, and J. W. Jeong, "Cinnamic aldehyde suppresses hypoxia-induced angiogenesis via inhibition of hypoxia-inducible factor-1α expression during tumor progression," *Biochemical Pharmacology*, vol. 98, no. 1, pp. 41–50, 2015.

[30] S. Vishnupriya, L. C. Priya Dharshini, K. M. Sakthivel, and R. R. Rasmi, "Autophagy markers as mediators of lung injury-implication for therapeutic intervention," *Life Sciences*, vol. 260, p. 118308, 2020.

[31] H. Folkerts, S. Hilgendorf, E. Vellenga, E. Bremer, and V. R. Wiersma, "The multifaceted role of autophagy in cancer and the microenvironment," *Medicinal Research Reviews*, vol. 39, no. 2, pp. 517–560, 2019.

[32] M. Wang, X. Zhao, D. Zhu et al., "HIF-1α promoted vasculogenic mimicry formation in hepatocellular carcinoma through LOXL2 up-regulation in hypoxic tumor microenvironment," *Journal of Experimental & Clinical Cancer Research*, vol. 36, no. 1, p. 60, 2017.

[33] G. Yang, S. Xu, L. Peng, H. Li, Y. Zhao, and Y. Hu, "The hypoxia-mimetic agent $CoCl_2$ induces chemotherapy resistance in LOVO colorectal cancer cells," *Molecular Medicine Reports*, vol. 13, no. 3, pp. 2583–2589, 2016.

[34] M. Zhu, X. Liu, S. Wang et al., "PKR promotes choroidal neovascularization via upregulating the PI3K/Akt signaling pathway in VEGF expression," *Molecular Vision*, vol. 22, pp. 1361–1374, 2016.

[35] Z. Sun, M. A. A. Mohamed, S. Y. Park, and T. H. Yi, "Fucosterol protects cobalt chloride induced inflammation by the inhibition of hypoxia-inducible factor through PI3K/Akt pathway," *International Immunopharmacology*, vol. 29, no. 2, pp. 642–647, 2015.

Hindawi
Disease Markers
Volume 2022, Article ID 9431044, 7 pages
https://doi.org/10.1155/2022/9431044

Research Article

Analysis of Macular Retinal Thickness and Microvascular System Changes in Children with Monocular Hyperopic Anisometropia and Severe Amblyopia

Lin-Lin Liu,[1] **Yu-Chuan Wang**,[2] **Miao Cao**,[2] **Fang Liu**,[2] **Shuang Zhang**,[1] **Jing Liu**,[1] **Jin-Chang Liu**,[1] **Lian-Feng Xie**,[1] **and Hui Wang**[1]

[1]*The Department of Ophthalmology of the 1st Affiliated Hospital, Gannan Medical University, Ganzhou, 341000 Jiangxi Province, China*
[2]*Postgraduates at Gannan Medical University, Ganzhou, 341000 Jiangxi Province, China*

Correspondence should be addressed to Lin-Lin Liu; 2766541487@qq.com

Received 19 October 2021; Accepted 15 December 2021; Published 17 January 2022

Academic Editor: Ting Su

Objective. To study the changes of macular retinal thickness and microvascular system in children with monocular hyperopic anisometropia and severe amblyopia using optical coherence tomography angiography (OCTA) and to explore the value of OCTA in the diagnosis and treatment of amblyopia. *Methods*. Thirty-two children with monocular hyperopic anisometropia and severe amblyopia who were treated in the Department of Ophthalmology of the First Affiliated Hospital of Gannan Medical College from January 2020 to December 2020 were included in the study. Eyes with amblyopia ($n = 32$) served as the experimental group, and the contralateral healthy eyes ($n = 32$ eyes) served as the control group. All children underwent comprehensive ophthalmological examination including slit lamp, eye position, visual acuity, optometry, eye movement, intraocular pressure, ocular axis, and fundus examination to rule out organic lesions. Macular 6 mm × 6 mm scans were performed on both eyes of all subjects by the same experienced clinician using an OCTA instrument. After ImageJ processing, the vessel density, inner layer, and full-layer retinal thickness (RT) of superficial retinal capillary plexus (SCP) were obtained. All data were analyzed by SPSS21.0 software, and a paired t-test was used for comparison between groups. $P < 0.05$ was considered to indicate statistical significance. *Results*. The vessel densities of macular SCP in the amblyopia and control groups were 47.66 ± 2.36% and 50.37 ± 2.24% in the outer superior, 49.19 ± 2.64% and 51.44 ± 2.44% in the inner inferior, 49.63 ± 2.51% and 51.41 ± 3.03% in the outer inferior, and 45.56 ± 3.44% and 50.44 ± 3.52% in the outer temporal regions, respectively. The vessel density of macular SCP in the amblyopia group was significantly lower than that in contralateral healthy eyes in the outer superior, inner inferior, outer inferior, outer temporal, and central regions. There was no significant difference between the two groups in the inner superior, inner nasal, outer nasal, and inner temporal regions. The macular RT in the amblyopia group and the control group is 90.38 ± 6.09 μm and 87.56 ± 5.55 μm in the outer temporal, respectively. The RT in the macular inner layer in the outer temporal region of the amblyopia group was thicker than that of the control group ($P < 0.05$). There was no significant difference in the other eight regions between the two groups. The whole macular RT in the amblyopia group was thicker than that in the control group in nine regions, and the central area of macular RT in the amblyopia and control groups was 229.06 ± 6.70 μm and 214.50 ± 10.36 μm, respectively. *Conclusion*. The OCTA results showed the overall RT of macula in 9 areas in the amblyopia group was thicker than that in the control group, which could show that the macular retinal thickness can be a potential way to distinguish the children with monocular hyperopic anisometropia and severe amblyopia.

1. Introduction

Amblyopia is a common ophthalmic disease in children. Although eye examination does not show any organic lesion, the corrected visual acuity cannot reach the normal level. During the critical period of visual development, children are prone to amblyopia due to binocular abnormal action or form stripping. The incidence of amblyopia in China is 2–4% [1]. In recent years, the prevention and treatment of strabismus amblyopia in China has made steady progress, and remarkable achievements have been made in clinical diagnosis, treatment, epidemiological investigation, and early screening, but the specific pathogenesis of amblyopia is still under continuous exploration and research.

Optical coherence tomography angiography (OCTA) is a new ophthalmological imaging method, which is applied to the vascular imaging of the retina, choroid, and optic nerve. Compared with traditional fundus angiography, OCTA has the advantages of being noninvasive and fast, offers high-resolution and three-dimensional imaging, and can more accurately measure the size of capillary non-perfusion area and neovascularization [2]. The application potential of OCTA has attracted the attention of several ophthalmologists, but there are few studies on fundus thickness and microcirculation changes in children with amblyopia. We analyzed the changes of macular retinal thickness and microvascular system in children with monocular hyperopic anisometropia and severe amblyopia.

2. Materials and Methods

2.1. General Information. Thirty-two children with monocular hyperopic anisometropia and severe amblyopia who were treated in the Department of Ophthalmology of the First Affiliated Hospital of Gannan Medical College from January 2020 to December 2020 were included in the study. Eyes with amblyopia ($n = 32$) served as the experimental group, and the contralateral healthy eyes ($n = 32$) served as the control group. The following inclusion criteria were set in accordance with the consensus of amblyopic diagnostic experts in 2021 [3]: (1) children with monocular hyperopic anisometropic amblyopia and normal contralateral eyes; (2) severe amblyopia—best-corrected visual acuity ≤ 0.2; and (3) no organic eye lesions and systemic diseases. The exclusion criteria were as follows: (1) systemic and ocular diseases that cause changes in fundus microcirculation; (2) patients who were unable to cooperate with the examination due to various reasons; and (3) those with other eye diseases such as strabismus, ptosis, and cataract. This study was conducted in accordance with the tenets of the Helsinki Declaration, and the study was explained to the children and their parents/legal guardians; the latter provided written consent on behalf of the children. This study was approved by the Ethics Committee of the First Affiliated Hospital of Gannan Medical College.

2.2. Methods

2.2.1. Routine Inspection. All selected patients underwent comprehensive ophthalmologic examination including slit lamp, eye position, visual acuity, optometry, eye movement, intraocular pressure, ocular axis, and fundus examination; all kinds of organic lesions were excluded. Moreover, the general indices of all candidates were recorded and analyzed, including age, sex, visual acuity, intraocular pressure, equivalent spherical optometry, and axial length. Objective optometry under the condition of ciliary paralysis was performed according to the expert consensus on the prevention and treatment of amblyopia in children (2021 Chinese Edition).

2.2.2. OCTA Check. All included children were examined by the same experienced doctor for OCTA examination. The examination procedures were fully explained to the children at the start, and their cooperation was obtained. In this study, all subjects were performed by the AngioVue OCTA tester (OPTOVUE, USA), and ImageJ software was used to analyze all data. In this study, OCTA adopted a 6 mm × 6 mm macular scanning mode and Early Treatment Diabetic Retinopathy Study (ETDRS) zoning. The OCTA macular scanning mode could automatically scan macular superficial retinal vascular plexus (SCP) and deep retinal vascular plexus (DCP). The vessel density of SCP, macular inner retinal thickness (RT), and full-layer RT were detected and analyzed. The scanning area of SCP images 10 μm from the internal limiting membrane (ILM) to the inner plexiform layer (IPL). The thickness of the inner layer of the retina is the distance from ILM to IPL, and the thickness of the whole layer is the distance from the ILM to the retinal pigment epithelium (RPE). The OCTA macular scan divides the macula into three circles: central fovea (diameter: 1 mm), perifovea (diameter: 1–3 mm ring), and central concave edge (diameter of the central ring: 3–6 mm). The paracavity and central concave edge were divided into the upper, lower, nasal, and temporal quadrants, which are subsequently divided into nine regions (Figure 1): the inner superior (IS), outer superior (OS), inner nasal (IN), outer nasal (ON), inner inferior (II), outer inferior (OI), inner temporal (IT), outer temporal (OT), and central (C) regions.

2.3. Statistical Methods. SPSS21.0 software (IBM Corporation, Armonk, NY, USA) was used for statistical analysis, and the quantitative data in accordance with normal distribution were expressed as the mean ± standard deviation (SD). The retinal SCP vessel density and the inner layer and full-thickness RT between amblyopic eyes and control eyes were compared by a paired t-test; $P < 0.05$ was considered to indicate statistically significant differences between the two groups.

3. Results

3.1. Basic Information of Patients. This study included 32 children (64 eyes, 18 male and 14 female) with monocular hyperopic anisometropia and severe amblyopia. Thirty-two eyes with amblyopia were included in the study group, and 32 contralateral healthy eyes were included in the control group. The mean age of the children was 6.2 ± 3.7 years. The homologous paired t-test was used in this study, which

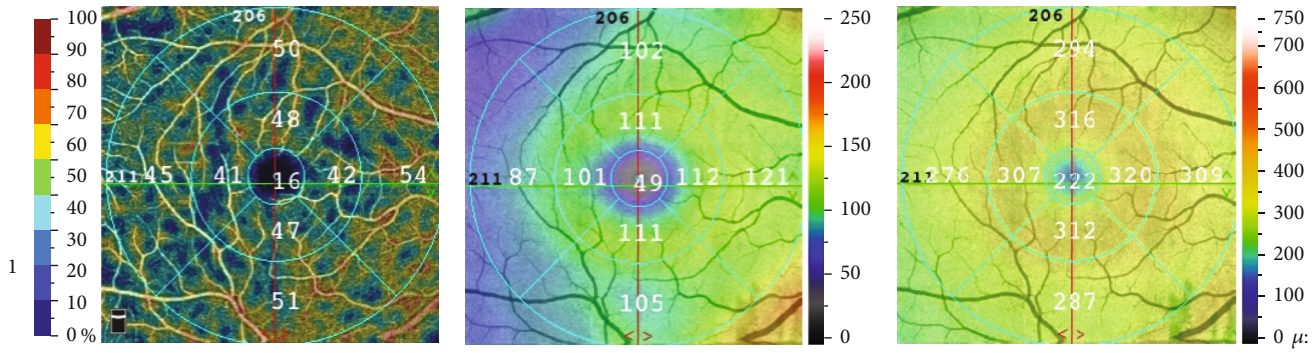

Figure 1: (a) Superficial vessel density of macula. (b) Inner thickness of macula, defined as the distance between the internal limiting membrane (ILM) and inner plexiform layer (IPL). (c) Full thickness of macula, defined as the distance from the ILM to the retinal pigment epithelium (RPE). The parafoveal and the foveal rim were divided into the upper, lower, nasal, and temporal quadrants. The macula was divided into nine regions, and their thickness values were displayed, respectively.

Table 1: Characteristics of eyes with amblyopia and healthy eyes.

Characteristic	Amblyopia eyes ($n = 32$)	Healthy eyes ($n = 32$)	t/χ^2	P value
Best-corrected visual acuity	0.12 ± 0.06	1.04 ± 0.09	45.28	<0.001
Mean intraocular pressure (mmHg)	16.72 ± 1.89	16.56 ± 1.90	0.407	0.687
Spherical equivalent refraction (D)	6.05 ± 1.90	0.31 ± 0.51	15.55	<0.001
Length of optic axis (mm)	23.00 ± 0.34	23.45 ± 0.20	7.219	<0.001

Table 2: Comparison of superficial vessel density at different locations between eyes with amblyopia eye and healthy eyes.

Location (%, mean ± SD)	Amblyopia eyes ($n = 32$) (%)	Healthy eyes ($n = 32$) (%)	t value	P value
IS	52.63 ± 2.12	51.81 ± 1.94	1.946	0.061
OS	47.66 ± 2.36	50.37 ± 2.24	5.988	<0.001
IN	51.03 ± 3.23	49.25 ± 4.42	2.063	0.048
ON	52.63 ± 1.64	51.78 ± 1.83	1.851	0.074
II	49.19 ± 2.64	51.44 ± 2.44	4.313	<0.001
OI	49.63 ± 2.51	51.41 ± 3.03	3.368	0.002
IT	51.50 ± 1.72	50.25 ± 3.38	1.816	0.079
OT	45.56 ± 3.44	50.44 ± 3.52	12.158	<0.001
C	18.75 ± 3.44	22.34 ± 2.53	11.950	<0.001

SD: standard deviation; IS: inner superior; OS: outer superior; IN: inner nasal; ON: outer nasal; II: inner inferior; OI: outer inferior; IT: inner temporal; OT: outer temporal; C: central.

had strong balance and comparability, and there was no need to compare age and sex. In this study, the best-corrected visual acuity (BCVA), intraocular pressure (IOP), spherical equivalent (SE), and ocular axis were compared between eyes with amblyopia and healthy eyes. The results are shown in Table 1. There was no significant difference in IOP between the two groups, but there were significant intergroup differences in BCVA, SE, and ocular axis.

3.2. Vessel Density of SCP in Each Group. The vessel density of macular OS, II, OI, OT, and SCP in amblyopic eyes was lower than that in the control eyes ($P < 0.05$), but there were no significant intergroup differences with respect to macular IS, IN, ON, and IT. The results are shown in Table 2 and Figure 2.

3.3. Retinal Thickness of Macular Inner Layer Retina and of Whole Retina in Each Group. The RT in the inner layer of macular OT in amblyopic eyes was thicker than that in the control eyes ($P < 0.05$), but there were no significant differences in other areas between the two groups. The whole RT in the nine macular regions of amblyopic eyes was thicker than that of the control eyes ($P < 0.05$). The results are shown in Table 3 and Figure 3.

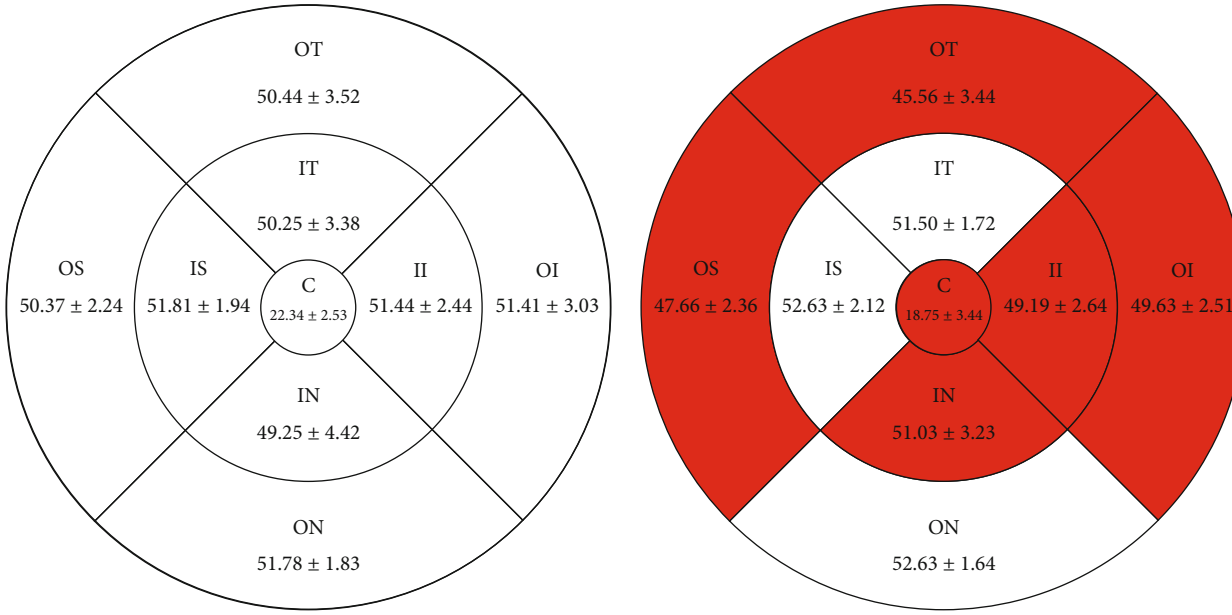

Figure 2: Results of superficial vessel density at different locations between amblyopia eye and healthy eye control (mean ± SD).

Table 3: Comparison of macular retinal thickness at different locations between amblyopia eye and healthy eye controls.

Location	Amblyopia eyes ($n = 32$) (μm)	Healthy eyes ($n = 32$) (μm)	t value	P value
Macular inner retinal thickness (μm), mean ± SD				
IS	104.69 ± 5.70	105.16 ± 5.16	1.305	0.201
OS	100.87 ± 4.11	100.72 ± 4.83	0.181	0.857
IN	101.28 ± 5.51	101.13 ± 5.73	0.469	0.643
ON	114.38 ± 5.05	113.88 ± 5.12	1.806	0.081
II	103.44 ± 5.66	103.88 ± 5.88	1.238	0.225
OI	101.13 ± 4.20	100.50 ± 3.68	1.341	0.190
IT	97.28 ± 4.92	96.75 ± 5.04	1.848	0.074
OT	90.38 ± 6.09	87.56 ± 5.55	8.057	<0.001
C	47.78 ± 3.81	47.25 ± 2.55	1.240	0.224
Macular full retinal thickness (μm), mean ± SD				
IS	324.25 ± 10.66	313.03 ± 7.01	8.965	<0.001
OS	295.94 ± 7.49	285.88 ± 8.64	8.790	<0.001
IN	316.09 ± 12.22	306.75 ± 9.92	7.550	<0.001
ON	307.91 ± 8.25	297.31 ± 9.17	12.386	<0.001
II	309.41 ± 15.94	301.47 ± 13.76	6.711	<0.001
OI	281.50 ± 12.11	272.34 ± 10.43	7.282	<0.001
IT	309.41 ± 10.49	299.19 ± 9.39	7.660	<0.001
OT	276.66 ± 11.99	268.06 ± 11.06	7.313	<0.001
C	229.06 ± 6.70	214.50 ± 10.36	8.185	<0.001

SD: standard deviation; IS: inner superior; OS: outer superior; IN: inner nasal; ON: outer nasal; II: inner inferior; OI: outer inferior; IT: inner temporal; OT: outer temporal; C: central.

4. Discussion

In the past, OCT was usually used to study retinal thickness, but OCT cannot detect changes to the retinal microcirculatory system. With the continuous development of medical imaging technology, magnetic resonance imaging (MRI), functional MRI (fMRI), OCT, and OCTA are now commonly used to study amblyopia. In particular, OCTA technology has recently emerged and played a revolutionary role in the study of retinal microvascular system [4]. OCTA

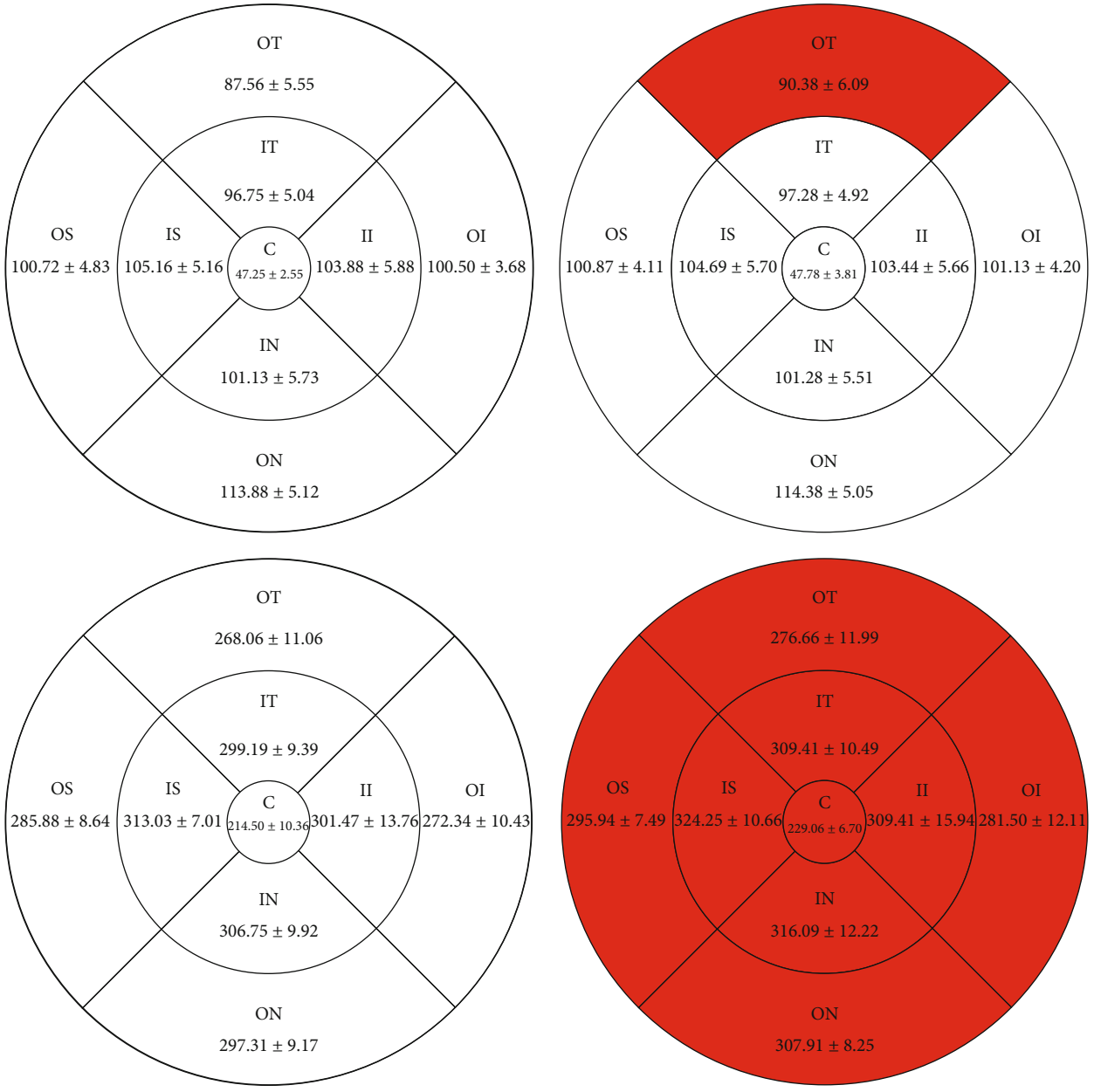

Figure 3: Results of macular retinal thickness at different locations between amblyopia eye and healthy eye controls (mean ± SD).

can minimally, simply, and conveniently display the retinal morphology in great detail and can detect the vessel signals of the retinal microvascular system and the tiny changes to RT. Further, OCTA's application on retinal microvascular system research has aroused the interest of multiple scholars. In related research on the retina of patients with amblyopia, Nishikawa et al. [5] scanned the macular area of OCTA in 22 children with monocular amblyopia. It was seen that the vessel density of the central fovea and accessory central fovea in amblyopic eyes was lower than that in the healthy contralateral eyes, and the central foveal avascular area in amblyopic eyes was significantly smaller than that in the contralateral eyes. Some researchers [6–11] found that the vascular density of SCP and DCP decreased in amblyopic eyes. However, other studies [12, 13] reported that the blood vessel density of SCP and DCP in amblyopic eyes remained unchanged compared with healthy eyes.

Recent studies [14] showed that the vessel density of SCP in amblyopic eyes was lower than that in the control group. Huynh et al. [15–17] found that the macular thickness in amblyopic eyes was thicker than that in contralateral eyes. Li et al. [18] showed that the process of amblyopia may involve changes to the retinal microcirculatory system, and the macular fovea of amblyopic eyes was thicker than that of normal eyes. Atakan et al. [9, 19, 20] found no significant change between the amblyopic and control groups. Khan et al. [21] found the following results in their study on the relationship between retinal microvessel density and ocular axis in the macular region: the longer the eye axis, the smaller the superficial perfusion area and blood vessel

density, and the retinal macular vessel density is inversely proportional to the size of ocular axis. Some previous studies [22–24] reported a negative correlation between AL and central foveal macular thickness in children with healthy eyes, although another study did not find this correlation [25]. Therefore, conclusions about the retinal microvessels and thickness in patients with amblyopia are fairly inconsistent.

Our results showed that in the study of retinal SCP vessel density in children with monocular hyperopic anisometropic amblyopia, the SCP vessel density in amblyopic eyes was significantly lower than that in contralateral healthy eyes in the macular OS, II, OI, OT, and C regions; however, there were no significant intergroup differences in SCP vessel density in the macular IS, IN, ON, and IT regions. This study also found that the inner layer RT of macular OT in amblyopic eyes was significantly higher than that in the contralateral healthy eyes, while the inner layer RT in the remaining eight regions only showed minor changes, but these changes were not significantly different between the two groups. The full-layer RT in nine macular regions of amblyopic eyes was thicker than that of contralateral healthy eyes, and the difference was statistically significant. At present, most studies on retinal vessel density and RT of amblyopia have not been classified according to the type of amblyopia and refractive state. The etiology of amblyopia and refractive state may affect the retinal vessel density and RT.

In this study, OCTA was used to analyze the retina of children with severe amblyopia caused by monocular hypermetropia, and the results were more comparable, which may be why our results are distinct from other studies. At present, most researchers study the average thickness and mean vessel density of the macular fovea, and few scholars subdivide the macular region into nine regions for comparative analyses. The decrease of vessel density in amblyopic eyes may indicate that these eyes need less nutrition to receive retinal artery blood supply, resulting in abnormal macular fovea development and retardation in amblyopic eyes. Because the nasal side of the retinal vascular system develops earlier than the temporal side and the microcirculation in different regions is not uniformed, we thought it was more meaningful to subdivide the macula into nine regions in this study.

Our study has some limitations. First, the sample size of the study is small. Second, the data accuracy was affected by the poor matching degree detected by OCTA in children. Third, the control group of myopic anisometropic amblyopia and other types of amblyopia have not been established at the same time. Fourth, the effects of equivalent spherical lens and ocular axis on retinal vessel density and retinal thickness cannot be excluded. Last, the current OCTA technique cannot detect the vessel velocity of retinal microcirculation and the elasticity and diameter of the microvessels.

In conclusion, the emergence of OCTA technology has significant advantages to study the retinal microvascular system changes. The clinical application of OCTA may have a certain exploration value in the pathogenesis, diagnosis, and treatment of amblyopia and is expected to play an important role in its diagnosis and treatment.

Data Availability

The data can be found at OCTA Article original data of figure files.

Conflicts of Interest

The authors declare that they have no conflicts of interest.

References

[1] J. Ge, *Ophthalmology 2nd edition*, People's Health Publishing House, Beijing, 2011.

[2] S. Zhang and L.-L. Liu, "Clinical application of optical coherence tomography angiography in ophthalmology," *Journal of Gannan Medical College*, vol. 41, no. 3, pp. 318–322, 2021.

[3] Strabismus and Pediatric Ophthalmology Group of Ophthalmology Branch of Chinese Medical Association, strabismus and Pediatric Ophthalmology Group of Ophthalmologists Branch of Chinese Medical Association, "Consensus of experts on prevention and treatment of Children's amblyopia in China (2021)," *Chinese Journal of Ophthalmology*, vol. 57, pp. 336–340, 2021.

[4] Q.-Y. Li, C.-Y. Yu, and Y. Shao, "Advances in imaging research of amblyopia," *International Journal of Ophthalmology*, vol. 21, no. 6, pp. 1012–1016, 2021.

[5] N. Nishikawa, J. Chua, Y. Kawaguchi et al., "Macular microvasculature and associated retinal layer thickness in pediatric amblyopia: magnification-corrected analyses," *Investigative Ophthalmology & Visual Science*, vol. 62, no. 3, p. 39, 2021.

[6] M. Lonngi, F. G. Velez, I. Tsui et al., "Spectral-domain optical coherence tomographic angiography in children with amblyopia," *JAMA Ophthalmology*, vol. 135, no. 10, pp. 1086–1091, 2017.

[7] I. Yilmaz, O. B. Ocak, B. S. Yilmaz, A. Inal, B. Gokyigit, and M. Taskapili, "Comparison of quantitative measurement of foveal avascular zone and macular vessel density in eyes of children with amblyopia and healthy controls: an optical coherence tomography angiography study," *Journal of AAPOS*, vol. 21, no. 3, pp. 224–228, 2017.

[8] I. Sobral, T. M. Rodrigues, M. Soares et al., "OCT angiography findings in children with amblyopia," *Journal of AAPOS*, vol. 22, no. 4, pp. 286–289.e2, 2018.

[9] A. Lekskul, W. Wuthisiri, and T. Padungkiatsagul, "Evaluation of retinal structure in unilateral amblyopia using spectral domain optical coherence tomography," *Journal of AAPOS*, vol. 22, no. 5, pp. 386–389, 2018.

[10] S. Araki, A. Miki, K. Goto et al., "Macular retinal and choroidal thickness in unilateral amblyopia using sweptsource optical coherence tomography," *BMC Ophthalmology*, vol. 17, no. 1, p. 167, 2017.

[11] S. Doguizi, M. Yilmazoglu, H. Kiziltoprak, M. A. Sekeroglu, and P. Yilmazbas, "Quantitative analysis of retinal microcirculation in children with hyperopic anisometropic amblyopia: an optical coherence tomography angiography study," *Journal of AAPOS*, vol. 23, no. 4, pp. 201.e1–201.e5, 2019.

[12] S. Araki, A. Miki, K. Goto et al., "Foveal avascular zone and macular vessel density after correction for magnification error in unilateral amblyopia using optical coherence tomography angiography," *BMC Ophthalmology*, vol. 19, no. 1, p. 171, 2019.

[13] E. S. Wong, X. J. Zhang, N. Yuan et al., "Association of optical coherence tomography angiography metrics with detection of impaired macular microvasculature and decreased vision in amblyopic eyes: the Hong Kong Children Eye Study," *JAMA Ophthalmology.*, vol. 138, no. 8, pp. 858–865, 2020.

[14] Y. Feng, L.-Y. Zhang, Z.-T. Zheng et al., "Changes of macular retinal thickness and microvascular system in patients with anisometropic amblyopia: a study based on OCTA," *New Progress in Ophthalmology*, vol. 41, no. 6, pp. 570–574, 2021.

[15] S. C. Huynh, C. Samarawickrama, X. Y. Wang et al., "Macular and nerve fiber layer thickness in amblyopia: the Sydney Childhood Eye Study," *Ophthalmology*, vol. 116, no. 9, pp. 1604–1609, 2009.

[16] C. E. al-Haddad, G. M. Mollayess, C. G. Cherfan, D. F. Jaafar, and Z. F. Bashshur, "Retinal nerve fibre layer and macular thickness in amblyopia as measured by spectral-domain optical coherence tomography," *The British Journal of Ophthalmology*, vol. 95, no. 12, pp. 1696–1699, 2011.

[17] Z. Rajavi, H. Sabbaghi, N. Behradfar, M. Yaseri, M. Aghazadeh Amiri, and M. Faghihi, "Macular thickness in moderate to severe amblyopia," *Korean Journal of Ophthalmology*, vol. 32, no. 4, pp. 312–318, 2018.

[18] J. Li, P. Ji, and M. Yu, "Meta-analysis of retinal changes in unilateral Amblyopia using optical coherence tomography," *European Journal of Ophthalmology*, vol. 25, no. 5, pp. 400–409, 2015.

[19] M. Atakan, S. Culfa, U. Calli, A. D. Penbe, and T. G. Atakan, "Evaluation of retinal nerve fiber layer and macular thickness in amblyopia," *Journal of Clinical & Experimental Ophthalmology*, vol. 6, no. 3, p. 437, 2015.

[20] W. Chen, J. Lou, F. Thorn et al., "Retinal microvasculature in amblyopic children and the quantitative relationship between retinal perfusion and thickness," *Investigative Ophthalmology & Visual Science*, vol. 60, no. 4, pp. 1185–1191, 2019.

[21] M. H. Khan, A. K. C. Lam, J. A. Armitage, L. Hanna, C. H. To, and A. Gentle, "Impact of axial eye size on retinal microvasculature density in the macular region," *Journal of Clinical Medicine*, vol. 9, no. 8, p. 2539, 2020.

[22] S. C. Huynh, X. Y. Wang, E. Rochtchina, and P. Mitchell, "Distribution of macular thickness by optical coherence tomography: findings from a population-based study of 6-year-old children," *Investigative Ophthalmology & Visual Science*, vol. 47, no. 6, pp. 2351–2357, 2006.

[23] M. A. El-Dairi, S. G. Asrani, L. B. Enyedi, and S. F. Freedman, "Optical coherence tomography in the eyes of normal children," *Archives of Ophthalmology*, vol. 127, no. 1, pp. 50–58, 2009.

[24] L. Cheng, M. Wang, J. Deng et al., "Macular ganglion cellinner plexiform layer, ganglion cell complex, and outer retinal layer thicknesses in a large cohort of Chinese children," *Investigative Ophthalmology & Visual Science*, vol. 60, no. 14, pp. 4792–4802, 2019.

[25] M. E. Lim, K. Jiramongkolchai, L. Xu et al., "Handheld optical coherence tomography normative inner retinal layer measurements for children <5 years of age," *American Journal of Ophthalmology*, vol. 207, pp. 232–239, 2019.

Hindawi
Disease Markers
Volume 2021, Article ID 2080962, 6 pages
https://doi.org/10.1155/2021/2080962

Research Article

Association of Iris Structural Measurements with Corneal Biomechanics in Myopic Eyes

Lin Fu,[1] **Yufeng Ye**,[1] **Xu Jia**,[1] **Yunjie Zhang**,[1] **Xiaoyu Chen**,[2] **Hengli Lian**,[1] **Weihua Yang**,[3] **and Qi Dai**[1]

[1]*School of Ophthalmology and Optometry, Eye Hospital, Wenzhou Medical University, Wenzhou 325027, China*
[2]*Wenzhou Medical University, Wenzhou 325027, China*
[3]*Affiliated Eye Hospital, Nanjing Medical University, Nanjing 210029, China*

Correspondence should be addressed to Weihua Yang; benben0606@139.com and Qi Dai; dq@mail.eye.ac.cn

Received 20 October 2021; Accepted 7 December 2021; Published 31 December 2021

Academic Editor: Ting Su

Purpose. To evaluate the relationship between iris sectional parameters on swept-source optical coherence tomography (SS-OCT) with corneal biomechanics measured by Corneal Visualization Scheimpflug Technology (Corvis ST) in young adults with myopia. *Methods*. 117 patients with myopia aged ≥18 years were recruited from the Eye Hospital of Wenzhou Medical University, who had complete SS-OCT and Corvis ST data. Only the left eye of each participant was selected for analysis. Iris sectional parameters included iris thickness at 750 μm from the scleral spur (IT750), iris sectional area (I-area), and iris curvature (I-curv) measured from four quadrants. Associations between the iris parameters and corneal biomechanics were analyzed using linear regression models. *Results*. The mean age of the included young adults was 26.26 ± 6.62 years old with 44 males and 73 females. The iris parameters were different among the four quadrants. The nasal, temporal, and inferior quadrants of IT750, together with nasal and temporal quadrants of I-area, were correlated with corneal biomechanical parameters after being adjusted for age, gender, pupil diameter, and axial length. Thicker IT750 and larger I-area were related to a softer cornea. However, no association was found between I-curv and corneal biomechanics. *Conclusions*. Iris sectional parameters measured from SS-OCT images were associated with corneal biomechanical properties in myopic eyes. Thicker IT750 and larger I-area indicate a softer cornea. IT750 and I-area may provide useful information on corneal biomechanical properties in myopic eyes.

1. Introduction

Myopia is one of the most common causes of preventable visual impairment and blindness, with a predicted prevalence of 50% in the world's population in 2050.[1]. High or pathological myopia can result in irreversible ocular blinding diseases, such as choroidal neovascularization, retinal detachment, and glaucoma [2–4]. This will definitely lead to heavy cost burden on the families and society. Together with the increased prevalence of myopia, there has been an urge to view this major public health problem and better understand the pathophysiology of myopia.

The development of myopia is believed to be induced by various patterns of ocular expansions, including equatorial expansion [5], axial expansion [6], and posterior pole expansion [7]. Accompanied by these expansions, the pathogenesis of myopia includes the biomechanical alternations of the eyeball outer wall, including the cornea, scleral, lamina cribrosa, and peripapillary ring [8, 9]. The corneal stiffness was reported to be reduced with the increase in the myopic degree from Corneal Visualization Scheimpflug Technology (Corvis ST, Oculus, Wetzlar, Germany) studies [10–12]. Accompanied by these expansions, the inner tissue especially the iris would also be changed. In a population of 18 to 66 years old, eyes with concave iris configuration are mostly from myopic eyes and no hyperopic eyes displayed a concave iris [13]. This suggests that the iris structural features may be related to myopia. However, the underlying mechanism so far is not clear. It may be related to the development and biomechanics of the cornea and sclera, the structure of the iris and choroid, and the microcirculation of blood vessels.

As iris stroma and corneal stroma are both of mesodermal origin [14, 15], in our previous work, we found that the iris surface features including crypts and furrows were associated with corneal biomechanical parameters [16]. We postulate that the iris structural features may also be related to corneal characteristics. With the advantages of SS-OCT and Corvis ST, we are aiming to explore the relationships of iris structural measurements with corneal biomechanics in myopic eyes in this study. This will enrich the understanding of the pathophysiology of myopia and may help to identify the risk factors of myopia.

2. Methods

2.1. Participants. In this prospective, cross-sectional study, myopic subjects were recruited from a population of refractive surgery candidates in Eye Hospital of Wenzhou Medical University which aged older than 18 years and without any ocular pathology other than refractive error. Data from the left eyes of all subjects were selected for analysis to eliminate an intereye correlation issue.

This study was conducted following the tenets of the Declaration of Helsinki and was approved by the Institutional Review Board of Wenzhou Medical University (IRB approval number 2020-128-K-113). This study was registered on Chinese Clinical Trial Registry with the registration number of ChiCTR2100052498. All the subjects signed an informed consent form at the time of recruitment.

2.2. Ocular Examinations. Detailed ophthalmological examinations were performed by an experienced ophthalmologist for all subjects, including slit-lamp examination, refraction measurement (spherical equivalence (SE)), best-corrected visual acuity, anterior segment images scanned by swept-source optical coherence tomography (SS-OCT, Casia SS-1000 OCT, Tomey, Nagoya, Japan), corneal tomography with the Pentacam (Oculus, Wetzlar, Germany), corneal biomechanical properties assessed by the Corvis ST (Oculus, Wetzlar, Germany), and ocular axial length measured by the IOL-Master (Carl Zeiss Meditec, Jena, Germany).

2.3. Iris Measurements from SS-OCT. All subjects underwent a standard swept-source optical coherence tomography (SS-OCT, Casia SS-1000 OCT, Tomey, Nagoya, Japan) examination by a single examiner who was masked to the clinical data. The horizontal and vertical scans of the nasal, temporal, superior, and inferior four quadrants of all the participants were obtained using SS-OCT under standardized dark condition (20 lux). Images with the best quality were obtained for the iris measurements. The iris thickness at 750 μm from the scleral spur (IT750) and iris area (I-area) was measured as the cross-sectional area from the pupil to the scleral spur, and the iris curvature (I-curv) was measured as the distance from the greatest convexity to the line drawing from the most central to the most peripheral point of the iris pigment epithelium (Figure 1) as previously defined using ImageJ software [17, 18]. The mean values of the 4 quadrants were used for the analysis.

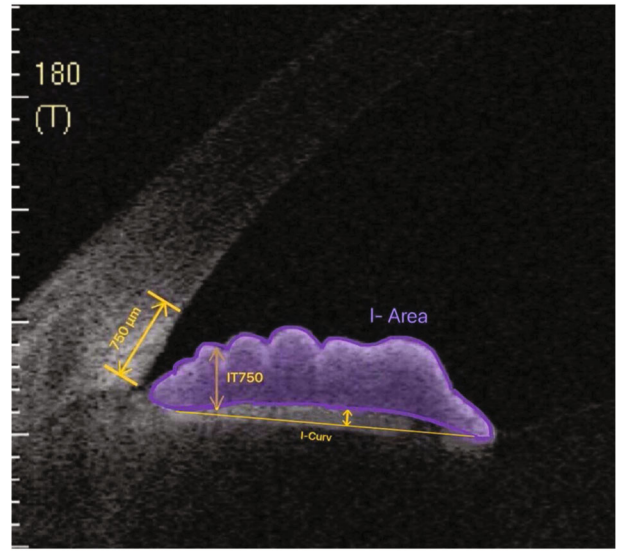

Figure 1: Measurement of the cross-sectional iris thickness, iris area, and iris curvature on anterior segment optical coherence tomography. IT750: iris thickness at 750 μm from the scleral spur; I-area: iris area; I-curv: iris curvature.

2.4. Corvis ST Measurement. The corneal biomechanical properties were obtained using the Corvis ST. Due to an airflow released by the instrument, the cornea generates an inward movement through the first applanation to the highest degree of concavity and then moves outward through the second applanation to the natural shape. In this process, 140 sequential horizontal images of the cornea were captured with a high-speed Scheimpflug camera at a speed of 4330 frames per second in 30 ms. Meanwhile, the biomechanical parameters were calculated by the device including bIOP; maximum DA (DA max) at the first applanation; time at the highest concavity (HC time); time at the first and second applanation (A1 time and A2 time, respectively); corneal velocity at the first and second applanation (A1 velocity and A2 velocity, respectively); DA; deflection length (DLL); deflection amplitude (DLA) and delta arc length (dArcL) at A1, HC, and A2; PD, radius, and maximum deflection amplitude at the first applanation (DLA Max); maximum delta arc length (dArcLM); maximum inverse radius (max inverse radius); maximum deformation amplitude ratio (DA ratio max) at 2 mm and 1 mm; central corneal thickness (CCT); integrated radius; and SP-A1.

2.5. Statistical Analysis. All statistical analyses were performed using SPSS version 23.0 software (SPSS for Windows, Chicago, IL, USA). Demographic data and ocular characteristics from the left eyes of the participants were described using the mean ± SD. One-way analysis of variance was used to compare the difference of iris measurements in 4 quadrants of left eyes. Linear regression models were performed to assess the associations between iris measurements (independent variable) and corneal biomechanical parameters measured by Corvis ST (dependent variable). They were adjusted for potential confounders such as age and gender in model 1 and additional ones of pupil

Table 1: Demographics and baseline characteristics of participants ($n = 117$).

Characteristics	Mean (SD) or no. (%)
Age (yrs)	26.26 (6.62)
Gender	
Male	44 (37.6)
Female	73 (62.4)
Pupil diameter (mm)	3.05 (0.54)
ACD (mm)	3.70 (0.25)
Axial length (mm)	25.92 (1.13)
bIOP (mmHg)	15.41 (2.02)
CCT (μm)	544.81 (34.18)
Refraction (SE)	-5.53 (2.22)
IT7500 (mm)	0.40 (0.09)
Iris area (mm^2)	1.41 (0.24)
Iris curvature (mm)	0.19 (0.21)

ACD = angle chamber distance; CCT = central corneal thickness; SE = spherical equivalent; SD = standard deviation.

diameters and axial length in model 2. A $P < 0.05$ was set to be statistically significant.

3. Results

In total, 18 subjects were excluded due to the following reasons: poor image quality (10), IOP or bIOP higher than 21 mmHg (5), and coexisting with posterior staphyloma (3). 117 patients were recruited for this study. The demographics and the characteristics of their ocular parameters are displayed in Table 1. Most of the included participants were young adults, and all of them were myopes. The mean values of corneal biomechanical parameters measured by the Dynamic Scheimpflug Analyzer (Corvis ST) are shown in Table 2.

We measured the iris parameters in the superior, temporal, inferior, and nasal four quadrants (Figure 2). The IT750 was thicker in the inferior and nasal quadrants than in the superior and temporal quadrants (all $P < 0.05$). The IT750 in the inferior quadrant did not differ from the one in the nasal quadrant, and there were no differences of IT750 between the superior and temporal quadrants. The iris area in the superior and inferior quadrants was larger than that in the temporal and nasal quadrants (all $P < 0.0001$). For the iris configuration, the temporal iris was the most concave and the nasal iris was the least concave among the four quadrants (all $P < 0.01$). It was similar between the superior and inferior quadrants ($P = 0.77$). Moreover, the iris curvature was consistent among the four quadrants in most of the eyes except in one eye, and the iris was concave in the temporal quadrant and was convex in the other three quadrants. Therefore, in this population, there were 91 (77.8%) eyes in the superior, inferior, and nasal quadrants and 92 (78.6%) eyes in the temporal quadrant with the concave iris.

All quadrants of the IT750, iris area, and iris curvature were analyzed for the relationship with corneal biomechanical parameters. The correlated parameters are shown in Table 3. Our results showed that the correlation differs in different quadrants of the iris features.

Table 2: Corneal biomechanical parameters measured by the Dynamic Scheimpflug Analyzer ($n = 117$).

Parameters	Mean (SD)
DA max (mm)	1.05 (0.09)
A1 time (ms)	7.44 (0.24)
A1 velocity (ms)	0.15 (0.02)
A2 time (ms)	22.00 (0.36)
A2 velocity (ms)	-0.27 (0.02)
HC time (ms)	16.66 (0.44)
PD (mm)	4.98 (0.23)
Radius (mm)	6.72 (0.66)
A1 DA (mm)	0.15 (0.01)
HC DA (mm)	1.05 (0.09)
A2 DA (mm)	0.32 (0.06)
A1 DLL (mm)	2.22 (0.23)
HC DLL (mm)	6.32 (0.78)
A2 DLL (mm)	2.89 (0.63)
A1 DLA (mm)	0.09 (0.01)
HC DLA (mm)	0.92 (0.09)
A2 DLA (mm)	0.10 (0.01)
DLA max (mm)	0.93 (0.09)
A1 dArcL (mm)	-0.02 (0.00)
HC dArcL (mm)	-0.13 (0.02)
A2 dArcL (mm)	-0.02 (0.01)
dArcLM (mm)	-0.15 (0.03)
Max inverse radius (mm^{-1})	0.18 (0.02)
DA ratio max (2 mm)	4.28 (0.34)
DA ratio max (1 mm)	1.56 (0.04)
Integrated radius (mm^{-1})	9.00 (0.90)
SP-A1	106.23 (17.83)

DA: deformation amplitude; A1: the first applanation; A2: the second applanation; HC: highest concavity; PD: peak distance; DLL: deflection length; DLA: deflection amplitude; dArcL: delta arc length; dArcLM: delta arc length max; SP-A1: stiffness parameter at the first applanation.

For the IT750, temporal IT750 was related to more corneal biomechanical parameters than other quadrants. It was positively associated with PD, radius, HC DLL, and A2 DLL and negatively related to max inverse radius after being adjusted for age, gender, pupil diameter, and axial length in model 2. In addition, nasal IT750 was related to HC DLL, and inferior IT750 was associated with dArcLM positively in model 2. No correlation was found between superior IT750 and the corneal biomechanics.

For the iris area, there were two quadrants showing association with corneal biomechanical parameters in model 2. The nasal iris area was negatively related to the max inverse radius, and the temporal iris area was positively correlated with A2 time adjusted for age, gender, pupil diameter, and axial length. Although A2 velocity was negatively associated with the nasal iris area and inferior iris area in model 1

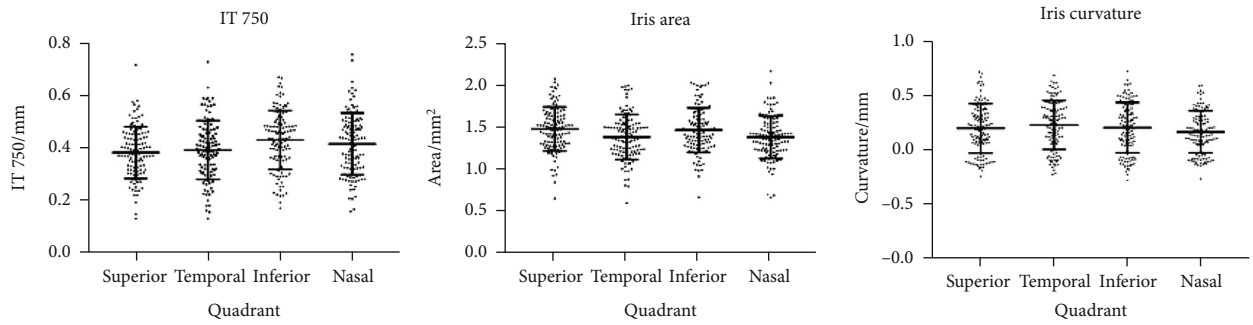

Figure 2: The distribution of iris parameters in four quadrants.

Table 3: Associations between iris surface parameters and corneal biomechanical parameters.

	Model 1*		Model 2‡	
	β	P value	β	P value
Nasal IT750				
HC DLL	0.032	0.022	0.034	0.017
Nasal IT750				
PD	0.061	0.156	0.107	0.021
Radius	0.032	0.031	0.033	0.029
HC DLL	0.028	0.034	0.029	0.026
A2 DLL	0.036	0.021	0.034	0.027
Max inverse radius	-1.744	0.005	-1.825	0.004
Inferior IT750				
dArcLM	0.797	0.047	0.825	0.042
Nasal iris area				
A2 velocity	-2.430	0.016	-1.861	0.063
Max inverse radius	-2.696	0.074	-3.171	0.027
Temporal iris area				
A2 time	0.153	0.031	0.137	0.046
Inferior iris area				
A2 velocity	-2.386	0.024	-1.528	0.136
Inferior iris curvature				
HC DLL	0.052	0.045	0.048	0.064

*Model 1 was adjusted for age and gender. †Model 2 was adjusted for age, gender, pupil diameter, and axial length. HC: highest concavity; DLL: deflection length; PD: peak distance; A2: the second applanation; dArcLM: delta arc length max.

adjusted for age and gender, it showed no association with them after being adjusted for age, gender, pupil diameter, and axial length in model 2.

Finally, in model 2, the iris curvature demonstrated no correlation with all the corneal biomechanical parameters measured by Corvis ST. Only the inferior iris curvature showed a positive correlation with HC DLL when adjusting age and gender in model 1.

4. Discussion

In this cross-sectional study, we have provided new data on the distribution of iris structural parameters measured by SS-OCT including IT750, I-area, and I-curv in myopic patients and their associations with corneal biomechanics measured by Corvis ST. We showed that the iris parameters on SS-OCT differ among the ocular four quadrants in this myopic population. Although not all the quadrants of the iris parameters were related to corneal biomechanics, our results indicate that thicker IT750 and larger I-area in the nasal, temporal, and inferior quadrants were related to a softer cornea after being adjusted for age, gender, pupil diameter, and axial length.

IT750 and I-area are frequently studied in angle closure glaucoma and rarely described in myopes. Surprisingly, our results showed that IT750 and I-area were related to corneal biomechanical properties in this myopic population. I-area and IT750 are also the parameters associated with narrow angles diagnosed on gonioscopy [19]. Larger I-area and thicker IT750 are the risk factors for the narrow angle [19]. In the present study, these were related to a softer cornea. The determinant of angle width was always focused on the iris position, while the role of cornea in the angle width has not been studied. As part of the anterior chamber angle, corneal properties may also play an important role in the angle width. As greater I-area and IT750 were correlated with the softer cornea in this study, the softer cornea may also contribute to the narrow angle. The relationship between the iris and cornea demonstrated in our study provided further insights into the angle closure pathogenesis. Moreover, for the refractive surgery candidates, eyes with larger I-area and thicker IT750 may give the hint of a softer cornea to the surgeon.

Previously, iris structural parameters were widely studied in angle closure glaucoma, and the iris curvature was strongly related to angle width [20]. However, the role of the cornea in the angle width was neglected although the cornea is the outer border of angle width. Whether the corneal biomechanics influence the angle width and the iris contour is unknown, it is reported that corneal hysteresis (CH), a corneal biomechanical parameter measured from an ocular response analyzer (ORA), is associated with the scleral spur to spur distance [21, 22]. The cornea, scleral spur, and iris are all essential structures comprising the anterior chamber angle. As the neighboring structures, their relationships may play important roles in different ocular disorders.

The distribution of iris contour varies along age, gender, refraction, and different anterior segment diseases. Schuster et al. reported that none of the hyperopic eyes presented

with a concave iris and eyes with a concave iris consisted of emmetropia and myopia [13]. In the report of narrow angles, all the iris was convex [19], and in eyes with pigment dispersion syndrome (PDS) or pigmentary glaucoma (PG), a concave iris is frequently observed [23]. The iris curvature reported in other literatures was mostly from temporal and nasal measurements in one meridian [19]. In the present study, we measured 4 quadrants of iris configuration from the vertical and horizontal meridian. There were 91 (77.8%) eyes in the superior, inferior, and nasal quadrants having a concave iris and 92 (78.6%) eyes in the temporal quadrant showing a concave iris. Our result was a reversal to the percentage of 26% concave iris and 67% convex iris in myopia from 560 eyes of 326 individuals in Schuster et al.'s report [13]. The reason may be that their age range was from 18 to 66 years and most of them were male. The age range in our study was 18 years to 40 years, and male consisted of 37.6% [13].

The major limitation of this study is that the study population only consisted of myopic patients and most of them were young age. Since the iris properties changed with age and refraction, the results in this study may not be able to be applied to other different populations. Further research may be necessary to conduct on people with emmetropia and hyperopia with a wider age range.

5. Conclusions

In conclusion, iris parameters measured by SS-OCT were associated with corneal biomechanics measured using Corvis ST. A larger iris sectional area and thicker IT750 were associated with a softer cornea in myopic eyes. The association between iris configuration and corneal biomechanics may help to understand the pathogenesis in several ocular disorders.

Data Availability

The datasets used in this study are available based on reasonable request from the corresponding author Dr. Qi Dai, dq@mail.eye.ac.cn.

Ethical Approval

This study was in accordance with the tenets of the Declaration of Helsinki and was approved by the Institutional Review Board of Wenzhou Medical University (IRB approval number 2020-128-K-113).

Consent

Informed consents were obtained from all participants. They signed the informed consent forms and agreed to publish their data and photographs.

Conflicts of Interest

The authors declare that there is no conflict of interest regarding the publication of this article.

Authors' Contributions

Lin Fu and Yufeng Ye contributed to the work equally and should be regarded as co-first authors.

Acknowledgments

The work was supported by the Natural Science Foundation of Zhejiang Province (grant no. LQ19H120002), Wenzhou Basic Scientific Research Project (grant Y20180712), and Research Initiation Project of the Eye Hospital of Wenzhou Medical University (grant no. GKYQD2018001).

References

[1] B. A. Holden, T. R. Fricke, D. A. Wilson et al., "Global prevalence of myopia and high myopia and temporal trends from 2000 through 2050," *Ophthalmology*, vol. 123, no. 5, pp. 1036–1042, 2016.

[2] P. Zhou, S. Zheng, E. Wang, P. Men, and S. Zhai, "Conbercept for treatment of neovascular age-related macular degeneration and visual impairment due to diabetic macular edema or pathologic myopia choroidal neovascularization: a systematic review and meta-analysis," *Frontiers in Pharmacology*, vol. 12, p. 696201, 2021.

[3] G. Moussa, E. Samia-Aly, S. W. Ch'ng et al., "Effect of demographics and ethnicity on laser retinopexy in preventing retinal detachment in a tertiary eye hospital in 812 eyes," *Acta Ophthalmologica*, 2021.

[4] A. Ha, C. Y. Kim, S. R. Shim, I. B. Chang, and Y. K. Kim, "Degree of myopia and glaucoma risk: a dose-response meta-analysis," *American Journal of Ophthalmology*, 2021.

[5] P. K. Verkicharla, A. Mathur, E. A. Mallen, J. M. Pope, and D. A. Atchison, "Eye shape and retinal shape, and their relation to peripheral refraction," *Ophthalmic & Physiological Optics*, vol. 32, no. 3, pp. 184–199, 2012.

[6] D. A. Atchison, C. E. Jones, K. L. Schmid et al., "Eye shape in emmetropia and myopia," *Investigative Ophthalmology & Visual Science*, vol. 45, no. 10, pp. 3380–3386, 2004.

[7] A. Sorsby, B. Benjamin, M. Sheridan, J. Stone, and G. A. Leary, "Refraction and its components during the growth of the eye from the age of three," *Memorandum - Medical Research Council*, vol. 301, no. Special, pp. 1–67, 1961.

[8] S. Chansangpetch, R. Panpruk, A. Manassakorn et al., "Impact of myopia on corneal biomechanics in glaucoma and nonglaucoma patients," *Investigative Ophthalmology & Visual Science*, vol. 58, no. 12, pp. 4990–4996, 2017.

[9] A. Y. Yu, H. Shao, A. Pan et al., "Corneal biomechanical properties in myopic eyes evaluated via Scheimpflug imaging," *BMC Ophthalmology*, vol. 20, no. 1, p. 279, 2020.

[10] W. Long, Y. Zhao, Y. Hu et al., "Characteristics of corneal biomechanics in Chinese preschool children with different refractive status," *Cornea*, vol. 38, no. 11, pp. 1395–1399, 2019.

[11] A. Tubtimthong, S. Chansangpetch, N. Ratprasatporn et al., "Comparison of corneal biomechanical properties among axial myopic, nonaxial myopic, and nonmyopic eyes," *BioMed Research International*, vol. 2020, Article ID 8618615, 7 pages, 2020.

[12] F. Han, M. Li, P. Wei, J. Ma, V. Jhanji, and Y. Wang, "Effect of biomechanical properties on myopia: a study of new corneal

biomechanical parameters," *BMC Ophthalmology*, vol. 20, no. 1, p. 459, 2020.

[13] A. K. Schuster, J. E. Fischer, and U. Vossmerbaeumer, "Curvature of iris profile in spectral domain optical coherence tomography and dependency to refraction, age and pupil size - the MIPH Eye&Health Study," *Acta Ophthalmologica*, vol. 95, no. 2, pp. 175–181, 2017.

[14] K. O. Alstair and P. I. M. Denniston, *Oxford Handbook of Ophthalmology*, Oxford University Press, London, 2014.

[15] M. Lawrence, V. S. B. Levine, M. H. Goldstein et al., "Fundamentals and principles of ophthalmology," in *Basic and Clinical Science Course*, p. 40, American Academy of Ophthalmology, Italy, Third edition, 2014-2015.

[16] L. Fu, Q. Dai, P. Zhu et al., "Association between iris biological features and corneal biomechanics in myopic eyes," *Disease Markers*, vol. 2021, Article ID 5866267, 6 pages, 2021.

[17] B. Y. Xu, J. Lifton, B. Burkemper et al., "Ocular biometric determinants of anterior chamber angle width in Chinese Americans: the Chinese American Eye Study," *American Journal of Ophthalmology*, vol. 220, pp. 19–26, 2020.

[18] T. A. Tun, J. Chua, Y. Shi et al., "Association of iris surface features with iris parameters assessed by swept-source optical coherence tomography in Asian eyes," *The British Journal of Ophthalmology*, vol. 100, no. 12, pp. 1682–1685, 2016.

[19] B. Wang, L. M. Sakata, D. S. Friedman et al., "Quantitative iris parameters and association with narrow angles," *Ophthalmology*, vol. 117, no. 1, pp. 11–17, 2010.

[20] C. C. Sng, J. C. Allen, M. E. Nongpiur et al., "Associations of iris structural measurements in a Chinese population: the Singapore Chinese Eye Study," *Investigative Ophthalmology & Visual Science*, vol. 54, no. 4, pp. 2829–2835, 2013.

[21] A. Shah, S. Low, D. F. Garway-Heath, P. J. Foster, and K. Barton, "Iris concavity, corneal biomechanics, and their correlations with ocular biometry in a cohort of 10- to 12-year-old UK school boys: baseline data," *Investigative Ophthalmology & Visual Science*, vol. 55, no. 5, pp. 3303–3310, 2014.

[22] A. Shah, G. Lascaratos, D. F. Garway-Heath, P. J. Foster, and K. Barton, "Longitudinal study of iris concavity, corneal biomechanics, and correlations to ocular biometry in a cohort of 10- to 12-year-old UK schoolboys: 2-year follow-up data," *Investigative Ophthalmology & Visual Science*, vol. 55, no. 7, pp. 4645–4650, 2014.

[23] N. Niyadurupola and D. C. Broadway, "Pigment dispersion syndrome and pigmentary glaucoma - a major review," *Clinical & Experimental Ophthalmology*, vol. 36, no. 9, pp. 868–882, 2008.

Hindawi
Disease Markers
Volume 2021, Article ID 2629150, 15 pages
https://doi.org/10.1155/2021/2629150

Research Article

Transneuronal Degeneration in the Visual Pathway of Rats following Acute Retinal Ischemia/Reperfusion

Yanyan Fu,[1,2] **Tu Hu**,[1,2] **Qianyue Zhang**,[1,2] **Shuhan Meng**,[1,2] **Ying Lu**,[1,2] **Aiqun Xiang**,[1,2] **Yewei Yin**,[1,2] **Yuanjun Li**,[1,2] **Jiayu Song**,[1,3] **and Dan Wen**[1,2,3]

[1]*Department of Ophthalmology, Xiangya Hospital, Central South University, Changsha, 410008 Hunan, China*
[2]*Hunan Key Laboratory of Ophthalmology, China*
[3]*Central South University National Clinical Research Center for Geriatric Disorders Xiangya Hospital, China*

Correspondence should be addressed to Dan Wen; wendan@csu.edu.cn

Yanyan Fu and Tu Hu contributed equally to this work.

Received 7 October 2021; Accepted 8 November 2021; Published 7 December 2021

Academic Editor: Ting Su

The maintenance of visual function not only requires the normal structure and function of neurons but also depends on the effective signal propagation of synapses in visual pathways. Synapses emerge alterations of plasticity in the early stages of neuronal damage and affect signal transmission, which leads to transneuronal degeneration. In the present study, rat model of acute retinal ischemia/reperfusion (RI/R) was established to observe the morphological changes of neuronal soma and synapses in the inner plexiform layer (IPL), outer plexiform layer (OPL), and dorsal lateral geniculate nucleus (dLGN) after retinal injury. We found transneuronal degeneration in the visual pathways following RI/R concretely presented as edema and mitochondrial hyperplasia of neuronal soma in retina, demyelination, and heterotypic protein clusters of axons in LGN. Meanwhile, small immature synapses formed, and there are asynchronous changes between pre- and postsynaptic components in synapses. This evidence demonstrated that transneuronal degeneration exists in RI/R injury, which may be one of the key reasons for the progressive deterioration of visual function after the injury is removed.

1. Introduction

Retinal ischemia/reperfusion (RI/R) causes traumatic tissue and progressive degeneration of retina ganglion cells (RGCs) [1]. These pathological events have been considered as the major cause of RI/R-induced visual dysfunction for decades [2]. Intervention measures that only compete against the mechanisms of in situ RGC death cannot recover the degenerated visual function following RI/R [3, 4]. Thus, there may be some other key factors that contribute to visual dysfunction following RI/R injury.

Neuroscience studies have demonstrated the significant transneuronal degeneration in neurodegenerative diseases [5, 6], which can be manifested as cellular edema, apoptosis, and axonal degeneration [7, 8]. These remote pathological events were usually neglected but cause functional damage that ultimately affects prognosis. Diffusion tensor imaging (DTI) reveals that the white matter of the visual pathways demonstrates damage proportional to the amount of structural and functional changes in the optic nerve [9]. Functional magnetic resonance imaging (fMRI) further described the blood-flow abnormalities in the brain of patients with primary open-angle glaucoma [10]. Pathological studies have shown that the atrophy of the LGN plate, the deformation of neuronal dendrites, decreases of metabolic activity in LGN neurons, and even the thickness of the primary visual cortex emerged a significant reduction [11, 12]. A molecular study showed that the NLRP3 inflammasome can be activated by ATP-P2X7-NLRP3 signal channel after optic nerve damage and involved in the secondary degeneration of neurons in the V1 region of the visual cortex [13]. These studies suggested that the primary retinal neuronal damage has profound effects on synaptic-

linked distant neurons. However, what detailed mechanisms might involve in these transneuronal degenerations?

Scholars have found the synaptic plasticity alterations at the early stage of neurological diseases such as Alzheimer's disease (AD), epilepsy, and convulsions [6, 8, 14], which probably contribute to the transneuronal degeneration and be responsible for transferring damage signal between neurons [15, 16]. For further exploration, Kim et al. [17] revealed that tau protein deposition within axons and spread along synapse in corticopontine pathways can promote transneuronal degeneration in the frontotemporal lobar. Thus, a hypothesis is raised that the presynaptic terminal changes may break down the routing and sorting mechanisms for the cytoskeletal protein tau, which promote the formation of initial neurofibrillary pathology in the postsynaptic neurons via anterograde transneuronal mechanisms. In Wolfram syndrome, the downregulation of kinesin engine protein in synaptic terminals slows down the speed of axoplasmic transport, which leads to the decreasing in presynaptic vesicles and SYN, and this event participated in the extensive neuronal loss in LGN [18]. In addition, synapses can transfer damage signals by regulating the levels of cytokines such as inflammatory factors [19], brain-derived neurotrophic factor (BDNF) [20], and vascular endothelial growth factor (VEGF) [21]. Furthermore, synapses can also affect distal neurons by remodeling the dendritic structures and increasing the axon bundles [22]. Moreover, the alteration of mitochondria proliferation in axon terminus has profound effects on distant neurons [23]. Recently, other researchers found that SYN increased following high intraocular pressure- (HIOP-) induced retinal injuries [22, 24]. Previous studies revealed that SYN promoted the release of excitotoxic glutamate, which enhanced the activity of N-methyl-D-aspartate (NMDA). This event led to the accumulation of soluble amyloid-β (Aβ) in hippocampal excitatory neurons [25]. These studies demonstrated that transneuronal degeneration has a strong correlation with retinal synaptic plasticity.

Until now, the details of transneuronal degeneration after RI/R have not been elucidated yet. In this study, we established the acute RI/R model of rats and summarized the temporal and spatial alterations of neurons and synapses in OPL, IPL, and LGN after RI/R injury. This study may provide more detailed pathology data in the visual pathway and more reliable intervention time and targets.

2. Materials and Methods

2.1. Animals and RI/R Model. One hundred and twenty adult Sprague-Dawley (SD) rats (female: 250-300 g, 9-10 weeks old) were purchased from the animal center of Central South University (License number: SCUD (Changsha) 2011-0004, Changsha, China). All animals were housed in clean level conditions with free access to food and water under the temperature of $22 \pm 1^{\circ}$C, the humidity of 55 ± 5 %, and a 12-hour light/dark cycle. All experimental procedures were reviewed and approved by the Animal Care and Use Committees of the Laboratory Animal Research Center at Xiangya Medical School of Central South University.

All animals were randomly and equally divided into five experimental procedures (for retrograde tracing, HE staining, immunohistochemistry, western blot analysis, and transmission electron microscope), and twenty-four animals were included in each procedure. We have eight groups in the first four experimental procedures, which means rats allowed to survive, respectively, at 2 hours, 6 hours, 12 hours, 1 day, 3 days, 7 days, and 14 days after injury (plus the untreated control groups, a total of eight observation groups). For transmission electron microscope (TEM), we have four experimental observation times, respectively, at controls, 12 hours, 3 days, 7 days, and 14 days after injury, and three animals were used for each observation time ($n = 3$ rats, 6 eyes).

All animals in the RI/R group were treated following the procedures previously described [26]; the rats were anesthetized with a 2% pentobarbital sodium (0.3 mL/100 g). A 30-gauge intravenous infusion needle connected to the installation instrument with normal saline was inserted into the anterior chambers of the eyes. The intraocular pressure (IOP) was slowly elevated to 14.63 kPa (110 mmHg), maintained for 60 min, and then gradually lowered to normal pressure.

2.2. Tissue Preparation. The retinal flats were used for retrograde tracing. First, the eyecups were prepared following perfusion. Next, the eyecups were fixed in 4% paraformaldehyde for 1 h at room temperature, and the retina was detached from the eyecups. To stretch the retinas flat, they were placed with ganglion cell layers facing upward on microscope slides and incised with four 3 mm long cuts at their superior, inferior, temporal, and nasal sides. Finally, the retinas were cleaned using a soft brush, covered with antifade aqueous mounting medium, and covers lipped.

The frozen sections were used for HE staining and immunohistochemistry. The eyecups or brain tissue were postfixed, immersed in ascending sucrose. After the dehydration was completed, the tissues were buried in the O.C.T. compound (SAKURA, USA), and stored at -20°C, and prepared for frozen sections. The eyecups were subjected to sagittal sections with 5 μm thickness, and select sections with the optic nerve for standby. And brain tissue was subjected to coronary sections with 5 μm thickness, and select sections with the dLGN for standby.

For western blotting, retinas and dLGN were dissected from deeply anesthetized rats and then weighed and quickly frozen on dry ice and stored at 80C for further homogenization.

For transmission electron microscopy (TEM), retinas and dLGN were dissected from perfused rats and rinsed with clean saline and then fixed in 2.5% pentanediol solution (tissue fixation solution for TEM) for electroscopic tissue sections.

2.3. Counting of RGCs. For retrograde labeling of RGCs, 4 days before sacrifice, Cholera Toxin B subunit-FITC (CTB-FITC, 3 μL of 5% solution, Cat# abs80001, Absin, China) was introduced bilaterally into the dLGN according to the dLGN stereotaxic coordinates (bregma: 4.25 ± 0.18 mm,

lateral: 3.00 ± 0.01 mm, and depth: 1.81 ± 0.13 mm; Song et al., 2019) using the stereotaxic instrument (RWD Life Science Co., Ltd., Shenzhen, Guangdong Province, China). After the perfusion, the eyeballs were dissected from deeply anesthetized rats, and the anterior segments were removed, and the posterior segments were fixed in 4% paraformaldehyde (0.1 M PB, pH 7.4) for 30 min. The retina was then isolated, and the retinal flat was as described above. RGCs were counted as previously reported [27]. Briefly, five fields for each quadrant (twenty in total) were taken within the central periphery of the retina regions (2 mm from the optic disc, Supplementary Figure 1) in each retina flat. CTB-labeled RGCs were counted at 400x magnification in each field; the mean of the 20 visual fields represents the number of this one retina. Corresponding regions from each retina of experimental and control groups were used for counting.

2.4. Hematoxylin and Eosin Staining. HE staining was conducted according to routine protocols [17]. The 5 μm eyecup sections with the optic nerve were rewarmed and fixed in 4% paraformaldehyde for 15 min and then rinsed in double-distilled water (DDW). Then, the sections were stained with hematoxylin solution for 10 min followed by 1% acid ethanol (1% HCl in 70% ethanol) for 30 s and then rinsed in DDW. Then, the eyecup sections were stained with eosin solution for 1 min and followed by dehydration with graded alcohol (80%, 95%, and 100%) and clearing in xylene. The tissue surface was covered with glycerol, cover slides, and stored for morphological evaluation. Five sections were taken from each rat and observed under 200x microscopic magnification. The visual field of the central retina region (near the optic nerve) was selected, and the pathological image analysis software (CMIAS system) was used to measure the thickness of retinal OPL and IPL.

2.5. Immunohistochemistry. The brain tissue sections with the dLGN and the eyecup sections with the optic nerve were collected for immunofluorescent labeling. These sections were rewarmed and washed several times in PBS and then incubated with the anti-rabbit synaptophysin (1 : 500, Abcam, ab32127) and anti-mouse PSD-95 (1 : 500, Abcam, ab18258) overnight at 4°C. After several washes with PBS, sections were incubated with donkey anti-rabbit Alexa 594 (Jackson ImmunoResearch, 711-585-152) and goat anti-mouse Alexa 488 (Jackson ImmunoResearch, 115-545-062) for 2 hours at room temperature, followed by 0.5 μg/mL DAPI (Thermo Fisher Scientific) in PBS for 5 minutes at room temperature before mounting. Five sections were taken from each rat and observed under 200x and 400x magnification immunofluorescence microscopy; the exposure time for eye sections was kept at 1 s and brain tissue sections at 2-3 s. Finally, use the Image J analysis software to measure the average grayscale values of positive products in retinal IPL and OPL.

2.6. Western Blotting. As previously detailed [28], tissue samples were homogenized by sonication on ice in RIPA buffer containing a cocktail of protease inhibitors (Sigma, MO, USA). Sonication-digested homogenates were treated with centrifugation, protein concentration determination, and degeneration, respectively. Total protein in tissue extracts was measured using a standard BCA assay (Pierce). Tissue extract proteins were resuspended in 5× sample buffer (60 mM Tris–HCl pH 7.4, 25% glycerol, 2% SDS, 14.4 mM 2-mercaptoethanol, and 0.1% bromophenol blue) at a 4 : 1 ratio, boiled for 5 min, and resolved by SDS-PAGE. Proteins were transferred onto a nitrocellulose membrane, and blots were stained with Ponceau S (Sigma, St. Louis, MO, USA) to visualize the protein bands and ensure equal protein loading and uniform transfer. Blots were washed and blocked for 45 min with 5% nondried skim milk in TBST buffer. Blots were then probed for 24 h using anti-rabbit synaptophysin (1 : 500, Abcam, ab32127) and anti-mouse PSD-95 (1 : 500, Abcam, ab18258) and Actin (Sigma, St. Louis, MO, USA). Blots were then probed with horseradish peroxidase- (HRP-) conjugated goat anti-rabbit secondary antibody and HRP-donkey anti-mouse secondary antibody. Bound antibodies were detected using an enhanced chemiluminescence system (Amersham) and X-ray film. Relative intensity was measured using an Image-Master®VDS (Pharmacia Biotech), and the fold changes in these protein levels are indicated below the blot. Results are representative of five independent experiments. Data are expressed as mean ± SD.

2.7. Transmission Electron Microscopy. Electron microscopy was conducted using retinal and dLGN electron microscopic sections from controls and postsurgery (three rats per group). Retina and dLGN tissue were cut into 1 mm^3 cube with a vibratome and rinsed with clean saline. Tissues were fixed in 2.5% glutarol solution for 1 hour at room temperature or 3 hours at 4°C and then with 1% osmium tetroxide in 0.1 mmol/L cacodylate buffer for 2 hours. After rinsing with DDW, sections were treated with 1% aqueous uranyl acetate overnight, dehydrated in ethanol solutions of increasing concentration, up to 100%, followed by dry acetone, and then embedded in durcupan ACM. Ultrathin sections (0.1 μm) were cut and mounted on Formvar-coated slot grids, stained with 3% lead citrate, and examined with a Zeiss transmission EM (Zeiss).

2.8. Statistical Analysis. The IBM SPSS Statistics (23.0) software was applied in this study; all data are expressed as means ± SD. Comparisons between the control group, 2 hours, 6 hours,12 hours, 1 day, 3 days, 7 days, and 14 days were performed using the one-way ANOVA test, and Student's t-test was used in pairwise comparisons. Differences with $P < 0.05$ were considered statistically significant.

3. Results

3.1. Changes of Neuronal Soma in Visual Pathways following RI/R

3.1.1. RGC

(1) Mean Density of CTB-Labeled Retinal Ganglion Cells. We used cholera toxin subunit (CTB) as a retrograde tracer to mark RGCs, and the results obtained that the mean density

Table 1: Mean density of RGCs using CTB retrograde tracer ($n = 5$).

Groups	Control	I/R-2 h	I/R-6 h	I/R-12 h	I/R-1 d	I/R-3 d	I/R-7 d	I/R-14 d
MD-RGCs (cells/mm^2)	2325 ± 133	2450 ± 154	2350 ± 170	2457 ± 152	1500 ± 140	1475 ± 182	1425 ± 145	1137 ± 112
F		-626.52	-126.75	-661.24	4124.43	4499.64	5124.46	5939.16
P		0.825	1.581	1.304	<0.001**	<0.001**	<0.001**	<0.001**

Means ± standard error of the mean unless otherwise stated. MD-RGCs: mean density of labeled retinal ganglion cells. I/R-2 h: rats euthanized 2 hours post-RI/R injury; I/R-6 h: rats euthanized 6 hours post-RI/R injury; I/R-12 h: rats euthanized 12 hours post-RI/R injury; I/R-1 d: rats euthanized 1 day post-RI/R injury; I/R-1 d: rats euthanized 3 days post-RI/R injury; I/R-7 d: rats euthanized 7 days post-RI/R injury; I/R-14 d: rats euthanized 14 days post-RI/R injury. *$P < 0.05$ indicates that there were statistical differences when compared with the control groups. **$P < 0.01$ indicates that there were significant statistical differences when compared with the control groups.

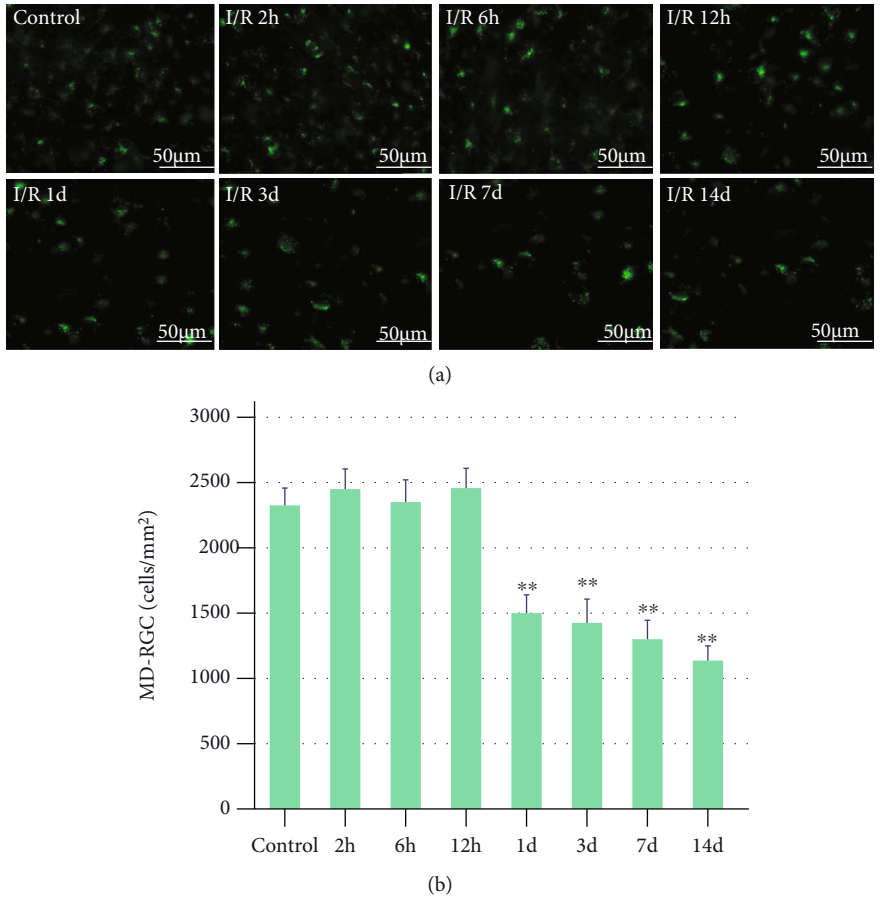

Figure 1: The mean density of RGC retrograde labeled by CTB (scale bar = 50 μm). (a) I/R-2 h to 14 d: representative photomicrographs were taken at high magnification of rats euthanized 2 hours, 6 hours, 12 hours, 1 day, 3 days, 7 days, and 14 days post-RI/R injury. (b) MD-RGCs: I/R-1 d, I/R-3 d, I/R-7 d, and I/R-14 d (rats euthanized 1 day, 3 days, 7 days, and 14 days post-RI/R injury) were less than those in the control group ($P < 0.001$). I/R-2 h: rats euthanized 2 hours post-RI/R injury; I/R-6 h: rats euthanized 6 hours post-RI/R injury; I/R-12 h: rats euthanized 12 hours post-RI/R injury; I/R-1 d: rats euthanized 1 day post-RI/R injury; I/R-1 d: rats euthanized 3 days post-RI/R injury; I/R-7 d: rats euthanized 7 days post-RI/R injury; I/R-14 d: rats euthanized 14 days post-RI/R injury. *$P < 0.05$ indicates that there were statistical differences when compared with the control groups. **$P < 0.01$ indicates that there were significant statistical differences when compared with the control groups.

of RGCs (MD-RGCs) in the peripheral retina was (2325 ± 133)/mm^2 in the control group. And there was no significant difference between I/R-2 h ($P = 0.825$), I/R-6 h ($P = 1.581$), I/R-12 h ($P = 1.304$) groups, and control group in mean density. Specific values for the different groups are shown in Table 1. The mean density of RGCs in I/R-1 d, I/R-3 d, I/R-7 d, and I/R-14 d were less than those in the control group ($P < 0.001$) (Figures 1(a) and 1(b)).

(2) Changes of RGCs Ultrastructure following RI/R. Under the TEM, normal RGCs showed round nuclei with smooth nuclear contours and account for a large proportion of

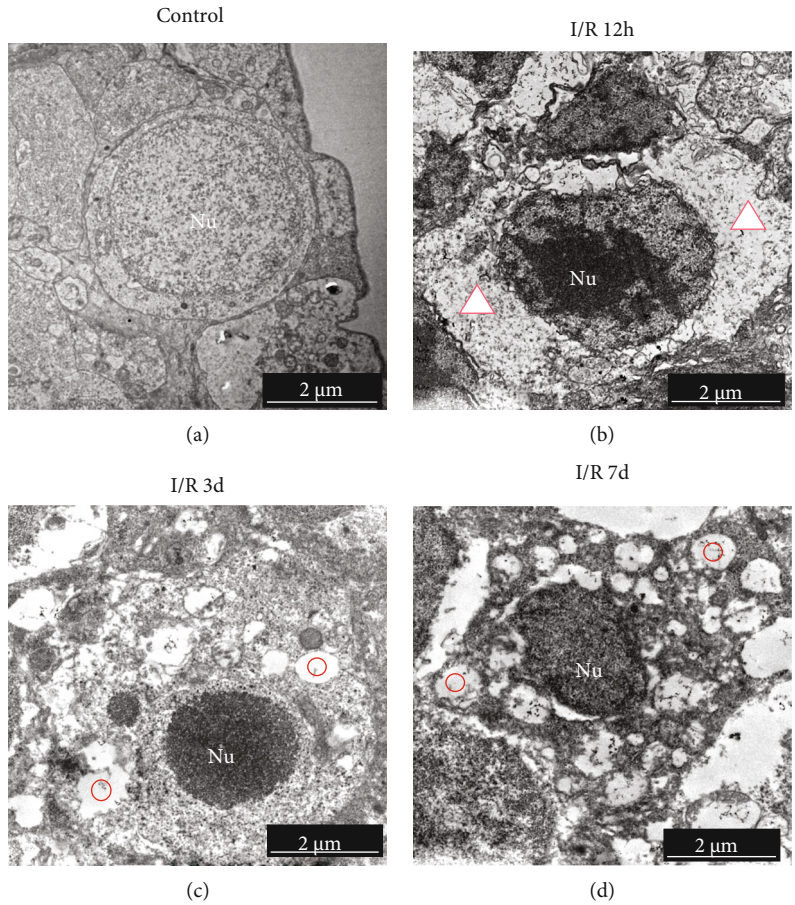

Figure 2: Changes of RGC ultrastructure after RI/R injury (10000×, bar = 2 μm). (a) Control group, Nu: nucleus of RGCs: the nucleus of RGCs presented round shape with smooth nuclear contours and accounted for most volume in the normal physiological state. (b) I/R-12 h group, the morphology of RGCs at 12 hours post-RI/R injury: the cytoplasmic edema was visible (red triangle) and nuclear chromatin became condensed, but the aggregation of chromatin and fragmentation of nuclei did not occur (Nu). (c) I/R-3 d group, the morphology of RGCs at 3 days post-RI/R injury: the cytoplasmic vacuole formed in RGCs (red circle). The chromatin continues to aggregate, and the volume of the nucleus shrunk (Nu). (d) I/R-7 d group, the morphology of RGCs at 7 days post-RI/R injury: more vacuolar can be seen in the cytoplasm of RGCs (red circle), and the fragmentation of nuclei began to appear; both the chromatin and the organelles began to dissolve; these phenomena suggest necrosis in RGCs. I/R-12 h: rats euthanized 12 hours post-RI/R injury; I/R-3 d: rats euthanized 3 days post-RI/R injury; I/R-7 d: rats euthanized 7 days post-RI/R injury.

volume in cell body (Figure 2(a)). At 12 hours after RI/R injury, we can see the cytoplasmic edema was prominent in RGCs (Figure 2(b), red triangle). Moreover, nuclear chromatin became condensed, but the aggregation of chromatin and fragmentation of nuclei did not occur (Figure 2(b), Nu). At 3 days after RI/R injury, the cytoplasmic vacuole (Figure 2(c), red circle) formed in RGCs. The chromatin continues to aggregate, and the volume of the nucleus shrunk (Figure 2(c), Nu). At 7 days after RI/R injury, more vacuole can be seen in the cytoplasm of RGCs, and the fragmentation of nuclei began to appear; both the chromatin and the organelles began to dissolve; these phenomena suggest necrosis in RGCs (Figure 2(d)).

3.1.2. Bipolar Cells. The nucleus of bipolar cells in INL was neatly arranged with a polygonal cross-section (Figure 3, ①). At 12 hours after RI/R injury, severe cellular edema of bipolar cells in the INL was observed, and some nuclei in INL were replaced by vacuoles (Figure 3, ②). At 3 days after injury, the macular edema of bipolar cells showed a slight trace of recovery but cell morphology becomes irregular and nuclear chromatin became condensed (Figure 3, ③). At 7 days after injury, the shape of bipolar cells became irregular, and the chromatin and the organelles began to dissolve, suggested the apoptosis of bipolar cells late after injury.

3.1.3. Photoreceptor Cells. Nucleus of photoreceptor (PR) cells in ONL was neatly arranged with a polygonal cross-section (Figure 3(a)). Outside the ONL are the inner segments (ISs) of photoreceptor (PR) cells; they were narrow and long, with a long spindle shape, were arranged orderly, and rich in mitochondria at the peripheral portion of neuronal soma (Figure 3(e)). The outer segment (OS) of photoreceptor (PR) cells contained many flattened membranous structures called discs. In the normal state, the disc is neatly folded inside with few gaps in between (Figure 3(i)). At 12 hours after RI/R injury, many PR cells' nuclei were replaced

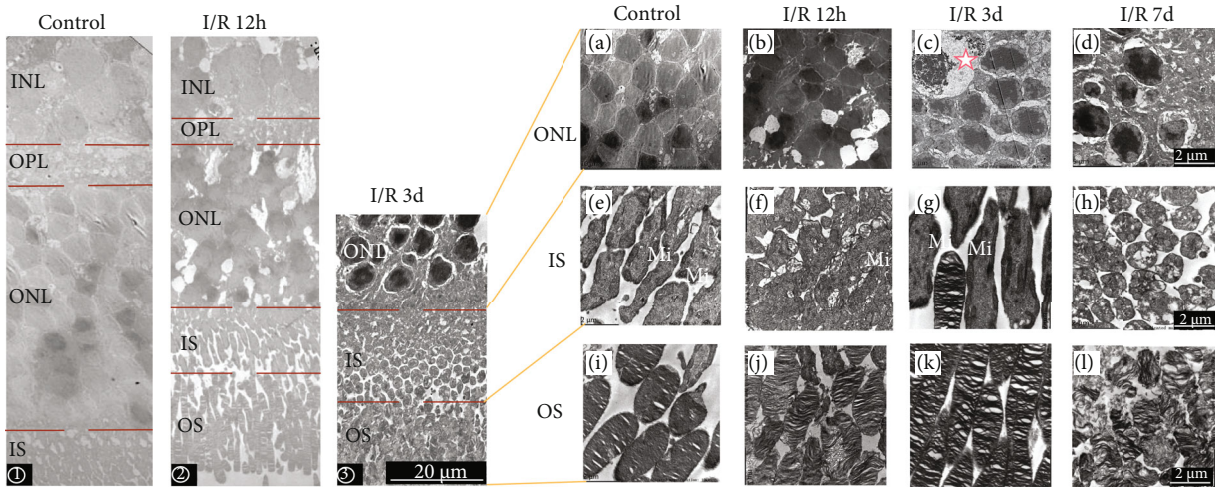

Figure 3: Ultrastructure changes of neurons in the retina after RI/R injury. ①–③: ultrastructure changes in each layer of the retina under 1000× TEM (bar = 20 μm). ① Control group. The boundaries between different layers were clear. The nucleus in ONL and INL was neatly arranged with a polygonal cross-section. ② Ultrastructure of each layer in the retina at 12 hours post-RI/R injury. Layer demarcation becomes unclear, and the arrangement of cells becomes loose, and obvious macular edema was observed. ③ Ultrastructure of each layer in the retina at 3 days post-RI/R injury. The macular edema showed a slight trace of recovery, but cell morphology becomes irregular, and nuclear chromatin became condensed. (a–l) Ultrastructure changes in each layer of the retina under 10000× TEM (bar = 2 μm). I/R-12 h: rats euthanized 12 hours post-RI/R injury; I/R-3 d: rats euthanized 3 days post-RI/R injury; I/R-7 d: rats euthanized 7 days post-RI/R injury. (a) Nucleus in ONL was neatly arranged with a polygonal cross-section. (e) Outside the ONL are the inner segments (ISs) of photoreceptor (PR) cells, and they were narrow and long, with a long spindle shape, were arranged orderly, and rich in mitochondria at the peripheral portion of the soma. (l) Outer segment (OS) of photoreceptor (PR) cells contained many flattened membranous structures called discs. In the normal state, the disc is neatly folded inside, with few gaps in between. (b, f, j) I/R-12 h group. (b) Some nucleus in ONL was replaced by vacuoles. (f) Edema in the IS made cells' volume increased significantly which decreased intercellular space. Mitochondria (Mi) were significantly increased and swelled. (j) OS swelled, the arrangement of membranous discs becomes disordered, and the space between membranous discs became widened. (c, g, k) I/R-3 d group. (c) Gliocyte proliferation in ONL (red star), cell edema, and chromatin aggregation allowed the nucleus to be deeply stained. (g) The edema in the IS showed a slight trace of recovery compared to the I/R-12 h group, while mitochondria continue to proliferate and hypertrophy (Mi). (k) The edema in the OS showed a slight trace of recovery. (d, h, l) I/R-7 d group. (d) Nucleus in ONL was lysed, and the number reduced. (h) Organelle was lysed, and the membrane was discontinuous in IS. (o) The membrane disc was loose, dissolved, and shrunk.

by vacuoles (Figure 3(b)), and edema in the IS made cells' volume increased significantly. Mitochondria (Mi) were significantly increased and swelled (Figure 3(f)). The OS swelled, and the arrangement of membranous discs becomes disordered; the space between membranous discs became widened (Figure 3(j)). At 3 days after RI/R injury, we found gliocyte proliferation chromatin aggregation in ONL (Figure 3(c), red star). At 3 days after injury, the edema in the IS showed a slight trace of recovery but while mitochondria continue to proliferate and hypertrophy (Figure 3(g), Mi). Then, nuclei in ONL were lysed, and the number reduced at 7 days after injury (Figure 3(d)). Organelle was lysed, the membrane was discontinuous in IS (Figure 3(h)), and the membrane disc was loose, dissolved, and shrunk (Figure 3(l)).

3.1.4. Neurons in LGN. Under normal physiological conditions, nerve fiber bundles in LGN were orderly arranged, axons were surrounded by a myelin sheath, and the endoneurium-encased myelin sheath and axons were clear and visible on the nerve fiber surface (green arrow). Axons were tightly surrounded, and there is no space between axons and myelin (Figure 4(a)). At 12 hours after RI/R injury, clear space (red arrow) appears in the myelin sheath representing early demyelination changes. The axons showed significant edema and mitochondrial hypertrophy and hyperplasia (Figure 4(b)). At 7 days after RI/R injury, there were heterotypic protein clusters (yellow arrow) within axons and the diameter of axons decreased significantly (Figure 4(c)).

3.2. Changes of Synapsis in Visual Pathways following RI/R Damage

3.2.1. Changes in IPL and OPL following RI/R Damage

(1) Morphological Changes in IPL and OPL. Observation under the optical microscope revealed that a normal 10-week-old female rat's thickness was 54.03 ± 6.78 μm for IPL and 11.16 ± 0.91 μm for OPL (Figure 5(a), control). At 2 to 12 hours after RI/R injury, the thickness of IPL continues to increase ($P < 0.01$) and reach the peak of thickness at 12 hours (133.89 ± 6.65 μm), which was 2.46 times of the control group. Subsequently, at 1 to 14 days after RI/R injury, the thickness of IPL continues to decrease, and it was significantly lower than the control group at 14 days ($P = 0.032$) (Figure 5(a)).

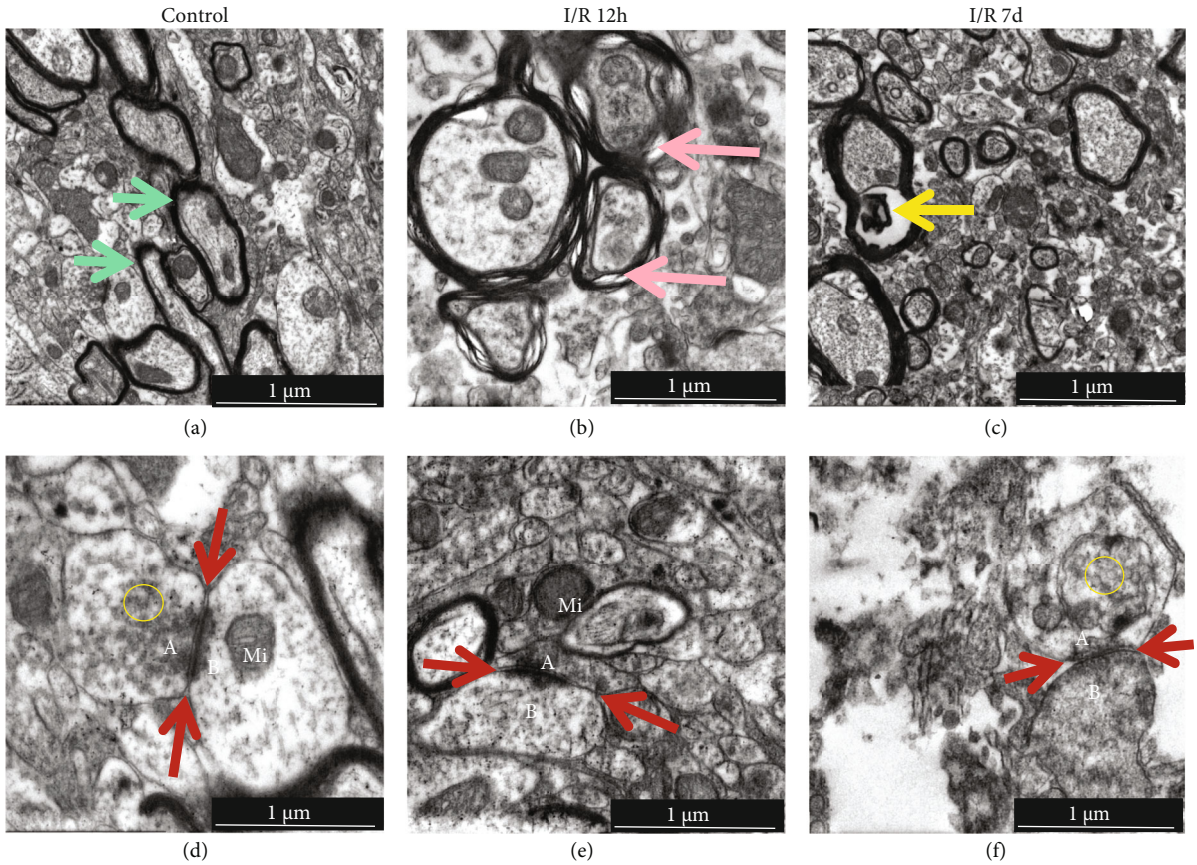

Figure 4: Ultrastructure changes of neurons in LGN after RI/R injury (TEM ×20000). I/R-12 h: rats euthanized 12 hours post-RI/R injury; I/R-3 d: rats euthanized 3 days post-RI/R injury; I/R-7 d: rats euthanized 7 days post-RI/R injury. (a) Control group: nerve fiber bundles in LGN were orderly arranged, axons were surrounded by a myelin sheath, and the endoneurium-encased myelin sheath and axons were clear and visible on the nerve fiber surface (green arrow). In normal conditions, axons were tightly surrounded and there is no space between axons and myelin. (b) I/R-12 h group: clear space (red arrow) appears in the myelin sheath suggesting early demyelination changes. The axons showed significant edema and mitochondrial hypertrophy and hyperplasia. (c) I/R-7 d group: there are heterotypic protein clusters (yellow arrow) within axons, and the diameter of axons decreased significantly; this is a phenomenon of axonal degeneration. (d) Control group, (red arrow): synaptic junction in LGN. The presynaptic (A) and postsynaptic (B) membranes are clear, presynaptic thickenings form a synaptic active zone (red arrow), and clusters of synaptic vesicles (yellow circle) and mitochondria were normal in size and structure (Mi). (e) I/R-12 h group: the synapsis in LGN showed significant edema which made the membrane of synapsis becomes thinner, and the synaptic active band becomes broadened (red arrow), whereas mitochondrial hyperplasia and hypertrophy in presynapses (Mi). (f) I/R-7 d group: membranes of the synapses were discontinuous, organelle was lysed, presynaptic vesicles reduced, and the synaptic structure became unclear.

The same trend was observed in OPL, and at 2 to 12 hours after injury, the thickness of OPL was all greater than that in the control group ($P < 0.05$), $15.06 \pm 1.17\,\mu$m for the I/R-2 h group, $17.04 \pm 1.32\,\mu$m for the I/R-6 h group, and $16.35 \pm 1.44\,\mu$m for the I/R-12 h group. At 1 to 14 days after injury, thickness values of OPL showed a downward trend, $15.27 \pm 1.93\,\mu$m for the I/R-1 d group, $12.39 \pm 1.77\,\mu$m for the I/R-3 d group, $11.88 \pm 1.21\,\mu$m for the I/R-7 d group, and $11.34 \pm 0.84\,\mu$m for the I/R-14 d group (Figure 5(b)). The specific thickness values are shown in Table 2.

Images of the TEM showed that numerous synapses were evenly distributed in the IPL and OPL, and they are closely arranged and uniform in size and shape under normal circumstances (Figure 6(a), red arrow). The presynaptic (Figure 6(d), A) and postsynaptic (Figure 6(d), B) membranes are clear, presynaptic thickenings form a synaptic active zone (Figure 6(d), red arrow), and clusters of synaptic vesicles (Figure 6(d), yellow circle) and mitochondria were normal in size and structure (Figure 6(d), Mi). At 12 hours after RI/R injury, neurons in IPL and OPL showed significant edema (Figure 6(b), red triangle), which made the membrane of synapsis becomes thinner, and mitochondrial hyperplasia and hypertrophy (Figure 6(b), Mi). Many small immature synapses were formed in the IPL and OPL (Figure 6(b), orange arrow). It can be seen under a higher magnification that neuronal edema and presynaptic vesicles (Figure 6(e), yellow circle) increased in both IPL and OPL, and the synaptic active zone became wider and longer (Figure 6(e), red arrow). At 7 days after RI/R injury, the small immature synapses disappeared and neuronal edema gradually recovered, and aggregation of chromatin and fragmentation of nuclei can be observed (Figure 6(c)). Under

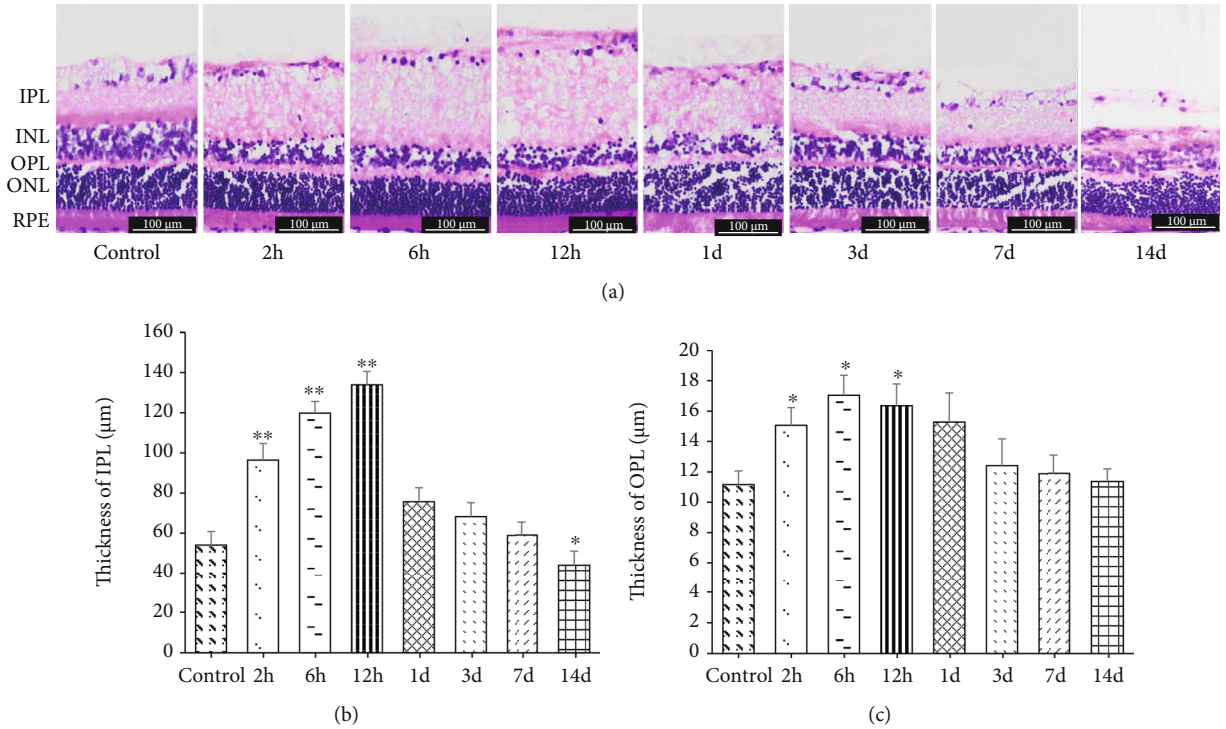

Figure 5: (a) Representative images of HE staining showed morphological alterations of neurons in the retina after RI/R injury (HE 200×, bar = 100 μm). 2 h: rats euthanized 2 hours post-RI/R injury; 6 h: rats euthanized 6 hours post-RI/R injury; 12 h: rats euthanized 12 hours post-RI/R injury; 1 d: rats euthanized 1 day post-RI/R injury; 3 d: rats euthanized 3 days post-RI/R injury; 7 d: rats euthanized 7 days. CMIAS image analysis system was used to quantify the thickness of (b) IPL and (c) OPL, and optical microscopy images were captured using an inverted microscope at 200x magnification. IPL: inner plexiform layer; INL: inner nuclear layer; OPL: outer plexiform layer; ONL: outer nuclear layer; RPE: retinal pigment epithelium. $^{*}P < 0.05$ indicates that there were statistical differences when compared with the control groups. $^{**}P < 0.01$ indicates that there were significant statistical differences when compared with the control groups.

Table 2: The thickness of retinal IPL and OPL in adult SD rats (μm; $n = 5$).

	Control	2 h	6 h	12 h	1 d	3 d	7 d	14 d
IPL	54.03 ± 6.78	96.39 ± 8.30	119.79 ± 5.82	133.89 ± 6.65	75.66 ± 7.01	68.22 ± 6.98	58.83 ± 6.45	43.7 ± 7.11
F		-23.735	-38.086	-46.734	-11.021	-6.458	-0.699	2.447
P		<0.001**	<0.001**	<0.001**	0.084	0.707	1.143	0.032*
OPL	11.16 ± 0.91	15.06 ± 1.17	17.04 ± 1.32	16.35 ± 1.44	15.27 ± 1.93	12.39 ± 1.77	11.88 ± 1.21	11.34 ± 0.84
F		-31.631	-46.44	-46.730	-6.168	-6.977	-2.983	0.889
P		0.048*	0.025*	0.007*	0.044*	0.776	1.581	1.330

Means ± standard error of the mean unless otherwise stated. 2 h: rats euthanized 2 hours post-RI/R injury; 6 h: rats euthanized 6 hours post-RI/R injury; 12 h: rats euthanized 12 hours post-RI/R injury; 1 d: rats euthanized 1 day post-RI/R injury; 3 d: rats euthanized 3 days post-RI/R injury; 7 d: rats euthanized 7 days post-RI/R injury; 14 d: rats euthanized 14 days post-RI/R injury. $^{*}P < 0.05$ indicates that there were statistical differences when compared with the control groups. $^{**}P < 0.01$ indicates that there were significant statistical differences when compared with the control groups.

higher magnification, we found membranes of the synapses were discontinuous, cell was lysed, organelles were separated, presynaptic vesicles reduced (Figure 6(f), yellow circle), and the synaptic structure became unclear. These phenomena suggest neuronal death in IPL late after injury.

(2) SYN and PSD-95 Expression in IPL and OPL. The expression of SYN and PSD-95 was mainly enriched in IPL and OPL; there are more positive products in IPL than in OPL (Figures 7(a)–7(p)). Quantitative analysis of gray value showed the expression of SYN in IPL increased significantly in I/R-2 h, I/R-6 h, and I/R-12 h groups ($P = 0.012$, 0.038, 0.022) (Figures 7(a)–7(d)). At 1 day after RI/R, the SYN expression began to decrease (Figure 7(e)) and keep this downtrend from 1 day to 14 days after the injury (Figures 7(e)–7(h)). The expression of SYN in the I/R-3 d, I/R-7 d, and I/R-14 d groups was all lower than the control group ($P = 0.027$, 0.008, 0.044) (Figure 7, A). The expression of PSD-95 was unchanged in I/R-2 h, I/R-6 h, and I/R-12 h groups when compared with the control group ($P = 1.175$, 1.838, 0.651) (Figures 7(i)–7(l), A) and began to decrease at 1 day after injury, whereas significantly lower than the

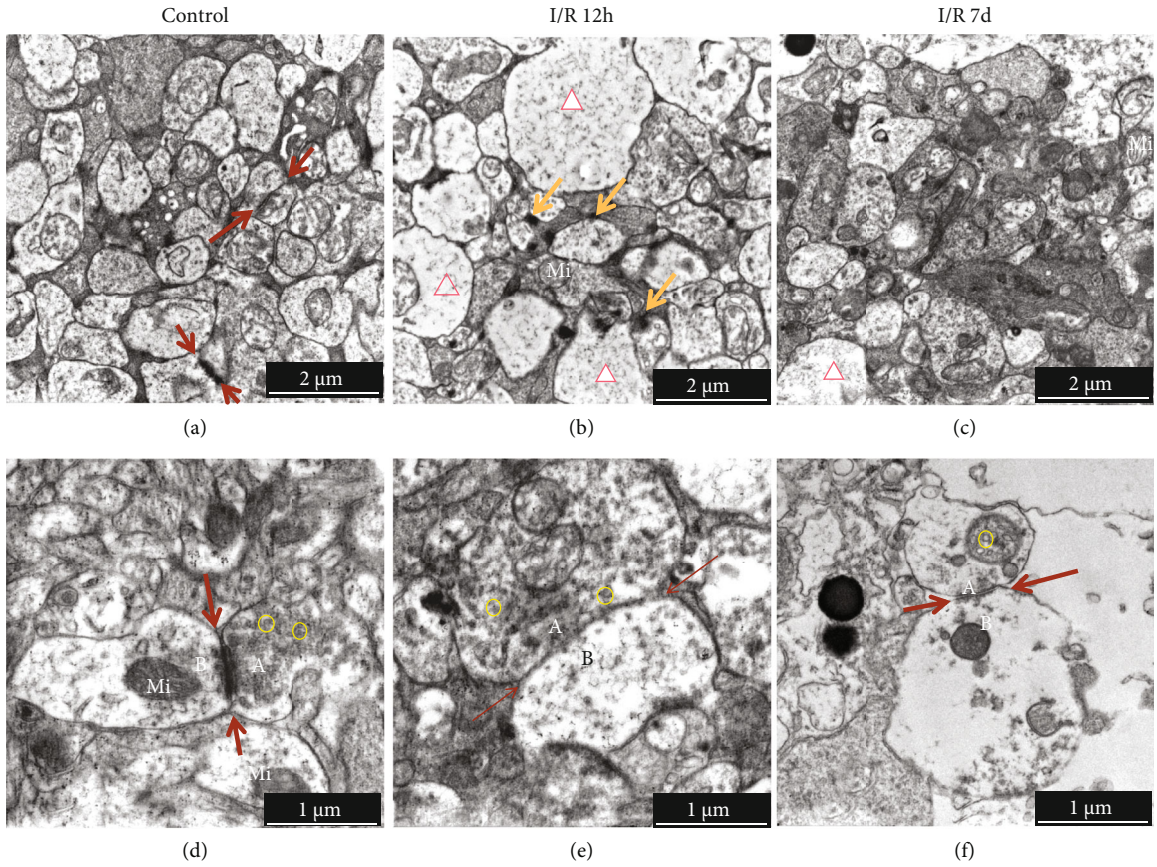

Figure 6: Ultrastructure changes in IPL and OPL after RI/R injury (TEM ×10000, ×20000). I/R-12 h: rats euthanized 12 hours post-RI/R injury; I/R-7 d: rats euthanized 7 days post-RI/R injury. (a) Control group (10000×; bar = 2 μm): numerous synapses were evenly distributed (red arrow), and they are closely arranged and uniform in size and shape under normal circumstances. (d) Control group (20000×; bar = 1 μm). The presynaptic (A) and postsynaptic (B) membranes are clear, presynaptic thickenings form a synaptic active zone (red arrow), and clusters of synaptic vesicles (yellow circle) and mitochondria were normal in size and structure (Mi). (b) I/R-12 h group (bar = 2 μm): neurons in IPL and OPL showed significant edema (red triangle) and mitochondrial hyperplasia and hypertrophy (Mi). Many small immature synapses formed in the IPL and OPL (orange arrow). (e) I/R-12 h group (bar = 1 μm): neuronal edema made the membrane of synapsis becomes thinner, presynaptic vesicles (yellow circle) increased in both IPL and OPL, and the synaptic active zone became wider and longer (red arrow). (c) I/R-7 d group (bar = 2 μm): the small immature synapses disappeared, and neuronal edema gradually recovered, and aggregation of chromatin and fragmentation of nuclei can be observed. (f) I/R-7 d group (bar = 1 μm): membranes of the synapses were discontinuous, cell was lysed, organelles were separated, presynaptic vesicles reduced (yellow circle), and the synaptic structure became unclear (red arrow). These phenomena suggest neuronal death in IPL and OPL.

control group in I/R-1 d, I/R-3 d, and I/R-14 d groups ($P = 0.004$, 0.018, 0.005) (Figures 7(m)–7(p), C).

Quantitative analysis of gray value showed the expression of SYN and PSD-95 in OPL had the same change trend as the expression in IPL. SYN increased significantly in I/R-2 h, I/R-6 h, and I/R-12 h groups ($P = 0.012$, 0.038, 0.022) (Figures 7(a)–7(d)) and began to decrease at 1 day after RI/R (Figure 7(e)). It kept this downtrend from 1 day to 14 days after the injury (Figures 7(e)–7(h)). The expression of SYN in the I/R-1 d, I/R-3 d, I/R-7 d, and I/R-14 d groups was all lower than the control group ($P < 0.05$) (Figure 7, C). Meanwhile, the expression of PSD-95 was unchanged in I/R-2 h, I/R-6 h, and I/R-12 h groups ($P = 0.121$, 0.852, 0.733) (Figures 7(i)–7(l), A) and began to decrease at 1 day after the injury, whereas significantly lower than the control group in I/R-1 d, I/R-3 d, and I/R-14 d groups ($P = 0.011$, 0.017, 0.042) (Figures 7(m)–7(p), C). It indicated that the expression of SYN in both IPL and OPL presents an asynchronous change with the expression of PSD-95.

In addition, western blot (WB) analysis also showed the same expression trend in the whole retina. SYN with the molecular weight of 38 kd was detected to be increased early after injury. From 2 hours to 1 day after the injury, the expression of SYN was significantly higher than control group ($P < 0.001$; $P < 0.001$; $P = 0.009$; $P = 0.011$). Then, from 1 d after injury, the expression began to decrease ($P < 0.05$), and this downward trend continued from 1 d to 14 d (Figures 8(a) and 8(c)). And PSD-95 with the molecular weight of 95 kd, expression remained unchanged from 2 hours to 12 hours after injury ($P > 0.05$). In I/R-1 d, I/R-3 d, I/R-7 d, and I/R-14 d groups, PSD-95 expression was significantly lower than the control group ($P = 0.017$, 0.003, 0.034, 0.001) (Figures 8(b) and 8(d)).

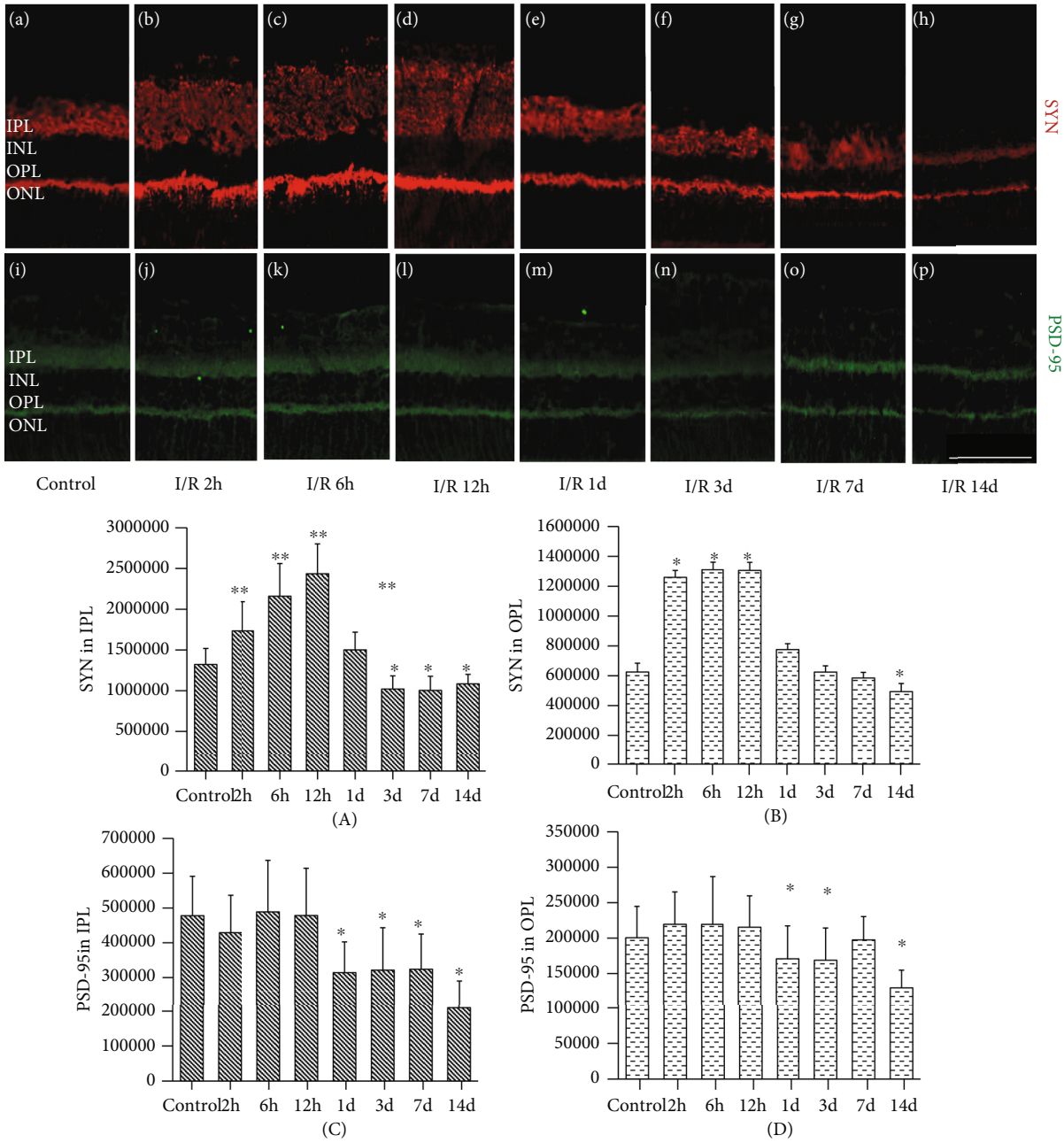

Figure 7: Immunofluorescence images of SYN and PSD-95 expression in the retina after RI/R injury (400x, bar = 50 μm). I/R-2 h: rats euthanized 2 hours post-RI/R injury; I/R-6 h: rats euthanized 6 hours post-RI/R injury; I/R-12 h: rats euthanized 12 hours post-RI/R injury; I/R-1 d: rats euthanized 1 day post-RI/R injury; I/R-1 d: rats euthanized 3 days post-RI/R injury; I/R-7 d: rats euthanized 7 days post-RI/R injury; I/R-14 d: rats euthanized 14 days post-RI/R injury. SYN: synaptophysin (red); PSD-95: postsynaptic density-95 (green); IPL: inner plexiform layer; INL: inner nuclear layer; OPL: outer plexiform layer; ONL: outer nuclear layer. The Image J analysis software was used to determine the average gray value of the SYN expression in (A) IPL and (B) OPL, the average gray value of the PSD-95 expression in (C) IPL and (D) OPL. $^{*}P < 0.05$ indicates that there were statistical differences when compared with the control groups. $^{**}P < 0.01$ indicates that there were significant statistical differences when compared with the control groups.

3.2.2. Changes in dLGN following RI/R

(1) Morphological Changes in dLGN. Within the neuropil of LGN, synapses are evenly distributed and have a clear structure. The presynaptic and postsynaptic membranes were clear (Figure 4(d)), presynaptic thickenings form a synaptic active zone (Figure 4(d), red arrow), and clusters of synaptic vesicles (Figure 4(d), yellow circle) and mitochondria were normal in size and structure (Figure 4(d), Mi). At 12 hours after RI/R injury, multiple small newborn synapses formed within the neuropil, native synapsis in LGN showed significant edema which made the presynaptic and postsynaptic membrane become thinner, and the synaptic active band was broadened (Figure 4(e), red arrow), whereas

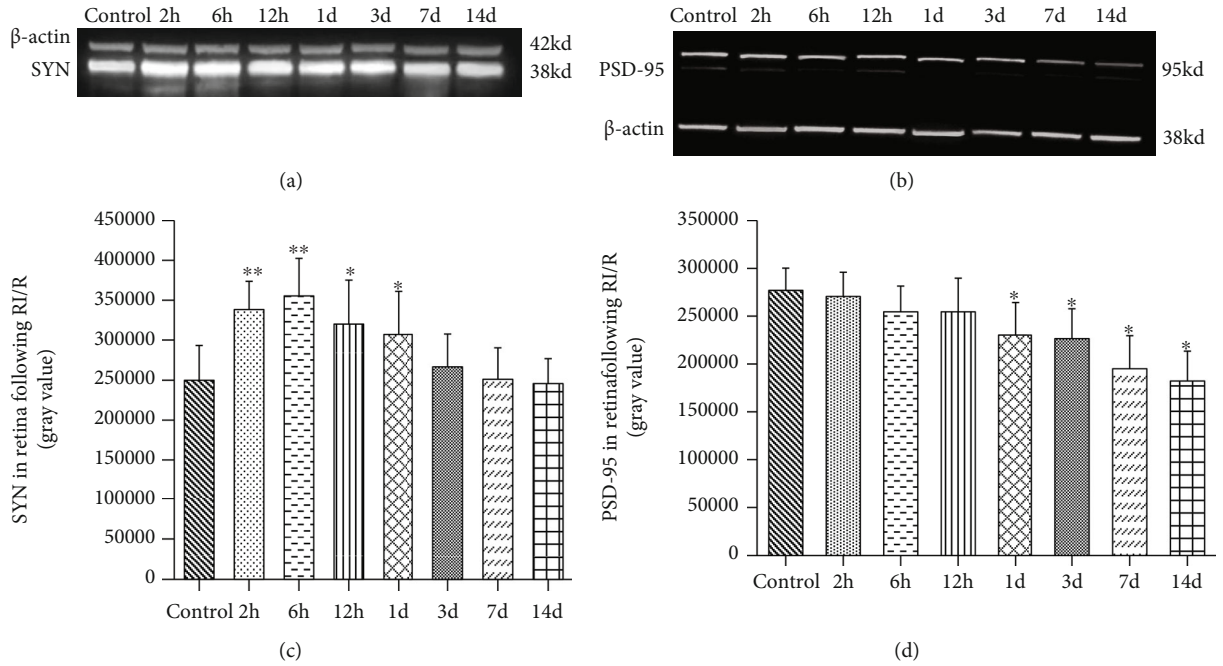

Figure 8: Western blotting results of SYN and PSD-95 expression in the retina after RI/R injury. (a) 2 h: rats euthanized 2 hours post-RI/R injury; 6 h: rats euthanized 6 hours post-RI/R injury; 12 h: rats euthanized 12 hours post-RI/R injury; 1 d: rats euthanized 1 day post-RI/R injury; 3 d: rats euthanized 3 days post-RI/R injury; 7 d: rats euthanized 7 days. Synaptophysin (SYN), a presynaptic vesicle protein, was significantly increased in the retina at 2 hours to 1 day after RI/R compared to the control group. From 3 days to 14 days, the SYN expression showed a downward trend. (b) PSD-95, a postsynaptic vesicle protein, remains unchanged at 2 hours to 12 hours after RI/R compared to the control group. The PSD-95 expression was significantly reduced in the retina at 1 day to 14 days after RI/R. Use the Image J analysis software to determine the average gray value of the (c) SYN expression and the (d) PSD-95 expression in retina. $^{*}P < 0.05$ indicates that there were statistical differences when compared with the control groups. $^{**}P < 0.01$ indicates that there were significant statistical differences when compared with the control groups.

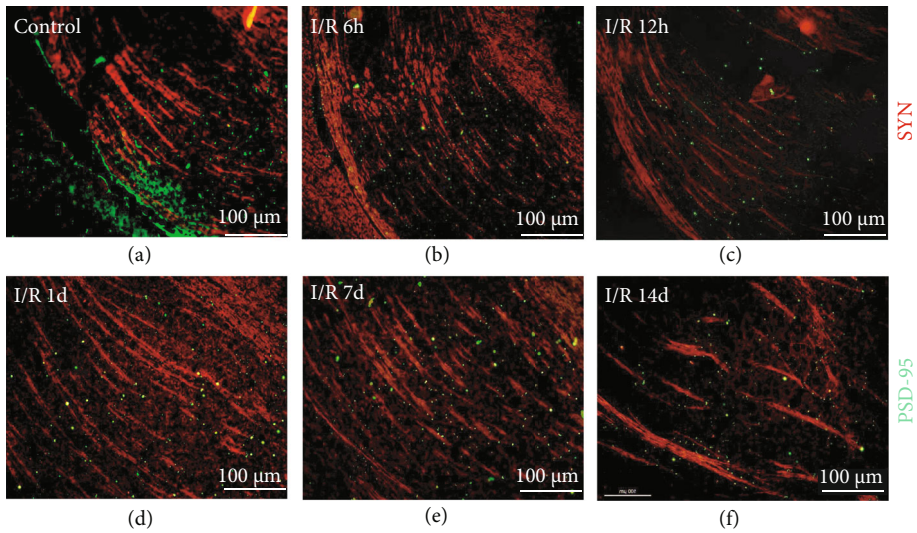

Figure 9: Immunofluorescence images of SYN and PSD-95 expression in dLGN after RI/R injury (100×, bar = 100 μm). Representative photomicrographs taken at 100× immunofluorescence microscopy of rats' coronal plane of LGN on the left side, with (a) control group and (b) 6 hours; (c) 12 hours; (d) 1 day; 3 days; (e) 7 days; (f) 14 days post-RI/R injury. I/R-2 h: rats euthanized 2 hours post-RI/R injury; I/R-6 h: rats euthanized 6 hours post-RI/R injury; I/R-12 h: rats euthanized 12 hours post-RI/R injury; I/R-1 d: rats euthanized 1 day post-RI/R injury; I/R-1 d: rats euthanized 3 days post-RI/R injury; I/R-7 d: rats euthanized 7 days post-RI/R injury; I/R-14 d: rats euthanized 14 days post-RI/R injury.

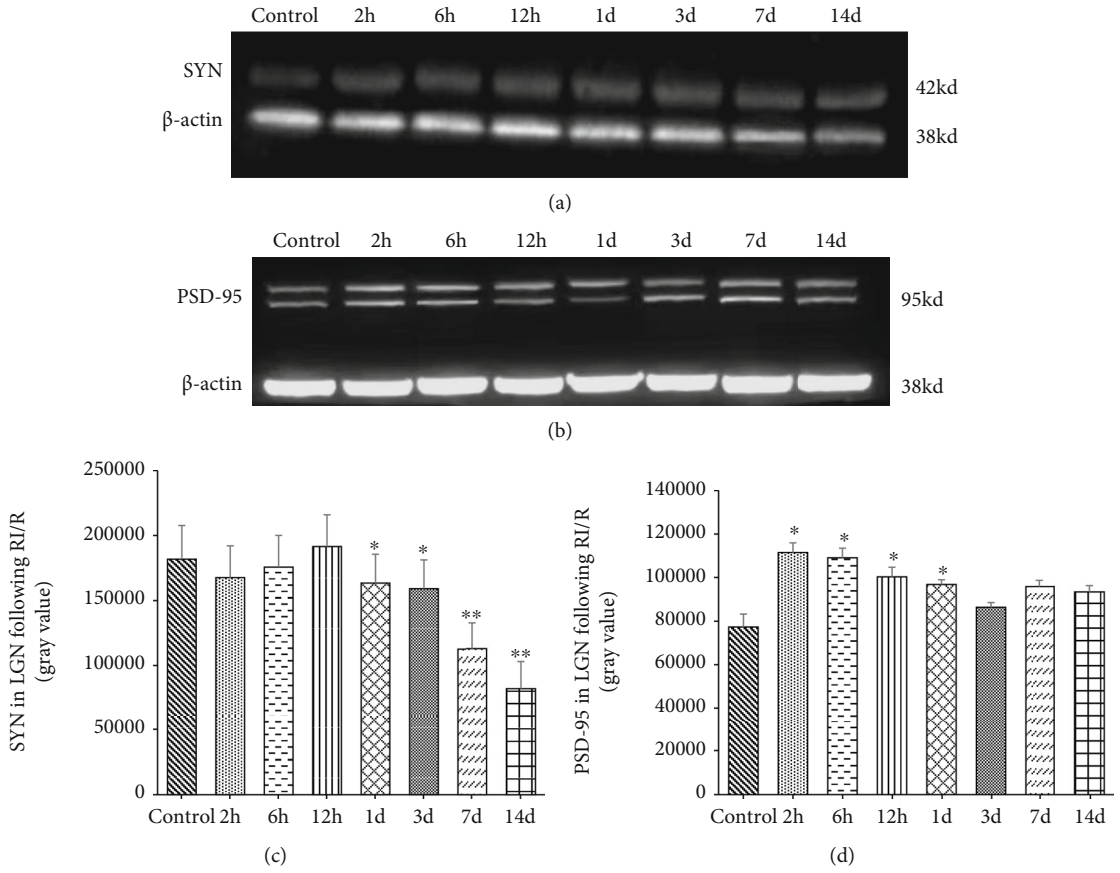

Figure 10: Western blot result of SYN and PSD-95 expression in LGN after RI/R injury. (a) 2 h: rats euthanized 2 hours post-RI/R injury; 6 h: rats euthanized 6 hours post-RI/R injury; 12 h: rats euthanized 12 hours post-RI/R injury; 1 d: rats euthanized 1 day post-RI/R injury; 3 d: rats euthanized 3 days post-RI/R injury; 7 d: rats euthanized 7 days. Synaptophysin (SYN) remains unchanged at 2 hours to 12 hours after RI/R compared to the control group. The SYN expression was significantly reduced in the retina at 1 day to 14 days after RI/R. (b) PSD-95 was significantly increased in the retina at 2 hours to 1 day after RI/R compared to the control group. From 3 days to 14 days, the PSD-95 expression showed a downward trend. (c) Use the Image J analysis software to determine the average gray value of the SYN expression in LGN. (d) Use the Image J analysis software to determine the average gray value of the PSD-95 expression in LGN. $^{*}P < 0.05$ indicates that there were statistical differences when compared with the control groups. $^{**}P < 0.01$ indicates that there were significant statistical differences when compared with the control groups.

mitochondrial hyperplasia and hypertrophy in presynapses (Figure 4(e), Mi). At 7 days after RI/R injury, membranes of the synapses were discontinuous, organelle was lysed, presynaptic vesicles reduced, and the synaptic structure became unclear (Figure 4(f)).

(2) SYN and PSD-95 Expression in dLGN. The resulting Immunofluorescence images revealed that dLGN is spindle-shaped on the coronal section; SYN was fluorescently labeled in red and distributed in the axoplasm of nerve fibers. Retinal termini were stained and present red lines in Figure 9, according to the location of the RGC projections reported in the Claire Bc study [27]. PSD-95 was fluorescently labeled in green and distributed at each axon terminus of nerve fibers like stars. In I/R-6 h, I/R-12 h, and I/R-1d groups, the distribution of retinal termini had no significant changes when compared with control groups (Figure 9, control, I/R 6 h, I/R 12 h, and I/R 1 d). At 7 days to 14 days after injury, discontinuous changes occur in the nerve fibers of dLGN, and the number of nerve fibers was significantly smaller in the same field of view (Figure 9, I/R 7 d and I/R 14 d).

Western blot (WB) analysis showed the expression of these two synaptic active proteins in the whole dLGN. SYN with the molecular weight of 38 kd remained unchanged from 2 hours to 12 hours after injury ($P > 0.05$). Then, from 1 day after the injury, the expression of SYN began to decrease ($P < 0.05$). In I/R-1 d, I/R-3 d, I/R-7 d, and I/R-14 d groups, SYN expression was significantly lower than the control group ($P = 0.017, 0.003, 0.034, 0.001$) (Figures 10(a) and 10(c)). And PSD-95 with a molecular weight of 95 kd was detected to be increased early after injury. From 2 hours to 1 day after the injury, the expression of PSD-95 was significantly higher than the control group ($P = 0.031, 0.022, 0.017, 0.007$). Then, from 1 d after injury, the expression of PSD-95 began to decrease ($P < 0.05$), and this downward trend continued from 1 d to 14 d (Figures 10(b) and 10(d)).

4. Discussion

Transneuronal degeneration has been proved to be associated with the pathological processes of a variety of neurological diseases, including Alzheimer's disease [6], amyotrophic lateral sclerosis [14], and brain trauma [8]. For the visual signal pathway, the significant loss of relay neurons in M and P layers of dLGN connected to the glaucomatous eye [29], which increased linearly with the loss of retinal afferent fibers, while Hendrickson et al. reported neuronal atrophy in dLGN after injury in the visual cortex [30]. These evidences suggest that primary neuron injury visual pathway presents anterograde and retrograde transneuronal degeneration on synaptic-linked distant neurons. It has been demonstrated that intervention measures that only compete against the mechanisms of in situ RGC death cannot satisfactorily recover the degenerated visual function following RI/R. Regrettably, previous research merely focused on preventing RGCs from death [27, 31], while ignoring the transneuronal degeneration following RI/R [32].

Presently, we found that relay cell edema, intracellular mitochondrial proliferation, and the increase in the number of presynaptic vesicles and mitochondria in IPL were emerged in the early stage after RI/R injury (2 hours to 12 hours, RGCs did not appear to be significantly lost). This shows that in the early stage of RI/R injury, abnormal mitochondria after an injury have appeared in the upper and lower neurons of RGCs. As the main place of cell productivity, mitochondria are prone to abnormal ultrastructural changes in the face of pathological factors such as ischemia and hypoxia [33]. The proliferation and hypertrophy of mitochondria are the typical manifestations of increased energy consumption after cell injury. Alexei put forward the lysosome mitochondrial axis-mediated cell death theory in 2010. This theory expounds that the change of mitochondrial membrane permeability can cause the change of lysosome permeability through ROS and/or Bcl-2 family-dependent manner and finally lead to cell death [34]. We found in the late stage after RI/R injury, mitochondrial dissolution in the presynaptic membrane of IPL and OPL also appeared, and then, bipolar and photoreceptor cells began to undergo apoptosis. Based on these experimental evidences, we speculated the early hyperplasia mitochondria may contribute to the apoptosis of bipolar and photoreceptor cells through the lysosomal-mitochondrial axis. This may be the reason for significant alterations in distal neurons after removal of RGC situ damage.

In addition, we observed that in the early stage of RI/R injury, synapses in IPL also showed significant plasticity changes. It is manifested by the formation of new small synapses, the increase in the number of presynaptic vesicles and the widening of the synaptic active band. This indicates that presynaptic structures and functions from the neurons in ONL are flourishing at this time. Previous studies have shown that the early newborn synapses are established rapidly after injury [35]. And by changing the expression level of synaptic active protein [22, 24], adjusting the level of cytokines [19–21], or by changing the content of mitochondria to transmit damage signals [23], the distal neurons are affected. These are the compensatory responses of neurons in early response to injury signals. Park et al. described in the chronic ocular hypertension model that RGCs showed more complex dendritic structure and more axon bundles than the control group 4 weeks after the induction of high intraocular pressure and formed more synaptic connections with bipolar cells [22]. These phenomena suggest that neurons in INL attempt to compensate for postinjury signal transmission by establishing more synaptic connections with RGCs. Interestingly, although the activity of presynaptic-related structures and functions in IPL in the early stage (2 h-12 h) after RI/R injury was observed in this study, there was no significant change in postsynaptic-related structures and functions. We speculate that as the earliest and most severely damaged kind of retinal neurons after RI/R injury (under the electron microscope, vacuolation and dissolution of organelles were observed in the RGCs' cytoplasm in the early stage after injury), the damaged/stressed RGCs could not respond to the increased presynaptic activity of bipolar cells. This asynchronous expression of this synaptic active protein may not only affect the effective signal transmission but also increase the energy consumption of upper neurons in RGCs. This may be one of the important reasons why patients with acute angle-closure glaucoma still have progressive loss of vision after the ocular hypertension injury is relieved. Of course, the mechanisms by which synaptic plasticity changes cause transneuronal degeneration remains to be further explored.

Previous studies reported that the relay cell soma in the LGN after RGC injury in the glaucoma model was atrophied, accompanied by the loss of nerve fibers. We also observed transneuronal changes in LGN in the early postinjury period, which were specifically manifested as neuronal edema, myelinated nerve demyelination, and new synapse formation. RI/R injury affects the transport function of ATP-dependent Na+/K+ pump on the cell membrane [36], which leads to intracellular sodium ion accumulation, cell edema, and volume increase. In this study, it was found that the early edema response was not only limited to neurons in the retina but also involved LGN neurons. Demyelination of myelinated nerves is a typical manifestation of neurodegenerative changes. The mechanism of demyelination involves oxidative stress theory [37], mitochondrial dysfunction theory, and excitotoxin theory [38]. The nerve impulse conduction of myelinated nerve fibers completes the jumping conduction through the adjacent *Nodes of Ranvier*. The thicker the myelin sheath and the longer the nodal body, the faster the conduction velocity. The change in demyelination makes the conduction rate of the nerve fiber significantly reduced [39]. Chang et al. [40] also detected an increase in the level of myelin alkaline protease in LGN after injury in the rat ocular hypertension model and believed that the degree of demyelination of LGN neurons was positively correlated with the degree of retinal damage.

In addition, similar alterations in synaptic active protein also appeared in the synapses between RGCs and relay cells in dLGN in the early stage after injury. Specifically, the expression of postsynaptic component PSD-95 in dLGN increased, while the expression of presynaptic vesicle protein

SYN remained unchanged. Combined with previous studies, we believe that transneuronal degeneration in LGN after RI/R injury is still closely related to the changes in synaptic plasticity. Although the unsynchronous changes of synaptotagmins in LGN are similar to those in IPL, the changes in LGN are symmetrical with those in IPL. Relay cells showed a change process similar to bipolar cells, including the increase of synaptic vesicle protein, the widening of the synaptic active band, and the proliferation and hypertrophy of mitochondria. Evangelho et al. also mentioned that the anterograde axoplasmic transport function of injured RGCs was insufficient, and RGCs were in a state of dysfunction from soma to axon [41]. This may explain why PSD-95, an increased postsynaptic component of relay cells, lacks the response to the presynaptic components of RGCs.

In conclusion, our present study suggests that transneuronal degeneration exists in RI/R injury. Synaptic structures in the retina and LGN probably be associated with transneuronal degeneration through asynchronous changes of active proteins and mitochondrial abnormalities. This transneuronal degeneration may be one of the key reasons for the progressive deterioration of visual function after the injury is removed. By intervening in the early alterations of adjacent neurons and synapses to RGCs after RI/R injury, it will provide a new idea/inspiration for the recovery of visual function after ischemic retinopathy.

Data Availability

The experimental data used to support the findings of this study are included within the article.

Disclosure

Yanyan Fu's current address is Xiangya Hospital, Central South University, Changsha, 410008, Hunan, China.

Conflicts of Interest

The authors declare that they have no competing interests.

Authors' Contributions

Yanyan Fu and Tu Hu contributed equally to this work and are co-first authors.

Acknowledgments

This research was supported by the National Natural Science Foundation of China. The study was also supported by the National Natural Youth Science Foundation of China, "The role of LCN2 induced M1-astrocyte in visual dysfunction following retinal ischemia/reperfusion" (Project number: 81900890, recipient: Tu Hu), the Natural Youth Science Foundation of Hunan Province, "Role of Act-MMP3 regional expression in the selective loss of neurons in ganglion cell layers following retinal ischemia/reperfusion injury" (Project number: 2021JJ40991, recipient: Tu Hu), the China Postdoctoral Science Fund Project (Project number: 2018M643004, recipient: Tu Hu), and the Natural Science Foundation of Hunan Province(Project number: 2021JJ70147, recipient: Dan Wen).

Supplementary Materials

Supplementary Figure 1: stretched retinal image taken by immunofluorescence microscopy (40×). Sampling method for counting RGC numbers per fascicle. Each retina was taken at 5 images at high magnification (400x) visual field in every quadrant (superior, inferior, temporal, and nasal sides) along 1~1.5 mm from the ONH. The mean of 20 images represents the mean density of one stretched retina. *(Supplementary Materials)*

References

[1] G. Minhas, J. Sharma, and N. Khan, "Cellular stress response and immune signaling in retinal ischemia reperfusion injury [J]," *Frontiers in Immunology*, vol. 7, no. 7, p. 444, 2016.

[2] N. N. Osborne, R. J. Casson, J. P. Wood, G. Chidlow, M. Graham, and J. Melena, "Retinal ischemia: mechanisms of damage and potential therapeutic strategies," *Progress in Retinal and Eye Research*, vol. 23, no. 1, pp. 91–147, 2004.

[3] J. García-Campos, A. Villena, F. Díaz, L. Vidal, M. Moreno, and I. Pérez de Vargas, "Morphological and functional changes in experimental ocular hypertension and role of neuroprotective drugs [J]," *Histology and Histopathology*, vol. 22, no. 12, pp. 1399–1411, 2007.

[4] M. Almasieh, Y. Zhou, M. E. Kelly, C. Casanova, and A. Di Polo, "Structural and functional neuroprotection in glaucoma: role of galantamine- mediated activation of muscarinic acetylcholine receptors [J]," *Cell Death & Disease*, vol. 1, 2010.

[5] K. Li, S. Wang, X. Luo et al., "Progressive memory circuit impairments along with Alzheimer's disease neuropathology spread: evidence from in vivo neuroimaging," *Cerebral Cortex*, vol. 30, no. 11, pp. 5863–5873, 2020, PMID: 32537637.

[6] J. H. Su, G. Deng, and C. W. Cotman, "Transneuronal Degeneration in the Spread of Alzheimer's Disease Pathology: Immunohistochemical Evidence for the Transmission of Tau Hyperphosphorylation," *Neurobiology of Disease*, vol. 4, no. 5, pp. 365–375, 1997.

[7] A. Friesacher, L. T. Lopez Torres, C. Valmaggia, R. Rüesch, and M. G. Todorova, "Linking the presence of macular oedema to structural and functional alterations in retinitis pigmentosa," *Klinische Monatsblätter für Augenheilkunde*, vol. 238, no. 4, pp. 418–427, 2021.

[8] A. C. Conti, R. Raghupathi, J. Q. Trojanowski, and T. K. McIntosh, "Experimental brain injury induces regionally distinct apoptosis during the acute and delayed post-traumatic period," *The Journal of Neuroscience*, vol. 18, no. 15, pp. 5663–5672, 1998.

[9] S. Sidek, N. Ramli, K. Rahmat, N. M. Ramli, F. Abdulrahman, and L. K. Tan, "Glaucoma severity affects diffusion tensor imaging (DTI) parameters of the optic nerve and optic radiation," *European Journal of Radiology*, vol. 83, no. 8, pp. 1437–1441, 2014.

[10] J. Lestak, J. Tintera, Z. Svata, L. Ettler, and P. Rozsival, "Glaucoma and CNS. Comparison of fMRI results in high tension and normal tension glaucoma," *Biomedical Papers of the*

Medical Faculty of the University Palacky, Olomouc, Czech Republic, vol. 158, no. 1, pp. 144–153, 2014.

[11] Y. H. Yücel, Q. Zhang, R. N. Weinreb, P. L. Kaufman, and N. Gupta, "Effects of retinal ganglion cell loss on magno-, parvo-, koniocellular pathways in the lateral geniculate nucleus and visual cortex in glaucoma," *Progress in Retinal and Eye Research*, vol. 22, no. 4, pp. 465–481, 2003.

[12] A. J. Weber, H. Chen, W. C. Hubbard, and P. L. Kaufman, "Experimental glaucoma and cell size, density, and number in the primate lateral geniculate nucleus," *Investigative Ophthalmology & Visual Science*, vol. 41, no. 6, pp. 1370–1379, 2000.

[13] Z. Zhang, W. Liu, Y. Huang et al., "NLRP3 deficiency attenuates secondary degeneration of visual cortical neurons following optic nerve injury," *Neuroscience Bulletin*, vol. 36, no. 3, pp. 277–288, 2020.

[14] J. A. Kiernan and A. J. Hudson, "Changes in SIZES of cortical and lower motor NEURONS in amyotrophic lateral sclerosis," *Brain*, vol. 114, no. 2, pp. 843–853, 1991.

[15] A. Fornito, A. Zalesky, and M. Breakspear, "The connectomics of brain disorders," *Nature Reviews. Neuroscience*, vol. 16, no. 3, pp. 159–172, 2015, PMID: 25697159.

[16] R. Linden and V. H. Perry, "Retrograde and anterograde-transneuronal degeneration in the parabigeminal nucleus following tectal lesions in developing rats," *The Journal of Comparative Neurology*, vol. 218, no. 3, pp. 270–281, 1983, PMID: 6886075.

[17] E. J. Kim, J. L. Hwang, S. E. Gaus et al., "Evidence of corticofugal tau spreading in patients with frontotemporal dementia," *Acta Neuropathologica*, vol. 139, no. 1, pp. 27–43, 2020.

[18] M. T. Pallotta, G. Tascini, R. Crispoldi et al., "Wolfram syndrome, a rare neurodegenerative disease: from pathogenesis to future treatment perspectives," *Journal of Translational Medicine*, vol. 17, no. 1, p. 238, 2019.

[19] D. V. Hansen, J. E. Hanson, and M. Sheng, "Microglia in Alzheimer's disease," *The Journal of Cell Biology*, vol. 217, no. 2, pp. 459–472, 2018.

[20] B. Lu, G. Nagappan, and Y. Lu, "BDNF and synaptic plasticity, cognitive function, and dysfunction," *Handbook of Experimental Pharmacology*, vol. 220, pp. 223–250, 2014, PMID: 24668475.

[21] S. Deyama and R. S. Duman, "Neurotrophic mechanisms underlying the rapid and sustained antidepressant actions of ketamine," *Pharmacology, Biochemistry, and Behavior*, vol. 188, p. 172837, 2020.

[22] H. Y. Park, J. H. Kim, and C. K. Park, "Alterations of the synapse of the inner retinal layers after chronic intraocular pressure elevation in glaucoma animal model," *Molecular Brain*, vol. 13, no. 7, p. 53, 2014.

[23] R. H. Fishman, A. Ornoy, and J. Yanai, "Correlated ultrastructural damage between cerebellum cells after early anticonvulsant treatment in mice," *International Journal of Developmental Neuroscience*, vol. 7, no. 1, pp. 15–26, 1989, PMID: 2711866.

[24] L. Zhou, H. Wang, J. Luo et al., "Regulatory effects of inhibiting the activation of glial cells on retinal synaptic plasticity," *Neural Regeneration Research*, vol. 9, no. 4, pp. 385–393, 2014.

[25] O. J. Olajide, I. T. Gbadamosi, E. O. Yawson et al., "Hippocampal degeneration and behavioral impairment during Alzheimer-like pathogenesis involves glutamate excitotoxicity," *Journal of Molecular Neuroscience*, vol. 71, no. 6, pp. 1205–1220, 2021.

[26] J. F. Huang, L. Shang, M. Q. Zhang et al., "Differential neuronal expression of receptor interacting protein 3 in rat retina: involvement in ischemic stress response," *BMC Neuroscience*, vol. 14, p. 16, 2013.

[27] L. Liu, Q. Sun, R. Wang et al., "Methane attenuates retinal ischemia/reperfusion injury via anti-oxidative and anti-apoptotic pathways," *Brain Research*, vol. 1646, pp. 327–333, 2016.

[28] B. T. Kurien and R. H. Scofield, "Western blotting," *Methods*, vol. 38, no. 4, pp. 283–293, 2006.

[29] Y. H. Yucel, Q. Zhang, R. N. Weinreb, P. L. Kaufman, and N. Gupta, "Atrophy of relay neurons in magno- and parvocellular layers in the lateral geniculate nucleus in experimental glaucoma," *Investigative Ophthalmology & Visual Science*, vol. 42, no. 13, pp. 3216–3222, 2001.

[30] A. Hendrickson, C. E. Warner, D. Possin, J. Huang, W. C. Kwan, and J. A. Bourne, "Retrograde transneuronal degeneration in the retina and lateral geniculate nucleus of the V1-lesioned marmoset monkey," *Brain Structure & Function*, vol. 220, no. 1, pp. 351–360, 2015.

[31] J. Yang, N. Yang, J. Luo et al., "Overexpression of S100A4 protects retinal ganglion cells against retinal ischemia-reperfusion injury in mice," *Experimental Eye Research*, vol. 201, article 108281, 2020.

[32] M. You, R. Rong, Z. Zeng, X. Xia, and D. Ji, "Transneuronal degeneration in the brain during glaucoma," *Frontiers in Aging Neuroscience*, vol. 13, article 643685, 2021.

[33] S. J. Annesley and P. R. Fisher, "Mitochondria in health and disease," *Cell*, vol. 8, no. 7, p. 680, 2019.

[34] Y. C. Wong, D. Ysselstein, and D. Krainc, "Mitochondria-lysosome contacts regulate mitochondrial fission via RAB7 GTP hydrolysis," *Nature*, vol. 554, no. 7692, pp. 382–386, 2018.

[35] S. D. Skaper, L. Facci, M. Zusso, and P. Giusti, "Synaptic plasticity, dementia and Alzheimer disease," *CNS & Neurological Disorders Drug Targets*, vol. 16, no. 3, pp. 220–233, 2017, PMID: 28088900.

[36] M. Rahgozar, D. A. Willgoss, G. C. Gobé, and Z. H. Endre, "ATP-dependent K^+ channels in renal ischemia reperfusion injury," *Renal Failure*, vol. 25, no. 6, pp. 885–896, 2003, PMID: 14669848.

[37] S. Ljubisavljevic, "Oxidative stress and neurobiology of demyelination," *Molecular Neurobiology*, vol. 53, no. 1, pp. 744–758, 2016.

[38] H. Lassmann, "Multiple sclerosis pathology," *Cold Spring Harbor Perspectives in Medicine*, vol. 8, no. 3, article a028936, 2018.

[39] R. H. Miller and S. Mi, "Dissecting demyelination," *Nature Neuroscience*, vol. 10, no. 11, pp. 1351–1354, 2007, PMID: 17965654.

[40] S. J. Chang, J. H. Cherng, D. H. Wang, S. P. Yu, N. H. Liou, and M. L. Hsu, "Transneuronal degeneration of thalamic nuclei following middle cerebral artery occlusion in rats," *BioMed Research International*, vol. 2016, 2016.

[41] K. Evangelho, M. Mogilevskaya, M. Losada-Barragan, and J. K. Vargas-Sanchez, "Pathophysiology of primary open-angle glaucoma from a neuroinflammatory and neurotoxicity perspective: a review of the literature," *International Ophthalmology*, vol. 39, no. 1, pp. 259–271, 2019.

Hindawi
Disease Markers
Volume 2021, Article ID 2135942, 6 pages
https://doi.org/10.1155/2021/2135942

Research Article

The Role of Conjunctival Microvasculation Combined with Echocardiography in Evaluating Pulmonary Arterial Hypertension in Systemic Lupus Erythematosus

Jiangbiao Xiong, Shujiao Yu, Ren Liu, Xia Fang, and Rui Wu

The First Affiliated Hospital of Nanchang University, Nanchang 330006, China

Correspondence should be addressed to Rui Wu; tcmclinic@163.com

Received 1 October 2021; Accepted 17 November 2021; Published 26 November 2021

Academic Editor: Ting Su

Objective. To explore the role of conjunctival microvasculation combined with echocardiography in evaluating the prognosis of pulmonary arterial hypertension in systemic lupus erythematosus (SLE-PAH). *Methods*. We prospectively compared the conjunctival microvascular changes in 17 SLE-PAH patients and 34 SLE patients without PAH in our hospital from January 2020 to December 2020, and we observed the characteristics of conjunctival microvascular changes in SLE-PAH patients. We analyzed the correlation between the corresponding conjunctival microvascular changes and cardiopulmonary function and evaluated the predictive value of the vessel density (VD) and the microvascular flow index (MFI) of conjunctival microvasculation combined with echocardiography in SLE-PAH. *Results*. Compared with SLE patients without PAH, the ischemic areas in conjunctival microvasculation were significantly increased in SLE-PAH patients. The VD and MFI of conjunctival microvasculation are significantly correlated with N-terminal prohormone of brain natriuretic peptide and 6-minute walking distance. Combined with the VD and MFI, it can improve the accuracy of echocardiography in assessing the risk of death due to SLE-PAH (94.1% vs. 82.2%). *Conclusion*. The ischemic area, VD, and MFI of conjunctival microvasculation in SLE-PAH patients can indicate the occurrence of severe SLE-PAH and improve the accuracy of echocardiography in evaluating the prognosis of SLE-PAH.

1. Introduction

Systemic lupus erythematosus (SLE) is an autoimmune disease involving multiple organs. Pulmonary arterial hypertension (PAH), one of its serious complications, is difficult to treat and is one of the causes of death due to SLE [1, 2]. Right heart catheterization is the gold standard for the clinical diagnosis and assessment of pulmonary hypertension, but due to its invasiveness and high cost, it is not suitable as a mean of regular evaluation during treatment. Echocardiography is recommended for its simplicity for the indirect diagnosis and dynamic assessment of pulmonary hypertension [3, 4]. However, the consistency of the echocardiography and right heart catheterization results is still controversial [5]. Therefore, looking for more markers to improve the accuracy of the clinical assessment of pulmonary hypertension, early identification of high-risk patients, and timely intervention are essential to improve the prognosis of SLE-PAH patients. A previous study confirmed that conjunctival microvasculation can effectively assess the hypercoagulable or prethrombotic state of SLE [6]. Thus, this study observed the characteristics of conjunctival microvasculation in SLE-PAH patients and evaluated its value combined with echocardiography in the assessment of SLE-PAH.

2. Materials and Methods

2.1. Subjects. Seventeen consecutive SLE-PAH patients who were admitted to the Department of Rheumatology and Immunology of the First Affiliated Hospital of Nanchang

University from January 2020 to December 2020 and a control group of 34 SLE patients without PAH who were hospitalized during the same period were selected based on the matched course of the disease, age, and sex. All patients were evaluated based on the 2019 European League Against Rheumatism/American College of Rheumatology Classification Criteria for Systemic Lupus Erythematosus [7]. Patients with pulmonary hypertension were divided into three groups: low, medium, and high risk according to the 2015 European Guidelines for the diagnosis and risk assessment of pulmonary hypertension [8]. Clinical evaluations, including pulmonary hypertension functional classification, 6-minute walking distance (6MWD), serum uric acid (SUA), N-terminal prohormone of brain natriuretic peptide (NT-proBNP), and red blood cell volume distribution width (RDW), were performed.

2.2. Conjunctival Microvasculation. An SLM-7E digital slit lamp was used to detect conjunctival microvasculation. Each subject rotated their eyeballs up, down, left, and right to fully expose the required observation range. Eight conjunctival microvasculation images were observed and recorded when the binoculars were in four different positions. The observations included the following: ischemic area: more than 3 capillary grid areas without vessels under a 40x microscope; reticulum deformity: the capillaries increase, the mesh decreases, and the dendrites become grid-like; microangioma can be divided into local round, fusiform, cystic dilation, or isolated and scattered around the vessel; and wound spot: vascular blind end-shaped brown, purple, or dark blue material deposition [6]. Bleeding is exudative (fuzzy vessel wall), and there are ruptures (spots, patches) around capillaries. For vessel density (VD) calculation method, the image under a 40x mirror was divided into 16 grids with three horizontal lines and three vertical lines, and the number of lines passing through the grid was calculated and averaged. For microvascular flow index (MFI), the image under a 100x microscope was divided into four directions, and the average was taken after integration. Normal flow was counted as 3 points, sluggish flow was 2 points, intermittent flow was 1 point, and no flow for at least 20 seconds was 0 points [9].

2.3. Echocardiography. A color Doppler ultrasound with a probe frequency of 1.7 ~ 3.4 MHz was used to detect right atrial pressure (RAP), systolic pulmonary artery pressure (sPAP), and tricuspid annular plane systolic excursion (TAPSE) [10].

2.4. Statistical Analysis. SPSS 22.0 was used for data analysis. The *t*-test was used to compare the two sample means conforming to the normal distribution; otherwise, the Mann–Whitney test was used. The chi-square test was used for comparisons between enumeration dates. The Kruskal–Wallis test was used for multigroup comparisons of ranked data. Spearman's test was used for the correlation analysis, and multiple discriminant analysis was used to compare the accuracy of the predictive risk assessment. The difference was statistically significant at $P < 0.05$.

Table 1: Comparisons of the characteristics between SLE-PAH patients and SLE patients without PAH.

Characteristics	SLE-PAH ($n = 17$)	SLE without PAH ($n = 34$)	P value
Female sex, *n* (%)	15 (88%)	31 (91%)	0.625
Age, years ± SD	44.4 ± 14.6	41.7 ± 12.9	0.751
Pleural effusion, *n* (%)	2 (6.7%)	7 (4.7%)	0.646
Raynaud's phenomenon, *n* (%)	17 (56.7%)	48 (32.0%)	0.010*
Oral ulcer, *n* (%)	4 (13.3%)	26 (17.3%)	0.592
Alopecia, *n* (%)	8 (26.7%)	66 (44.0%)	0.078
Rash, *n* (%)	9 (30.0%)	50 (33.3%)	0.723
Pericardial effusion, *n* (%)	6 (20.0%)	2 (1.3%)	≈0.00*
Lupus nephritis, *n* (%)	5 (16.7%)	30 (20.0%)	0.674
Cytopenia, *n* (%)	3 (10.0%)	6 (4.0%)	0.169
Elevated ESR, *n* (%)	19 (63.3%)	80 (53.3%)	0.315
Low C3, *n* (%)	26 (86.7%)	114 (76.0%)	0.200
Low C4, *n* (%)	23 (76.7%)	103 (68.7%)	0.383
Anti-dsDNA antibody, *n* (%)	18 (60.0%)	62 (41.3%)	0.060
LA, *n* (%)	24 (80.0%)	66 (44.0%)	≈0.00*
ACA, *n* (%)	17 (56.7%)	13 (8.7%)	≈0.00*
Conjunctival microvasculation			
Ischemic areas, *n* (%)	6 (35.3%)	5 (14.7%)	0.042*
Reticulum deformity, *n* (%)	4 (23.5%)	13 (38.2)	0.233
Microangioma, *n* (%)	8 (47.1%)	7 (41.2)	0.101
Twisting, *n* (%)	16 (94.1%)	27 (79.4)	0.242
Dilation, *n* (%)	8 (47.1%)	24 (70.6)	0.131
Wound spot, *n* (%)	13 (76.5)	17 (50)	0.081
Hemorrhage, *n* (%)	5 (29.4%)	6 (17.6)	0.472

SD: standard deviation; ESR: erythrocyte sedimentation rate; LA: lupus anticoagulant; ACA: anticardiolipin antibodies. *$P < 0.05$.

3. Results

3.1. Comparison of the Characteristics between SLE Patients with and without PAH. Comparison of the clinical data showed that Raynaud's phenomenon, pericardial effusion, and positive rates of antiphospholipid antibodies in SLE-PAH patients were significantly higher than those in SLE patients without PAH. Conjunctival microvasculation in all patients with SLE had various manifestations, such as twisting, dilation, ischemia, hemorrhage, reticular malformation, and wound spots. Among them, conjunctival vasodilation, vascular distortion, and injury points were the most common, followed by ischemic areas, reticulum deformity, hemorrhage, and microangioma. The incidence of SLE-PAH ischemic areas was significantly higher than that of SLE patients without PAH ($P < 0.05$) (Table 1).

Table 2: Correlation between VD and MFI of conjunctival microvasculation and SLE-PAH-related parameters.

			sPAP	NT-proBNP	6MWD	SUA	RDW	RAP	TAPSE
Spearman's rho	VD	Correlation coefficient	-0.441	-0.528*	0.574*	-0.560*	-0.323	-0.637**	0.539*
		Sig. (2-tailed)	0.076	0.029	0.016	0.019	0.306	0.006	0.026
	MFI	Correlation coefficient	-0.537*	-0.546*	0.504*	-0.350	-0.305	-0.689**	0.683**
		Sig. (2-tailed)	0.026	0.023	0.039	0.168	0.335	0.002	0.003

VD: vessel density; MFI: microvascular flow index; sPAP: systolic pulmonary artery pressure; NT-proBNP: N-terminal prohormone of brain natriuretic peptide; 6MWD: 6-minute walking distance; SUA: serum uric acid; RDW: red blood cell volume distribution width; RAP: right atrial pressure; TAPSE: tricuspid annular plane systolic excursion. $^{*}P < 0.05$, $^{**}P < 0.01$.

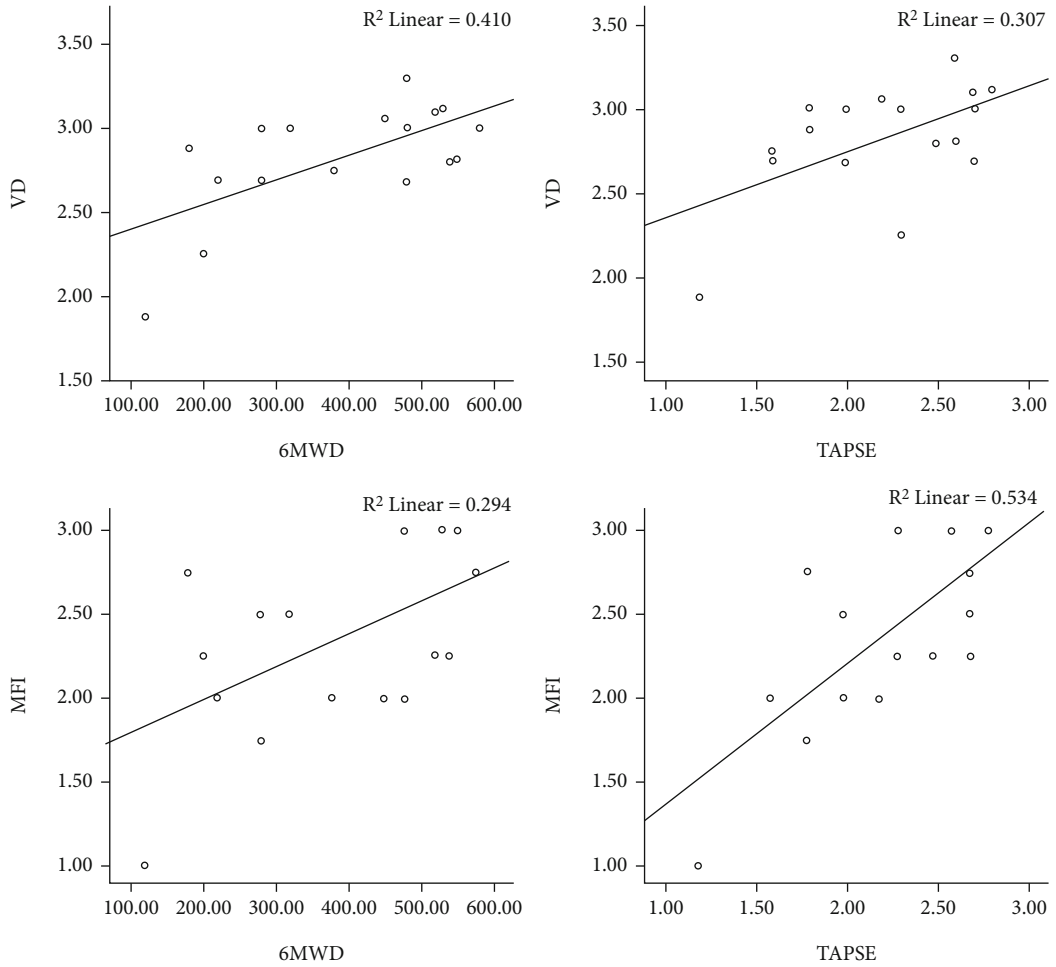

Figure 1: Scatter plot of the correlation analysis of VD, MFI, 6MWD, and TAPSE.

3.2. Correlation between VD and MFI of Conjunctival Microvasculation and SLE-PAH-Related Parameters. Spearman correlation analysis indicated that VD was significantly negatively correlated with NT-proBNP, UA, and RAP; meanwhile, MFI was significantly negatively correlated with NT-proBNP, sPAP, and RAP. In addition, VD and MFI were positively correlated with 6MWD and TAPSE, respectively (Table 2, Figure 1).

3.3. Comparison of the Parameters between Different Risk Groups and Discriminant Analysis. According to the risk assessment in pulmonary arterial hypertension in the 2015 ESC/ERS guidelines for the diagnosis and treatment of pulmonary hypertension, SLE-PAH patients were divided into low risk, intermediate risk, and high risk groups. The results suggested that TAPSE, NT-proBNP, VD, and MFI were significantly different in the three risk groups, but there was no significant difference in terms of sPAP, RDW, RAP, and SUA. Multivariate discriminant analysis revealed that the accuracy of the echocardiographic parameters, PAH, RAP, and TAPSE for PAH risk assessment was 82.4%, and the accuracy after combining VD and MFI could be increased to 94.1% (Table 3, Figure 2).

Table 3: Comparison of the parameters between different risk groups.

Parameters	Low risk ($n = 7$)	Intermediate risk ($n = 7$)	High risk ($n = 3$)	P value$^{\triangle}$
sPAP (mmHg)	32.0 ± 8.0	59.8 ± 31.2	61.5 ± 9.2	0.23
TAPSE (cm)	2.7 ± 0.1	2.1 ± 0.4	1.4 ± 0.3	0.012*
RAP (mmHg)	5.8 ± 1.5	8.2 ± 3.7	15 ± 0	0.147
NT-proBNP (pg/mL)	247.8 ± 250.1	1456.5 ± 719.8	5418.5 ± 2617	0.003*
SUA (ummol/L)	430.8 ± 117.9	436.7 ± 92.3	518.5 ± 89.8	0.67
RDW (%)	15.4 ± 2.3	21.7 ± 10.2	18.5 ± 1.7	0.315
VD (n/mm^2)	2.7 ± 0.3	2.3 ± 0.2	1.7 ± 0.4	0.006*
MFI	2.8 ± 0.4	2.3 ± 0.3	1.5 ± 0.7	0.019*
Conjunctival microvascular changes	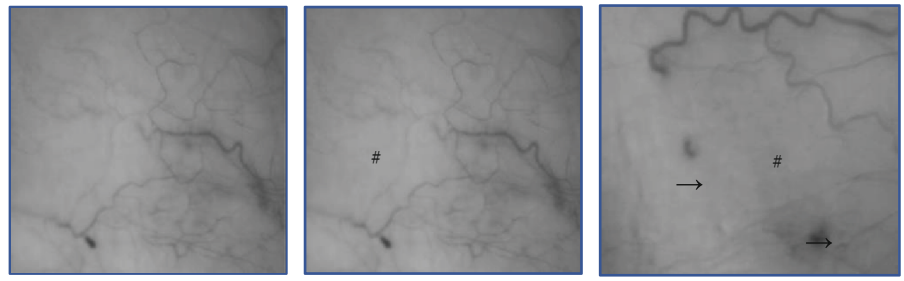			

sPAP: systolic pulmonary artery pressure; TAPSE: tricuspid annular plane systolic excursion; RAP: right atrial pressure; NT-proBNP: N-terminal prohormone of brain natriuretic peptide; SUA: serum uric acid; RDW: red blood cell volume distribution width; VD: vessel density; MFI: microvascular flow index. *$P < 0.05$. △ Kruscal-Wallis test; # ischemic areas; ⟶ microangioma.

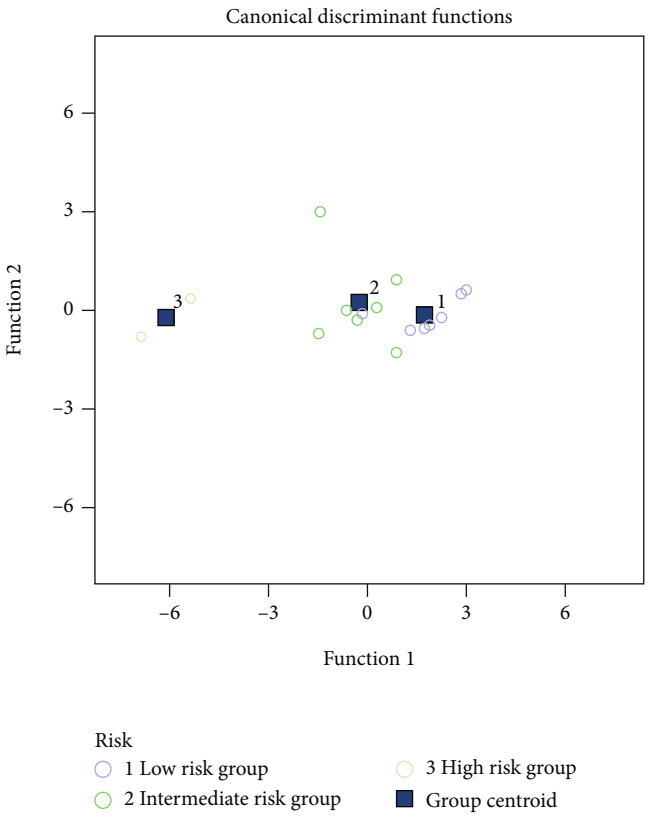

Figure 2: Discriminant analysis of the echocardiography combined with VD and MFI in three groups of patients with different risk stratifications.

4. Discussion

Systemic lupus erythematosus is an autoimmune disease that often occurs in women of childbearing age. Studies have shown that SLE-PAH is one of the most important causes of death in SLE patients following neuropsychiatric lupus and lupus nephritis. In particular, severe PAH has a very poor prognosis, and most of the late deaths are due to progressive heart and lung failure [11]. Early recognition and treatment of pulmonary hypertension, regular assessment and treatment of the standard, and control of pulmonary hypertension to a low-risk state are currently important treatment strategies for pulmonary hypertension [12–14]. Effective and accurate assessment of pulmonary hypertension is an indispensable part in the standard treatment [15].

Microcirculation refers to the blood circulation between arterioles and venules. It is the peripheral part of the circulatory system and an important place for the exchange of substances between blood and tissue cells. The conjunctiva is a common site for detecting systemic microcirculation, which is less affected by external temperature, is closer to the changes in visceral microcirculation, and can better reflect diseases of the visceral vessels [16]. Pulmonary hypertension can cause increased right heart load, reduced pulmonary flow, and mismatched ventilation and perfusion, resulting in tissue ischemia and hypoxia, and affect peripheral microcirculation through oxidative stress and vasoconstriction [17]. The local microvessels of the conjunctiva are significantly reduced, and the capillaries are closed, showing a state of disconnection, disappearance, local paleness, and even the appearance of ischemic areas, which are the manifestations of severe microcirculation disorders. This study showed that

6 (35.3%) patients in the SLE-PAH group had ischemic areas, all of whom had moderate to severe pulmonary hypertension. The incidence of ischemia was significantly higher than that of lupus patients without PAH (35.3% versus 14.7%, $P = 0.042$), which suggested that the ischemic areas were features of conjunctival microvasculation in SLE patients with severe pulmonary hypertension. By observing the VD and MFI of conjunctival microvasculation through a slit lamp at a magnification of 40-100 times, we found that the VD and MFI were significantly correlated with NT-proBNP and 6MWD ($P < 0.05$), suggesting that the changes in VD and MFI might be related to decreased cardiopulmonary function. Importantly, this study also found that the VD and MFI of conjunctival microvasculation could improve the accuracy of echocardiographic-related parameters in assessing the risk of pulmonary hypertension.

Invasive hemodynamic monitoring of pulmonary hypertension has certain risks, high technical requirements, and high costs, and it is not suitable for long-term repeated use [18]. The ultrasound parameters of the risk assessment in pulmonary arterial hypertension in the 2015 ESC/ERS guidelines included only RAP and the right atrium area [8]. However, this study found that compared with RAP, TAPSE showed more significant changes in different risk groups, which suggested that it might have more advantages in the risk assessment of SLE-PAH [19–21].

The study has several limitations. First, when conjunctival microcirculation is detected, involuntary movements of the eyeball will cause instability in image acquisition and affect the accuracy of the data. Second, the sample size of SLE-PAH patients was not large enough. In the future, a larger sample will be needed for the verification of these findings.

5. Conclusion

This study proposes a new method for evaluating the prognosis of SLE-PAH. The ischemic area, VD, and MFI of conjunctival microcirculation combined with echocardiography can improve the accuracy of risk assessment of PAH in SLE.

Data Availability

The data used to support the findings of this study will be available from the corresponding author upon reasonable request.

Conflicts of Interest

The authors declare that there are no conflicts of interest.

Authors' Contributions

Jiangbiao Xiong and Shujiao Yu contributed equally to this work.

References

[1] L. J. Chen, H. C. Chang, and L. Y. Lu, "Prolonged survival after single lung transplantation for pulmonary hypertension secondary to systemic lupus erythematosus," *Journal of the Chinese Medical Association*, vol. 67, no. 5, pp. 248–251, 2004.

[2] Y. Fei, X. Shi, F. Gan et al., "Death causes and pathogens analysis of systemic lupus erythematosus during the past 26 years," *Clinical Rheumatology*, vol. 33, no. 1, pp. 57–63, 2014.

[3] E. Bossone, A. D'Andrea, M. D'Alto et al., "Echocardiography in pulmonary arterial hypertension: from diagnosis to prognosis," *Journal of the American Society of Echocardiography*, vol. 26, no. 1, pp. 1–14, 2013.

[4] L. M. Wright, N. Dwyer, D. Celermajer, L. Kritharides, and T. H. Marwick, "Follow-up of pulmonary hypertension with echocardiography," *JACC: Cardiovascular Imaging*, vol. 9, no. 6, pp. 733–746, 2016.

[5] J. D. Rich, S. J. Shah, R. S. Swamy, A. Kamp, and S. Rich, "Inaccuracy of Doppler echocardiographic estimates of pulmonary artery pressures in patients with pulmonary hypertension: implications for clinical practice," *Chest*, vol. 139, no. 5, pp. 988–993, 2011.

[6] R. Wu, "Role of eye's sign in patients with neuropsychiatric disorders of systemic lupus erythematosus," *Rheumatology International*, vol. 34, no. 4, pp. 583–586, 2014.

[7] M. Aringer, K. Costenbader, D. Daikh et al., "2019 European League Against Rheumatism/American College of Rheumatology classification criteria for systemic lupus erythematosus," *Arthritis & Rhematology*, vol. 71, no. 9, pp. 1400–1412, 2019.

[8] N. Galiè, M. Humbert, J.-L. Vachiery et al., "2015 ESC/ERS guidelines for the diagnosis and treatment of pulmonary hypertension: the joint task force for the diagnosis and treatment of pulmonary hypertension of the European Society of Cardiology (ESC) and the European Respiratory Society (ERS): endorsed by: Association for European Paediatric and Congenital Cardiology (AEPC), International Society for Heart and Lung Transplantation (ISHLT)," *European Heart Journal*, vol. 37, no. 1, pp. 67–119, 2016.

[9] D. De Backer, S. Hollenberg, C. Boerma et al., "How to evaluate the microcirculation: report of a round table conference," *Critical Care (London, England)*, vol. 11, no. 5, p. R101, 2007.

[10] K. Tello, J. Wan, A. Dalmer et al., "Validation of the Tricuspid Annular Plane Systolic Excursion/Systolic Pulmonary Artery Pressure Ratio for the Assessment of Right Ventricular-Arterial Coupling in Severe Pulmonary Hypertension," *Circulation: Cardiovascular Imaging*, vol. 12, no. 9, article e009047, 2019.

[11] A. Dhala, "Pulmonary arterial hypertension in systemic lupus erythematosus: current status and future direction," *Clinical & Developmental Immunology*, vol. 2012, article 854941, pp. 1–12, 2012.

[12] A. Boucly, J. Weatherald, L. Savale et al., "Risk assessment, prognosis and guideline implementation in pulmonary arterial hypertension," *European Respiratory Journal*, vol. 50, no. 2, p. 1700889, 2017.

[13] W.-C. Huang, C.-H. Hsu, S.-H. Sung et al., "2018 TSOC guideline focused update on diagnosis and treatment of pulmonary arterial hypertension," *Journal of the Formosan Medical Association*, vol. 118, no. 12, pp. 1584–1609, 2019.

[14] M. M. Hoeper, H. J. Bogaard, R. Condliffe et al., "Definitions and diagnosis of pulmonary hypertension," *Journal of the American College of Cardiology*, vol. 62, no. 25, pp. D42–D50, 2013.

[15] N. Galiè, R. N. Channick, R. P. Frantz et al., "Risk stratification and medical therapy of pulmonary arterial hypertension," *European Respiratory Journal*, vol. 53, no. 1, p. 1801889, 2019.

[16] A. Prabu, K. Patel, C.-S. Yee et al., "Prevalence and risk factors for pulmonary arterial hypertension in patients with lupus," *Rheumatology (Oxford, England)*, vol. 48, no. 12, pp. 1506–1511, 2009.

[17] S. Dimopoulos, G. Tzanis, C. Manetos et al., "Hyperoxia affects peripheral tissue microcirculation in patients with pulmonary arterial hypertension," *Critical Care*, vol. 16, no. S1, p. P206, 2012.

[18] M. D'Alto, K. Dimopoulos, J. G. Coghlan, G. Kovacs, S. Rosenkranz, and R. Naeije, "Right heart catheterization for the diagnosis of pulmonary hypertension: controversies and practical issues," *Heart Failure Clinics*, vol. 14, no. 3, pp. 467–477, 2018.

[19] S. Alerhand and S. M. Hickey, "Tricuspid annular plane systolic excursion (TAPSE) for risk stratification and prognostication of patients with pulmonary embolism," *Journal of Emergency Medicine*, vol. 58, no. 3, pp. 449–456, 2020.

[20] T. Dutta and W. S. Aronow, "Echocardiographic evaluation of the right ventricle: clinical implications," *Clinical Cardiology*, vol. 40, no. 8, pp. 542–548, 2017.

[21] S. Saeed, J. Smith, K. Grigoryan, V. Lysne, R. Rajani, and J. B. Chambers, "The tricuspid annular plane systolic excursion to systolic pulmonary artery pressure index: association with all-cause mortality in patients with moderate or severe tricuspid regurgitation," *International Journal of Cardiology*, vol. 317, pp. 176–180, 2020.

Hindawi
Disease Markers
Volume 2021, Article ID 3015238, 7 pages
https://doi.org/10.1155/2021/3015238

Research Article

Machine Learning Classification of Mild Traumatic Brain Injury Using Whole-Brain Functional Activity: A Radiomics Analysis

Xiaoping Luo,[1] **Dezhao Lin**,[2] **Shengwei Xia**,[1] **Dongyu Wang**,[1] **Xinmang Weng**,[1] **Wenming Huang**,[1] **and Hongda Ye**[1]

[1]*Department of Radiology, Wenzhou Chinese Medicine Hospital, Wenzhou, 325000 Zhejiang, China*
[2]*Department of Emergency, Wenzhou Chinese Medicine Hospital, Wenzhou, 325000 Zhejiang, China*

Correspondence should be addressed to Xiaoping Luo; wzluoxp@163.com

Received 9 September 2021; Accepted 2 November 2021; Published 18 November 2021

Academic Editor: Ting Su

Objectives. To investigate the classification performance of support vector machine in mild traumatic brain injury (mTBI) from normal controls. *Methods*. Twenty-four mTBI patients (15 males and 9 females; mean age, 38.88 ± 13.33 years) and 24 age and sex-matched normal controls (13 males and 11 females; mean age, 40.46 ± 11.4 years) underwent resting-state functional MRI examination. Seven imaging parameters, including amplitude of low-frequency fluctuation (ALFF), fractional amplitude of low-frequency fluctuation (fALFF), regional homogeneity (ReHo), degree centrality (DC), voxel-mirrored homotopic connectivity (VMHC), long-range functional connectivity density (FCD), and short-range FCD, were entered into the classification model to distinguish the mTBI from normal controls. *Results*. The ability for any single imaging parameters to distinguish the two groups is lower than multiparameter combinations. The combination of ALFF, fALFF, DC, VMHC, and short-range FCD showed the best classification performance for distinguishing the two groups with optimal AUC value of 0.778, accuracy rate of 81.11%, sensitivity of 88%, and specificity of 75%. The brain regions with the highest contributions to this classification mainly include bilateral cerebellum, left orbitofrontal cortex, left cuneus, left temporal pole, right inferior occipital cortex, bilateral parietal lobe, and left supplementary motor area. *Conclusions*. Multiparameter combinations could improve the classification performance of mTBI from normal controls by using the brain regions associated with emotion and cognition.

1. Introduction

Traumatic brain injury (TBI), a major public health problem and a leading cause of disability, affects half the world's population [1]. Approximately 70%-90% of TBI patients are mild TBI (mTBI), and 30-40% of whom cannot fully recover even at 6 months postinjury [1, 2]. Patients with mild head injury often manifest as dizziness, headache, and memory and attention deficit, which was considered to be associated with abnormal changes of brain networks [3]. Recently, functional and structural neuroimaging methods have been widely used to address the functional and morphological changes of mTBI [4–11]. Zhou et al. found abnormal functional connectivity within the default mode network in mTBI patients, which was associated with cognitive neurological dysfunction and posttraumatic symptoms (i.e., depression, anxiety, fatigue, and postconcussion syndrome) [12]. Nakamura et al. found that mTBI was associated with changes in the "small world" networks [13]. Zhan et al. found decreased ReHo value in the left insula, left pre-/postcentral gyrus, and left supramarginal gyrus in mTBI patients [14]. However, the potential neurobiological mechanism of the mTBI left unclear.

Most current studies focus attentions on investigating group differences between two different labels (knowing the classes of all subject before statistics); however, group-based methods cannot classify different types for individual classification and are not sensitive for feature selection [15]. Support vector machine (SVM) classifier is an efficient and sensitive neuroimaging biological indicator for feature selection and classification. There is a growing application of the SVM algorithm into several diseases, such as insomnia [16, 17], epilepsy [15], and autistic spectrum disorder [18]. However, the mTBI has not been studied. Differences in

Table 1: Demographic and clinical features of patients with acute mTBI and healthy controls.

	mTBI	Healthy controls	t value	p value
Age, years	38.88 ± 13.33	40.46 ± 11.40	-0.442	0.66
Sex (male, female)	24 (15, 9)	24 (13, 11)	0.343	0.558
Education, years	8.88 ± 3.58	8.54 ± 3.41	0.330	0.743
Postinjury, days	3.58 ± 3.28	N/A	N/A	N/A
GCS	14.42 ± 0.88	N/A	N/A	N/A
DRS	2.58 ± 2.36	N/A	N/A	N/A
MAS	44.38 ± 5.86	N/A	N/A	N/A
ABS	14.42 ± 0.78	N/A	N/A	N/A
HAMA	3.83 ± 3.61	0.08 ± 0.28	5.077	<0.001
MMSE	29.04 ± 1.63	29.83 ± 0.20	-2.284	0.03
ADL	21.71 ± 8.07	14.04 ± 6.06	4.654	<0.001
BDI	1.58 ± 1.91	0.08 ± 0.28	3.808	0.001

brain regions in mTBI were not the same when we analyzed the between-group differences by different neuroimaging methods, which may be associated with the sensitivity of different methods in searching features (brain areas). Therefore, we hypothesized that the combination of different neuroimaging methods may improve the sensitivity for feature selection. To address these hypotheses, the present study is the first to apply the SVM algorithm to perform the classification for mTBI.

2. Materials and Methods

2.1. Subjects. This case-control study comprised 170 subjects from our hospital between May 2014 and May 2021, among whom a total of 146 subjects were excluded, including 139 subjects unmatched diagnosis with mTBI, 4 mTBI with more than 1.5 mm maximum translation in x, y, or z directions and/or 1.5 degree of motion rotation, and 3 mTBI with missing data. Finally, 24 patients with acute mTBI (15 males and 9 females; mean age, 38.88 ± 13.33 years; mean years of education, 8.88 ± 3.58 years; and mean time of postinjury, 3.58 ± 3.28 days) and 24 age and sex-matched (13 males and 11 females; mean age, 40.46 ± 11.4 years; and mean years of education, 8.54 ± 3.41 years) healthy controls were included. All subjects were asked to complete the following questionnaires, including the Glasgow Coma Scale (GCS), Disability Rating Scale (DRS), Motor Assessment Scale (MAS), Agitated Behavior Scale (ABS), Hamilton Anxiety Scale (HAMA), Clinical Dementia Rating (CDR), Mini Mental State Examination (MMSE), Activates of Daily Living (ADL), and Beck Depression Inventory (BDI).

Inclusion criteria for patients with acute mTBI were as follows: (a) have a diagnosis of mTBI within two weeks, (b) age between 18 and 65 years, (c) time of lack of consciousness less than 30 min, and (d) time of posttraumatic amnesia less than 24 hours. Exclusion criteria for patients with acute mTBI were as follows: (a) involvement in litigation, (b) a history of psychiatric disorders, (c) a history of addiction, and (d) a history of traumatic brain injury. This study was approved by the Human Research Ethics Committee in accordance with the Declaration of Helsinki, and written informed consent was obtained.

2.2. MRI Parameters. MRI data were acquired with a clinical 3-Tesla MRI scanner (Trio Tim, SIEMENS, Erlangen, Germany), including T1WI, T2WI, T2-FLAIR, high-resolution T1WI, functional MRI, and SWI. A total of 176 three-dimensional high-resolution anatomical T1-weighted volumes were acquired in a sagittal orientation (rapid-gradient-echo sequence, repetition time = 1900 ms, echo time = 2.26 ms, thickness = 1.0 mm, matrix = 256 × 256, and field of view = 240 mm × 240 mm). For functional images, a total of 250 volumes (Echo-Planar Imaging pulse sequence, 30 transverse slices, repetition time = 2000 ms, echo time = 40 ms, thickness = 4.0 mm, matrix = 64 × 64, field of view = 240 mm × 240 mm, and flip angle 90°) were acquired.

2.3. Data Processing. All functional MRI data preprocessing were performed with DPABI (version 2.1, http://rfmri.org/DPABI) toolbox. First, the first ten volumes were deleted, and the remaining volumes were converted their data format. The following steps of slice timing, head motion correction, spatial normalization, smooth (Gaussian kernel of $8 \times 8 \times 8\,mm^3$), linear regression of possible spurious covariates, linearly detrended, and temporally band-pass filtered (0.01-0.1 Hz) were performed for data preprocessing. After the step of head motion correction, a "head motion scrubbing regressors" procedure was implemented, and the subjects who had more than 1.5 degree of motion rotation and/or 1.5 mm maximum translation in x, y, or z directions were excluded. Furthermore, the head motion effect was regressed out with Friston 24 head motion parameter model. During the step of spatial normalization, all data were spatially normalized to Montreal Neurological Institute (MNI) space and resampled at a resolution of $3 \times 3 \times 3\,mm^3$.

2.4. Feature Selection and Binary Classification. We calculated seven MRI parameters, including ALFF, fALFF, ReHo, degree centrality, long-term FCD, short-term FCD, and VMHC. The maps of MRI parameters were segmented into

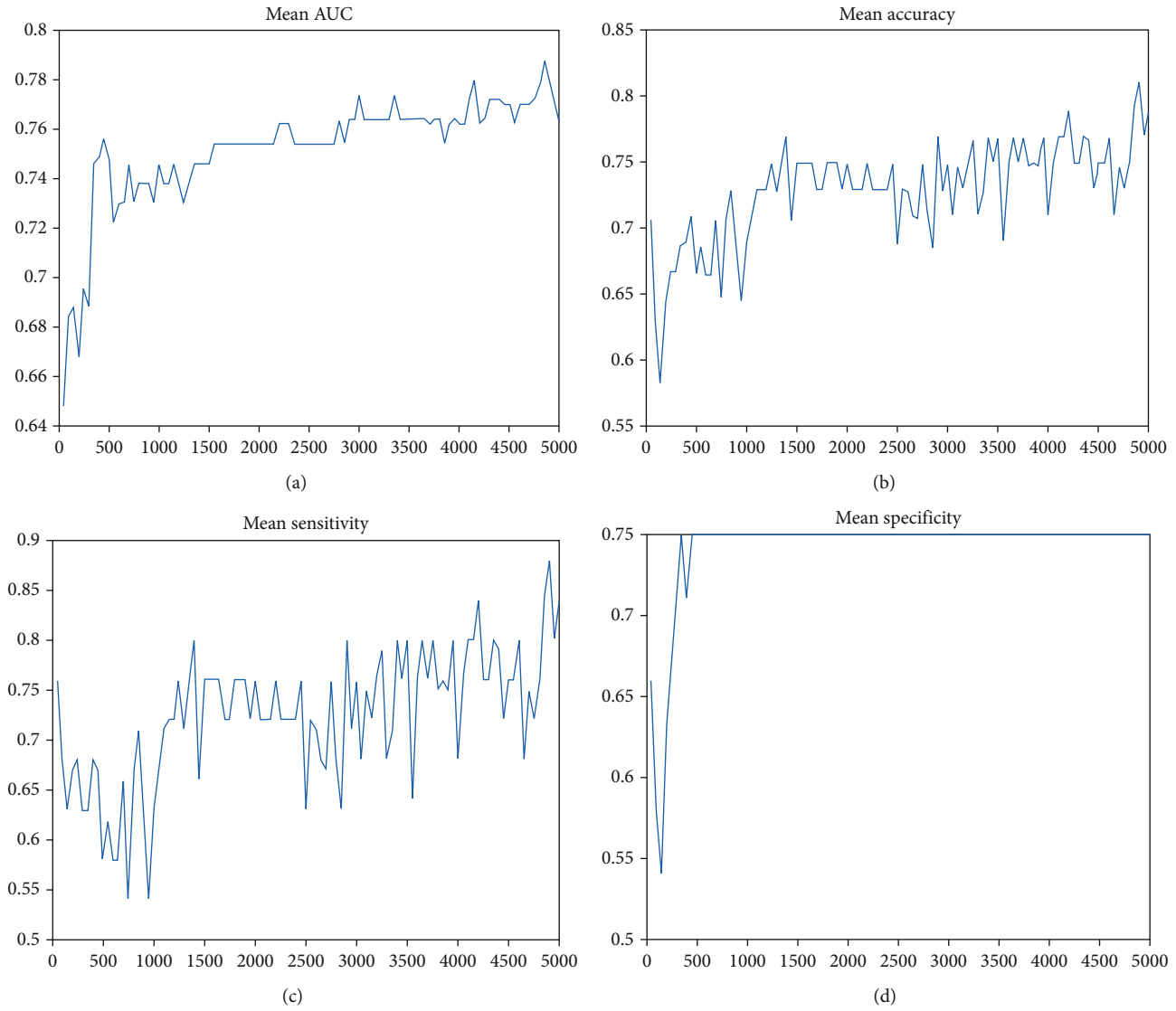

Figure 1: Schematic diagram overview of machine learning classification framework. Note: this figure shows the classification of the combination of ALFF, fALFF, DC, VMHC, and short-term FCD in distinguishing the mTBI from the normal controls. The classification received the highest (a) AUC value, (b) classification accuracy, (c) sensitivity, and (d) specificity among all combination.

116 regions of interest (ROIs) using the automated anatomical labeling (AAL) atlas. The total of 812 features was extracted in the following classification with multivariate pattern analysis (MVPA).

We used a LIBSVM toolbox (http://www.csie.ntu.edu.tw/~cjlin/libsvm/) to perform the classification, and a 5-fold cross-validation was used to validate the classification performance of the classifier. Permutation test was used to evaluate the probability of the classification performance for 5000 times randomly. The clusters of brain regions with higher than 70% of classification accuracy were considered as accuracies. The area under curve (AUC), sensitivity, and specificity of the classifier were quantified.

2.5. Statistical Analyses. Comparisons of demographic factors were performed using two-sample t-tests. Chi-square (χ^2) test was used for categorical data. Statistical analysis was performed using IBM SPSS 21.0 version. Data are presented as mean ± standard deviation. All the quoted results are two-tailed values, and $p < 0.05$ was considered as statistically significant.

3. Results

3.1. Sample Characteristics. There were no significant differences in mean age ($t = -0.442$, $p = 0.66$), sex ($\chi^2 = 0.343$, $p = 0.558$), and educational level ($t = 0.33$, $p = 0.743$) between the healthy controls and patients with mTBI. Compared with healthy controls, patients with mTBI had higher HAMA score ($t = 5.077$, $p < 0.001$), ADL score ($t = 4.654$, $p < 0.001$), and BDI score ($t = 3.808$, $p = 0.001$), and a lower MMSE score ($t = -2.284$, $p = 0.03$). The mean time between injury and MRI examination of patients with mTBI was 3.58 ± 3.28 days. The mean GCS score, DRS score,

Table 2: Weight ranking of the 116 brain regions to the classification of the combination with ALFF, fALFF, DC, VMHC, and short-term FCD.

	ROI weight	Voxel size
Vermis_10	1.948	34
Cerebellum_9_R	1.470	156
Cerebellum_10_L	1.465	40
Cerebellum_9_L	1.455	158
Frontal_Mid_Orb_L	1.417	224
Frontal_Sup_Orb_L	1.398	280
Cuneus_L	1.353	472
Cerebellum_Crus2_R	1.329	539
Cerebellum_7b_L	1.265	98
Cerebellum_Crus2_L	1.257	543
Frontal_Mid_Orb_L	1.256	273
Temporal_pole_Mid_L	1.222	177
Occipital_Inf_R	1.220	316
Parietal_Sup_L	1.136	575
Paracentral_lobule_R	1.134	221
Frontal_Sup_R	1.118	1120
Cuneus_R	1.117	416
Cerebellum_Crus1_R	1.103	723
Occipital_Inf_L	1.103	263
Vermis_7	1.102	54
Calcarine_L	1.076	649
Occipital_Sup_R	1.074	407
Rectus_L	1.070	258
Postcentral_R	1.055	1050
Paracentral_lobule_L	1.053	340
Precentral_R	1.009	941
Parietal_Inf_R	1.008	397
Occipital_Sup_L	0.998	373
Cerebellum_10_R	0.997	37
Cerebellum_7b_R	0.975	78
Cerebellum_8_L	0.961	303
Cerebellum_6_L	0.960	524
Vermis_9	0.959	50
Temporal_Inf_R	0.959	1076
Occipital_Mid_L	0.954	947
Cerebellum_Crus1_L	0.950	725
Lingual_L	0.945	662
Supp_motor_area_L	0.937	630
Frontal_Mid_R	0.931	1448
Calcarine_R	0.925	528
Temporal_Mid_L	0.922	1437
Parietal_Sup_R	0.921	569
Cerebellum_4_5_L	0.919	352
Frontal_Sup_medial_L	0.918	847
Lingual_R	0.916	683
Angular_R	0.916	511
Temporal_pole_Sup_R	0.918	325
Cerebellum_6_R	0.908	532
Precuneus_R	0.908	927
Temporal_Sup_R	0.907	942
Frontal_Sup_L	0.890	987
Angular_L	0.860	341
Precuneus_L	0.851	1008
Cingulum_post_L	0.850	111
Frontal_Inf_Tri_L	0.848	675
Frontal_Mid_L	0.847	1323
Temporal_pole_Sup_L	0.828	329
Temporal_Sup_L	0.825	694
Temporal_pole_Mid_R	0.822	264
Cerebellum_8_R	0.810	298
Cerebellum_3_R	0.801	65
Occipital_Mid_R	0.796	578
Supp_motor_area_R	0.790	695
Vermis_4_5	0.788	176
Frontal_Sup_medial_R	0.787	589
Frontal_Inf_Tri_R	0.783	560
Supramarginal_R	0.779	562
Precentral_L	0.764	931
Heschl_R	0.763	60
Frontal_Mid_Orb_R	0.762	296
Frontal_Sup_Orb_R	0.752	296
Frontal_Inf_Orb_L	0.752	504
Cerebellum_3_L	0.750	42
Supramarginal_L	0.750	357
Fusiform_L	0.747	665
Temporal_Inf_L	0.745	948
Vermis_1_2	0.738	9
Rectus_R	0.728	208
Parietal_Inf_L	0.723	687
Cerebellum_4_5_R	0.719	239
Frontal_Inf_Oper_R	0.715	396
Caudate_L	0.703	270
Postcentral_L	0.702	1069
Fusiform_R	0.688	759
Pallidum_L	0.685	76
Vermis_6	0.675	87
Amygdala_L	0.672	63
Putamen_L	0.660	280
Frontal_Inf_Orb_R	0.660	498
Frontal_Mid_Orb_R	0.657	271
Vermis_8	0.652	60
Insula_R	0.646	497
Rolandic_Oper_L	0.645	301
Cingulum_Mid_L	0.635	579
Olfactory_L	0.632	80

Table 2: Continued.

	ROI weight	Voxel size
Thalamus_R	0.631	296
Frontal_Inf_Oper_L	0.628	309
Parahippocampal_L	0.624	298
Pallidum_R	0.621	67
Cingulum_Ant_R	0.621	385
Temporal_Mid_R	0.619	1311
Cingulum_Ant_L	0.598	425
Thalamus_L	0.596	280
Cingulum_Mid_R	0.574	612
Vermis_3	0.549	62
Rolandic_Oper_R	0.548	404
Heschl_L	0.548	72
Olfactory_R	0.538	88
Cingulum_post_R	0.522	69
Caudate_R	0.511	287
Parahippocampal_R	0.506	318
Hippocampus_L	0.493	279
Amygdala_R	0.474	73
Insula_L	0.465	545
Putamen_R	0.436	309
Hippocampus_R	0.411	282

MAS score, and ABS score in patients with mTBI were 14.42 ± 0.88, 2.58 ± 2.36, 44.38 ± 5.86, and 14.42 ± 0.78, respectively. The details are shown in Table 1.

3.2. Classification Performance. First, we compared the classification performances of the seven MRI parameters and found they could not differentiate well between healthy controls and patients with mTBI (AUC: 0.66 ± 0.03, range, 0.61~0.69; accuracy rate: $66.4\% \pm 3.4\%$, range, 60.2%~70.9%; sensitivity: $64.1\% \pm 7.9\%$, range, 49.0%~75.0%; and specificity: $68.4\% \pm 5.6\%$, range, 61.0%~75.0%). Second, we combined these MRI parameters and found the features with the highest contributions to the classification to discriminate between mTBI and healthy controls. We found that the combination with ALFF, fALFF, DC, VMHC, and short-term FCD significantly reached up the classification accuracy, sensitivity, and specificity and received the highest classification performances among all combination with classification accuracy of 81.1% ($p < 0.001$), sensitivity of 88.0% ($p < 0.001$), and specificity of 75.0% ($p < 0.001$) (Figure 1).

3.3. Consensus Features and Region Weight. In this study, all consensus features were mapped to AAL116 template (116 brain regions), and each of the 116 brain regions was given a weight value which indicates the contribution to classification model. For the combination with ALFF, fALFF, DC, VMHC, and short-term FCD, Table 2 shows the weight ranking of the 116 brain regions from highest to lowest.

Among the 116 brain regions, a total of 51 brain regions showed higher contributions to the classification than the average weight value (contribution), including the bilateral cerebellum, left orbitofrontal cortex, left cuneus, left temporal pole, right inferior occipital gyrus, bilateral parietal lobe, and left supplementary motor area (Table 2).

4. Discussion

In this case-control study, we documented two novel findings. First, we developed an SVM classifier that was a useful neuroimaging biomarker for mTBI classification. We found that the combination with ALFF, fALFF, DC, VMHC, and short-term FCD received the highest classification performances among all combination (accuracy = 81.1%, sensitivity = 88.0%, and specificity = 75.0%). Second, the consensus brain regions with the highest contributions to classification were located in the bilateral cerebellum, left orbitofrontal cortex, left cuneus, left temporal pole, right inferior occipital gyrus, bilateral parietal lobe, and left supplementary motor areas (contribution above the average value among 116 brain regions).

Our study is the first to apply the SVM classifier to find a promising model for mTBI classification. Although several previous studies have offered insights into brain functional and structural abnormalities of mTBI using traditional group-level statistical differences based on one single imaging method, they could not be translated into predictive or diagnostic neurobiological biomarkers for mTBI. The emergence of radiomics has broadened the scope of routine medical imaging, which carried multimodality medical information to reflect the development and progression of diseases [19, 20]. Machine learning classification based on the radiomics strategy allows detecting subtle, nonstrictly localized effects that may remain invisible to the conventional analysis with univariate statistics [21, 22], which are being increasingly used in functional MRI data [15, 16]. These findings could explain the high classification performance of the SVM classifier.

Cerebellum is associated with emotion, motor, and advanced cognitive function [23]. The cerebellum anterior lobe is associated with sensorimotor function, and the cerebellum posterior lobe is associated with the regulation of coordinating movement, balance and sleep, and emotional changes [24–28]. Brain volume atrophy and reduction of metabolism functional activity can be found in subjects after TBI [29–31]. Peskind et al. found that soldiers with mTBI showed reduction of glucose metabolism in the cerebellar vermis, cerebellar hemisphere, and pons and functional deficits in attention, language, and working memory [31]. In addition, cerebellar activation was also significantly reduced during auditory-related task stimulation [30]. These studies suggest that the cerebellum plays an important role in the neuropathological basis of mTBI, which supports our findings of high contributions of the cerebellum to the SVM classifier.

The prefrontal lobe is one of the brain areas that are most vulnerable to the mTBI. Even minor brain damage can easily cause a damage of the frontal lobe. Studies have found that abnormal functional changes in the frontal lobe are one of the neural mechanisms of emotional numbness, attention, planning, high alertness, and psychological avoidance in patients with posttraumatic injury [32–34]. Keightley et al.

found that adolescents with mTBI showed weaker working memory and language function and reduced brain activity in supplementary motor areas, dorsolateral prefrontal lobe, and superior parietal lobe than that of healthy adolescents [35]. Pardini et al. and Jantzen et al. found that parietal lobe and orbitofrontal cortex are associated with severity of mTBI and postconcussion symptoms [36, 37]. Our findings support these studies. Therefore, the abnormal functional changes in the frontal-parietal lobe may be associated with the posttraumatic injury severity and symptoms, which contribute to the high contributions to the SVM classifier.

Abnormal functional connectivity between temporal pole and parietal lobe and decreased glucose metabolism in these two areas were found in mTBI patients relative to normal controls [31, 38, 39]. The temporal pole is closely related to the functions such as social interaction, face recognition, semantic memory, mental speculation, and emotion and is responsible for the synthesis of complex and finely processed perceptual input of internal emotions [40]. The abnormal function of the temporal pole in mTBI patients will help us understand the biological mechanism of daily life disorders of mTBI.

5. Conclusions

In this study, we developed an SVM classifier that can be severed as a promising sensitive neuroimaging biomarker for mTBI classification based on a combination of multiple imaging indicators. Our analysis using the model showed that the bilateral cerebellum, left orbitofrontal cortex, left cuneus, left temporal pole, right inferior occipital gyrus, bilateral parietal lobe, and left supplementary motor areas exhibited the highest contributions to the classification model. These findings may expand our understanding of the neurobiological mechanism of mTBI. However, there are several limitations that should be addressed. First, the sample size of our study was relatively small. A larger number of sample sizes and multiple center studies are necessary to corroborate our findings. Second, the data of subacute mTBI and follow-up were scarce. Third, this study only used SVM to perform the classification, and other classification methods should be introduced to compare their performances. Fourth, location and size of the lesion, disease of severity, and subtype of mild traumatic brain injury were not considered in the classification.

Data Availability

The data that support the findings of this study are available from the corresponding author upon reasonable request.

Conflicts of Interest

The authors of this manuscript declare no relationships with any companies, whose products or services may be related to the subject matter of the article.

Authors' Contributions

X.L., D.L., S.X., and D.W. conceived and designed the whole experiment; X.W., W.H., and H.Y. collected the data; X.L., D.L., and H.Y. take responsibility for the integrity of the data, the accuracy of the data analysis, and the statistical data analysis; X.L. wrote the main manuscript text and undertook the critical interpretation of the data. All authors contributed to the final version of the paper and have read, as well as, approved the final manuscript.

Acknowledgments

This work was supported by the Zhejiang Provincial Medical and Health Science and Technology Project (grant No. 2017KY632).

References

[1] A. I. R. Maas, D. K. Menon, P. D. Adelson et al., "Traumatic brain injury: integrated approaches to improve prevention, clinical care, and research," *The Lancet Neurology*, vol. 16, no. 12, pp. 987–1048, 2017.

[2] P. McMahon, A. Hricik, J. K. Yue et al., "Symptomatology and functional outcome in mild traumatic brain injury: results from the prospective TRACK-TBI study," *Journal of Neurotrauma*, vol. 31, no. 1, pp. 26–33, 2014.

[3] S. M. Slobounov, M. Gay, K. Zhang et al., "Alteration of brain functional network at rest and in response to YMCA physical stress test in concussed athletes: RsFMRI study," *NeuroImage*, vol. 55, no. 4, pp. 1716–1727, 2011.

[4] H. J. van der Horn, M. E. Scheenen, M. E. de Koning, E. J. Liemburg, J. M. Spikman, and J. van der Naalt, "The default mode network as a biomarker of persistent complaints after mild traumatic brain injury: a longitudinal functional magnetic resonance imaging study," *Journal of Neurotrauma*, vol. 34, no. 23, pp. 3262–3269, 2017.

[5] Z. Wang, M. Zhang, C. Sun et al., "Single mild traumatic brain injury deteriorates progressive interhemispheric functional and structural connectivity," *Journal of Neurotrauma*, vol. 38, no. 4, pp. 464–473, 2021.

[6] K. Braeckman, B. Descamps, and C. Vanhove, "Advanced diffusion imaging in the hippocampus of rats with mild traumatic brain injury," *Journal of Visualized Experiments: JoVE*, vol. 150, 2019.

[7] D. F. Tate, M. Gusman, J. Kini et al., "Susceptibility weighted imaging and white matter abnormality findings in service members with persistent cognitive symptoms following mild traumatic brain injury," *Military Medicine*, vol. 182, no. 3, pp. e1651–e1658, 2017.

[8] S. Rosenthal, M. Gray, H. Fatima, H. I. Sair, and C. T. Whitlow, "Functional MR imaging: blood oxygen level-dependent and resting state techniques in mild traumatic brain injury," *Neuroimaging Clinics of North America*, vol. 28, no. 1, pp. 107–115, 2018.

[9] E. D. Bigler, "Volumetric MRI findings in mild traumatic brain injury (mTBI) and neuropsychological outcome," *Neuropsychology Review*, pp. 1–37, 2021.

[10] N. S. Dailey, R. Smith, J. R. Vanuk, A. C. Raikes, and W. D. S. Killgore, "Resting-state functional connectivity as a biomarker

of aggression in mild traumatic brain injury," *Neuroreport*, vol. 29, no. 16, pp. 1413–1417, 2018.

[11] V. C. Rausa, J. Shapiro, M. L. Seal et al., "Neuroimaging in paediatric mild traumatic brain injury: a systematic review," *Neuroscience and Biobehavioral Reviews*, vol. 118, pp. 643–653, 2020.

[12] Y. Zhou, M. P. Milham, Y. W. Lui et al., "Default-mode network disruption in mild traumatic brain injury," *Radiology*, vol. 265, no. 3, pp. 882–892, 2012.

[13] T. Nakamura, F. G. Hillary, and B. B. Biswal, "Resting network plasticity following brain injury," *PLoS One*, vol. 4, no. 12, article e8220, 2009.

[14] J. Zhan, L. Gao, F. Zhou et al., "Decreased regional homogeneity in patients with acute mild traumatic brain injury: a resting-state fMRI study," *The Journal of Nervous and Mental Disease*, vol. 203, no. 10, pp. 786–791, 2015.

[15] X. J. Dai, Q. Xu, J. Hu et al., "BECTS substate classification by granger causality density based support vector machine model," *Frontiers in Neurology*, vol. 10, p. 1201, 2019.

[16] X. J. Dai, B. X. Liu, S. Ai et al., "Altered inter-hemispheric communication of default-mode and visual networks underlie etiology of primary insomnia: altered inter-hemispheric communication underlie etiology of insomnia," *Brain Imaging and Behavior*, vol. 14, no. 5, pp. 1430–1444, 2020.

[17] C. Li, Y. Mai, M. Dong et al., "Multivariate pattern classification of primary insomnia using three types of functional connectivity features," *Frontiers in Neurology*, vol. 10, p. 1037, 2019.

[18] C. Ecker, V. Rocha-Rego, P. Johnston et al., "Investigating the predictive value of whole-brain structural MR scans in autism: a pattern classification approach," *NeuroImage*, vol. 49, no. 1, pp. 44–56, 2010.

[19] V. Kumar, Y. Gu, S. Basu et al., "Radiomics: the process and the challenges," *Magnetic Resonance Imaging*, vol. 30, no. 9, pp. 1234–1248, 2012.

[20] P. Lambin, E. Rios-Velazquez, R. Leijenaar et al., "Radiomics: extracting more information from medical images using advanced feature analysis," *European Journal of Cancer*, vol. 48, no. 4, pp. 441–446, 2012.

[21] K. A. Norman, S. M. Polyn, G. J. Detre, and J. V. Haxby, "Beyond mind-reading: multi-voxel pattern analysis of fMRI data," *Trends in Cognitive Sciences*, vol. 10, no. 9, pp. 424–430, 2006.

[22] J. D. Haynes and G. Rees, "Decoding mental states from brain activity in humans," *Nature Reviews. Neuroscience*, vol. 7, no. 7, pp. 523–534, 2006.

[23] L. F. Koziol, D. Budding, N. Andreasen et al., "Consensus paper: the cerebellum's role in movement and cognition," *Cerebellum*, vol. 13, no. 1, pp. 151–177, 2014.

[24] J. D. Schmahmann, "Disorders of the cerebellum: ataxia, dysmetria of thought, and the cerebellar cognitive affective syndrome," *The Journal of Neuropsychiatry and Clinical Neurosciences*, vol. 16, no. 3, pp. 367–378, 2004.

[25] C. J. Stoodley and J. D. Schmahmann, "Functional topography in the human cerebellum: a meta-analysis of neuroimaging studies," *NeuroImage*, vol. 44, no. 2, pp. 489–501, 2009.

[26] X. J. Dai, H. H. Gong, Y. X. Wang et al., "Gender differences in brain regional homogeneity of healthy subjects after normal sleep and after sleep deprivation: a resting-state fMRI study," *Sleep Medicine*, vol. 13, no. 6, pp. 720–727, 2012.

[27] X. J. Dai, X. Nie, X. Liu et al., "Gender differences in regional brain activity in patients with chronic primary insomnia: evidence from a resting-state fMRI study," *Journal of Clinical Sleep Medicine*, vol. 12, no. 3, pp. 363–374, 2016.

[28] X. J. Dai, D. C. Peng, H. H. Gong et al., "Altered intrinsic regional brain spontaneous activity and subjective sleep quality in patients with chronic primary insomnia: a resting-state fMRI study," *Neuropsychiatric Disease and Treatment*, vol. 10, pp. 2163–2175, 2014.

[29] G. K. Spanos, E. A. Wilde, E. D. Bigler et al., "Cerebellar atrophy after moderate-to-severe pediatric traumatic brain injury," *AJNR. American Journal of Neuroradiology*, vol. 28, no. 3, pp. 537–542, 2007.

[30] Z. Yang, R. A. Yeo, A. Pena et al., "An FMRI study of auditory orienting and inhibition of return in pediatric mild traumatic brain injury," *Journal of Neurotrauma*, vol. 29, no. 12, pp. 2124–2136, 2012.

[31] E. R. Peskind, E. C. Petrie, D. J. Cross et al., "Cerebrocerebellar hypometabolism associated with repetitive blast exposure mild traumatic brain injury in 12 Iraq war Veterans with persistent post-concussive symptoms," *NeuroImage*, vol. 54, Suppl 1, pp. S76–S82, 2011.

[32] G. P. Lee, K. J. Meador, D. W. Loring et al., "Neural substrates of emotion as revealed by functional magnetic resonance imaging," *Cognitive & Behavioral Neurology Official Journal of the Society for Behavioral & Cognitive Neurology*, vol. 17, no. 1, p. 9, 2004.

[33] J. D. Bremner, L. H. Staib, D. Kaloupek, S. M. Southwick, R. Soufer, and D. S. Charney, "Neural correlates of exposure to traumatic pictures and sound in Vietnam combat veterans with and without posttraumatic stress disorder: a positron emission tomography study," *Biological Psychiatry*, vol. 45, no. 7, pp. 806–816, 1999.

[34] B. C. McDonald, L. A. Flashman, and A. J. Saykin, "Executive dysfunction following traumatic brain injury: neural substrates and treatment strategies," *NeuroRehabilitation*, vol. 17, no. 4, pp. 333–344, 2002.

[35] M. L. Keightley, R. S. Saluja, J. K. Chen et al., "A functional magnetic resonance imaging study of working memory in youth after sports-related concussion: is it still working?," *Journal of Neurotrauma*, vol. 31, no. 5, pp. 437–451, 2014.

[36] J. E. Pardini, D. A. Pardini, J. T. Becker et al., "Postconcussive symptoms are associated with compensatory cortical recruitment during a working memory task," *Neurosurgery*, vol. 67, no. 4, pp. 1020–1027, 2010.

[37] K. J. Jantzen, B. Anderson, F. L. Steinberg, and J. A. Kelso, "A prospective functional MR imaging study of mild traumatic brain injury in college football players," *AJNR. American Journal of Neuroradiology*, vol. 25, no. 5, pp. 738–745, 2004.

[38] A. A. Vakhtin, V. D. Calhoun, R. E. Jung, J. L. Prestopnik, P. A. Taylor, and C. C. Ford, "Changes in intrinsic functional brain networks following blast-induced mild traumatic brain injury," *Brain Injury*, vol. 27, no. 11, pp. 1304–1310, 2013.

[39] O. Bonne, A. Gilboa, Y. Louzoun et al., "Cerebral blood flow in chronic symptomatic mild traumatic brain injury," *Psychiatry Research*, vol. 124, no. 3, pp. 141–152, 2003.

[40] I. R. Olson, A. Plotzker, and Y. Ezzyat, "The enigmatic temporal pole: a review of findings on social and emotional processing," *Brain*, vol. 130, Part 7, pp. 1718–1731, 2007.

Hindawi
Disease Markers
Volume 2021, Article ID 5866267, 6 pages
https://doi.org/10.1155/2021/5866267

Research Article

Association between Iris Biological Features and Corneal Biomechanics in Myopic Eyes

Lin Fu,[1] **Qi Dai**,[1] **Pengzhi Zhu**,[2] **Xu Jia**,[1] **Fangjun Bao**,[1] **Xiaoyu Chen**,[3] **Yana Fu**,[1] **Hengli Lian**,[1] **Weihua Yang**,[4] **and Yufeng Ye**[1]

[1]*School of Ophthalmology and Optometry, Eye Hospital, Wenzhou Medical University, Wenzhou 325027, China*
[2]*Guangdong Medical Devices Quality Surveillance and Test Institute, Guangzhou 510663, China*
[3]*Wenzhou Medical University, Wenzhou 325027, China*
[4]*Affiliated Eye Hospital, Nanjing Medical University, Nanjing 210029, China*

Correspondence should be addressed to Weihua Yang; benben0606@139.com and Yufeng Ye; yeyufeng2000@126.com

Received 24 September 2021; Accepted 5 November 2021; Published 18 November 2021

Academic Editor: Ting Su

Purpose. Iris biological features such as surface features and profile characteristics reflected the development of iris stroma and microvessels. Iris vessels and microcirculation are still lack of effective detection methods, and we can directly observe only the iris surface biological characteristics. This cross-sectional study evaluated the association between iris surface biological features and corneal biomechanics in young adults with myopia. *Methods*. We recruited 152 patients with myopia aged ≥18 years, from the Eye Hospital of Wenzhou Medical University, who had complete Corneal Visualization Scheimpflug Technology (Corvis ST) data and graded iris surface features. Iris surface features included crypts, furrows, and color measured from digital slit lamp images. The biomechanical properties of the cornea were assessed using Corvis ST. Only 1 eye of each participant was randomly selected for analysis. Associations between the iris surface features and corneal biomechanics were analyzed using linear regression models. The grade of iris crypts, furrows, and color and corneal biomechanical parameters measured with Corvis ST was the main outcome measures. *Results*. The iris crypts were significantly associated with deflection amplitude at the first applanation (A1 DLA, $\beta = 0.001$, $P = 0.013$), A1 delta arc length (A1 dArcL) ($\beta = -0.001$, $P = 0.01$), maximum delta arc length (dArcLM) ($\beta = -0.004$, $P = 0.03$), and stiffness at the first applanation (SP-A1) ($\beta = -2.092$, $P = 0.016$). The iris furrows were only associated with integrated radius ($\beta = -0.212$, $P = 0.025$). Iris color was found not related with corneal biomechanical parameters measured via Corvis ST. *Conclusions*. Iris surface features were associated with corneal biomechanical properties in myopic eyes; more iris crypts were associated with lower corneal stiffness while more extensive furrows were related with higher corneal stiffness. Iris crypts and furrows may provide useful information on corneal biomechanical properties in myopic eyes.

1. Introduction

Cornea is an important part of the refractive system of the human eye, and its refractive power accounts for more than 3/4 of the whole refractive system. Laser corneal refractive surgery can correct ametropia by cutting the corneal stroma to change the curvature of the anterior surface. Refractive surgery for myopia will reduce the number of central corneal lamellar and change the structure and biomechanical properties of cornea [1]. Different cutting methods and depths have different effects, which may affect the predictability of surgery and the occurrence of complications such as refractive regression and keratectasia [2, 3]. Therefore, the biomechanical properties of the cornea play an important role in the maintenance of the cornea shape and the design of refractive surgery, especially in the diagnosis of some latent corneal diseases such as keratoconus and other keratectasia before refractive surgery. Sufficient evaluation of the corneal biomechanical properties has a strong guiding significance for the safety of refractive surgery.

Noninvasive measures of corneal biomechanics in vivo mainly include electronic speckle pattern interferometry

(ESPI), ocular response analyzer (ORA), and Corneal Visualization Scheimpflug Technology (Corvis ST, Oculus, Wetzlar, Germany). [4] However, in China, only a few refractive surgery centers have the equipment to examine the corneal biomechanics. In the absence of such equipments, doctors cannot determine the patient's corneal biomechanical properties initially. Cornea is also part of the outmost layer of the eyeball, and the corneal biomechanics was reported to have relationship with the elasticity of the sclera, lamina cribrosa, and peripapillary ring [4]. So far, as we know, the expansions in the inner ocular tissue, particularly the iris, are less studied. The iris has a variety of biological features such as intuitive surface features and profile morphological characteristics of iris stroma and microvessels. All these characteristics reflect the development of iris stroma and vascular circulation. Iris blood vessels and microcirculation still lack of effective detection methods, and we can directly observe only the iris surface biological characteristics.

A grading system was recently established to evaluate the iris surface features, including iris crypts, furrows, and color that are observable under a slit lamp. [5] However, the role of iris surface features in ocular function and their associations with other ocular tissues are yet to be fully elucidated. Chua et al. [6] speculated that as crypts surrogate iris stroma, iris having more crypts is more compressible. Thus, iris crypts may be related with iris biomechanics. Nevertheless, to date, the human iris biomechanics has not been measured in vivo.

As part of cornea and iris are of mesodermal origin, we postulate that the iris biomechanics is related with corneal biomechanics [7, 8]. No modality is currently available to directly measure iris biomechanics in humans. Exploring the relationship between the corneal biomechanical properties and iris features may improve the safety of refractive surgeries. Iris surface features, which can be examined under a slit lamp, have been suggested to be associated with iris biomechanics. Thus, this study is aimed at exploring the relationships of iris surface features including iris crypts, furrows, and color with corneal biomechanics.

2. Methods

2.1. Participants. This prospective study recruited Chinese refractive surgery candidates aged older than 18 years. Participants with ocular pathology other than refractive error were excluded. A simple randomization method was used to select the left eye or the right eye based on a randomized number table according to the order the participants that were recruited.

Approval was obtained from the Institutional Review Board (IRB) of Wenzhou Medical University (IRB approval number: 2020-128-K-113), and the study was conducted according to the tenets of the Declaration of Helsinki. Written informed consent was obtained from all participants.

2.2. Ocular Examinations. All participants underwent standard detailed ophthalmic examinations including slit lamp examination, manifest refraction measurement (spherical equivalence, [SE]), and best corrected distance visual acuity. All examinations were performed by an experienced ophthalmologist. The patients also underwent corneal tomography with the Pentacam (Oculus, Wetzlar, Germany), anterior chamber depth (ACD) measurement using the IOL-Master (Carl Zeiss Meditec, Jena, Germany), and biomechanical property assessment using the Corvis ST (Oculus, Wetzlar, Germany).

2.3. Iris Photography and Grading. Iris photography was performed with reference to the procedure by Sidhartha et al. [5] Briefly, the color iris images of both eyes were taken using a slit lamp digital camera (DC3; Topcon, Tokyo, Japan) at ×16 magnification in a dark room (20 lux) without flash. The images were captured under an illumination of 45° temporally and a brightness of 30% maximum light beam with a width of >20 mm and height of 14 mm.

The iris crypts and furrows were graded as follows (Figure 1): iris crypts were categorized into 5 grades as grade 1, no crypts; grade 2, 1-3 crypts, grade 3, at least 4 crypts with a diameter < 1 mm; grade 4, at least 4 crypts with a diameter > 1 mm; and grade 5, numerous crypts with a diameter > 1 mm, nearly covering the whole iris. Meanwhile, furrows were categorized into three grades based on circumferential extent and the number of furrows: grade 1, no furrows; grade 2, less than 5 furrows and the extent was ≤180°; and grade 3, at least 5 furrows present, and the extent was ≥180°. The iris color was also graded according to Sidhartha's criteria in which darker iris was given higher grades [5]. Iris color was divided into 5 grades, but no patient in this study manifested grade 5 iris color.

2.4. Corvis ST Measurement. The corneal biomechanical properties were assessed using the Corvis ST following a standard procedure described previously [9]. A rapid air puff was released to the cornea to induce corneal deformation. Dynamic corneal deformation was recorded using a high-speed Scheimpflug camera with full corneal cross-sections. The camera can capture 4330 frames per second and 140 sequential horizontal images with a range of 8.5 mm. The parameters of corneal dynamic response were calculated with a recording measurement time of 30 ms. The biomechanical corrected intraocular pressure (bIOP) was also generated using Corvis ST. The measurements were regarded as reliable when an "OK" quality score was displayed on the device monitor.

The biomechanical parameters measured with Corvis ST recorded were IOP; bIOP; maximum DA (DA max) at the first applanation; time at the highest concavity (HC time); time at the first and second applanation (A1 time and A2 time, respectively); corneal velocity at the first and second applanation (A1 velocity and A2 velocity, respectively); DA; deflection length (DLL); deflection amplitude (DLA) and delta arc length (dArcL) at A1, HC, and A2; PD, radius, and maximum deflection amplitude at the first applanation (DLA max); maximum delta arc length (dArcLM); maximum inverse radius (max inverse radius); maximum DA ratio (DA ratio max) at 2 mm and 1 mm; central corneal thickness (CCT); integrated radius; and SP-A1.

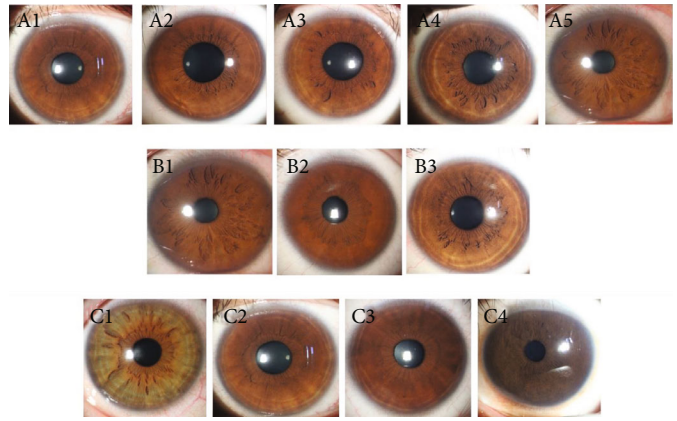

Figure 1: Representative photographs used in grading the iris surface features. A1-A5: grade 1 to grade 5 iris crypts. B1-B3: grade 1 to grade 3 iris furrows. C1 to C4: grade 1 to grade 4 iris color. No grade 5 iris color was observed in this study.

2.5. Statistical Analyses. The associations between corneal biomechanical parameters measured with Corvis ST (dependent variable) and iris surface features (independent variable) were assessed using linear regression models. Model 1 was adjusted for age and sex, and model 2 was further adjusted for potential confounders including ACD, CCT, and bIOP. All statistical analyses were performed using SPSS version 23.0 software (SPSS for Windows, IBM Corp., Armonk, NY, USA). A P value <0.05 was considered statistically significant.

3. Results

After excluding 27 patients due to poor quality of iris photography ($n = 7$), unreliable Corvis measurements ($n = 9$), and IOP higher than 21 mmHg ($n = 11$), 152 patients were included in the final analyses. Table 1 shows the demographic and ocular characteristics of the participants. The mean age was 25.21 ± 5.93 years, and 39.5% were female. The mean refraction (SE) was −5.75 ± 2.39 D. With respect to the grade of the iris surface features, only 1 eye (0.7%) showed grade 5 iris crypts, and most patients had grade 1 (34.2%) and grade 2 (40.8%) features. The distribution of the iris furrows showed a reverse pattern: only 10 eyes (6.6%) were grade 1, and 103 eyes (67.8%) were grade 3. Table 2 shows the mean values of the corneal biomechanical parameters measured via Corvis ST.

The association between the iris surface features and corneal biomechanical parameters is shown in Table 3. After controlling the age and sex, the crypt grade was positively correlated with the A1 DLA ($\beta = 0.001$, $P = 0.014$) and negatively correlated with A1 dArcL ($\beta = -0.001$, $P = 0.017$). Similarly, a higher iris crypt grade remained significantly associated with larger A1 DLA ($\beta = 0.001$, $P = 0.013$) and shorter A1 dArcL ($\beta = -0.001$, $P = 0.01$) after adjusting for additional covariates including ACD, CCT, and bIOP. Moreover, higher iris crypt grades were associated with smaller SP-A1 ($\beta = -2.092$, $P = 0.016$) which represents corneal stiffness and dArcLM ($\beta = -0.004$, $P = 0.03$) as well. Iris furrows were only associated with integrated radius after adjustment for ACD, CCT, and bIOP. With the increasing of iris furrows, the integrated radius ($\beta = -0.212$, $P = 0.025$) decreased. No association was found between the iris color and corneal biomechanical parameters measured via Corvis ST.

4. Discussion

The role of iris surface features in ocular function and their associations with other ocular tissues are yet to be clarified. The distribution of iris surface features varies by age, race, and gender [10]. Therefore, in this study, we focus our target population on young myopes who are refractive surgery candidates to see the impact of iris surfaces features on corneal biomechanics and assist preoperative evaluations of corneal status before laser refractive surgeries.

Our study found that iris surface features are associated with corneal biomechanics. Specifically, more iris crypts were associated with larger A1 DLA, shorter A1 dArcL, dArcLM, and reduced SP-A1. Further, more extensive iris furrows were related with smaller integrated radius. Since shorter ArcLM, larger A1 DLA and integrated radius suggest lower level of corneal stiffness [11, 12]. Hence, these findings indicate that eyes with more iris crypts have softer corneas, while more furrows have stiffer cornea. Meanwhile, iris color was not associated with corneal biomechanics. Therefore, the features of iris crypts and furrows may provide useful hints regarding the corneal biomechanical characteristics of myopic eyes.

Iris crypts are result of the hypoplasia or atrophy of the iris stroma typically located at the midcentral area of the iris. Iris furrows are the sites where the iris folded and contracted as protuberant lines on the peripheral iris. Previous literature only supports indirect relationships between iris surface features and iris biomechanics in glaucoma studies [13, 14]. For example, in a finite element study of patients with a history of angle closure glaucoma, iris stiffness was higher in the patients than that in healthy participants [13]. Conversely, the presence of more iris crypts was associated with a thinner iris thickness [5] and a lower rate of acute primary angle closure [15]. Therefore, it is said that

Table 1: Clinicodemographic patient characteristics ($n = 152$).

Characteristics	Value
Age, years	25.21 [5.93]
Sex	
Male	92 (60.5%)
Female	60 (39.5%)
Pupil diameter, mm	3.15 [0.62]
ACD, mm	3.70 [0.25]
Axial length, mm	25.96 [1.07]
bIOP, mmHg	15.38 [1.88]
CCT, μm	540.66 [34.02]
Refraction, SE	-5.75 [2.39]
Iris crypt	
Grade 1	52 (34.2%)
Grade 2	62 (40.8%)
Grade 3	27 (17.8%)
Grade 4	10 (6.6%)
Grade 5	1 (0.7%)
Iris furrow	
Grade 1	10 (6.6%)
Grade 2	39 (25.7%)
Grade 3	103 (67.8%)
Iris color	
Grade 1	4 (2.6%)
Grade 2	28 (18.4%)
Grade 3	109 (71.7%)
Grade 4	11 (7.2%)
Grade 5	0 (0%)

Data are presented as the mean (standard deviation) or as n (%). ACD: anterior chamber depth; bIOP: biomechanical corrected intraocular pressure; CCT: central corneal thickness; SE: spherical equivalent of refractive error.

Table 2: Mean value of the corneal biomechanical parameters.

Corvis parameters	Mean [SD]
DA max, mm	1.06 [0.10]
A1 time, ms	7.42 [0.23]
A1 velocity, ms	0.15 [0.02]
A2 time, ms	22.02 [0.35]
A2 velocity, ms	-0.28 [0.03]
HC time, ms	16.7 [0.36]
PD, mm	4.99 [0.24]
Radius, mm	6.68 [0.71]
A1 DA, mm	0.15 [0.01]
HC DA, mm	1.06 [0.10]
A2 DA, mm	0.32 [0.06]
A1 DLL, mm	2.24 [0.18]
HC DLL, mm	6.42 [0.42]
A2 DLL, mm	2.71 [0.56]
A1 DLA, mm	0.09 [0.01]
HC DLA, mm	0.93 [0.09]
A2 DLA, mm	0.1 [0.01]
DLA max, mm	0.94 [0.09]
A1 dArcL, mm	-0.02 [0]
HC dArcL, mm	-0.13 [0.02]
A2 dArcL, mm	-0.02 [0]
dArcLM, mm	-0.15 [0.02]
Max inverse radius (mm^{-1})	0.19 [0.02]
DA ratio max, 2 mm	4.32 [0.35]
DA ratio max, 1 mm	1.56 [0.04]
Integrated radius (mm^{-1})	9.11 [0.86]
SP-A1	102.44 [18.39]

SD: standard deviation; DA: deformation amplitude; Max: maximum; A1: the first applanation; A2: the second applanation; HC: highest concavity; PD: peak distance; DLL: deflection length; DLA: deflection amplitude; dArcL: delta arc length; dArcLM: delta arc length max; SP-A1: stiffness parameter at the first applanation.

in angle closure glaucoma (ACG) eyes, iris crypt may be a protective factor [13].

The reason that there is relationship between iris surfaces features and corneal biomechanics is that the iris stroma and corneal stroma are adjacent ocular tissues and from the same embryonic origin of mesoderma [7, 8]. In addition, ocular tissues are said to be expanded in various patterns, such as posterior pole expansion [16], equatorial expansion [17], and axial expansion [18], in persons with myopia. The iris crypts, iris furrows, and cornea may also be a result of ocular expansion. Moreover, our results showed that iris crypts correlated with deflection parameter A1 DLA but not with deformation parameter of A1 DA. Corneal deflection amplitude is the pure corneal component of the corneal DA minus the whole eye movement. This suggested that corneal deflection, which excludes the influence of eye movement, is more related with iris crypts than corneal DA.

For patients preparing for laser refractive surgery, the most dangerous postoperative complication is the development of keratectasia such as keratoconus [2, 3, 19]. Especially for some patients with high myopia and thin cornea,

Table 3: Associations between iris surface features and corneal biomechanical parameters.

	Model 1*		Model 2†	
	β	P value	β	P value
Iris crypt				
A1 DLA	0.001	0.014	0.001	0.013
A1 dArcL	-0.001	0.017	-0.001	0.010
dArcLM	-0.002	0.309	-0.004	0.030
SP-A1	-1.942	0.255	-2.092	0.016
Iris furrows				
Integrated radius	-0.190	0.100	-0.212	0.025

*Model 1 was adjusted for age and sex. †Model 2 was adjusted for age, sex, anterior chamber depth, central corneal thickness, and bIOP. A1: the first applanation; DLA: deflection amplitude; dArcL: delta arc length; dArcLM: delta arc length max; SP-A1: stiffness parameter at the first applanation.

the risk of keratoconus will be greatly increased by close to the upper limit of corneal cutting, if the patient had abnormal corneal biomechanics before surgery. For doctors without corneal biomechanical examination equipment, even if equipped with Pentacam or some similar equipment, it is sometimes difficult to screen out preclinical keratoconus patients. The results of this study suggest that laser refractive surgeons should pay special attention to corneal biomechanical properties in patients with high levels of crypts and less furrows and reduce the amount of cutting or change the surgical option if no corneal biomechanical measurement conditions are available.

The main limitation of this study is that we only included participants with myopia, and the mean age is 25.21 ± 5.93 years, which is a young population. Our results only represented the associations between the iris surface features and corneal biomechanical properties in persons with myopia as we want to see the role of iris surface features on the refractive surgeries. Further studies should be carried out to also enroll individuals with emmetropic and hyperopic eyes of a wider age range, if it is needed. Another limitation is the cross-sectional study design, which prevented us from evaluating the causal relationship between corneal biomechanics and iris surface features. However, it is difficult to identify a causal relationship between the features. A longitudinal design may help to investigate the dynamic changes of these parameters and enrich understanding of their relationships.

5. Conclusion

Iris surface features were associated with the corneal biomechanics measured using Corvis ST. More iris crypts indicated softer corneas while more furrows suggested stiffer corneas in myopic eyes. The iris surface features may aid the assessment of corneal biomechanical properties in persons with myopia.

Data Availability

The datasets used and/or analyzed during the current study are available from the corresponding author on reasonable request.

Conflicts of Interest

The authors declare that there is no conflict of interest regarding the publication of this article.

Authors' Contributions

Lin Fu, Qi Dai, and Pengzhi Zhu contributed to the work equally and should be regarded as cofirst authors.

Acknowledgments

The study was supported by the Research Initiation Project of the Eye Hospital Wenzhou Medical University under Grant No. GKYQD2018001, Nature and Science Foundation of Zhejiang Province under Grant No. LQ18H120007, and the Wenzhou Basic Scientific Research Project under Grant Y20180712.

References

[1] E. K. Dackowski, P. D. Lopath, and R. S. Chuck, "Preoperative, intraoperative, and postoperative assessment of corneal biomechanics in refractive surgery," *Current Opinion in Ophthalmology*, vol. 31, no. 4, pp. 234–240, 2020.

[2] E. W. L. Lim and L. Lim, "Review of laser vision correction (LASIK, PRK and SMILE) with simultaneous accelerated corneal crosslinking-long-term results," *Current Eye Research*, vol. 44, no. 11, pp. 1171–1180, 2019.

[3] M. Ang, D. Gatinel, D. Z. Reinstein, E. Mertens, J. L. Alio Del Barrio, and J. L. Alio, "Refractive surgery beyond 2020," *Eye (London, England)*, vol. 35, no. 2, pp. 362–382, 2021.

[4] S. Chansangpetch, R. Panpruk, A. Manassakorn et al., "Impact of myopia on corneal biomechanics in glaucoma and nonglaucoma patients," *Investigative Ophthalmology & Visual Science*, vol. 58, no. 12, pp. 4990–4996, 2017.

[5] E. Sidhartha, P. Gupta, J. Liao et al., "Assessment of iris surface features and their relationship with iris thickness in Asian eyes," *Ophthalmology*, vol. 121, no. 5, pp. 1007–1012, 2014.

[6] J. Chua, S. G. Thakku, T. A. Tun et al., "Iris crypts influence dynamic changes of iris volume," *Ophthalmology*, vol. 123, no. 10, pp. 2077–2084, 2016.

[7] S. Ernyei, "Mesodermal Dysgenesis of Cornea and Iris (Rieger): Associated with hypoplasia of the stroma of the iris," *American Journal of Ophthalmology*, vol. 59, no. 1, pp. 106–108, 1965.

[8] H. Bernsmeier and G. Kluxen, "Irisangiographie und Endothelmikroskopie bei dysgenesis mesodermalis iridis et corneae," *Klinische Monatsblätter für Augenheilkunde*, vol. 183, no. 8, pp. 128–131, 1983.

[9] L. Tian, D. Wang, Y. Wu et al., "Corneal biomechanical characteristics measured by the CorVis Scheimpflug technology in eyes with primary open-angle glaucoma and normal eyes," *Acta Ophthalmologica*, vol. 94, no. 5, pp. e317–e324, 2016.

[10] M. Edwards, D. Cha, S. Krithika, M. Johnson, and E. J. Parra, "Analysis of iris surface features in populations of diverse ancestry," *Royal Society Open Science*, vol. 3, no. 1, 2016.

[11] V. S. De Stefano and W. J. Dupps Jr., "Biomechanical diagnostics of the cornea," *International Ophthalmology Clinics*, vol. 57, no. 3, pp. 75–86, 2017.

[12] C. J. Roberts, A. M. Mahmoud, J. P. Bons et al., "Introduction of two novel stiffness parameters and interpretation of air puff-induced biomechanical deformation parameters with a dynamic Scheimpflug analyzer," *Journal of Refractive Surgery*, vol. 33, no. 4, pp. 266–273, 2017.

[13] A. D. Pant, P. Gogte, V. Pathak-Ray, S. K. Dorairaj, and R. Amini, "Increased iris stiffness in patients with a history of angle-closure glaucoma: an image-based inverse modeling analysis," *Investigative Ophthalmology & Visual Science*, vol. 59, no. 10, pp. 4134–4142, 2018.

[14] Y. Jung, H. Chun, and J. I. Moon, "Corneal deflection amplitude and visual field progression in primary open-angle glaucoma," *PLoS One*, vol. 14, no. 8, article e0220655, 2019.

[15] V. Koh, J. Chua, Y. Shi et al., "Association of iris crypts with acute primary angle closure," *The British Journal of Ophthalmology*, vol. 101, no. 10, pp. 1318–1322, 2017.

[16] A. Sorsby, B. Benjamin, M. Sheridan, J. Stone, and G. A. Leary, "Refraction and its components during the growth of the eye from the age of three," *Journal of the Royal Statistical Society. Series A (General)*, vol. 125, 1962.

[17] P. K. Verkicharla, A. Mathur, E. A. Mallen, J. M. Pope, and D. A. Atchison, "Eye shape and retinal shape, and their relation to peripheral refraction," *Ophthalmic & Physiological Optics*, vol. 32, no. 3, pp. 184–199, 2012.

[18] D. A. Atchison, C. E. Jones, K. L. Schmid et al., "Eye shape in emmetropia and myopia," *Investigative Ophthalmology & Visual Science*, vol. 45, no. 10, pp. 3380–3386, 2004.

[19] N. Li, X. J. Peng, and Z. J. Fan, "Progress of corneal collagen cross-linking combined with refractive surgery," *International Journal of Ophthalmology*, vol. 7, no. 1, pp. 157–162, 2014.

Hindawi
Disease Markers
Volume 2021, Article ID 3803601, 9 pages
https://doi.org/10.1155/2021/3803601

Research Article

Cyclophosphamide Attenuates Fibrosis in Lupus Nephritis by Regulating Mesangial Cell Cycle Progression

Yuehong Ma,[1,2] Ling Fang,[3] Rui Zhang,[1] Peng Zhao,[4] Yafeng Li,[1,2] and Rongshan Li[1]

[1]*Shanxi Key Laboratory of Kidney Disease, Department of Nephrology, Shanxi Provincial People's Hospital, Taiyuan, China*
[2]*Shanxi Precision Medicine Center, Shanxi Provincial People's Hospital, Taiyuan, China*
[3]*Shanxi Institute of Scientific and Technical Information, Taiyuan, China*
[4]*Department of Dermatology, Shanxi Provincial People's Hospital, Taiyuan, China*

Correspondence should be addressed to Yafeng Li; dr.yafengli@gmail.com and Rongshan Li; rongshanli163@163.com

Received 18 August 2021; Revised 13 October 2021; Accepted 21 October 2021; Published 15 November 2021

Academic Editor: Ting Su

Objectives. Most patients with systemic lupus erythematosus (SLE) develop lupus nephritis (LN) with severe kidney manifestations. Renal fibrosis can be primarily attributed to overproliferation of mesangial cells (MCs), which are subject to drug treatment. Nevertheless, the detailed mechanisms remain elusive. We sought to identify the effect of cyclophosphamide (CTX), a drug commonly used for LN treatment, on MC proliferation and explore its underlying mechanisms. *Material/Methods*. Cell proliferation and fibrosis in mouse kidney tissues were determined by histopathology staining techniques. Flow cytometry was used for cell cycle analysis. Cell cycle regulators were examined *in vitro* following treatment of immortalized human MCs with platelet-derived growth factor subunit B (PDGF-B). Quantitative real-time PCR and western blot analyses were used to measure the mRNA and protein levels of candidate cell cycle regulators, respectively. *Results*. CTX inhibited cell overproliferation induced by platelet-derived growth factor subunit B *in vitro* and *in vivo*. CTX (40 mg/l) was sufficient to induce G0/G1 phase cell cycle arrest. CTX treatment downregulated many critical cell cycle regulators including cyclins and cyclin-dependent kinases but upregulated cyclin-dependent kinase inhibitors. Additionally, CTX-treated samples showed significantly reduced fibrosis, as indicated by lower expression of interleukin-1β and α-smooth muscle actin. *Conclusion*. CTX inhibits proliferation of MCs by modulating cell cycle regulator and therefore arresting them at G1 phase. CTX treatment significantly alleviates the severity of renal fibrosis. These findings provide novel insights into the mechanisms by which CTX affects LN.

1. Introduction

Systemic lupus erythematosus (SLE) is an autoimmune disease characterized by widespread inflammation in affected organs attacked by the immune system. Up to 70% SLE patients develop renal involvement, which are clinically diagnosed as lupus nephritis (LN). LN remains a leading cause of disability and death worldwide. Chronic nephritis, nephrotic syndrome, and even acute nephritis with alternating active and stable phases are commonly seen in LN patients [1, 2]. Additionally, 1 out 10 SLE patients ends up developing end-stage renal diseases [3, 4], and LN-related renal failure is the major cause of death among patients with SLE. While the clinical characteristics of LN are complex, glomerular injury represents a predominant symptom. Glomerular injuries are histologically classified based on glomerular immune complex deposition and mesangial cell (MC) overproliferation.

The three most abundant cell types in glomeruli are MCs, podocytes, and glomeruli epithelial cells, with MCs comprising approximately 1/3 of the total cell population. MC functions are vital in tissue homeostasis by providing structural support to the glomeruli and producing and maintaining the mesangial matrix. In addition, MCs can regulate the filtration surface area as a result of their contractility and can phagocytose apoptotic

cells or immune components [5]. Finally, MCs are also involved in immune responses in the glomerulus [6, 7].

MC proliferation is triggered by renal cell injury or inflammation. Interfering with the cell cycle at any stage can lead to cell cycle arrest, ultimately rendering apoptosis [8]. Several studies have demonstrated that tacrolimus, cyclosporine A, and methylprednisone (MP) can inhibit the proliferation of MCs and are promising therapeutic agents in treating glomerular diseases [9–13]. Previous studies have shown that tacrolimus inhibits cell cycle progression by decreasing the percentage of cells in S phase and increasing the percentage of cells in G0/G1 phase [14]. Similarly, cyclosporine A also prevents human MCs from entering S phase in a dose-dependent manner. MCs exposed to low micromolar levels of cyclosporine A showed significantly increased apoptotic cells. In addition, treatment with MP inhibited the proliferation of human MCs (HMCs) in a time- and concentration-dependent manner. Similar to that with cyclosporine A, treatment with MP (1–10 mg/l) for 48 h also promoted HMC apoptosis [14].

Although cyclophosphamide (CTX) pulse is widely used to treat LN in clinical practice, how CTX affects cell cycle and renal fibrosis remains to be determined. 3H-thymidine incorporation assay showed similar patterns between control and CTX-treated groups $(5 \times 10^{-5}\,\text{mol/L})$, suggesting that CTX did not alter the mesangial cell cycle at low concentrations [15]. However, whether high dose of CTX influences the cell cycle remains unclear. Understanding the mechanisms by which CTX affects the cell cycle and fibrosis will be useful for disease monitoring and treating LN. We therefore initiated the present study to investigate how CTX influenced the cell cycle progression, apoptosis, and fibrosis of HMCs.

2. Materials and Methods

2.1. Cell Proliferation Assay. Cell Counting Kit-8 (CCK-8, Boster Biotechnology Co., Wuhan, China) was used to measure cell proliferation according to manufacturer's protocol. Briefly, HMCs were cultured in 96-well plates (1×10^5 cells/well), followed by treatment with 20 ng/ml platelet-derived growth factor subunit B (PDGF-B) for 24 h with or without CTX (40 or 80 mg/l). The cells were then incubated in 10 μl CCK-8 solution at 37°C for 2 h in the dark. The optical density (OD) was measured at 450 nm using a Biotek microplate reader (Agilent Technologies, Santa Clara, CA, USA). The cell viability was calculated using the following formula: cell survival (%) = (mean OD of treated cells/mean OD of control cells) × 100.

2.2. Animals. Six young (6–7-week-old) female C57BL/6J mice weighing 20 ± 1.5 g were purchased from the Laboratory Animal Center, Shanxi Provincial People's Hospital (Taiyuan, Shanxi). Female MRL/lpr LN mice were purchased from the Model Animal Institute of Nanjing University (induced from Jackson Laboratories, USA). The mice were housed under controlled environmental conditions (temperature 24 ± 2°C, 12 h light-dark cycle, and humidity 40%-70%), given free access to water, and fed a standard laboratory diet. The study was conducted in accordance with protocols approved by the Laboratory Animal Center, Shanxi Provincial People's Hospital. Twelve female MRL/lpr LN mice were randomly divided into 2 groups: LN group and LN+CTX group. Mice in the LN+CTX group were exposed to CTX by oral perfusion (20 mg/kg·d, 12 weeks), whereas the LN group received saline for 12 weeks. The animals were sacrificed 12 h after the last oral injection. Serum was collected by centrifuging at 5000 rpm for 15 min at 4°C and stored at −20°C for determining BUN and Scr levels. Renal tissues were obtained and kept in 10% neutral-buffered formalin and embedded in paraffin for histopathological analysis. Additional renal samples were immediately frozen in liquid nitrogen and stored at −80°C until analysis.

2.3. Flow Cytometry. Cell cycle arrest after cyclophosphamide (CTX) treatment was examined by flow cytometry. The human mesangial cells (HMCs) were harvested from T25 culture flasks (Nest Biotechnology, Wuxi, China) 24 h after treatment and fixed with 70% ethanol at 4°C for 24 h. After washing once with ice-cold phosphate-buffered saline, the cells were treated with ribonuclease (100 mg/ml) at 37°C for 30 min, followed by staining with propidium iodide (50 mg/ml) at 4°C for 30 min in the dark. The cells were analyzed by using an FC500 flow cytometer (Beckman Coulter, Beckman, Palo Alto, CA, USA) to determine the proportions of cells within the G1, S, and G2/M phases.

2.4. Quantitative Real-Time Polymerase Chain Reaction (qRT-PCR) Analysis. RNA was extracted from HMCs treated with 20 ng/ml PDGF-B for 24 h. The RNA concentration was measured using a Biotek microplate reader (Agilent Technologies, Santa Clara, CA, USA). 500 ng RNA was reverse-transcribed into cDNA using PrimeScript™ RT Master Mix (Takara, Shiga, Japan) according to manufacturer's protocol. qRT-PCR was performed with TB Green® Premix Ex Taq™ II (Tli RNaseH Plus) (Takara). Primer sequences used for qRT-PCR are as follows: CDK2 F-ATCTT TGCTG AGATG GTGAC TCG and CDK2 R-ACTTG GGGAA ACTTG GCTTG T, CDK4 F-TTGCG GCCTG TGTCT ATGGT and CDK4 R-CAAGG GAGAC CCTCA CGCC, cyclin E F-CCGGT ATATG GCGAC ACAAG and cyclin E R-CACAG AGATC CAACA GCTTC AT, cyclin D1 F-GATCA AGTGT GACCC GGACT and cyclin D1 R-CTTGG GGTCC ATGTT CTGCT, p21 F-ATGTG CACGG AAGGA CTTTG and p21 R-CGTTT GGAGT GGTAG AAATC TGG, and β-actin F-ACCTT CTACA ATGAG CTGCG and β-actin R-CCTGG ATAGC AACGT ACATG G. Relative gene expression was normalized to that of β-actin.

2.5. Western Blot Analysis. HMCs and kidney tissues were homogenized in lysis buffer (Boster Biotechnology Co., Wuhan, China). Proteins were separated by 10% SDS-PAGE and transferred onto a PVDF membrane (EMD Millipore, Billerica, MA, USA). Primary antibodies against cyclin D1, cyclin E, CDK2, CDK4, p21 (Santa Cruz Biotechnology, Dallas, TX, USA), IL-1β (ab234437; Abcam, Cambridge, UK), and α-smooth A (ab5694; Abcam) and corresponding secondary antibodies (Boster Biotechnology Co., Wuhan, China) were used. Membranes were developed and visualized using the Quantity One analysis system (Bio-Rad, Hercules, CA, USA).

2.6. Kidney Tissue Preparation for Pathology. Kidney tissues were collected from anesthetized mice after perfusion. To prepare sliced sections for histology, kidney tissue was fixed with 4% paraformaldehyde, embedded in paraffin, cut to 4 μm thickness, and stained with hematoxylin and eosin (HE) or periodic acid-Schiff (PAS) for morphological evaluation, PAS for mesangial expansion, and Masson for fibrosis. This study was approved by the local Ethics Committee of Shanxi Provincial People's Hospital, China (no.: 201987).

2.7. Data Analyses. Experimental data with three biological repeats were analyzed statistically by paired t-tests using the SPSS 23.0 software (SPSS, Inc., Chicago, IL, USA) and are presented as the means ± standard error of the mean.

3. Results

3.1. CTX Reduces Proteinuria and Improves Renal Function in MRL/lpr Mice. Treatment of MRL/lpr mice with 40 or 80 mg/l CTX ameliorated the symptoms of LN. Specifically, proteinuria, renal function abnormities, and kidney pathological lesions were reduced. The reduction in proteinuria was similar between the two dosage groups (Figure 1(a)).

3.2. CTX Inhibits Cellular Proliferation in Glomeruli In Vivo. To examine the cellular effect of CTX treatment on mice with LN, we have performed HE and PAS staining. Compared to the control mice, CTX-treated mice showed increased MC proliferation and accelerated progression of kidney fibrosis at week 12. We also examined both groups at week 17, and the difference was found to be more significant. Remarkably, mice treated with CTX for 12 weeks showed delayed disease progression compared to untreated mice. Pathological evaluation of MRL/lpr mice at week 17 revealed glomeruli with thickened pink capillary loops, which are typical of the so-called "wire loops" of LN. In mice treated with CTX, the surrounding renal tubules were unremarkable, and the opening of capillary loops was improved (Figure 1(b)).

3.3. MCs Treated with CTX Contribute to Decreased Inflammation and Fibrosis in LN. Masson staining showed that CTX-treated mice delayed the progress of renal fibrosis, compared to the MRL/lpr LN mice (Figure 2(a)). And meanwhile, we investigated how CTX affects cellular inflammation and fibrosis. Interleukin- (IL-) 1β is a key cytokine mediating inflammatory responses while α-smooth muscle actin (α-SMA) is a marker for tissue fibrogenesis. IL-1β was expressed at relatively high levels in LN samples, indicating their inflammatory origins. However, as shown by the qRT-PCR and western blot results, IL-1β levels were significantly reduced following treatment with CTX, suggesting an ameliorated inflammatory response. α-SMA showed the same tendency following CTX treatment (Figure 2(b)). These results suggested that CTX could potentially mitigate both inflammation and fibrosis in LN patients.

3.4. CTX Reduces HMC Proliferation and Arrests the Cell Cycle in G0/G1 Phase. We next assessed how CTX influences HMC proliferation *in vitro*. Cellular proliferation in CTX and PDGF-B-treated group was significantly reduced compared to that in cells treated by PDGF-B alone. We also found that the inhibitory effect of CTX depended not only on its dosage but also on its exposure time, although the difference was negligible at the high concentration. We found that neither 40 nor 80 mg/l CTX affected HMC proliferation following a 24-hour treatment. However, the inhibition rate of cell proliferation has the similar tendency with 24 h after treatment with 40 and 80 mg/l CTX for 48 h, but has significance in statistics (Figure 3(a)).

One plausible explanation of the reduced HMC proliferation upon CTX exposure was the shifted cell cycle. Therefore, we performed flow cytometry analysis to test this hypothesis. Consistent with our results of cellular proliferation, PDGF-B treatment increased the proportion of cells in S phase while decreasing the percentage of G1 cells. These results indicated that PDGF-B could shift cell cycle towards S phase (Figure 3(b)). In contrast, cells exposed to both PDGF-B and CTX were significantly enriched for the G1 phase population ($p < 0.05$), while deprived of the S phase population ($p < 0.0001$). These results suggested that CTX could override PDGF in halting the cells in G1 phase and blocking cell cycle.

3.5. Effects of CTX on Cyclins and Cyclin-Dependent Kinases. Cyclins and cyclin-dependent kinases (CDKs) are essential drivers of cell cycle events. To determine the mechanisms by which CTX affects HMC proliferation, we examined the expression of genes that are known to regulate G1 phase, such as cyclin D1, cyclin E, CDK2, and CDK4 (Figure 4). Both transcription and protein levels of the candidate factors were upregulated when cells were treated with 20 ng/l PDGF-B. Significantly, we found that treatment with CTX at 40 mg/l was sufficient to abolish the upregulation induced by PDGF-B. We also examined the effect of high dosage of CTX and found that 80 mg/l CTX inhibited the expression of all the proteins except for CDK4, which showed higher levels than that in PDGF-B-treated cells (Figure 4(a)).

3.6. CTX Reverses the PDGF-B-Induced Decrease in p21 Level. To gain further insights into how CTX regulates cell cycle components, we focused on p21, a cyclin-dependent kinase inhibitor, in quiescent and proliferating HMCs. In quiescent HMCs, both the mRNA and protein levels of p21 were detectable. However, the expression of p21 was decreased in cells incubated with PDGF-B. Significantly, this effect was reversed by 40 mg/l CTX treatment. Interestingly, treatment with 80 mg/l CTX only decreased p21 mRNA expression but not protein expression (Figure 4(b)). Altogether, these results suggested that CTX can reverse the downregulation of cyclin-dependent kinase inhibitor induced by PDGF-B exposure.

4. Discussion

Many SLE patients develop LN that is associated with poor prognosis and increased morbidity and mortality [16]. One shared phenotype of many glomerular diseases, including LN, is MC overproliferation [12]. MCs are involved in many

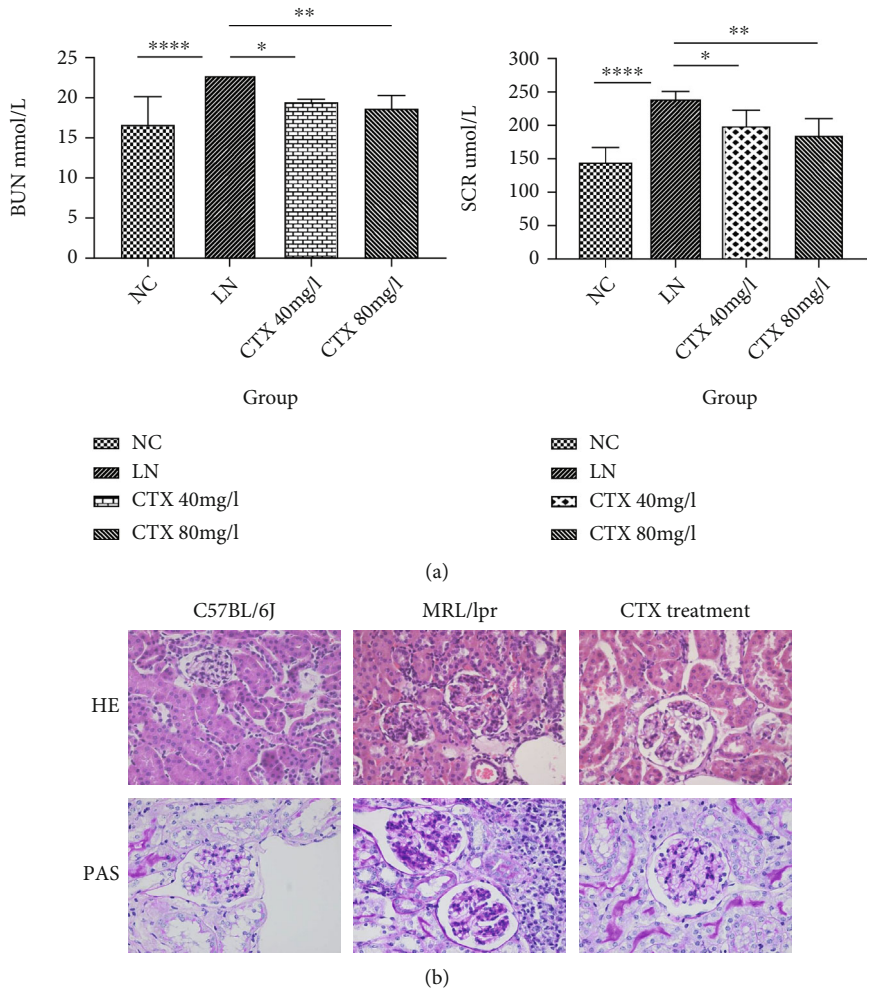

Figure 1: (a) Renal function in lupus nephritis after CTX treatment. CTX reduced the levels of blood urea nitrogen (BUN) and serum creatinine (SCR) of lupus nephritis (LN) mice. Data are presented as the means ± SEM ($n = 6$). $^{*}p < 0.05$, $^{**}p < 0.001$, and $^{****}p < 0.00001$, lupus nephritis vs. control. (b) CTX 40 mg/l inhibits cell proliferation in glomeruli and necrosis of capillary loops. Glomerular pathology was detected by HE staining and PAS staining at week 17 ($n = 6$/group, 400x original magnification).

biological processes in the renal glomerulus, such as secreting cell matrix, producing cytokines, and supporting glomerular capillary plexus, phagocytosis, and clearance of macromolecular substances, as well as contraction of smooth muscle cells. Once activated by inflammatory stimuli, MCs can also interact with migrating and infiltrating inflammatory cells, which in turn amplifies local inflammation responses, fibrosis, and the development of glomerulosclerosis [17, 18].

Similar to tacrolimus and cyclosporine A, MP is known to interfere with cell cycles by inducing G1-phase arrest and preventing cells from entering mitosis [14]. Consistent with this result, another study showed that glucocorticoids could decrease S/G2/M-phase populations in HEK293 cells by suppressing NF-κB activities [19]. Mounting evidence has shown the antiproliferative effects of glucocorticoids across numerous cell types [20–24], and MP is likely to be effective on CDK inhibitors such as p21/Cip1 and p57/Kip2 [25, 26]. Alternatively, MP may also suppress the expression of c-myc or cyclins, which can stimulate cell cycle progression [20].

To dive into the prime feature of LN, we first analyzed the effects of CTX treatment on cell proliferation *in vitro*. Cell cycle progression is tightly regulated and coordinated by growth factors, oncogenic stimuli, and regulatory components such as cyclin/CDK complexes [27, 28]. Our data showed that the cell cycle was shifted by treating MCs with 40 mg/l or 80 mg/l CTX. As our results indicated that CTX mainly affected G0/G1 phase, we focused on regulators of these stages. Cyclin D and cyclin E, together with CDK2 and CDK4, facilitate the transition from G1 to G2 phases, whereas p21 has a strong inhibitory effect. Our results showed that PDGF-B could upregulate cyclin D, cyclin E, CDK2, and CDK4, while the expression of p21 was markedly reduced. Interestingly, in proliferating MCs, CTX downregulated the expression of cyclin D, cyclin E, CDK2, and CDK4 and upregulated p21 expression. These results suggested an antiproliferative effect of CTX in MCs.

An *in vitro* model of LN suggested that MCs could contribute to renal inflammation by secreting proinflammatory

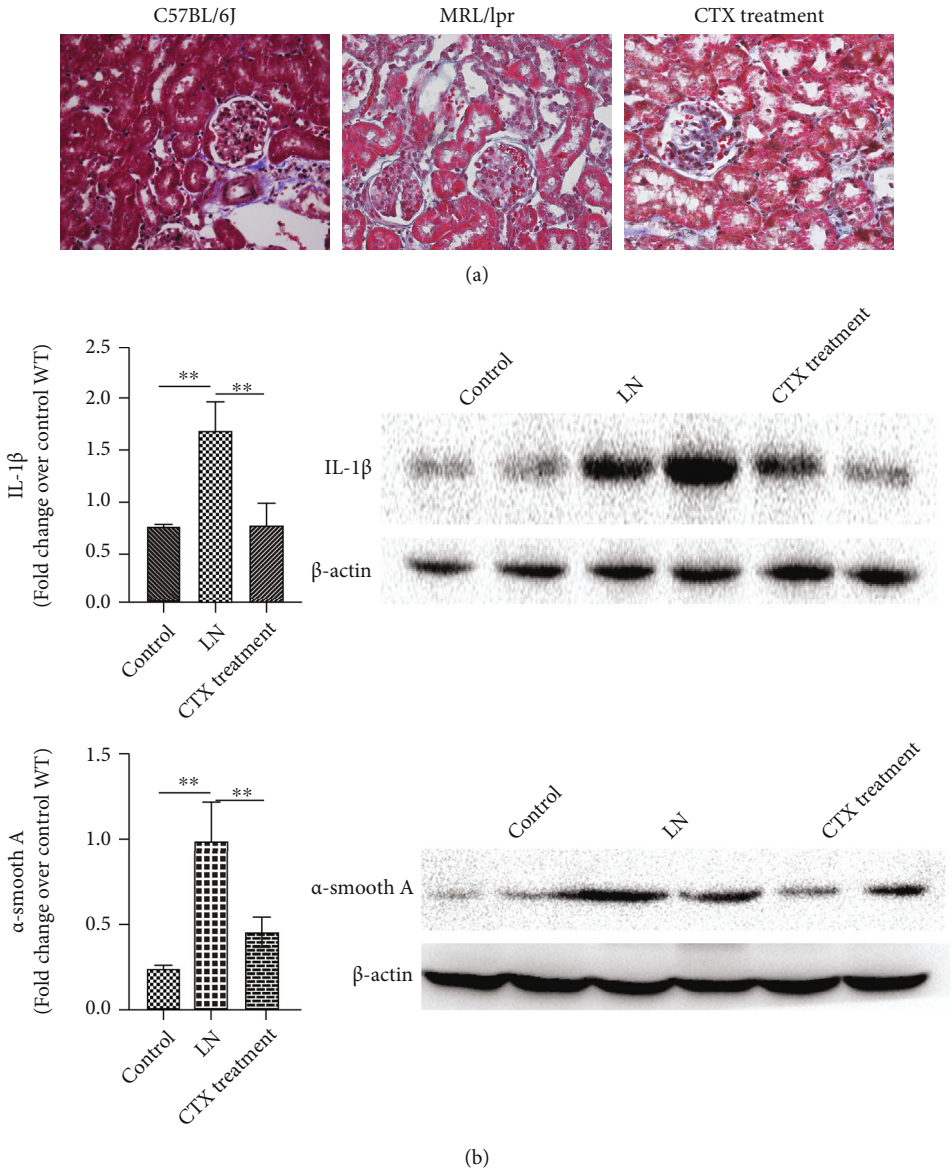

Figure 2: (a) CTX 40 mg/l delays the progress of kidney fibrosis. Glomerular pathology was detected by Masson staining at week 17 ($n = 6$/group, 400x original magnification). (b) Interleukin- (IL-) 1β and α-SMA in LN following CTX (40 mg/l) treatment. Multiplex analysis was used to determine the protein levels of IL-1β and α-SMA. The blots were representatives of independent biological triplicates and were analyzed by Friedman's test with Dunn's post hoc test, $^{**}p < 0.01$.

cytokines to local niches [7]. Studies based on human and animal models also showed that renal tubular epithelial-myofibroblast phenotypic transformation is critical in the pathogenesis of renal diseases associated with renal interstitial fibrosis, where α-SMA is an important marker of this transformation [29]. Additionally, fibrosis and key inflammatory factors, such as IL-1β, appear to be closely related [30].

Our study indicated that CTX could benefit renal fibrosis patients by targeting key cell cycle regulators. We found that expression of the fibrotic protein α-SMA and inflammatory factor IL-1β was markedly reduced in the LN mouse model after treatment with CTX, which delayed the progression of renal fibrosis and inflammation. Although we did not observe the same impact of CTX on HMCs, this discrepancy can be explained by the different concentrations of CTX administered *in vitro* and *in vivo*. While CTX (5×10^{-5} mol/L) did not alter the mesangial cell cycle [15], these data reveal a strong correlation between cell cycle, inflammation, and fibrosis. As an important hub of LN-related phenotypes including cell proliferation and immune cell activation, MC remains to be a promising therapeutic target. Our work elucidated detailed mechanisms by which CTX attenuates MC overproliferation and renal fibrosis and therefore laid a foundation for CTX therapy.

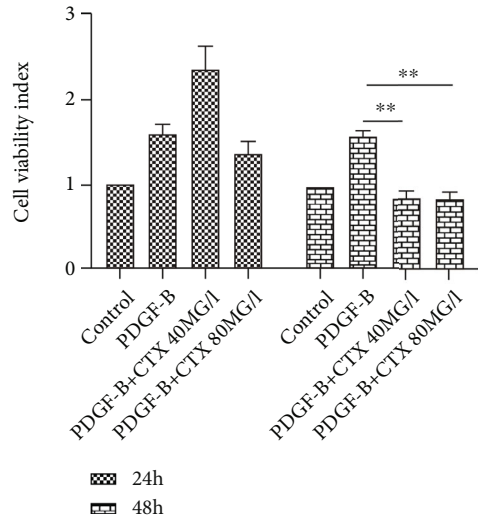

(a)

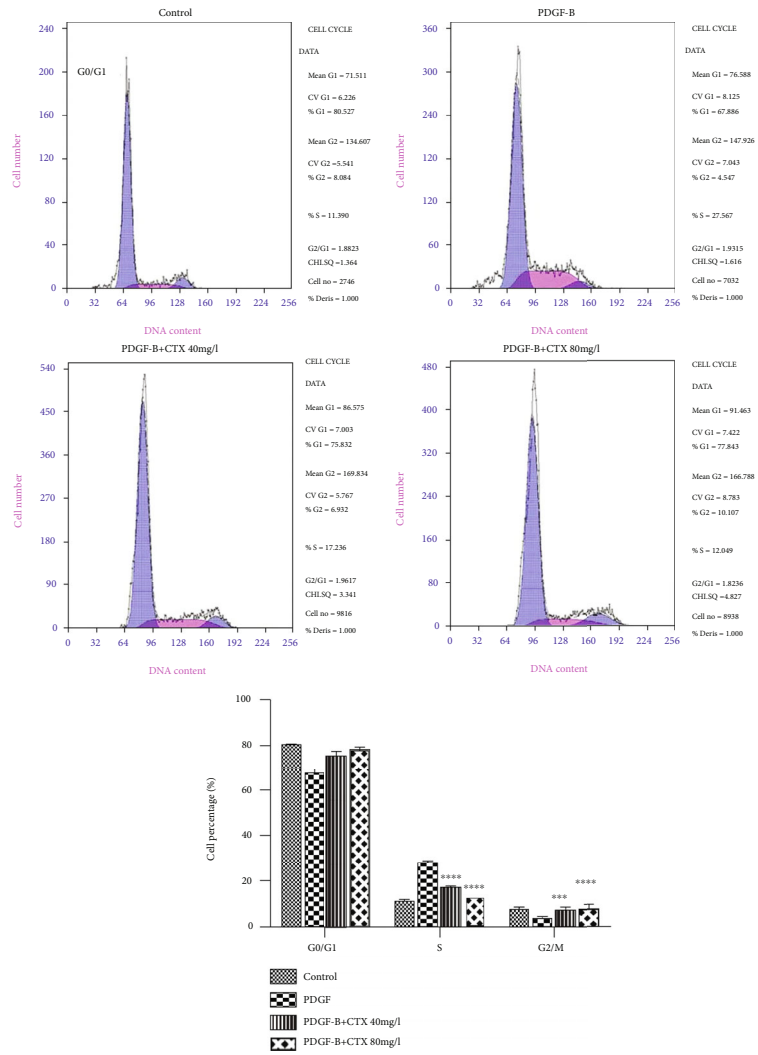

(b)

Figure 3: CTX reduces HMC proliferation by arresting the cell cycle in G1 phase. (a) CTX inhibited cell proliferation induced by PDGF-B at 48 h but not 24 h ($n = 6$/group). (b) Flow cytometry analysis showing cells in different phases of cell cycle. CTX arrested cells in G1 phase in a concentration-dependent manner; therefore, the percentage of cells in S phase was significantly lower ($n = 6$/group). Data are presented as the means ± SD, $^{*}p < 0.05$, $^{***}p < 0.001$, and $^{****}p < 0.0001$.

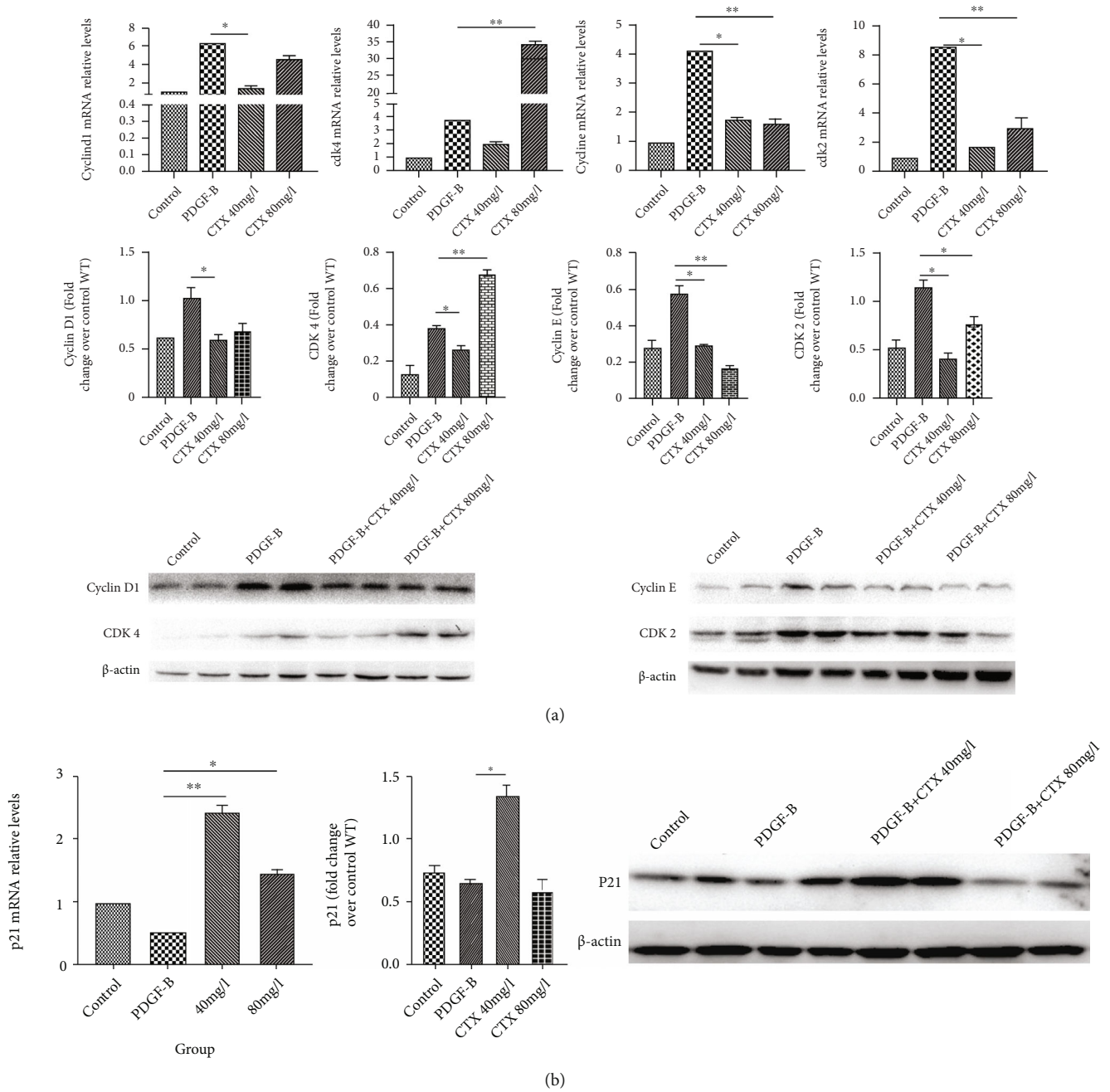

Figure 4: (a) Effect of CTX on candidate genes. HMCs were treated with 20 ng/ml PDGF-B for 48 h with or without CTX (40 or 80 mg/l). The expression levels of candidate genes were detected by western blotting and qRT-PCR. Blots were representatives of independent biological triplicates. $^{*}p < 0.05$ and $^{**}p < 0.01$. Data are presented as the means ± SD ($n = 3$). (b) Effect of CTX on cell cycle proteins. CTX (40 and 80 mg/l) upregulated p21 mRNA and protein in HMCs as demonstrated by qRT-PCR and western blotting assays, respectively. The western blots were representatives of independent biological triplicates. $^{*}p < 0.05$ and $^{**}p < 0.01$. Data are presented as the means ± SD ($n = 3$).

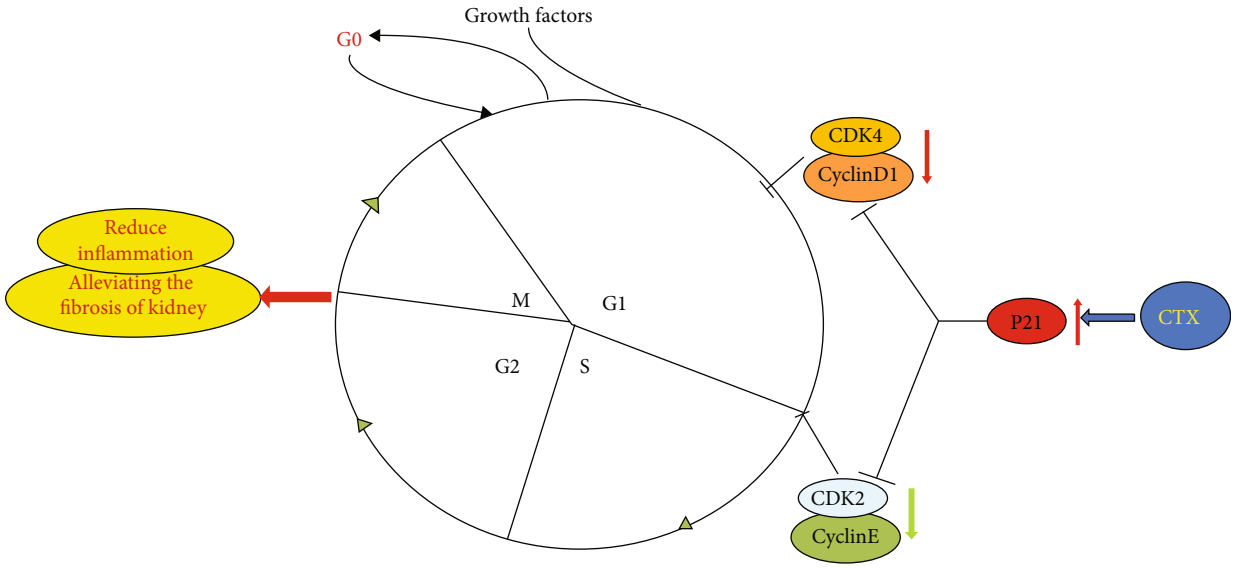

Figure 5: Proposed mechanisms of effects of CTX on mesangial cell proliferation.

5. Conclusion

In conclusion, a high dose of CTX inhibited the proliferation of HMCs and induced HMC apoptosis. Moreover, CTX dramatically reduced the expression of IL-1β and α-SMA, which are involved in the inflammatory response and fibrosis within the glomerulus. Therefore, we proposed that CTX might regulate cell proliferation by controlling the production of intracellular inflammatory fibrosis mediators and the cell cycle regulators. Overall, these data laid the foundation of CTX shock therapy for LN (Figure 5).

Data Availability

The data used to support the findings of this study are available from the first author upon request.

Conflicts of Interest

We do not have any competing interest to declare.

Authors' Contributions

Yuehong Ma and Ling Fang contributed equally to this work.

Acknowledgments

This work was financially supported by the National Natural Science Foundation of China (grant number: 81570626), Foundation of Health Commission of Shanxi Province of China (grant number: 2020033), and Social Development Project of Science and Technology Department of Shanxi Province of China (grant number: 201803D31158).

References

[1] J. H. Berden, "Lupus nephritis," *Kidney International*, vol. 52, no. 2, pp. 538–558, 1997.

[2] G. B. Appel and A. Valeri, "The course and treatment of lupus nephritis," *Annual Review of Medicine*, vol. 45, no. 1, pp. 525–537, 1994.

[3] S. Almaani, A. Meara, and B. H. Rovin, "Update on lupus nephritis," *Clinical Journal of the American Society of Nephrology*, vol. 12, no. 5, pp. 825–835, 2017.

[4] M. G. Tektonidou, A. Dasgupta, and M. M. Ward, "Risk of end-stage renal disease in patients with lupus nephritis, 1971-2015: a systematic review and Bayesian meta-analysis," *Arthritis & Rhematology*, vol. 68, no. 6, pp. 1432–1441, 2016.

[5] H. E. Abboud, "Mesangial cell biology," *Experimental Cell Research*, vol. 318, no. 9, pp. 979–985, 2012.

[6] D. Schlondorff, "Roles of the mesangium in glomerular function," *Kidney International*, vol. 49, no. 6, pp. 1583–1585, 1996.

[7] R. D. Wright, P. Dimou, S. J. Northey, and M. W. Beresford, "Mesangial cells are key contributors to the fibrotic damage seen in the lupus nephritis glomerulus," *Journal of Inflammation*, vol. 16, no. 1, pp. 1–4, 2019.

[8] O. Pastukhov, S. Schwalm, I. Romer, U. Zangemeister-Wittke, J. Pfeilschifter, and A. Huwiler, "Ceramide kinase contributes to proliferation but not to prostaglandin E2 formation in renal mesangial cells and fibroblasts," *Cellular Physiology and Biochemistry*, vol. 34, no. 1, pp. 119–133, 2014.

[9] E. S. Akool, A. Doller, A. Babelova et al., "Molecular mechanisms of TGFβ receptor-triggered signaling cascades rapidly induced by the calcineurin inhibitors cyclosporin A and FK506," *Journal of Immunology*, vol. 181, no. 4, pp. 2831–2845, 2008.

[10] M. S. Anil Kumar, M. Irfan Saeed, K. Ranganna et al., "Comparison of four different immunosuppression protocols without long-term steroid therapy in kidney recipients monitored by surveillance biopsy: Five- year outcomes," *Transplant Immunology*, vol. 20, no. 1-2, pp. 32–42, 2008.

[11] J. Boletis, A. Balitsari, V. Filiopoulos et al., "Delayed renal graft function: the influence of immunosuppression," *Transplantation Proceedings*, vol. 37, no. 5, pp. 2054–2059, 2005.

[12] Y. Kurogi, "Mesangial cell proliferation inhibitors for the treatment of proliferative glomerular disease," *Medicinal Research Reviews*, vol. 23, no. 1, pp. 15–31, 2003.

[13] H. Ren, N. Guo, and D. Lu, "Successful engraftment of HLA-identical sibling cord blood transplantation in an adult with chronic myelogenous leukemia," *Zhonghua Xue Ye Xue Za Zhi*, vol. 22, no. 12, pp. 621–624, 2001.

[14] X. Zhou, B. Workeneh, Z. Hu, and R. Li, "Effect of immunosuppression on the human mesangial cell cycle," *Molecular Medicine Reports*, vol. 11, no. 2, pp. 910–916, 2015.

[15] D. R. Cha, S. M. Feld, C. Nast, J. LaPage, and S. G. Adler, "Apoptosis in mesangial cells induced by ionizing radiation and cytotoxic drugs," *Kidney International*, vol. 50, no. 5, pp. 1565–1571, 1996.

[16] R. Mina and H. I. Brunner, "Pediatric lupus–are there differences in presentation, genetics, response to therapy, and damage accrual compared with adult lupus?," *Rheumatic Diseases Clinics of North America*, vol. 36, no. 1, pp. 53–80, 2010, vii-viii.

[17] R. L. Pereira, R. J. Felizardo, M. A. Cenedeze et al., "Balance between the two kinin receptors in the progression of experimental focal and segmental glomerulosclerosis in mice," *Disease Models & Mechanisms*, vol. 7, no. 6, pp. 701–710, 2014.

[18] W. Hu, Y. Chen, S. Wang et al., "Clinical-morphological features and outcomes of lupus podocytopathy," *Clinical Journal of the American Society of Nephrology*, vol. 11, no. 4, pp. 585–592, 2016.

[19] L. G. Bladh, J. Lidén, A. Pazirandeh et al., "Identification of target genes involved in the antiproliferative effect of glucocorticoids reveals a role for nuclear factor-(kappa)B repression," *Molecular Endocrinology*, vol. 19, no. 3, pp. 632–643, 2005.

[20] I. Rogatsky, J. M. Trowbridge, and M. J. Garabedian, "Glucocorticoid receptor-mediated cell cycle arrest is achieved through distinct cell-specific transcriptional regulatory mechanisms," *Molecular and Cellular Biology*, vol. 17, no. 6, pp. 3181–3193, 1997.

[21] E. Smith, R. A. Redman, C. R. Logg, G. A. Coetzee, N. Kasahara, and B. Frenkel, "Glucocorticoids inhibit developmental stage-specific osteoblast cell cycle. Dissociation of cyclin A-cyclin-dependent kinase 2 from E2F4-p130 complexes," *The Journal of Biological Chemistry*, vol. 275, no. 26, pp. 19992–20001, 2000.

[22] K. Rhee, D. Reisman, W. Bresnahan, and E. A. Thompson, "Glucocorticoid regulation of G1 cyclin-dependent kinase genes in lymphoid cells," *Cell Growth & Differentiation*, vol. 6, no. 6, pp. 691–698, 1995.

[23] A. Helmberg, N. Auphan, C. Caelles, and M. Karin, "Glucocorticoid-induced apoptosis of human leukemic cells is caused by the repressive function of the glucocorticoid receptor," *The EMBO Journal*, vol. 14, no. 3, pp. 452–460, 1995.

[24] I. Sanchez, L. Goya, A. K. Vallerga, and G. L. Firestone, "Glucocorticoids reversibly arrest rat hepatoma cell growth by inducing an early G1 block in cell cycle progression," *Cell Growth & Differentiation*, vol. 4, no. 3, pp. 215–225, 1993.

[25] S. Corroyer, E. Nabeyrat, and A. Clement, "Involvement of the cell cycle inhibitor CIP1/WAF1 in lung alveolar epithelial cell growth arrest induced by glucocorticoids," *Endocrinology*, vol. 138, no. 9, pp. 3677–3685, 1997.

[26] H. H. Cha, E. J. Cram, E. C. Wang, A. J. Huang, H. G. Kasler, and G. L. Firestone, "Glucocorticoids stimulate p21 gene expression by targeting multiple transcriptional elements within a steroid responsive region of the p21waf1/cip1 promoter in rat hepatoma cells," *The Journal of Biological Chemistry*, vol. 273, no. 4, pp. 1998–2007, 1998.

[27] L. Hilakivi-Clarke, C. Wang, M. Kalil, R. Riggins, and R. G. Pestell, "Nutritional modulation of the cell cycle and breast cancer," *Endocrine-Related Cancer*, vol. 11, no. 4, pp. 603–622, 2004.

[28] T. Li, X. Zhao, Z. Mo et al., "Formononetin promotes cell cycle arrest via downregulation of Akt/cyclin D1/CDK4 in human prostate cancer cells," *Cellular Physiology and Biochemistry*, vol. 34, no. 4, pp. 1351–1358, 2014.

[29] G. S. Jung, Y. J. Hwang, J. H. Choi, and K. M. Lee, "Lin28a attenuates TGF-beta-induced renal fibrosis," *BMB Reports*, vol. 53, no. 11, pp. 594–599, 2020.

[30] S. C. W. Tang and W. H. Yiu, "Innate immunity in diabetic kidney disease," *Nature Reviews. Nephrology*, vol. 16, no. 4, pp. 206–222, 2020.

Hindawi
Disease Markers
Volume 2021, Article ID 7124835, 10 pages
https://doi.org/10.1155/2021/7124835

Research Article

Pericytes of Indirect Contact Coculture Decrease Integrity of Inner Blood-Retina Barrier Model *In Vitro* by Upgrading MMP-2/9 Activity

Tianye Yang,[1,2] Liang Guo,[1] Yuan Fang,[3,4] Mingli Liang,[1] Yongzheng Zheng,[3,4] Mingdong Pan,[3,4] Chun Meng,[1,4] and Guanghui Liu[3,4]

[1]*Department of Bioengineering, College of Biological Science and Biotechnology, Fuzhou University, Fuzhou, Fujian, China*
[2]*Lunan Pharmaceutical Group Co. Ltd., Linyi, Shandong, China*
[3]*Department of Ophthalmology, Affiliated People's Hospital (Fujian Provincial People's Hospital), Fujian University of Traditional Chinese Medicine, Fuzhou, Fujian, China*
[4]*Eye Institute of Integrated Chinese and Western Medicine, Fujian University of Traditional Chinese Medicine, Fuzhou, Fujian, China*

Correspondence should be addressed to Chun Meng; mengchun@fzu.edu.cn and Guanghui Liu; latiny@gmail.com

Received 11 July 2021; Accepted 28 August 2021; Published 29 September 2021

Academic Editor: Ting Su

Inner blood-retina barrier (iBRB) is primarily formed of retinal microvascular endothelial cells (ECs) with tight junctions, which are surrounded and supported by retinal microvascular pericytes (RMPs) and basement membrane. Pericytes are believed to be critically involved in the physiology and pathology of iBRB. However, the underlying mechanism remains to be fully elucidated. We developed a novel *in vitro* iBRB model which was composed of primary cultures of rat retinal ECs and RMPs based on Transwell system. We tested the involvement of pericytes in the migration and invasion of ECs, examined the expression and activity of matrix metalloproteinase- (MMP-) 2/MMP-9 in the culture, evaluated the TEER and permeability of iBRB, and assessed the expression of ZO-1, occludin, claudin-5, and VE-cadherin of endothelial junctions. We found that RMPs with indirect contact of ECs can increase the expression of MMP-2 and upgrade the activity of MMP-2/9 in the coculture, which subsequently decreased TJ protein abundance of ZO-1 and occludin in ECs, promoted the migration of ECs, and finally reduced the integrity of iBRB. Taken together, our data show that RMP relative location with ECs is involved in the integrity of iBRB via MMP-2/9 and has important implications for treating diabetic retinopathy and other retinal disorders involving iBRB dysfunction.

1. Introduction

Inner blood-retina barrier (iBRB), mainly consisting of endothelial cells (ECs), retinal microvascular pericytes (RMPs), and basement membrane, plays a key role in retinal homeostasis [1]. Under physiological conditions, blood-retina barrier (BRB) restricts nonspecific transport between neural retina and peripheral blood and prevents the passage of pathogens, toxins, toxicants, proteins, and neurotransmitters into the retina [2]. Under pathological conditions, such as hyperglycemia, hypoxia, oxidative stress, or inflammation, disruption of integrity of interendothelial junctions leads to the increase of iBRB permeability and gathering of harmful substances in the retina [3].

The barrier function is exerted primarily by the EC layer. The sophisticated junctions between adjacent ECs, including tight junctions (TJs), adherens junctions (AJs), gap junctions, and desmosomes, are the basis of iBRB [4]. Besides their involvement in cell to cell adhesion, these structures sustain cell survival, cell polarity, and paracellular permeability [5]. TJs, forming a paracellular diffusion barrier to limit the movement of molecules across EC layer, take a central role in the maintenance [4]. It has previously been demonstrated that increasing of iBRB permeability is related

with the degradation of TJs of ECs *in vitro* and *in vivo* [5, 6]. Thus, the regulation of iBRB permeability is critical both for protecting the retina from harmful components of peripheral blood and for the treatment of retinal disorders.

iBRB is regulated principally by interactions among ECs, pericytes, and extracellular matrix (ECM). Pericytes are located in the outer wall of EC tubes [7]. As part of the microvasculature, pericytes maintain vascular stability and enhance endothelial barrier function by direct contact and paracrine regulation [1, 8], while pericytes detached from ECs would lead to unstabilization of endothelial barrier [5], decrease in transendothelial electrical resistance (TEER), and increase in permeability [9]. Due to multiple effects on ECs, the role of RMPs in iBRB should be further explored. Basement membrane, a specialized ECM of retinal microvessel, encloses ECs and pericytes and provides the intermediates for cell communication. The molecular components of basement membrane, secreted by the neighboring ECs and pericytes, act as a crucial clue for appropriate TJ assembly and iBRB properties to maintain function of mature iBRB [10, 11].

Matrix metalloproteinases (MMPs), one of the major mediators of barrier degradation, modulate the structure and function of ECM molecules under physiological and pathological processes [12–14]. The involvement of MMPs in iBRB disruption during diabetic retinopathy, retinal ischemia, and retinal neovascularization has been demonstrated in numerous studies [15–17]. The association between the expression levels of different MMPs and the presence of ECs and pericytes has also been suggested [18], but it has not been fully elucidated.

MMP-2/9, members of the most ubiquitous members of MMPs family, are not only able to degrade ECM protein but also able to cleave TJ proteins [19]. They are known as mediators of endothelial barrier disruption and TJ protein proteolysis [20]. MMP-2/9 can be secreted both by ECs and pericytes [18, 21–23]. MMP-2 activity can increase when ECs are cocultured with pericytes [24].

Here, we used an *in vitro* iBRB model system composed of primary cultures of rat ECs and RMPs, studied the expression and activity of MMP-2/9 secreted by ECs and RMPs under indirect contact coculture, and explored the effect of MMP-2/9 on the maintenance of iBRB function *in vitro*. We for the first time provide evidence demonstrating that indirect EC-RMP cell to cell interaction increases MMP-2 expression, upgrades MMP-2/9 activity, disrupts TJs of ECs, and decreases the integrity of iBRB *in vitro*. This evidence is pivotal for further understanding RMP modulation of iBRB properties with respect to the future development of specific strategies for treatment of certain retina diseases or pathological conditions with iBRB involvement due to MMP imbalance.

2. Materials and Methods

2.1. Preparation and Cultivation of Rat Retinal ECs and RMPs. All experimental procedures were conducted in accordance with the ARVO Statement for the Use of Animals in Ophthalmic and Vision Research and approved by the Institutional Ethics Committee for Animal Use in Research and Education at Fuzhou University (Fujian, China).

The retinas for primary retinal cell culture were isolated from 3-week-old male rats (Sprague Dawley rat; SLAC, Shanghai, China). The rat retinal ECs and RMPs were obtained and identified as reported [25, 26]. Three-dimensional (3D) capillary-tube formation assay was used to assess the function of ECs and RMPs *in vitro* as previously described [26]. Briefly, ECs and RMPs were labeled by cell tracker (Molecular Probes, OR, USA) before 3D coculture in Matrigel (BD Biosciences, CA, USA). After 24 hours of coculture, the cells were evaluated by fluorescent microscopy (Nikon, Tokyo, Japan). The cells of the 3^{rd}-7^{th} passage were used for further experiment after they were proved being functional cells by the assay.

2.2. In Vitro iBRB Model. Three basic *in vitro* iBRB models, shown as the schematic description, were designed based on Transwell system (0.4 μm pores, Corning, NY, USA). The EC monolayer (model ECs) was made by ECs alone (Figure 1(a)). The direct contact coculture (model DC) was made through ECs directly coculturing with RPMs cells (Figure 1(b)). The indirect contact coculture (model IDC) was made by ECs and RMPs with indirect contact (Figure 1(c)). Transwell system allows cells of coculture to communicate directly or indirectly through the pores of the polyethylene terephthalate membrane. For establishing model DC, RMPs and ECs were layered separately on each side of a 24-well Transwell membrane. RMPs were seeded on the outside of the membrane when the Transwell insert was inverted. 12 h later, when RMPs adhered to the membrane, the insert with RMPs was placed in well of a 24-well plate (Corning, NY, USA), and ECs were seeded on the inner side of the membrane. For establishing model IDC, Transwell inserts with EC monolayer were placed into 24-well plates culturing with 80% confluent layers of RMPs. All iBRB models were seeded with ECs or RMPs at the same passage number and density (6×10^4 cells/mL). The cells were grown on the inserts for 48 h before being used in each experiment.

2.3. Migration Assay and Invasion Assay. The ability of cells to migrate was assessed by scratch wound healing assay. The cells (ECs or ECs mixed with RMPs) were seeded onto 24-well plates and cultured to confluence. A scratch was made by a 10 μl sterile pipette tip in the monolayer perpendicularly across the center of the well. The floating cells were washed away with serum-free cell culture media. The wound closure was visualized by time-lapse imaging with a phase-contrast microscope (Nikon, Tokyo, Japan). Phase-contrast images of five selected fields were acquired at 0, 24, and 32 h. The area of the gap that has not been covered by the cells was analyzed using the ImageJ software (ImageJ 1.8.0; National Institutes of Health, MD, USA).

The invasive ability of cells was evaluated using Transwell system (8 μm pore size, Corning, NY, USA). The Transwell chambers were coated with 0.1 mL Matrigel (50 μg/mL) and put into the 24-well plates. EC suspension (1×10^5 cells) was seeded to the upper chamber of Transwell. RMP

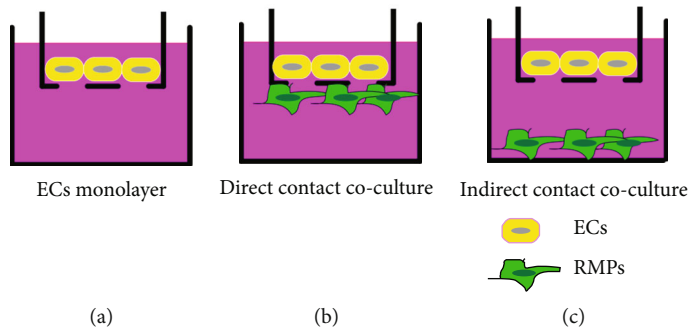

Figure 1: Schematic diagrams of iBRB models *in vitro*. (a) Model ECs. EC monolayer without RMPs. (b) Model DC. Coculture of ECs directly contacted with RMPs. (c) Model IDC. Coculture of ECs indirectly contacted with RMPs.

suspension (1×10^5 cells) was added to the lower chamber of 24-well plates. 10% serum growth media was added to the chamber, and the cells were allowed to invade for 32 hours at 37°C in a 5% CO_2 humidified incubator. Then, the cells were fixed with 20% methanol and stained with 0.5% crystal violet. The cells on the top surface of the filter were removed by a cotton swab, and the cells that had invaded into the bottom surface of the filter were imaged and counted under with phase-contrast microscope over five random fields of each well.

2.4. Zymography. The activity of MMP-2/9 was estimated by substrate gelatin zymography according to George et al. [27]. Supernatants of the cell culture were collected and mixed with 5x sample buffer (10% glycerinum, 10% SDS, 1% bromophenol blue, 500 mM Tris–HCl, pH 6.8), and equal sample volumes were loaded on 10% SDS polyacrylamide gels which contained 0.1% gelatin (Sigma, MO, USA). After the electrophoresis step, the gels were treated twice with 2.7% Triton-X 100 solution for 30 min each and then incubated in developing buffer (50 mM Tris, 200 mM NaCl, 5 mM $CaCl_2$, and 1 mM ZnCl, pH 7.5) for 20 h at 37°C. After the incubation, the gels were stained in staining solution (25% alcohol, 10% acetic acid, and 0.25% coomassie blue) for 60 min and then treated with destaining solution (25% alcohol and 10% acetic acid) for 1 h. The densitometric analysis was performed using the ImageJ software.

2.5. Transendothelial Electrical Resistance Measurements. Transendothelial electrical resistance measurements were performed once endothelial cultures of 3 models reached 95%-100% confluent. In Transwell (0.4 μm pore size) cultures, TEER was conducted by a Millicell device (Millicell-ERS-2, MA, USA) and chopstick-like electrodes as described elsewhere [28]. One electrode was immersed in the upper chamber of Transwell and the other electrode in the lower chamber of a 24-well plate. An equilibration period at room temperature for 20 min was performed prior to the measurement. TEER value was calculated as the resistance (Ω) of cell culture inserts minus background resistance (Ω) of cell-free inserts. The difference was multiplied with the area of insert ($0.33 cm^2$), resulting in a TEER value given as a mean in $\Omega \cdot cm^2$.

2.6. Sodium Fluorescein Permeability Measurement. Permeability measurement was assessed by sodium fluorescein since ECs form a barrier against the free diffusion of sodium fluorescein. Sodium fluorescein (100 μg/mL) was added to the apical side of Transwell filter. Permeability of the cell layer to sodium fluorescein was measured according to previous report [29]. Briefly, sodium fluorescein permeates through the monolayer into the basolateral chamber. The amount of sodium fluorescein accumulating in the basolateral chamber is an indicator of the permeability of cell layer. Permeability of the cell layer was examined as fluorescence with a Varioskan LUX Multimode Microplate Reader (Thermo Scientific, MA, USA) at excitation wavelengths of 440 nm and emission wavelengths of 525 nm. GM6001 (Selleckcn, NY, USA), a broad inhibitor, was added in the medium of model IDC as comparison.

2.7. Western Blotting. Total proteins were isolated from the culture using RIPA lysis buffer (#P0013B, Beyotime, Jiangsu, China) mixed with protease inhibitor and PMSF. SDS-PAGE was used to separate the proteins. The separated proteins were transferred to a PVDF membrane (#88520, Millipore, MA, USA), which was blocked with 5% bovine serum albumin at room temperature for 2 h and then immunoblotted with antibodies against MMP-9 (#ab228402, Abcam, MA, USA), MMP-2 (#ab86607, Abcam, MA, USA), zonula occludens-1 (ZO-1, #ab96587, Abcam, MA, USA), occludin (#ab216327, Abcam, MA, USA), claudin-5 (#ab131259, Abcam, MA, USA), and vascular endothelial-(VE-) cadherin (#ab33168, Abcam, MA, USA). Chemiluminescence was detected with the ChemiDoc MP imager (Bio-Rad, CA, USA). β-Actin was used as a negative control, and the results were normalized to β-actin.

2.8. Statistical Analyses. All experiments were repeated at least three times. Statistical analyses were conducted using the JASP software package (Version 0.14.1, JASP Team, Amsterdam, Netherlands). Student's t-test was used to determine significant differences between two groups, and one-way ANOVA with the least significant difference test was performed to compare more than two groups. All data are presented as mean ± SD, and a value of $P < 0.05$ was considered statistically significant.

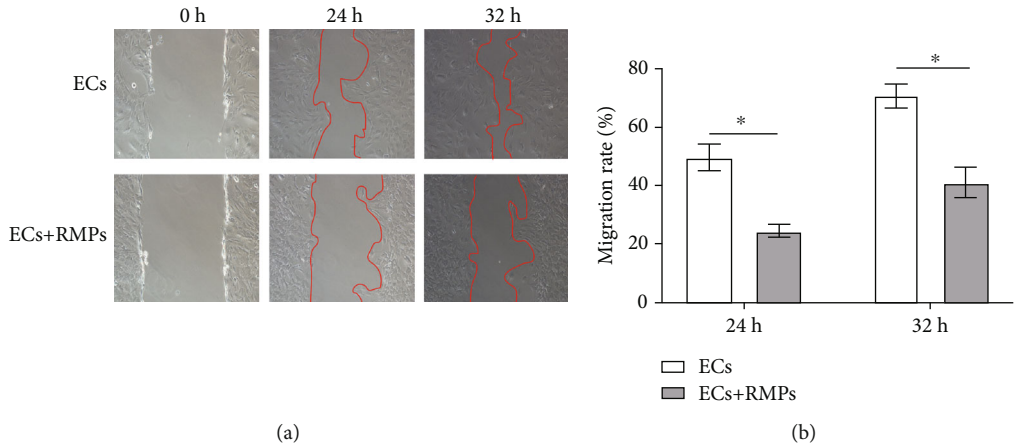

Figure 2: RMPs inhibit EC migration in direct contact coculture. (a) Typical pictures of wound-induced migration assay. Wound repair 24 h and 32 h after the mechanical scratch (top, ECs cultured alone; bottom, ECs cocultured with RMPs). The red lines indicate the edges of wounded area. (b) Quantitative analysis of wound repair 24 h and 32 h after making the scratch. Initial wound area at 0 h is defined as 100%. Migration rate = (1 − wound area at a specific time point/initial wound area) ∗ 100%. Analytical data are presented as the mean ± SD. $^*P < 0.01$.

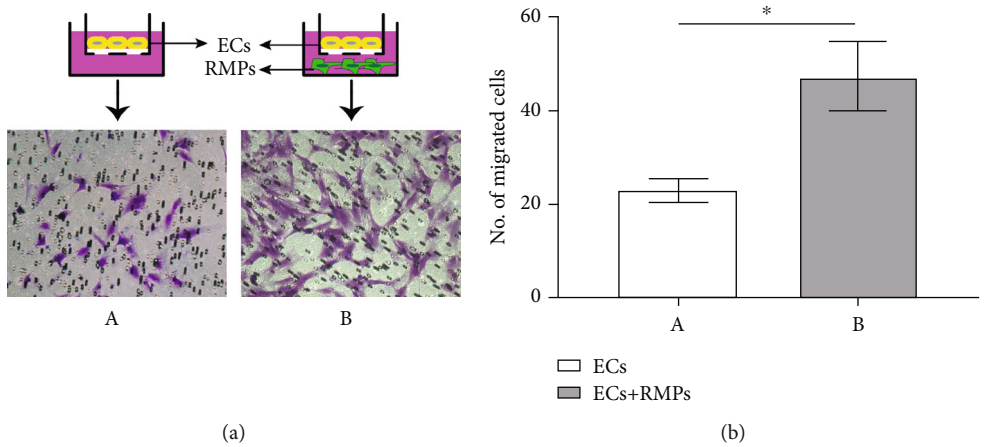

Figure 3: RMPs promote EC migration in indirect contact coculture. (a) EC suspensions are layered onto Matrigel-coated Transwell inserts, and RMP suspensions are layered onto the bottom of 24-well plates. RMPs promote invasion of ECs through Matrigel in invasion assays. (b) Number of cells traversing the insert is calculated as a measure of invasion. Analytical data are presented as the mean ± SD. $^*P < 0.01$.

3. Results

3.1. RMPs Inhibited EC Migration in Direct Contact Coculture and Prompted EC Migration in Indirect Contact Coculture. We used 2D culture to evaluate EC migration with the involvement of pericytes at the first step. In a wound-induced migration assay, the confluent cell monolayer was disrupted and cells were allowed to move into the cell-free area.

The mobility of ECs cocultured with RMPs was decreased in the scrape-wound assay as compared with ECs cultured alone (Figure 2(a)). The scratched areas of ECs cultured alone were almost fully repopulated in 32 h, whereas migration of ECs cocultured was greatly halted by RMPs. A decrease of 41.6% in inhibition of migration was observed in the coculture compared with that in the culture of ECs alone in 32 h (Figure 2(b)). It indicated the involvement of pericytes in the stability of ECs under condition of direct contact with each other.

ECs have to migrate and cross basement membrane before new vessel formation. To invade through basement membrane, ECs must degrade the components of it. We used 3D indirect contact coculture model to assess the ability of pericytes to modulate EC invasion in Matrigel invasion assays secondly. Significant difference in invasiveness was noted between the indirectly contact cocultured cells and ECs cultured alone in the assay. The invasive potential of ECs in indirect contact coculture was substantially increased (Figure 3(a)). In the Matrigel assay, quantitative analysis of invading cells showed that the invasiveness of indirectly

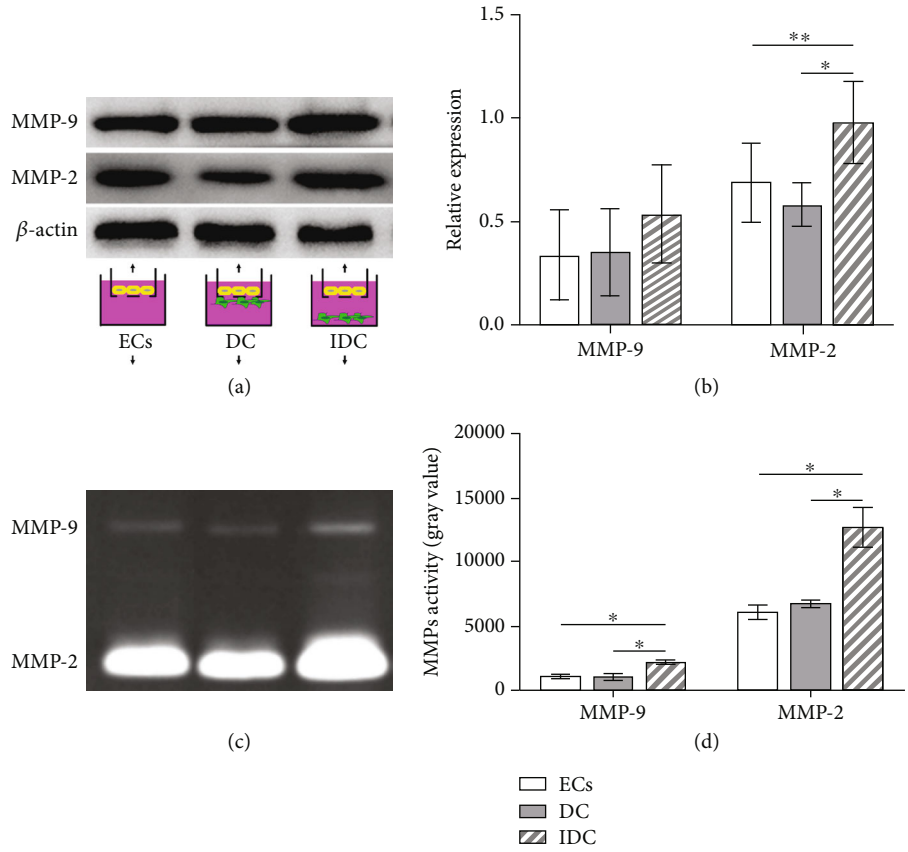

Figure 4: RMPs upgrade expression of MMP-2 and activity of MMP-2/9 of indirect contact coculture. (a) The abundance of MMP-9 and MMP-2 is confirmed via Western blot in model ECs, model DC, and model IDC. (b) MMP-9 and MMP-2 expression measurements are quantified via normalization to β-actin. (c) Activity of MMP-9 and MMP-2 is evaluated by zymography in 3 models. (d) Gray value of MMP-9 and MMP-2 activity measurements. $^{*}P < 0.01$ and $^{**}P < 0.05$.

contact cocultured ECs was greatly increased to 45% as compared with the ECs cultured alone (Figure 3(b)). It suggests that pericytes have a promoting effect on the invasion of ECs under indirect contact condition.

3.2. RMPs in Indirect Contact Coculture with ECs Upgraded the Expression of MMP-2 and Activity of MMP-2/9 in ECs. MMP-2/9 are the major mediators of basement membrane degradation and the key contributors to the invasion of ECs through basement membrane. To determine the relationship between RMP relative location and EC invasion and address the impact of RMPs on MMP expression of iBRB model *in vitro*, MMP-2/9 are evaluated. We performed Western blot and gelatin zymographical analysis of the culture and explored the secretion and activity of MMP-2/9.

Indirectly contact cocultured cells (model IDC) secreted significantly more MMP-2 than ECs cultured alone (model ECs) or direct contact coculture (model DC), but no difference was observed between ECs cultured alone and direct contact coculture. No difference of MMP-9 expression was shown among the 3 iBRB models (Figures 4(a) and 4(b)). Additionally, we observed that MMP-2/9 activity of indirectly contact cocultured cells by zymography was higher than that of ECs cultured alone and direct contact coculture (Figures 4(c) and 4(d)). These observations suggest that pericyte metabolites may enhance the expression of MMP-2 and the activity of MMP-2/9 to promote the invasion of ECs under the condition with indirect contact.

3.3. RMPs Downgraded TEER and Upgraded Permeability of iBRB under the Condition with Indirect Contact Coculture. Immigration of ECs occurs before the degradation of iBRB integrity, such as decrease of TEER or increase of permeability. TEER and permeability of iBRB models were evaluated and presented in Figure 5. TEER of model ECs was $33.00 \pm 3.30\,\Omega \cdot \mathrm{cm}^2$ and that of model DC was $39.60 \pm 1.65\,\Omega \cdot \mathrm{cm}^2$. TEER was significantly lower in model IDC ($26.18 \pm 1.16\,\Omega \cdot \mathrm{cm}^2$) than in model ECs and model DC. To clarify the role of RMPs in the BBB disruption involved with MMP-2/9, GM6001, a broad inhibitor, was added in the medium of model IDC. However, GM6001 significantly increased the value of TEER ($35.64 \pm 1.51\,\Omega \cdot \mathrm{cm}^2$) of model IDC (Figure 5(a)).

Opposite changes were found in sodium fluorescein permeability measurement. Permeability of sodium fluorescein is taken as the marker of paracellular permeation. Permeability of model ECs was 4500 ± 200 A.U. and that of model DC was 3500 ± 200 A.U. while RMPs can increase the permeability of sodium fluorescein in the coculture with indirect contact. The permeability value of model IDC

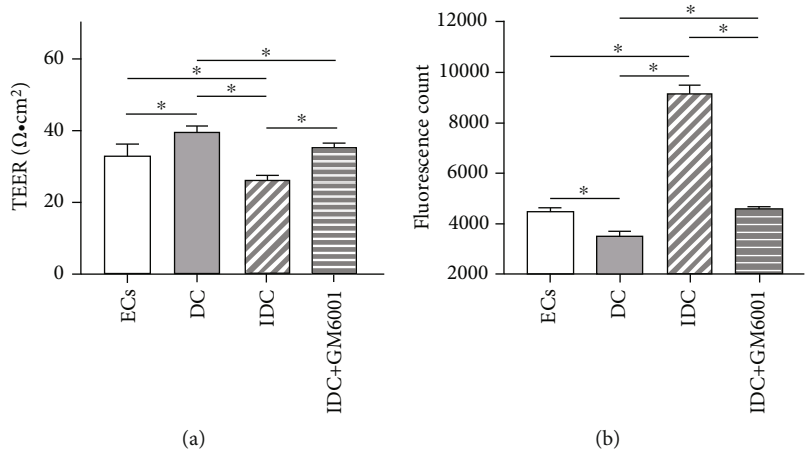

Figure 5: RMPs downgrade TEER and upgraded permeability of iBRB under the condition with indirect contact. (a) Value of TEER in model ECs, model DC, model IDC, and model IDC+GM6001. (b) Permeability of sodium fluorescein in model ECs, model DC, model IDC, and model IDC+GM6001. $^*P < 0.01$. Unit = arbitrary unit (A.U.).

(9233 ± 305.5 A.U.) was significantly higher than that of model ECs and model DC. GM6001 significantly decreased the permeability value of ECs to 4600 ± 100 A.U. in model IDC (Figure 5(b)).

Collectively, these observations suggest that RMPs may regulate iBRB TEER and permeability by MMP-2/9 under the condition with indirect contact coculture since the application of inhibitor GM6001 changes the TEER and permeability values of EC/RMP coculture with indirect contact (model IDC).

3.4. RMPs Decreased the Expression of ZO-1 and Occludin of iBRB under the Condition with Indirect Contact Coculture. It has been generally accepted that TJ proteins and adhesion molecules are in correlation with integrity of iBRB, and the junction proteins get disrupted when ECs start to migrate [4]. Thus, we investigated further whether RMPs may increase iBRB permeability by disrupting expression of the TJ proteins ZO-1, occludin, and claudin-5 under condition of indirect contact coculture, as well as the AJ protein VE-cadherin.

Expression of ZO-1 and occludin was significantly higher in model DC than in model ECs cultured alone. RMPs or its metabolite may influence ZO-1 and occludin expression. The expression of ZO-1 and occludin was significantly lower in model IDC than in model ECs and model DC. No difference of claudin-5 and VE-cadherin expression was observed among the 3 iBRB models (Figure 6). These results suggest that RMPs may reduce the iBRB integrity under condition of indirect contact coculture by upregulating MMP-2/9 activity, which subsequently, at least in part, decrease the abundance of ZO-1 and occludin directly or indirectly.

4. Discussion

In this study, we developed a novel *in vitro* iBRB model system composed of primary cultures of rat retinal ECs and RMPs on the permeable membrane of Transwell. Basing on this iBRB model system, we demonstrated that RMPs prompted EC migration in indirect contact coculture associated with the increasing of MMP-2 expression and upgrading of MMP-2/9 activity. We showed that RMPs decreased the expression of ZO-1 and occludin of ECs, downgraded TEER, and upgraded permeability of iBRB in indirect contact coculture by increasing the expression of MMP-2 and activity of MMP-2/9. Our results suggest that RMP relative location has an important impact on the integrity of iBRB mediated by MMP-2/9.

Inner BRB function is exerted primarily by EC layer and supported by RMPs. Pericytes, wrap around ECs lining the capillaries, are critical components of iBRB through communication with ECs. Relative surface coverage and density of pericytes on capillaries are positively correlated with endothelial barrier properties [30]. According to the difference of vascular bed, pericyte coverage of the abluminal vessel area of ECs is partial. The retina has the highest pericyte density of all vascular beds [31], the relative frequency of RMPs to ECs is 1 : 1 [32], and the frequency of RMP coverage on retinal capillaries was reported to be high up to 94.5% [33]. Therefore, the role of RMPs in iBRB and its coordination with ECs may deserve particular attention.

Pericytes interact with ECs by foot processes directly and offer important supports to ECs, such as stabilizing the newly formed endothelial tubes and modulating EC survival, proliferation, differentiation, migration, and invasion [34]. The requirement for pericytes has been demonstrated by *in vivo* models of induced pericyte loss that lead to increased permeability of BRB [35]. In our Transwell coculture system, RMPs on the bottom side of 24-well plates can communicate with ECs on the top side of Transwell through the 0.4 μm pores of the permeable membrane under indirect contact condition. Comparing to the EC monolayer cultured alone, the EC-RMP indirect contact coculture model led to an obvious migration and invasion of ECs and had more cells through the membrane of Matrigel. Interestingly, EC migration was significantly halted by RMPs in direct contact coculture (2D coculture). In previous report, it is generally

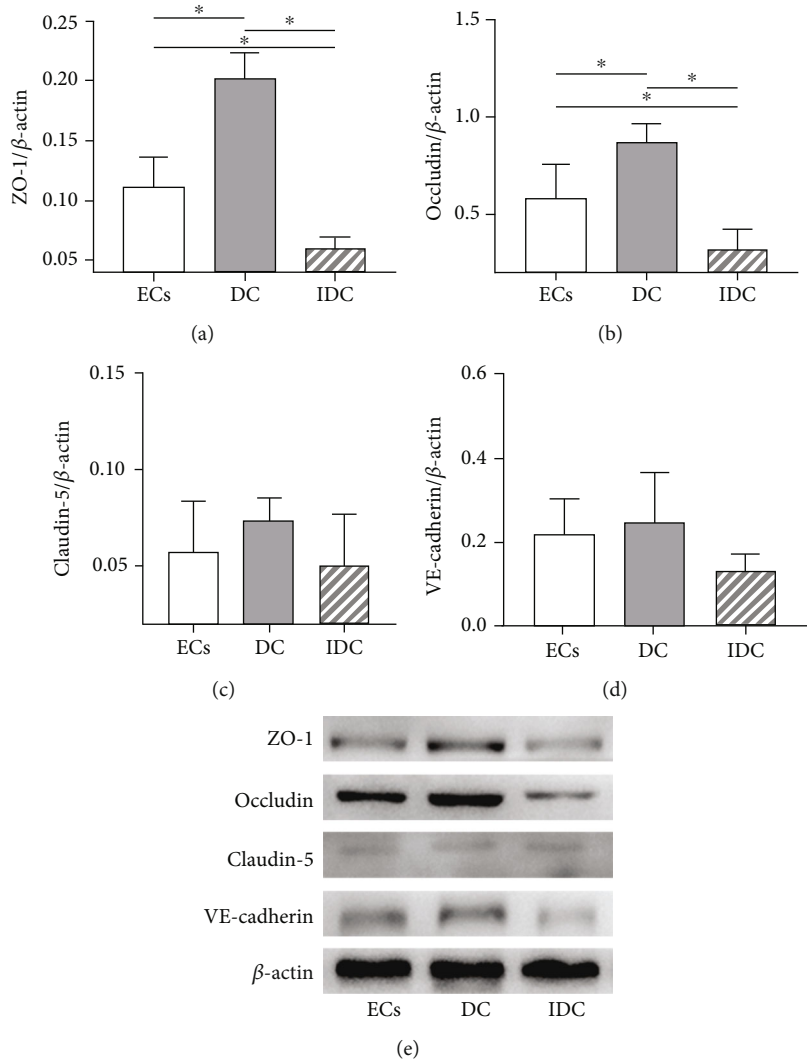

Figure 6: RMPs decrease the expression of ZO-1 and occludin of iBRB under the condition with indirect contact coculture. (a–d) ZO-1, occludin, claudin-5, and VE-cadherin measurements are quantified via normalization to β-actin. $^{*}P < 0.01$. (e) Abundance of ZO-1, occludin, claudin-5, and VE-cadherin is evaluated via Western blot in 3 iBRB models.

considered that pericytes restrict EC migration and stabilize the blood vessels [1, 36]. Our findings suggest that RMPs may have a negative role in iBRB stability when it loses direct contact with ECs, since EC migration and invasion through basement membrane are promoted by RMPs under the condition of indirect contact coculture.

Basement membrane, a specialized ECM of microvessel and intermediate for EC-RMP communication, degrades generally with EC migration and invasion. MMPs, one of the major mediators of endothelial barrier degradation, have been shown to regulate the structure and function of ECM molecules under physiological and pathological processes [12–16]. The correlation between the expression of different MMPs and the presence of ECs and pericytes has also been suggested. Takahashi et al. reported human pericytes induced MMP-9 activity but not MMP-2 in culture [37], and the result was confirmed by Underly et al. in mouse blood-brain barrier (BBB) *in vivo* [38]. Takata et al. also reported MMP-9 derived from pericytes lead to BBB damage [39]. On the other hand, Zozulya et al. observed no difference in MMP-2 expression of different EC-pericyte coculture but an elevated expression of MMP-9 from ECs cultured in direct contact to pericytes as compared to that from ECs free of pericytes [18]. Our Wb data indicated that MMP-2 expression was elevated in indirect contact coculture compared with that in EC culture or direct contact coculture, while MMP-9 was not differentially expressed. Zymography data show that MMP-2/9 of indirect contact coculture was generally in higher activity than that of model ECs and model DC. The inconsistent observations in previous literature and our study may be owed to the differences in the type and origin of cells and the culture methods used in different studies, which also highlights the need for a better and stable model of iBRB for mechanistic investigations. Our results suggest the promotion of EC migration and invasion in indirect contact coculture by RMPs may be caused by the increase of MMP-2 expression and MMP-2/9 activity. The suggestions are further

supported by the assay of TEER and sodium fluorescein permeability.

TEER, a measurement of electrical resistance across a cellular monolayer, reflects an amount of ionic molecule flux through cell layer and is a very sensitive and reliable method to confirm the integrity and permeability of the monolayer [9, 40]. Sodium fluorescein is commonly used as low-molecular-weight tracers, and permeability of sodium fluorescein represents an indication of paracellular permeation [9, 41]. Previous studies of *in vitro* coculture models have shown that addition of pericytes increases the TEER of EC monolayer [42–44]. In this study, RMPs directly cocultured with ECs had a positive role in iBRB, but RMPs indirectly contact cocultured with ECs decreased the TEER and increased the permeability of iBRB. The results are similar to the *in vitro* finding of BBB model which demonstrated pericytes can negatively regulate endothelial barrier integrity via paracrine in indirect contact coculture system [9]. Our results further revealed that MMP-2/9 mediate RMP regulation of iBRB integrity in indirect contact condition since the changes of integrity in model IDC can be inhibited by MMP broad inhibitor GM6001. But MMP-2/9-mediated RMP regulation may not be the only mechanism of RMP modulation of iBRB *in vitro* due to the incomplete inhibition of GM6001.

Generally, MMPs open endothelial barrier by degrading cellular junctions [20, 45]. TJs and AJs, both important in keeping permeability low while providing a high TEER, are specific type of cell-cell contacts that obstruct paracellular pathway for solute diffusion and regulate the paracellular passage of small molecules such as water and ions [6, 46]. TJs of ECs are mainly composed of claudins, occludin, ZO, and tight junction adhesion molecules, and VE-cadherin is the major compound of endothelial AJs [5]. Pericyte recruitment to ECs can induce TJ formation [35], while detachment of pericytes from ECs would lead to the unstabilization of EC junctions [5]. In the present study, no significant difference was observed in the expression of claudin-5 and VE-cadherin among the 3 iBRB models. The data suggest that decreasing the TJ protein's expression of ZO-1 and occludin may be the mechanism of RMP regulation on iBRB integrity under indirect contact condition. The suggestion may improve our understanding of the pathological phenomenon in diabetic retinopathy *in vivo* that the loss of RMPs or the loss of direct contacts of ECs with RMPs occurs before BRB dysfunction and EC migration. But how RMPs regulate MMP-2/9 to affect iBRB integrity when RMPs lose indirect contact with ECs remains to be elucidated. Future studies will address these limitations by conducting experiments in EC-specific MMP-2/9-KO mice, investigating the role of exosome in paracrine signals of RMPs and ECs and determining how RMPs contribute to the integrity and function of iBRB in clinical studies when the loss of direct contact of ECs with RMPs occurs.

5. Conclusions

In summary, the results presented here are the first to reveal the influence of RMP relative location on iBRB model *in vitro*. RMPs with indirect contact of ECs can increase expression of MMP-2 and upgrade activity of MMP-2/9, which subsequently decreases TJ protein abundance of ZO-1 and occludin in ECs, promotes the migration of ECs, and finally reduces the integrity of iBRB. Since the loss of direct contacts of ECs with RMPs is a general phenomenon in retinal pathology, our observations likely have important implications for treating diabetic retinopathy and other retinal disorders involving iBRB dysfunction.

Data Availability

The datasets used and/or analyzed during the current study are available from the corresponding author on reasonable request.

Conflicts of Interest

The authors declare that there is no conflict of interest regarding the publication of this article.

Authors' Contributions

Tianye Yang and Liang Guo contributed equally to this work.

Acknowledgments

This work was supported by a grant from the Natural Science Foundation of Fujian Province of China (grant number 2020J011037) and National Natural Science Foundation of China (grant number 81774369).

References

[1] H. Huang, "Pericyte-endothelial interactions in the retinal microvasculature," *International Journal of Molecular Sciences*, vol. 21, no. 19, p. 7413, 2020.

[2] N. Hudson and M. Campbell, "Inner blood-retinal barrier regulation in retinopathies," *Advances in Experimental Medicine and Biology*, vol. 1185, pp. 329–333, 2019.

[3] J. Cunha-Vaz, "The blood-retinal barrier in the management of retinal disease: EURETINA award lecture," *Ophthalmologica*, vol. 237, no. 1, pp. 1–10, 2017.

[4] M. Diaz-Coranguez, C. Ramos, and D. A. Antonetti, "The inner blood-retinal barrier: cellular basis and development," *Vision Research*, vol. 139, pp. 123–137, 2017.

[5] I. Klaassen, C. J. F. van Noorden, and R. O. Schlingemann, "Molecular basis of the inner blood-retinal barrier and its breakdown in diabetic macular edema and other pathological conditions," *Progress in Retinal and Eye Research*, vol. 34, pp. 19–48, 2013.

[6] C. Zihni, C. Mills, K. Matter, and M. S. Balda, "Tight junctions: from simple barriers to multifunctional molecular gates," *Nature Reviews. Molecular Cell Biology*, vol. 17, no. 9, pp. 564–580, 2016.

[7] C. A. Dessalles, A. Babataheri, and A. I. Barakat, "Pericyte mechanics and mechanobiology," *Journal of Cell Science*, vol. 134, no. 6, article jcs240226, 2021.

[8] L. Alarcon-Martinez, M. Yemisci, and T. Dalkara, "Pericyte morphology and function," *Histology and Histopathology*, vol. 36, no. 6, pp. 633–643, 2021.

[9] K. Hayashi, S. Nakao, R. Nakaoke, S. Nakagawa, N. Kitagawa, and M. Niwa, "Effects of hypoxia on endothelial/pericytic co-culture model of the blood- brain barrier," *Regulatory Peptides*, vol. 123, no. 1-3, pp. 77–83, 2004.

[10] R. R. Shivers, M. Pollock, P. D. Bowman, and B. G. Atkinson, "The effect of heat shock on primary cultures of brain capillary endothelium: inhibition of assembly of zonulae occludentes and the synthesis of heat-shock proteins," *European Journal of Cell Biology*, vol. 46, no. 1, pp. 181–195, 1988.

[11] A. Armulik, G. Genove, and C. Betsholtz, "Pericytes: developmental, physiological, and pathological perspectives, problems, and promises," *Developmental Cell*, vol. 21, no. 2, pp. 193–215, 2011.

[12] J. Liu, X. Jin, K. J. Liu, and W. Liu, "Matrix metalloproteinase-2-mediated occludin degradation and caveolin-1-mediated claudin-5 redistribution contribute to blood-brain barrier damage in early ischemic stroke stage," *The Journal of Neuroscience*, vol. 32, no. 9, pp. 3044–3057, 2012.

[13] A. Jablonska-Trypuc, M. Matejczyk, and S. Rosochacki, "Matrix metalloproteinases (MMPs), the main extracellular matrix (ECM) enzymes in collagen degradation, as a target for anticancer drugs," *Journal of Enzyme Inhibition and Medicinal Chemistry*, vol. 31, no. sup1, pp. 177–183, 2016.

[14] T. Klein and R. Bischoff, "Physiology and pathophysiology of matrix metalloproteases," *Amino Acids*, vol. 41, no. 2, pp. 271–290, 2011.

[15] J. Drankowska, M. Kos, A. Kościuk et al., "MMP targeting in the battle for vision: recent developments and future prospects in the treatment of diabetic retinopathy," *Life Sciences*, vol. 229, pp. 149–156, 2019.

[16] Y. Di, Q. Z. Nie, and X. L. Chen, "Matrix metalloproteinase-9 and vascular endothelial growth factor expression change in experimental retinal neovascularization," *International Journal of Ophthalmology*, vol. 9, no. 6, pp. 804–808, 2016.

[17] N. Mathalone, N. Lahat, M. A. Rahat, K. Bahar-Shany, Y. Oron, and O. Geyer, "The involvement of matrix metalloproteinases 2 and 9 in rat retinal ischemia," *Graefe's Archive for Clinical and Experimental Ophthalmology*, vol. 245, no. 5, pp. 725–732, 2007.

[18] A. Zozulya, C. Weidenfeller, and H. Galla, "Pericyte-endothelial cell interaction increases MMP-9 secretion at the blood- brain barrier in vitro," *Brain Research*, vol. 1189, pp. 1–11, 2008.

[19] G. A. Rosenberg and Y. Yang, "Vasogenic edema due to tight junction disruption by matrix metalloproteinases in cerebral ischemia," *Neurosurgical Focus*, vol. 22, no. 5, article E4, pp. 1–9, 2007.

[20] Y. Yang, E. Y. Estrada, J. F. Thompson, W. Liu, and G. A. Rosenberg, "Matrix metalloproteinase-mediated disruption of tight junction proteins in cerebral vessels is reversed by synthetic matrix metalloproteinase inhibitor in focal ischemia in rat," *Journal of Cerebral Blood Flow and Metabolism*, vol. 27, no. 4, pp. 697–709, 2007.

[21] G. A. Rosenberg, "Matrix metalloproteinases in neuroinflammation," *Glia*, vol. 39, no. 3, pp. 279–291, 2002.

[22] C. F. Chantrain, P. Henriet, S. Jodele et al., "Mechanisms of pericyte recruitment in tumour angiogenesis: a new role for metalloproteinases," *European Journal of Cancer*, vol. 42, no. 3, pp. 310–318, 2006.

[23] Y. Funahashi, C. J. Shawber, A. Sharma, E. Kanamaru, Y. K. Choi, and J. Kitajewski, "Notch modulates VEGF action in endothelial cells by inducing matrix metalloprotease activity," *Vasc Cell*, vol. 3, no. 1, p. 2, 2011.

[24] G. Thanabalasundaram, J. El-Gindi, M. Lischper, and H. J. Galla, "Methods to assess pericyte-endothelial cell interactions in a coculture model," *Methods in Molecular Biology*, vol. 686, pp. 379–399, 2011.

[25] H. Jianyan, W. Qiang, S. Beiwen, J. I. Li-Li, C. H. Yong-Dong, and Y. A. Liang, "Improved primary culture and identification of rat retinal microvascular endothelial cells in vitro," *Ophthalmology in China*, vol. 21, no. 4, pp. 261–263, 2012.

[26] G. Liu, C. Meng, M. Pan et al., "Isolation, purification, and cultivation of primary retinal microvascular pericytes: a novel model using rats," *Microcirculation*, vol. 21, no. 6, pp. 478–489, 2014.

[27] A. K. George, R. P. Homme, A. Majumder, S. C. Tyagi, and M. Singh, "Effect ofMMP-9gene knockout on retinal vascular form and function," *Physiological Genomics*, vol. 51, no. 12, pp. 613–622, 2019.

[28] C. G. Fresta, A. Fidilio, G. Caruso et al., "A new human blood-retinal barrier model based on endothelial cells, pericytes, and astrocytes," *International Journal of Molecular Sciences*, vol. 21, no. 5, p. 1636, 2020.

[29] E. K. Hollmann, A. K. Bailey, A. V. Potharazu, M. D. Neely, A. B. Bowman, and E. S. Lippmann, "Accelerated differentiation of human induced pluripotent stem cells to blood-brain barrier endothelial cells," *Fluids Barriers CNS*, vol. 14, no. 1, p. 9, 2017.

[30] P. A. Stewart and U. I. Tuor, "Blood-eye barriers in the rat: correlation of ultrastructure with function," *The Journal of Comparative Neurology*, vol. 340, no. 4, pp. 566–576, 1994.

[31] D. E. Sims, "Diversity within pericytes," *Clinical and Experimental Pharmacology & Physiology*, vol. 27, no. 10, pp. 842–846, 2000.

[32] A. Armulik, A. Abramsson, and C. Betsholtz, "Endothelial/pericyte interactions," *Circulation Research*, vol. 97, no. 6, pp. 512–523, 2005.

[33] T. Chan-Ling, M. E. Koina, J. R. McColm et al., "Role of $CD44^+$ stem cells in mural cell formation in the human choroid: evidence of vascular instability due to limited pericyte ensheathment," *Investigative Ophthalmology & Visual Science*, vol. 52, no. 1, pp. 399–410, 2011.

[34] P. Carmeliet, "Angiogenesis in health and disease," *Nature Medicine*, vol. 9, no. 6, pp. 653–660, 2003.

[35] R. Daneman, L. Zhou, A. A. Kebede, and B. A. Barres, "Pericytes are required for blood-brain barrier integrity during embryogenesis," *Nature*, vol. 468, no. 7323, pp. 562–566, 2010.

[36] K. Y. Aguilera and R. A. Brekken, "Recruitment and retention: factors that affect pericyte migration," *Cellular and Molecular Life Sciences*, vol. 71, no. 2, pp. 299–309, 2014.

[37] Y. Takahashi, T. Maki, A. C. Liang et al., "p38 MAP kinase mediates transforming-growth factor-β1-induced upregulation of matrix metalloproteinase-9 but not -2 in human brain pericytes," *Brain Research*, vol. 1593, pp. 1–8, 2014.

[38] R. G. Underly, M. Levy, D. A. Hartmann, R. I. Grant, A. N. Watson, and A. Y. Shih, "Pericytes as inducers of rapid, matrix metalloproteinase-9-dependent capillary damage during ischemia," *The Journal of Neuroscience*, vol. 37, no. 1, pp. 129–140, 2017.

[39] F. Takata, S. Dohgu, J. Matsumoto et al., "Brain pericytes among cells constituting the blood-brain barrier are highly sensitive to tumor necrosis factor-α, releasing matrix metalloproteinase-9 and migrating in vitro," *Journal of Neuroinflammation*, vol. 8, no. 1, p. 106, 2011.

[40] B. Srinivasan, A. R. Kolli, M. B. Esch, H. E. Abaci, M. L. Shuler, and J. J. Hickman, "TEER measurement techniques for in vitro barrier model systems," *Journal of Laboratory Automation*, vol. 20, no. 2, pp. 107–126, 2015.

[41] J. L. Barr, G. C. Brailoiu, E. M. Unterwald, and E. Brailoiu, "Assessment of blood-brain barrier permeability using miniaturized fluorescence microscopy in freely moving rats," *Methods in Molecular Biology*, vol. 2367, pp. 123–135, 2021.

[42] A. al Ahmad, M. Gassmann, and O. O. Ogunshola, "Maintaining blood-brain barrier integrity: pericytes perform better than astrocytes during prolonged oxygen deprivation," *Journal of Cellular Physiology*, vol. 218, no. 3, pp. 612–622, 2009.

[43] S. Nakagawa, M. A. Deli, H. Kawaguchi et al., "A new blood-brain barrier model using primary rat brain endothelial cells, pericytes and astrocytes," *Neurochemistry International*, vol. 54, no. 3-4, pp. 253–263, 2009.

[44] J. Wisniewska-Kruk, K. A. Hoeben, I. M. Vogels et al., "A novel co-culture model of the blood-retinal barrier based on primary retinal endothelial cells, pericytes and astrocytes," *Experimental Eye Research*, vol. 96, no. 1, pp. 181–190, 2012.

[45] S. J. Giebel, G. Menicucci, P. G. McGuire, and A. Das, "Matrix metalloproteinases in early diabetic retinopathy and their role in alteration of the blood-retinal barrier," *Laboratory Investigation*, vol. 85, no. 5, pp. 597–607, 2005.

[46] E. E. Schneeberger and R. D. Lynch, "The tight junction: a multifunctional complex," *American Journal of Physiology. Cell Physiology*, vol. 286, no. 6, pp. C1213–C1228, 2004.

Hindawi
Disease Markers
Volume 2021, Article ID 6482665, 13 pages
https://doi.org/10.1155/2021/6482665

Research Article

EAD-Net: A Novel Lesion Segmentation Method in Diabetic Retinopathy Using Neural Networks

Cheng Wan,[1] **Yingsi Chen**,[1] **Han Li**,[1] **Bo Zheng**,[2] **Nan Chen**,[3] **Weihua Yang**,[3] **Chenghu Wang**,[3] **and Yan Li**[4]

[1]*Nanjing University of Aeronautics and Astronautics, College of Electronic and Information Engineering, 211106, China*
[2]*Huzhou University, School of Information Engineering, 313000, China*
[3]*The Affiliated Eye Hospital of Nanjing Medical University, 210029, China*
[4]*The Affiliated Traditional Chinese Medicine Hospital of Southwest Medical University, 646000, China*

Correspondence should be addressed to Weihua Yang; benben0606@139.com, Chenghu Wang; wangchenghu1226@163.com, and Yan Li; liyan0511@139.com

Received 13 July 2021; Accepted 19 August 2021; Published 2 September 2021

Academic Editor: Ting Su

Diabetic retinopathy (DR) is a common chronic fundus disease, which has four different kinds of microvessel structure and microvascular lesions: microaneurysms (MAs), hemorrhages (HEs), hard exudates, and soft exudates. Accurate detection and counting of them are a basic but important work. The manual annotation of these lesions is a labor-intensive task in clinical analysis. To solve the problem, we proposed a novel segmentation method for different lesions in DR. Our method is based on a convolutional neural network and can be divided into encoder module, attention module, and decoder module, so we refer it as EAD-Net. After normalization and augmentation, the fundus images were sent to the EAD-Net for automated feature extraction and pixel-wise label prediction. Given the evaluation metrics based on the matching degree between detected candidates and ground truth lesions, our method achieved sensitivity of 92.77%, specificity of 99.98%, and accuracy of 99.97% on the e_ophtha_EX dataset and comparable AUPR (Area under Precision-Recall curve) scores on IDRiD dataset. Moreover, the results on the local dataset also show that our EAD-Net has better performance than original U-net in most metrics, especially in the sensitivity and F1-score, with nearly ten percent improvement. The proposed EAD-Net is a novel method based on clinical DR diagnosis. It has satisfactory results on the segmentation of four different kinds of lesions. These effective segmentations have important clinical significance in the monitoring and diagnosis of DR.

1. Introduction

Diabetes is a common chronic disease that has a large number of patients over the world. It is a global public health problem related to microcirculation disorders which seriously affects human health. Diabetic retinopathy (DR) is a common complication of diabetes, so it is also a serious chronic disease. DR is caused by the insufficient blood supply and capillary occlusion due to excessive blood sugar content. In severe cases, it would lead to irreversible damage and even blindness. Therefore, the timely monitoring and treatment are essential for DR patients. The analysis of microvascular lesion areas is one of the important ways of diagnosis. In retinal fundus images, typical symptoms of DR mainly include microaneurysms (MAs), hemorrhages (HEs), hard exudates, and soft exudates, which are the major features of DR.

As shown in Figure 1, the first detectable abnormalities of DR are MAs, which present as small red dots. MAs are formed due to the local distensions of capillary walls caused by high blood glucose on the surface of retina [2]. When MAs ruptured, they would cause intraretinal hemorrhages, which are also important features in the early stage of DR. HEs have irregular shapes and sizes, and their color is very similar to the background. Hard exudates are yellow lipid formations that leak as a result of increased capillary permeability, presenting as bright yellow exudates of irregular shape and well-defined boundaries. Soft exudates are

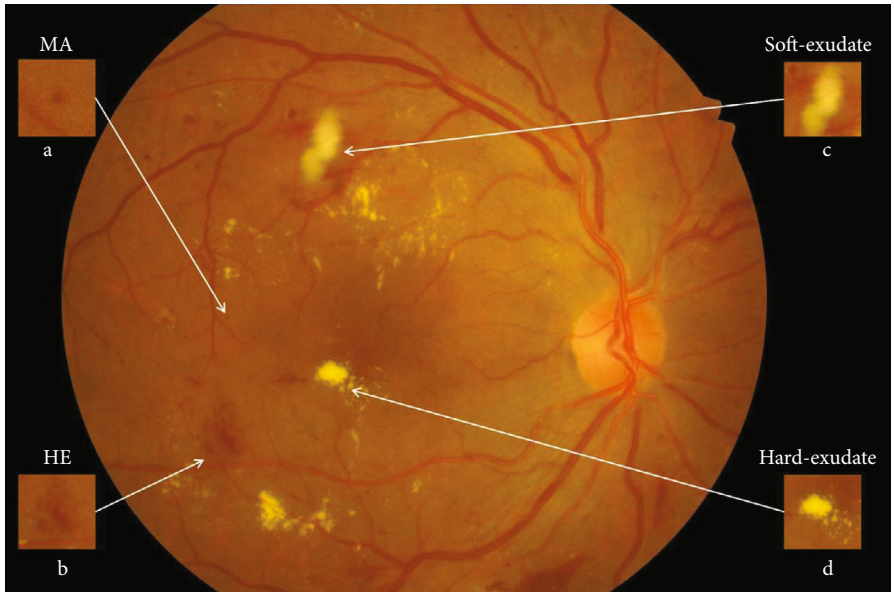

Figure 1: Lesions of DR in IDRiD_49.jpg from IDRiD dataset [1]. (a) Microaneurysm (MA). (b) Hemorrhage (HE). (c) Soft exudate. (d) Hard exudate.

essentially microinfarcts of the retinal nerve fiber layer, presenting as cotton-wool spots of irregular shape and fuzzy boundaries.

In recent years, many approaches have been applied to the lesion detection of DR, because detecting defective areas is an important step and one of the most labor-intensive tasks in clinical diagnosis. According to the characteristics of different lesion areas, we define the MAs and HEs as red lesions and define the hard exudates and soft exudates as bright lesions.

As for the detection of red lesions, since MAs and HEs are usually early abnormal signs of DR, the accurate detection of them is crucial for the early diagnosis. On account of similar circular shape and limited size range, the detections of MAs mainly include morphological operations [3, 4] and image filtering [5, 6]. Some other researches combine MA and HE detections, such as the algorithm based on curvelet transform proposed by Esmaeili et al. [7]. The candidate pixels belonging to red lesions and blood vessels are separated from a reconstructed retinal image with modified coefficients, and then, the full curvelet-based blood vessels are removed, leaving the remaining part as detected red lesions. Similarly, all dark-colored structures can be extracted as candidates, and then pixels belonging to vessels are eliminated by using a multilayer perception [8] or multiscale morphological closing operation [9]. However, the aforementioned algorithms might consider some actually red lesions as false positives to be removed, so these lesions are left out and directly affect the rate of detection. To solve the problem, an automatic red lesion detection algorithm using dynamic shape features [10, 11] is proposed. In this method, candidate regions do not need to be segmented precisely before feature extraction. Instead, a new set of shape features, called dynamic shape features, are extracted for each candidate region which is identified based on intensity and contrast.

As for the detection of bright lesions, Harangi and Hajdu [12] divided exudate detection into three stages: at first, a grayscale morphology-based candidate extractor method is used to recognize the bright lesions contained regions, then, an active contour method is applied to obtain the precise boundary segmentation, and finally, false exudate candidates are removed by a region-wise classifier. An unsupervised approach [13] for exudate segmentation is based on an ant colony optimization algorithm to solve the numerous manually labeling works needed in supervised methods. Many research works have been done for the detection of hard exudates: Banerjee and Kayal [14] proposed a method which employs morphological operations to eliminate optic disc, mean shift [15], and normalized cut [16] to extract hard exudates and Canny's operator to demarcate exudate boundary more clearly. Jaya et al. [17] proposed a hard exudate detection system designed using a fuzzy support vector machine (FSVM) classifier. In addition, only a few researches work for the detection of soft exudates (also called cotton wool spot) because it is difficult to filter out soft exudates from the background. Bui et al. [18] presented an automatic segmentation method which consists of image enhancement, optic disc removal, selective feature extraction, and a neural network model. Sreng et al. proposed an algorithm [19] based on the integration of principal component analysis (PCA) and support vector machine (SVM) for accurate detection of cotton wool spots. The authors also proposed another detection method [20] based on adaptive threshold and ant colony optimization (ACO) combined with SVM and achieved better performance.

With the development of convolutional neural networks (CNNs), various image segmentation algorithms have made breakthroughs in both speed and accuracy. One of the most popular methods for biomedical segmentation tasks was called U-net [21], which followed an encoder-decoder structure. There are many different improvements of the U-net

model, such as an ensemble MU-net [22], designed to detect exudates with limited data, and a multitask architecture [23] for the joint segmentation of different lesions. Besides, Quellec et al. [24] proposed a deep learning algorithm supervised at image level and produced heatmaps to improve DR detection. Javidi et al. presented dictionary learning-based algorithms to segment exudates using extension of morphological component analysis [25] and to detect microaneurysm using sparse representation [26]. Dai et al. [27] combined an image-to-text model and multisieving CNN to identify microaneurysm and solve the unbalanced data distribution problem. Pratt et al. [28] also proposed a CNN approach for DR diagnosis and grading and achieved good performance on a large dataset.

The main contribution of this paper can be summarized as follows. Since the pixel-level lesion segmentation, especially, the segmentation of both red lesions and bright lesions is still rare, we focus on segmenting four different lesion areas with a supervised method which can work with limited labeled datasets. In this paper, we present a novel convolutional neural network EAD-Net, which is composed of encoder module, dual attention module, and decoder module. Experimental results show that the proposed EAD-Net can achieve pixel-level accuracy for different kinds of lesions. Our method has competitive performance in both qualitative and quantitative analyses than other state-of-the-art methods.

2. Methods

In this section, we describe the datasets used and the methods employed to segment different kinds of lesions. Firstly, in addition to two public benchmark datasets for the comparison with other state-of-the-art algorithms, a local dataset with hundreds of clinical images is also introduced for validation. Secondly, we describe the architecture of EAD-Net and illustrate the detailed structures of encoder module, dual attention module, and decoder module, respectively. Thirdly, we introduce the network training process including data normalization, data augmentation, and parameter settings. Finally, we designed an evaluation method based on the matching degree between detected candidates and ground truth lesions to analyze the segmentation results more appropriately.

2.1. Datasets. In this paper, we evaluated the performance of our proposed network on two publicly available datasets: e_ophtha_EX [29] and IDRiD [1], for the comparison with other latest algorithms. Furthermore, we also evaluated our model on a local intelligent ophthalmology dataset compared with U-net as the baseline for additional validation.

The public e_ophtha_EX dataset consists of 82 labeled images with precise lesion annotation. These images have four different sizes ranging from 1440×960 to 2544×1696 pixels. 47 images have exudates which were marked by two ophthalmologists, and 35 images contain no exudates.

The public IDRiD (Indian Diabetic Retinopathy Image Dataset) consists of 81 images with a resolution of 4288×2848 pixels. It provides pixel-level annotations of four lesions. The partition of the training set and testing set is provided on IDRiD, with 54 images for training and the rest 27 images for testing. All images in the testing set have MAs, HEs, and hard exudates, and 14 images of them have soft exudates.

The local intelligent ophthalmology dataset is a general high-quality dataset for eye disease classification and lesion segmentation. Our study was conducted in collaboration with the Affiliated Eye Hospital of Nanjing Medical University. From more than 10,000 clinical color fundus images, 262 images were selected for this research and all images have been desensitized for common use. In this dataset, 63 images have MAs, 84 images have HEs, 86 images have hard exudates, and 29 images have soft exudates. In addition, their corresponding pixel-level annotation images are provided. In lesion annotation, there were five ophthalmologists involved. To minimize the probability of mislabeling, all the images were labeled by four ophthalmologists and checked by a chief ophthalmologist at last. The detailed annotation example is shown in Figure 2.

2.2. Network Architecture

2.2.1. Overview of the Proposed EAD-Net. The proposed EAD-Net can be divided into three parts: encoder module, dual attention module, and decoder module (as shown in Figure 3). The U-shaped structure composed of an encoder and decoder, as well as skip connections, enables the network to combine high-level semantic information and low-level feature. Furthermore, the dual attention modules can capture long-range contextual information in both spatial and channel dimensions and therefore obtain better feature representations.

Specifically, through convolution and pooling, we can get the Map1; then, we use a convolution block with residual structure in the downsampling process. With the residual structure, the gradient can propagate directly through the skip connection from later layers to the earlier layers, so the vanishing gradient problem can be inhibited. These factors guarantee the stability of the whole network in a training process. Before the skip connection, Map3 and Map4 are sent through a dual attention module [30], which is composed of a position attention module and a channel attention module. Finally, the feature maps of each dimension are put into the decoder module to accomplish the segmentation of different kinds of lesions. Figure 3 shows an overview of the EAD-Net architecture.

2.2.2. Encoder Module. Different from the widely used U-net, we choose a convolution block with a residual structure to replace the traditional encoder. And we only use the pooling layer once during the whole downsampling process. There are many tiny lesions in the segmentation of DR lesions, and too many pooling layers might go against recovering the features of the tiny targets in decoder stage. Therefore, in the later downsampling process, we use the convolution layer (stride is set to 2) to replace the pooling layer. The green hollow arrows in Figure 3 contain the conv block and identity block (as shown in Figure 4).

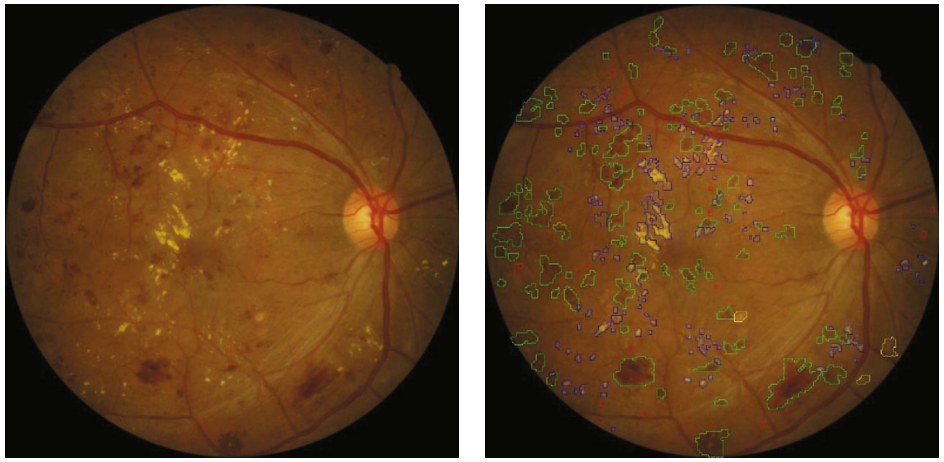

(a) (b)

Figure 2: Annotation example of the local dataset. (a) The original image. (b) The corresponding annotation result: MAs in the red area, HEs in the green area, hard exudates in the blue area, and soft exudates in the yellow area.

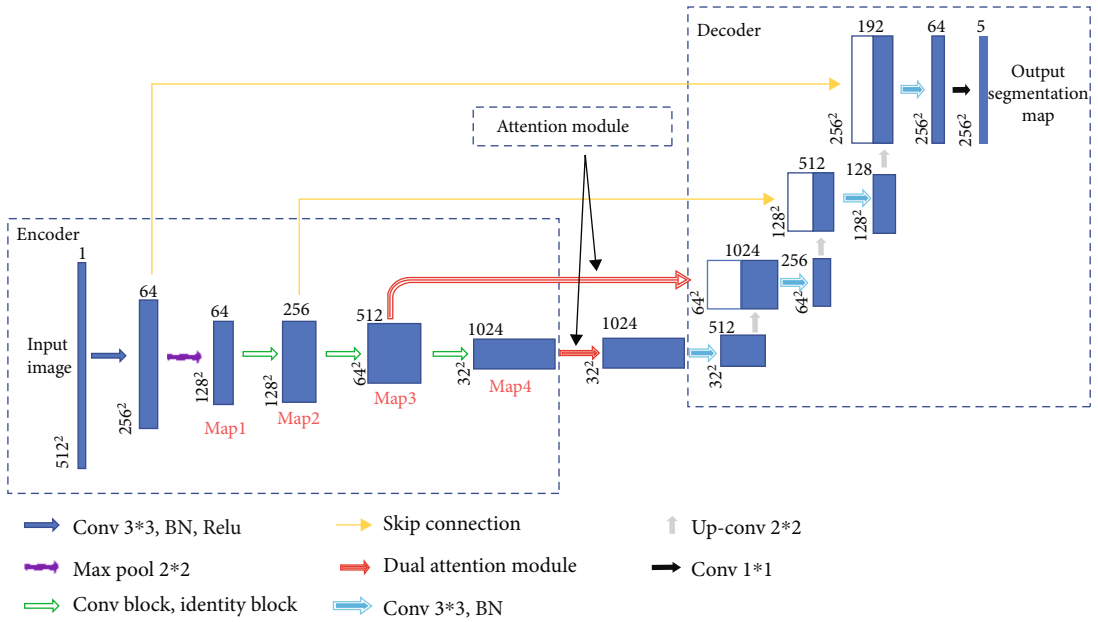

Figure 3: The overview of the EAD-Net architecture.

As we can see in Figure 4, conv block and identity block have almost the same structure. We learn from the idea of skip connection proposed in the ResNet [31]. In conv block, the input firstly passes through the same convolution, batch normalization, and Relu layers twice. Next, the result of the second Relu layer and the original input are added up after convolution and batch normalization. The added result is activated through the Relu layer to get the final output. What differentiates the two blocks is that in identity block the input is directly added up through a skip connection. One other thing to note is that the size of convolution kernels is set to the same 3×3.

The number of convolution kernels in the blocks shown in Figure 4 is subject to the bottleneck structure; that is, the output channel number of the input and output is generally four times as many as the channel number of the first two convolution parts. With this strategy, the number of training parameters can achieve a considerable reduction. It is worth noting that the number of channels indicated in the figure is not constant all the time. With the abovementioned proportional relationship, they will increase with the depending network, typically exponentially.

2.2.3. Dual Attention Module. Dual attention module is a self-attention mechanism proposed by Fu et al. [30] and was applied to semantic segmentation. It can capture long-range contextual information in both spatial and channel dimensions. The position attention module (PAM)

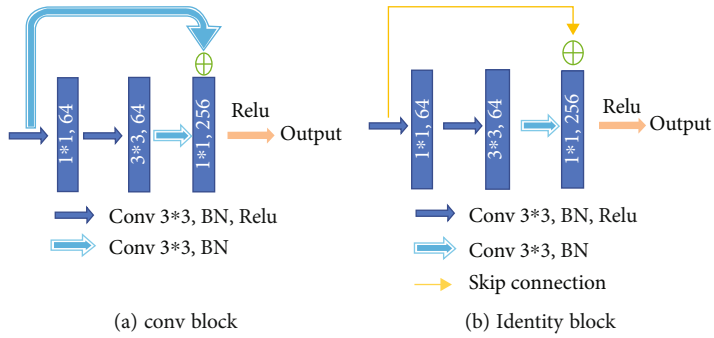

Figure 4: Detailed operations represented by the green arrow in the overview of the EAD-Net architecture.

selectively aggregates the features of each position through a weighted sum of all positions, while the channel attention module (CAM) selectively emphasizes one feature map through all feature maps. The outputs of two attention modules are aggregated to obtain the better feature representations. The structure of dual attention module is shown in Figures 5 and 6.

In order to accommodate the specific morphology of DR lesions, we have also proposed some corresponding improvements.

There are often many small and fuzzy lesions existing in the fundus images. As what we have mentioned previously, too many pooling layers might lead to too much semantic information loss. To avoid this problem, we only use the max pooling layer once. Moreover, in the later decoder structure, to obtain the pixel-wise output, a larger size of feature map needs to be upsampled from the deep feature map, which might also cause the information loss. So the dilated convolution [32] strategy is introduced as an improvement. The dilated convolution with different dilation rates can produce a larger receptive field and capture multiscale contextual information. The blue sample block in Figure 6 contains three dilated convolutions. We set the dilation rates to 1, 2, and 5, respectively, to avoid gridding effect.

2.2.4. Decoder Module. In the decoder module, we adopt the upsampling structure of U-net. The features of encoder and decoder at the same level can achieve global information fusion through concatenation. And the high-resolution information generated by the encoder output can provide more detailed guidance in the segmentation of lesions. The structure of decoder module is shown in Figure 7.

2.3. Network Training. In order to facilitate the processing of neural network, the size of all input images and labels is normalized into 1024×1024 pixels. The purpose of this step is to preprocess the images and unify the size of all datasets without losing images' details. Meanwhile, in order to keep the information of input images as much as possible and make the image undistorted when its size changed (that is, maintain the aspect ratio of the image), we take the following steps: firstly, remove the redundant black edges around the original image. Next, according to the long side after the interception, the short side is filled to be equal to the long side. Finally, the size of the filled image is transformed to obtain an image of 1024×1024 pixels. We also cut and resize the corresponding ground truth segmentation image in the same way. The normalization process is shown in Figure 8.

High-quality datasets are valuable in the field of medical segmentation. Considering the lack of training data, data augmentation is beneficial when training the neural network. The data augmentation transformations consist of horizontally and vertically flipping, scaling images in per axis, translating, and rotation. Notice that we did not apply all these methods to every input image; instead, we select some combinations of them randomly to accomplish the augmentation. After data augmentation, the number of training dataset images could be up to five times larger.

Using the images with original size will run out of hardware limitations. In order not to lose image information in the maximum case, all images are resized to 512×512 pixels before being sent to the network training. Since the partition of training set and testing set is provided on IDRiD, with 54 images for training and the rest 27 images for testing, we also applied this partition ratio to e_ophtha_EX and local datasets in this research. There was not any overlap between training and testing data. For each dataset, two-thirds of the images were randomly selected for training and the remaining third for testing. That is to say, the partition ratio of training set and testing set is set to 2 : 1.

In the training process, firstly, the network's hyperparameters are gradually adjusted by the effect on the validation set. In this way, we set the batch size to 2, dropout rate to 0.5, Adam as the optimizer, and BCEDiceLoss (binary cross entropy and dice loss) as the loss function. In addition, we use the loss value as a monitoring indicator during training the network. The learning rate is set to 0.0001 and is lowered by 10 times after five epochs when the indicator does not improve. An early stopping method is also applied to the training process. If the indicator does not improve after 15 epochs, the training process would stop. The network for comparison follows the same training settings.

All the programs in this paper are based on Python. The construction and training process of the network are applied on Keras platform. Parallel computing is conducted by GPU, and the hardware environment is NVIDA GTX 1080.

2.4. Evaluation Metrics. The evaluation can be classically done by simply calculating the number of correctly

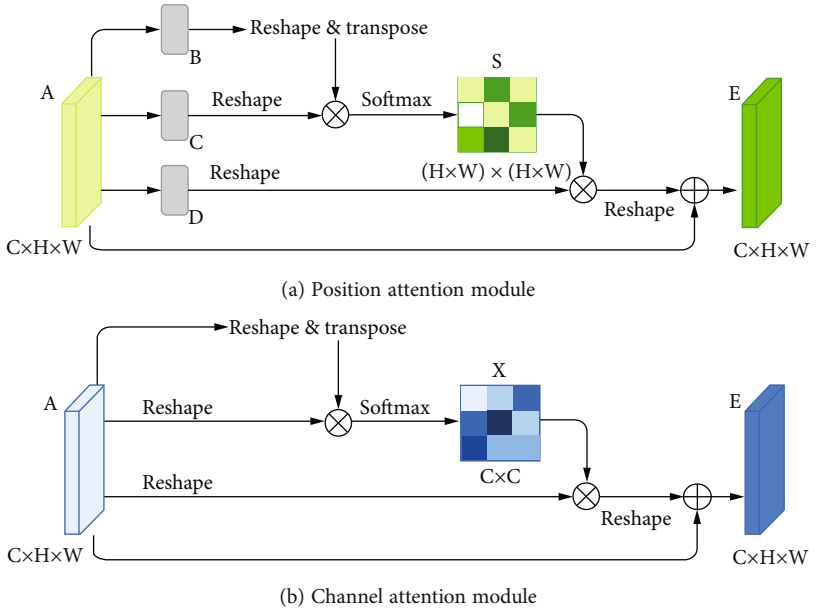

Figure 5: Illustration [30] of position attention module and channel attention module.

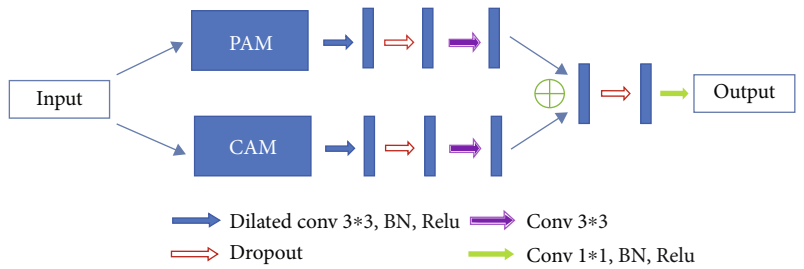

Figure 6: Detailed processing steps of dual attention module.

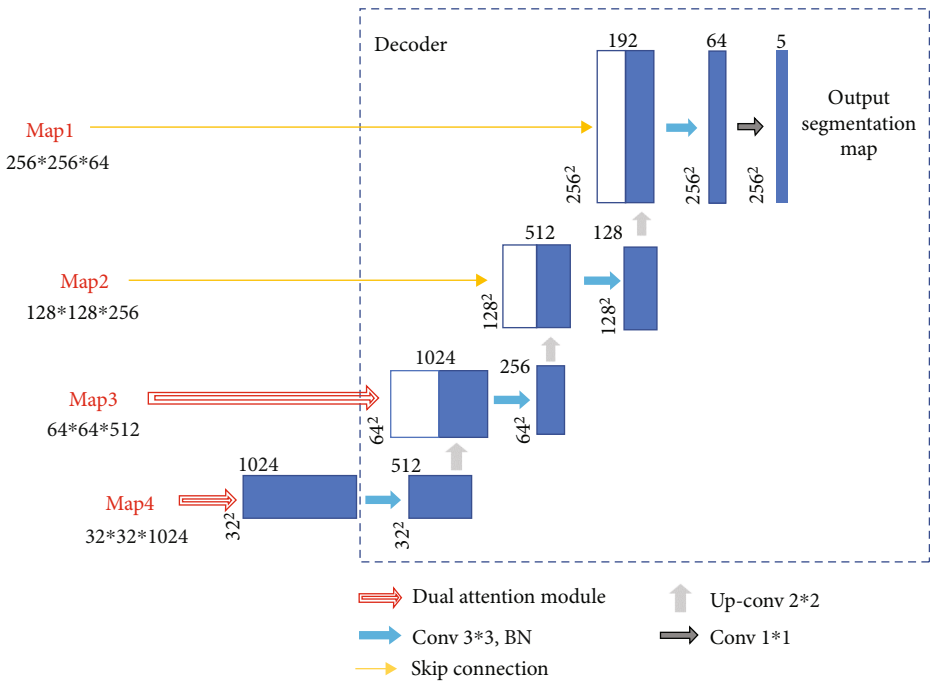

Figure 7: Illustration of the decoder module.

(a) (b) (c)

Figure 8: Size normalization process. (a) The original image. (b) Remove the redundant black edges. (c) The final result.

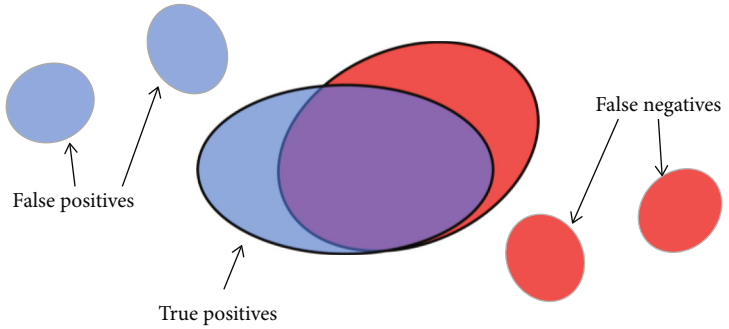

Figure 9: Illustration of the proposed evaluation method. Detected candidates are represented by blue areas and ground truth lesions by red areas. True positive pixels are defined by the matching degree of blue and red connected components.

identified pixels or by comparing the number of detected lesions with the number of real lesions. However, we consider that both of these methods have shortcomings in analyzing the segmentation of lesions. Suppose a situation as shown in Figure 9: there are three detected lesions (shown in blue) and three ground truth lesions (shown in red). Only the two large connected components in the middle are partially overlapped. It is clear that the larger the intersection area is, the greater the matching degree between the detected candidates and ground truth is.

On the one hand, if we only calculate the number of correctly identified pixels, in this case, the true positives only refer to the intersection area of blue and red, while half blue pixels and half red pixels in the nonoverlapping part are considered false positives and false negatives. This kind of evaluation method tends to get underestimated error rate on small connected components. On the other hand, it seems inappropriate to directly compare the number of detected lesions and ground truth lesions. For example, in Figure 9, there are 3 detected lesions and 3 ground truth lesions, but obviously, the results in the figure do not mean that the accuracy of lesion segmentation has reached 100%. Therefore, we applied the evaluation method proposed by Zhang et al. [29]: the matching degree between the detected candidates and the ground truth areas was considered. To be specific, if there are N detected candidates $\{D_1, D_2, \cdots, D_N\}$ and M ground truth lesions $\{G_1, G_2, \cdots, G_M\}$, the set of detected candidates can be expressed as

$$D = \bigcup_{1 \le i \le N} D_i, \tag{1}$$

and the set of ground truth lesions can be expressed as

$$G = \bigcup_{1 \le j \le M} G_j. \tag{2}$$

Then we can give the definition of true positive (TP), false positive (FP), false negative (FN), and true negative (TN) as follows.

A pixel is considered TP if and only if it belongs to any of the following sets:

(i)

$$D \cap G \tag{3}$$

(ii) D_i such that $(|D_i \cap G|/|D_i|) > \sigma$

(iii) G_j such that $(|G_j \cap D|/|G_j|) > \sigma$

$|\cdot|$ is the cardinality of a set, and the σ is a factor used to evaluate the proportion of overlapping area between the detected candidates and ground truth. The σ ranges from 0 to 1. When $\sigma = 0$, a detected candidate is considered TP if and only if it touches the ground truth. Taking into

Table 1: Evaluation of exudate detection on e_ophtha_EX dataset.

Model	Lesion-level results				
	SE	SP	PR	ACC	F1
U-net	79.86	99.97	78.77	99.95	79.31
*Playout et al. [23]	80.02	—	78.50	—	79.25
*Zheng et al. [22]	94.12	99.98	91.25	99.96	92.66
Fraz et al. [33]	81.20	94.60	90.91	89.25	—
Zhang et al. [29]	74	—	72	—	—
Imani and Pourreza [34]	80.32	99.83	77.28	—	—
Javidi et al. [25]	80.51	99.84	77.30	—	—
Guo et al. [35]	84.17	—	83.45	—	83.81
*Proposed EAD-Net	92.77	99.98	89.06	99.97	90.87

SE: sensitivity; SP: specificity; PR: precision; ACC: accuracy; F1: F1 score. * are methods based on U-net.

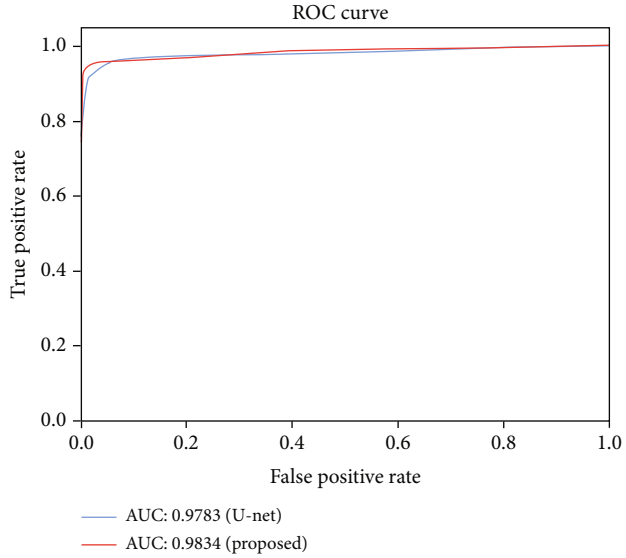

Figure 10: Evaluation on e_ophtha_EX dataset using ROC curves of U-net and the proposed EAD-Net.

consideration that in this case ($\sigma = 0$) a single very large detection mask would produce excellent results as long as it covers the whole ground truth set, a minimal overlap ratio is required. Finally, we set the σ to 0.2 to facilitate comparison with other methods.

A pixel is considered FP if and only if it belongs to any of the following sets:

(i) D_i such that $D_i \cap G = \phi$

(ii) $D_i \cap \bar{G}$ such that $(|D_i \cap G|/|D_i|) \leq \sigma$

A pixel is considered FN if and only if it belongs to any of the following sets:

(iii) G_j such that $G_j \cap D = \phi$

(iv) $G_j \cap \bar{D}$ such that $(|G_j \cap D|/|G_j|) \leq \sigma$

Pixels that do not fall into any of the above-mentioned three categories are considered TN.

Table 2: Comparison with top 10 teams in the lesion segmentation competition on IDRiD dataset.

Model (team)	MAs	HEs	Hard exudates	Soft exudates
VRT (1st)	0.4951	0.6804	0.7127	0.6995
PATech (2nd)	0.4740	0.6490	0.8850	—
iFLYTEK-MIG (3rd)	0.5017	0.5588	0.8741	0.6588
SOONER (4th)	0.4003	0.5395	0.7390	0.5369
SHAIST (5th)	—	—	0.8582	—
lzyuncc_fusion (6th)	—	—	0.8202	0.6259
SDNU (7th)	0.4111	0.4572	0.5018	0.5374
CIL (8th)	0.3920	0.4886	0.7554	0.5024
MedLabs (9th)	0.3397	0.3705	0.7863	0.2637
AIMIA (10th)	0.3792	0.3283	0.7662	0.2733
Proposed EAD-Net	0.2408	0.5649	0.7818	0.6083

The results are based on AUPR (Area under Precision-Recall curve).

Then, we computed the sensitivity, specificity, precision, accuracy, and the F1-score according to the following equations:

$$\begin{aligned} \text{Sensitivity} &= \frac{\text{TP}}{\text{TP} + \text{FN}}, \\ \text{Specificity} &= \frac{\text{TN}}{\text{TN} + \text{FP}}, \\ \text{Precision} &= \frac{\text{TP}}{\text{TP} + \text{FP}}, \\ \text{Accuracy} &= \frac{\text{TP} + \text{TN}}{\text{TP} + \text{TN} + \text{FP} + \text{FN}}, \\ \text{F1} &= \frac{2 \times \text{sensitivity} \times \text{precision}}{\text{sensitivity} + \text{precision}}. \end{aligned} \tag{4}$$

3. Results

In this section, we demonstrate the effectiveness of our EAD-Net on two public benchmark datasets and show the comparison with other state-of-the-art algorithms, especially with U-net and its variants. For additional validation, we also compared the performance of our EAD-Net with the baseline U-net on a local dataset.

3.1. Performance on the Public e_ophtha_EX Dataset. On the public e_ophtha_EX dataset, the results compared with other state-of-the-art methods are shown in Table 1. Our proposed EAD-Net outperforms other methods on most indicators. Compared with the latest study [35] proposed by Guo et al., our method is 8.6% higher in sensitivity and achieves 5.61% and 7.06% improvements in precision and F1-score. Compared with the state-of-the-art method [22] by Zheng et al., our method has competitive results in both specificity and accuracy, although there exists a small gap in sensitivity, precision, and F1-score.

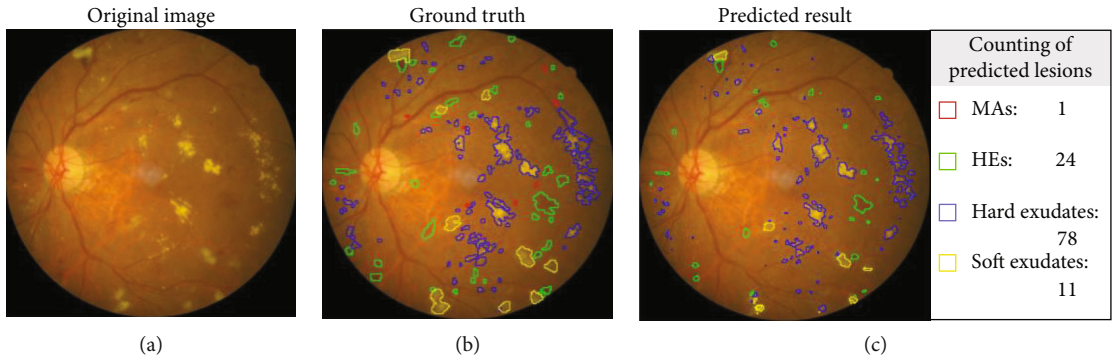

Figure 11: An example of segmentation results. (a) Original image. (b) The corresponding ground truth annotations of different lesions. (c) The predicted segmentation results. Note that the areas marked out in different colors represent different lesions: MAs in red, HEs in green, hard exudates in blue, and soft exudates in yellow. The predicted result in (c) also provides counting statistics of the four lesions. In the rectangular box on the right of (c), the number of lesions is obtained by connected components analysis of the corresponding lesion areas in the left of (c).

Figure 10 also shows the ROC (Receiver Operating Characteristic) curves with AUC (Area Under Curve) values of our method and the baseline, U-net. We can see that the EAD-Net has much better detection effect than the original U-net. The AUC value of the proposed method is 0.5% higher than the result of U-net. The improved performance demonstrates the effectiveness of the proposed EAD-Net.

3.2. Performance on the Public IDRiD Dataset. In this part, we used AUPR (Area under Precision-Recall curve) as evaluation metric, which is the same to the IDRiD challenge. The IDRiD challenge is a fundus image analysis challenge organized by the IEEE International Symposium on Biomedical Imaging (ISBI) conference. We compared our method with the top 10 teams in the lesion segmentation competition of IDRiD challenge. As we can see in Table 2, the proposed EAD-Net ranked No. 3 on HE segmentation, No. 6 on hard exudate segmentation, and No. 4 on soft exudate segmentation.

For the top 3 teams, they choose different network architectures for each segmentation task. And for each segmentation task, many hyperparameters need to be adjusted during the training stage. Therefore, these teams that performed well had to test four models for corresponding segmentation task during the test stage. In contrast, our study used a single network structure and only a few changes are needed for the hyperparameter settings. Even so, our proposed EAD-Net has achieved comparable results.

3.3. Performance on the Local Intelligent Ophthalmology Dataset. On the local intelligent ophthalmology dataset, we also evaluated the performance by comparing the matching degree between the ground truth and prediction. In this section, we performed a visual analysis of segmentation results and compared our proposed method with the original U-net, which was the baseline.

An example of segmentation results is shown in Figure 11: different color curves are used to represent the contours of different types of lesions. At the same time, through connected components analysis in the predicted images, we can also easily output the counting of different lesions (as shown in the rectangular box on the right of Figure 11(c)). These counting statistics are helpful as a reference for clinical diagnosis of DR severity. In addition, a more detailed comparison of ground truth and predicted segmentations for this example is shown in Figure 12. The different rows in Figure 12 represent different types of lesions. We use red to represent ground truth areas, blue to represent predicted lesions areas, and purple to represent the intersection of ground truth and prediction in the last column of Figure 12. From this, we can intuitively see which areas are correctly identified, which areas are misdiagnosed, and which areas are missed. For detailed definitions of the categories of predicted lesions (TP, FP, FN, or TN), please refer to Evaluation Metrics.

Compared with the baseline U-net, the results shown in Table 3 indicate that the proposed method outperforms the original U-net in most metrics, especially in the sensitivity and F1-score. And the AUCs of the EAD-Net are generally higher than U-net (as shown in Figure 13).

From all the above results on the local dataset, it can be concluded that the EAD-Net makes remarkable progress in the lesion segmentation compared with baseline U-net. However, although our network does well in the segmentation of the lesions with distinct features, such as HEs and hard exudates, the details in Figure 12 and the low sensitivity in Table 3 indicate that it is not that effective for small lesions, especially the tiny MAs. This problem would be discussed in more detail in the next section.

4. Discussion

The research of computer-aided diagnosis of DR based on fundus images is an emerging field. Most of the current DR-AI researches are based on the image labels, rather than the direct study of lesions. However, the diagnosis basis of clinical guidelines is precisely based on the identification and localization of lesions. Once the clinical guidelines are adjusted, none of the current DR-AI results can play a role. In contrast, lesion-based studies can be easily adapted to the adjustment of diagnostic rules. Therefore, we proposed a deep learning method based directly on lesions, which is

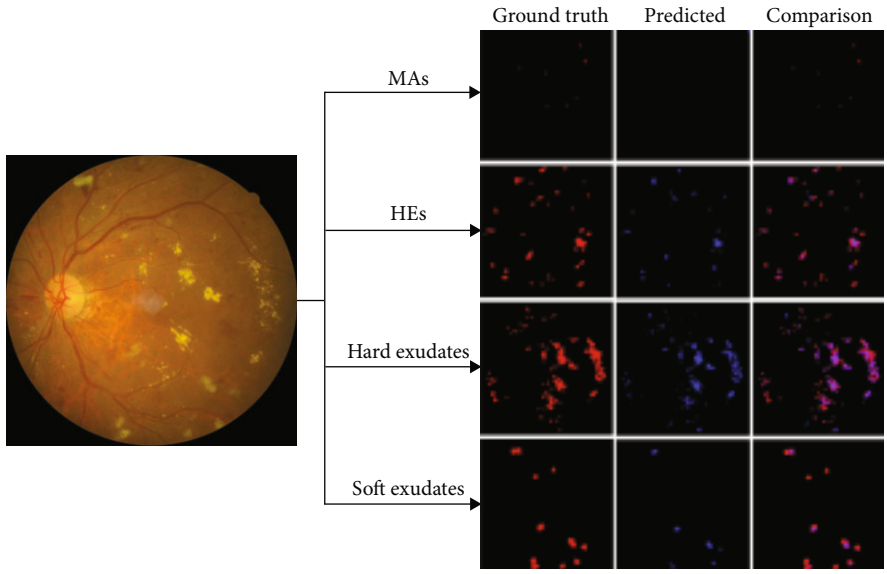

Figure 12: Detailed comparison of ground truth and predicted segmentations. Each row represents a kind of lesions. The last column represents the superimposed image of the first two images in the row. In red: ground truth areas; in blue: predicted lesions areas; in purple: the intersection of ground truth and prediction.

Table 3: Comparison with U-net on local intelligent ophthalmology dataset.

Lesion type	Model	Lesion based results				
		SE	SP	PR	ACC	F1
MAs	U-net	13.17	99.97	54.07	99.90	21.19
	EAD-Net	17.32	99.98	59.26	99.91	26.82
HEs	U-net	73.43	99.93	80.21	99.83	76.67
	EAD-Net	83.59	99.95	87.75	99.89	85.62
Hard exudates	U-net	68.38	99.99	98.42	99.96	80.70
	EAD-Net	84.60	99.99	93.51	99.98	88.83
Soft exudates	U-net	76.89	99.99	98.86	99.98	86.50
	EAD-Net	84.92	99.99	92.78	99.98	88.68

SE: sensitivity; SP: specificity; PR: precision; ACC: accuracy; F1: F1 score.

aimed at segmenting four typical lesions of DR: MAs, HEs, hard exudates, and soft exudates. In addition, the proposed method can easily output the counting of different lesions, so as to diagnose the severity of DR. In this paper, we designed a novel convolutional neural network named EAD-Net, which is composed of encoder module, dual attention module, and decoder module.

The proposed network has significant improvement in the segmentation of different lesions: MAs, HEs, hard exudates, and soft exudates. Different from the original U-net, we choose a convolution block with residual structure to replace the traditional encoder. Since there exist many small or fuzzy lesions and too many pooling layers might lead too much semantic information loss, we only use the max pooling layer once to avoid this problem. The dual attention module is designed to capture long-range contextual information in both spatial and channel dimensions, so that the network can obtain better feature representations. We also introduce the dilated convolution strategy as an improvement. By setting different dilation rates, we can get larger receptive field and multiscale contextual information. The high-resolution information generated by the encoder output can provide more detailed guidance in the segmentation of lesions.

Compared with other state-of-the-art methods, we achieve superior performance on two public benchmark datasets: e_ophtha_EX and IDRiD. As a variant of U-net, the proposed EAD-Net outperforms the baseline U-net at both lesion-level and image-level by a large margin. As an additional validation, the results on the local dataset also demonstrate the effectiveness of our method.

However, the drawback of EAD-Net is the limited detection performance for tiny lesions, such as MAs and small exudates. As an instance shown in Figure 11, there exist omissions and misidentifications of MAs, and some blood vessels are also detected as HEs. The reason might be that unlike natural images, medical images tend to be more complicated, and they are influenced by many factors, such as imaging equipment, and illumination effect. In the fundus images of DR, there exist many tiny and fuzzy lesions. It is not easy to find the boundary between these lesions and their adjacent pixels, and even professional doctors need a long time to locate them. To better analyze the experimental results, we calculated the distribution of labeled lesions in three datasets. The statistics information is shown in Table 4.

From Table 4, we can see that the ratio of MAs is very small, which makes it very difficult to accurately segment. However, since our study only used a single network structure, the drawback could be overcome by ensemble networks or more elaborate preprocessing in a further study.

In the three different datasets we used, there were 35 normal images and 47 abnormal images in the e_ophtha_EX dataset, while the 81 images in the IDRiD dataset and

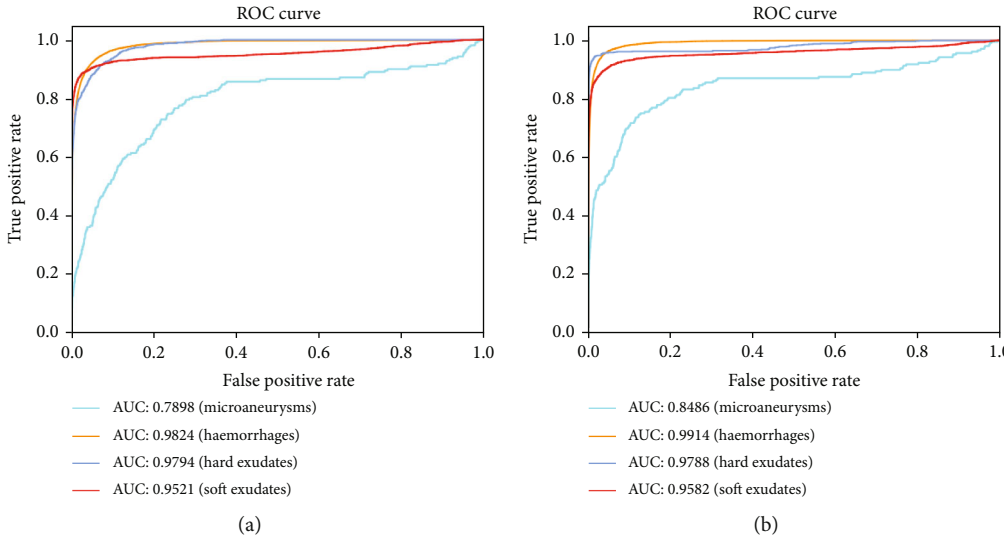

Figure 13: Evaluation on the local intelligent ophthalmology dataset. Different colored curves represent different types of lesions. (a) ROC curves of U-net. (b) ROC curves of EAD-Net.

Table 4: Statistical information of lesion areas of e-ophtha, IDRiD, and local intelligent ophthalmology datasets.

Dataset	MAs	HEs	Hard exudates	Soft exudates
E-ophtha	0.01% (148)	—	0.22% (47)	—
IDRiD	0.10% (81)	1.03% (80)	0.90% (81)	0.38% (40)
Local	0.02% (63)	0.91% (84)	0.48% (86)	0.32% (29)

Number1 (Number2) refers to the fact that there are Number2 images of this lesion type in the corresponding dataset, and the average percentage of this lesion area to the total image area is Number1. To maintain data consistency, only the images containing lesions have been used in Number1.

262 images in our local intelligent ophthalmology dataset were all with more or less different lesions. To a certain degree, the performance of our method on e_ophtha_EX dataset can demonstrate its robustness to normal samples. Furthermore, the fundus images of three datasets we used were from people in different countries, which proved that the proposed method was robust to a certain extent for different ethnic groups. In further studies, we need to conduct experiments on a larger and more balanced data distribution to adapt to various situations in a real world.

5. Conclusion

The DR-AI research based directly on lesions is in line with clinical diagnostic thinking of ophthalmology. In this paper, we propose a convolutional neural network architecture EAD-Net for the lesion segmentation task. The architecture can be divided into three parts: encoder module, dual attention module, and decoder module. On both public and local datasets, we compare the performance of the EAD-Net with other state-of-the-art methods and prove its superiority. Experimental results show that our network has satisfactory results on the segmentation of four different kinds of lesions. These effective segmentation results have important clinical significance in the screening and diagnosis of DR. With more accurate performance and appropriate diagnostic rules based on the lesions, the proposed method will be more suitable for the clinical application.

Data Availability

Datasets of e_ophtha_EX and IDRiD used to support this study are available at doi:10.1016/j.media.2014.05.004 and doi:10.3390/data3030025. These prior studies (and datasets) are cited at relevant places within the text as references [1, 29]. The local intelligent ophthalmology dataset used to support the findings of this study is from the Affiliated Eye Hospital of Nanjing Medical University and is currently under embargo while the research findings are commercialized. Requests for data, 6 months after publication of this article, will be considered by the corresponding author.

Conflicts of Interest

The authors declared no potential conflicts of interest with respect to the research, authorship, and publication of this article.

Acknowledgments

This work was supported by Chinese Postdoctoral Science Foundation (2019M661832), Jiangsu Planned Projects for Postdoctoral Research Funds (2019K226), Jiangsu Province Advantageous Subject Construction Project, and Nanjing Enterprise Expert Team Project. The materials in this work were partly supported by the Affiliated Eye Hospital of Nanjing Medical University.

References

[1] P. Porwal and S. Pachade, "Indian Diabetic Retinopathy Image Dataset (IDRiD): a database for diabetic retinopathy screening research," *Data*, vol. 3, no. 3, p. 25, 2018.

[2] T. Kauppi, V. Kalesnykiene, J. Kamarainen et al., "The DIARETDB1 diabetic retinopathy database and evaluation protocol," in *Proceedings of the British Machine Vision Conference*, vol. 1, pp. 1–10, Warwick, UK, 2007.

[3] B. Lay, C. Baudoin, and J. C. Klein, "Automatic detection of microaneurysms in retinopathy fluoro-angiogram," in *Proceedings of Spie the International Society for Optical Engineering*, vol. 1, pp. 165–173, San Diego, USA, 1984.

[4] H. Jelinek, M. J. Cree, D. R. Worsley, A. Luckie, and P. Nixon, "An automated microaneurysm detector as a tool for identification of diabetic retinopathy in rural optometric practice," *Clinical & Experimental Optometry*, vol. 89, no. 5, pp. 299–305, 2006.

[5] B. Antal and A. Hajdu, "An ensemble-based system for microaneurysm detection and diabetic retinopathy grading," *IEEE Transactions on Biomedical Engineering*, vol. 59, no. 6, pp. 1720–1726, 2012.

[6] B. Zhang, L. Zhang, J. You, and F. Karray, "Microaneurysm (MA) detection via sparse representation classifier with MA and non-MA dictionary learning," in *Proceedings of the International Conference on Pattern Recognition*, vol. 1, pp. 277–280, Istanbul, Turkey, 2010.

[7] M. Esmaeili, H. Rabbani, A. M. Dehnavi, and A. Dehghani, "A new curvelet transform based method for extraction of red lesions in digital color retinal images," in *2010 IEEE International Conference on Image Processing*, vol. 1no. 1, pp. 4093–4096, Hong Kong, China, 2010.

[8] C. Sinthanayothin, J. F. Boyce, T. H. Williamson, H. L. Cook, and D. Usher, "Automated detection of diabetic retinopathy on digital fundus images," *Diabetic Medicine*, vol. 19, no. 2, pp. 105–112, 2002.

[9] S. Ravishankar, A. Jain, and A. Mittal, "Automated feature extraction for early detection of diabetic retinopathy in fundus images," in *2009 IEEE Conference on Computer Vision and Pattern Recognition*, vol. 1, pp. 210–217, Miami, FL, USA, 2009.

[10] L. Seoud, T. Faucon, T. Hurtut, J. Chelbi, and J. P. Langlois, "Automatic detection of microaneurysms and haemorrhages in fundus images using dynamic shape features," in *2014 IEEE 11th International Symposium on Biomedical Imaging (ISBI)*, vol. 1, pp. 101–104, Beijing, China, 2014.

[11] L. Seoud, T. Hurtut, J. Chelbi, F. Cheriet, and J. P. Langlois, "Red lesion detection using dynamic shape features for diabetic retinopathy screening," *IEEE Transactions on Medical Imaging*, vol. 35, no. 4, pp. 1116–1126, 2016.

[12] B. Harangi and A. Hajdu, "Automatic exudate detection by fusing multiple active contours and regionwise classification," *Computers in Biology and Medicine*, vol. 54, no. 1, pp. 156–171, 2014.

[13] C. Pereira, L. Goncalves, and M. Ferreira, "Exudate segmentation in fundus images using an ant colony optimization approach," *Information Sciences*, vol. 296, no. 1, pp. 14–24, 2015.

[14] S. Banerjee and D. Kayal, "Detection of hard exudates using mean shift and normalized cut method," *Biocybernetics and Biomedical Engineering*, vol. 36, no. 4, pp. 679–685, 2016.

[15] D. Comaniciu and P. Meer, "Mean shift: a robust approach toward feature space analysis," *IEEE Transactions on Pattern Analysis and Machine Intelligence*, vol. 24, no. 5, pp. 603–619, 2002.

[16] J. Shi and J. Malik, "Normalized cuts and image segmentation," *IEEE Transactions on Pattern Analysis and Machine Intelligence*, vol. 22, no. 8, pp. 888–905, 2000.

[17] T. Jaya, J. Dheeba, and N. A. Singh, "Detection of hard exudates in colour fundus images using fuzzy support vector machine-based expert system," *Journal of Digital Imaging*, vol. 28, no. 6, pp. 761–768, 2015.

[18] T. Bui, N. Maneerat, and U. Watchareeruetai, "Detection of cotton wool for diabetic retinopathy analysis using neural network," in *2017 IEEE 10th International Workshop on Computational Intelligence and Applications (IWCIA)*, vol. 1, pp. 203–206, Hiroshima, Japan, 2017.

[19] S. Sreng, N. Maneerat, K. Y. Win, K. Hamamoto, and R. Panjaphongse, "Classification of cotton wool spots using principal components analysis and support vector machine," in *2018 11th Biomedical Engineering International Conference (BMEiCON)*, vol. 1, pp. 1–5, Chiang Mai, Thailand, 2018.

[20] S. Sreng, N. Maneerat, K. Hamamoto, and R. Panjaphongse, "Cotton wool spots detection in diabetic retinopathy based on adaptive thresholding and ant colony optimization coupling support vector machine," *IEEJ Transactions on Electrical and Electronic Engineering*, vol. 14, no. 6, pp. 884–893, 2019.

[21] O. Ronneberger, P. Fischer, and T. Brox, "U-net: convolutional networks for biomedical image segmentation," in *Medical Image Computing and Computer-Assisted Intervention – MICCAI 2015. MICCAI 2015*, Lecture Notes in Computer Science, N. Navab, J. Hornegger, W. Wells, and A. Frangi, Eds., pp. 234–241, Springer, Cham, 2015.

[22] R. Zheng, L. Liu, S. Zhang et al., "Detection of exudates in fundus photographs with imbalanced learning using conditional generative adversarial network," *Biomedical Optics Express*, vol. 9, no. 10, pp. 4863–4878, 2018.

[23] C. Playout, R. Duval, and F. Cheriet, "A novel weakly supervised multitask architecture for retinal lesions segmentation on fundus images," *IEEE Transactions on Medical Imaging*, vol. 38, no. 10, pp. 2434–2444, 2019.

[24] G. Quellec, K. Charriere, Y. Boudi, B. Cochener, and M. Lamard, "Deep image mining for diabetic retinopathy screening," *Medical Image Analysis*, vol. 39, no. 1, pp. 178–193, 2017.

[25] M. Javidi, A. Harati, and H. R. Pourreza, "Retinal image assessment using bi-level adaptive morphological component analysis," *Artificial Intelligence in Medicine*, vol. 99, article 101702, 2019.

[26] M. Javidi, H. R. Pourreza, and A. Harati, "Vessel segmentation and microaneurysm detection using discriminative dictionary learning and sparse representation," *Computer Methods and Programs in Biomedicine*, vol. 139, no. 1, pp. 93–108, 2017.

[27] L. Dai, R. Fang, H. Li et al., "Clinical report guided retinal microaneurysm detection with multi-sieving deep learning," *IEEE Transactions on Medical Imaging*, vol. 37, no. 5, pp. 1149–1161, 2018.

[28] H. Pratt, F. Coenen, D. M. Broadbent, S. P. Harding, and Y. Zheng, "Convolutional neural networks for diabetic retinopathy," *Procedia Computer Science*, vol. 90, no. 1, pp. 200–205, 2016.

[29] X. Zhang, G. Thibault, E. Decencière et al., "Exudate detection in color retinal images for mass screening of diabetic

retinopathy," *Medical Image Analysis*, vol. 18, no. 7, pp. 1026–1043, 2014.

[30] J. Fu, J. Liu, H. Tian et al., "Dual attention network for scene segmentation," in *2019 IEEE/CVF Conference on Computer Vision and Pattern Recognition (CVPR)*, vol. 1, pp. 3146–3154, Long Beach, CA, USA, 2019.

[31] K. He, X. Zhang, S. Ren, and J. Sun, "Deep residual learning for image recognition," in *2016 IEEE Conference on Computer Vision and Pattern Recognition (CVPR)*, vol. 1, pp. 770–778, Las Vegas, NV, USA, 2016.

[32] F. Yu and V. Koltun, "Multi-scale context aggregation by dilated convolutions," https://arxiv.org/abs/1511.07122.

[33] M. M. Fraz, W. Jahangir, S. Zahid, M. M. Hamayun, and S. Barman, "Multiscale segmentation of exudates in retinal images using contextual cues and ensemble classification," *Biomedical Signal Processing and Control*, vol. 35, no. 1, pp. 50–62, 2017.

[34] E. Imani and H. R. Pourreza, "A novel method for retinal exudate segmentation using signal separation algorithm," *Computer Methods and Programs in Biomedicine*, vol. 133, no. 1, pp. 195–205, 2016.

[35] S. Guo, T. Li, H. Kang, N. Li, Y. Zhang, and K. Wang, "L-Seg: an end-to-end unified framework for multi-lesion segmentation of fundus images," *Neurocomputing*, vol. 349, no. 1, pp. 52–63, 2019.

Hindawi
Disease Markers
Volume 2021, Article ID 3566749, 12 pages
https://doi.org/10.1155/2021/3566749

Research Article

Cysteine-Rich Intestinal Protein 1 Served as an Epithelial Ovarian Cancer Marker via Promoting Wnt/β-Catenin-Mediated EMT and Tumour Metastasis

Yujuan Liu,[1,2] **Wenyu Li**,[3] **Ji Luo**,[1] **Yiguo Wu**,[1] **Yuanyuan Xu**,[1] **Tingtao Chen**,[4] **Wei Zhang**,[1] **and Fen Fu**[1]

[1]*Department of Gynaecology and Obstetrics, The Second Affiliated Hospital of Nanchang University, No. 1 Mingde Road, Nanchang 330006, China*
[2]*Department of Gynaecology and Obstetrics, The First Hospital of Nanchang, No. 128 Xiangshan North Road, Nanchang 330006, China*
[3]*Queen Mary School, Nanchang University, No. 999 Xuefu Avenue, Nanchang 330031, China*
[4]*Institute of Translational Medicine, Nanchang University, No. 999 Xuefu Avenue, Nanchang 330031, China*

Correspondence should be addressed to Wei Zhang; 896102855@qq.com and Fen Fu; fu_fen@163.com

Received 15 June 2021; Accepted 22 July 2021; Published 9 August 2021

Academic Editor: Ting Su

Objective. To explore the expression, functions, and the possible mechanisms of cysteine-rich intestinal protein 1 (CRIP1) in epithelial ovarian cancer. *Methods*. Using open microarray datasets from The Cancer Genome Atlas (TCGA), we identified the tumorigenic genes in ovarian cancer. Then, we detected CRIP1 expression in 26 pairs of epithelial ovarian cancer tissue samples by immunohistochemistry (IHC) and performed a correlation analysis between CRIP1 and the clinicopathological features. In addition, epithelial ovarian cancer cell lines A2780 and OVCAR3 were used to examine CRIP1 expression by western blot and qRT-PCR. Various cell function experiments related to tumorigenesis were performed including the CCK8 assay, EdU, Annexin V-FITC/PI apoptosis assay, wound healing, and Transwell assay. In addition, the expression of epithelial-mesenchymal transition (EMT) markers was detected by western blot to illustrate the relationship between CRIP1 and EMT. Furthermore, KEGG pathway enrichment analysis and western blot were conducted to reveal the signaling pathways in which CRIP1 is involved in ovarian cancer pathogenesis. *Results*. CRIP1 was identified as an oncogene from the TCGA database. The IHC score demonstrated that the CRIP1 protein was expressed at a higher level in tumours than in tumour-adjacent tissues and was associated with a higher pathological stage, grade, and positive lymphatic metastasis. In cell models, CRIP1 was overexpressed in serous epithelial ovarian cancer. Cell function experiments showed that the knockdown of CRIP1 did not significantly affect cell proliferation or apoptosis but could exert an inhibitory effect on cell migration and invasion, and also induce changes in EMT markers. Furthermore, KEGG pathway enrichment analysis and western blot showed that CRIP1 could induce ovarian cancer cell metastasis through activation of the Wnt/β-catenin pathway. *Conclusion*. This study is the first to demonstrate that CRIP1 acts as an oncogene and may promote tumour metastasis by regulating the EMT-related Wnt/β-catenin signaling pathway, suggesting that CRIP1 may be an important biomarker for ovarian cancer metastasis and progression.

1. Introduction

Ovarian cancer, a type of malignancy in the ovary, is the most lethal gynaecological carcinoma as well as the fifth leading cause of cancer mortality among women [1]. Over 85% of ovarian cancers originate from the epithelium (known as epithelial ovarian cancer, EOC), with serous ovarian cancer being the most common histological subtype [2]. Currently, the main treatment options for epithelial ovarian cancer are tumour cell reduction surgery and platinum-based chemotherapy, immunotherapy, and targeted therapy. Although these therapeutic options are available, the overall five-year

survival rate remains low, at around 30%-40% [2]. It is estimated that 22,530 patients were diagnosed with ovarian cancer in 2019 in the United States, of which 13,980 patients died [3]. The high mortality may be due to a number of factors, including the lack of symptoms and detectable biomarkers for ovarian cancer in its early stage, distant invasion, and metastasis [4, 5]. Thus, it is of great importance to identify new predictive biomarkers for early diagnosis and have a better understanding of the mechanism of ovarian cancer metastasis, which is also an urgent issue for improving the efficacy of ovarian cancer treatment.

There are many factors contributing to the metastasis of ovarian cancer. Recently, accumulated evidence has indicated that a major driver of ovarian cancer metastasis is epithelial-mesenchymal transition (EMT), in which cancer cells lose their epithelial potential and acquire a mesenchymal phenotype, allowing cells to detach from the primary site and gain the ability to metastasise [6–9]. In addition, research has shown that the activity of EMT is regulated by many different signaling pathways [10], among which the canonical Wnt/β-catenin signaling pathway is pivotal for both ovarian carcinogenesis and EMT. Sun and colleagues [11] found that the high expression of Golgi phosphoprotein 3 (GOLPH3) in ovarian cancer patients could be regarded as an oncogene and was related to poor prognosis, as it could promote ovarian cancer cell proliferation, migration, and invasion by stimulating the Wnt/β-catenin signaling pathway and EMT. Dong et al. [12] also reported that PEST-containing nuclear protein (PCNP) promoted the ability of ovarian cancer cells to invade and metastasise in the same way. These findings not only highlight the significance of the Wnt/β-catenin signaling pathway in carcinogenesis and EMT but also revealed that some oncogenes are involved in ovarian cancer invasion and metastasis. This has enriched our knowledge of the mechanisms of ovarian cancer progression and provided a basis for cancer therapy, which has become more precise and individualised. However, the information in this field is still not complete. Due to the small number of studies on this topic, more in-depth research is necessary to further reveal the exact mechanisms of ovarian cancer invasion and metastasis and further improve current treatment strategies.

As a member of the LIM/double zinc finger protein family, cysteine-rich intestinal protein 1 (CRIP1) has a unique double zinc finger motif and is primarily expressed in the intestine [13]. It was first recognised as an intracellular zinc transport and absorption protein [14]. CRIP was also detected in immune cells such as peritoneal macrophages and peripheral blood mononuclear cells, suggesting it may be involved in host immune responses [15]. Moreover, in recent decades, the aberrant expression of CRIP1 in several cancers has attracted increasing attention. In metastatic colorectal cancer (CRC), CRIP1 was overexpressed and downregulation of CRIP1 was found to inhibit cell migration and invasion in the cell lines SW620 and HT29 [16]. Thus, it may function as an oncogene to regulate the migration and invasion of CRC cells and may be regarded as a new promising biomarker for poor prognosis and the metastasis of colon cancer. Similar results were also found in cervical cancer [17], thyroid carcinoma [18], and endometrial cancer [19]. In contrast, CRIP1 expression led to a favourable outcome and fewer metastases in osteosarcoma [20] and breast cancer [21]. Although the role of CRIP1 seems to be controversial in the abovementioned tumours, we are certain that CRIP1, as an oncogene or tumour suppressor gene, has a close relationship with tumour metastasis. However, the current studies of CRIP1 are finite and the underlying mechanisms of CRIP1-mediated tumour metastasis are largely unknown. Moreover, the relationship between ovarian cancer and CRIP1 has not yet been discussed.

In this study, our objective was to describe CRIP1 expression patterns, functions, and possible mechanisms in ovarian cancer. First, we used bioinformatics methods to screen out the oncogene CRIP1 in ovarian cancer from the TCGA database, showing that ovarian cancer with the high expression of CRIP1 had a poor prognosis. Subsequently, we used tissue samples and cell models to verify its expression. Then, we performed *in vitro* experiments to explore its function in invasion, migration, and EMT and further uncovered the possible mechanisms. The results show that the upregulation of CRIP1 can promote ovarian cancer invasion, metastasis, and EMT by activating the Wnt signaling pathway, suggesting that CRIP1 could be viewed as a valuable new biomarker for ovarian cancer.

2. Materials and Methods

2.1. Genetic Screening. Using the online differential gene expression analysis tool (http://gepia2.cancer-pku.cn/#degenes), we analysed the differential gene expression of ovarian cancer and normal ovarian tissues from The Cancer Genome Atlas (TCGA) database. Differentially expressed genes were determined by means of ANOVA. Genes with $\log_2 \mathrm{FC\,cut-off} > 1$ were considered upregulated, and $P < 0.05$ were considered statistically significant. Then, GDC TCGA Ovarian Cancer (OV) mRNA expression FPKM data and clinical survival data were downloaded from the website (https://xenabrowser.net/datapages/), and significant survival genes were obtained through the "Survival" and "SurvMiner" packages of the R software ($P < 0.05$). By further searching on PubMed, genes reported in the literature were no longer considered. After taking the intersection of the three, the target genes were obtained.

Subsequently, the target genes were ranked by $-\log_{10}$ (P value) to show the top five genes which were used for the analysis of survival and hazard ratio (HR) on the survival analysis website (https://kmplot.com/analysis/). HRs were applied to identify different genes, with HR < 1 indicating protective genes and HR > 1 indicating risk genes. The genes that were both significantly associated with overall survival and HR > 1 were identified as key genes. Finally, we analysed the relationship between key genes and ovarian cancer by using the online gene expression DIY tool (http://gepia2.cancer-pku.cn/#degenes).

2.2. Kyoto Encyclopaedia of Genes and Genomes (KEGG) Pathway Enrichment Analysis. The median expression value of the key gene in ovarian cancer samples from the TCGA database was selected as an optimal cut-off value to classify

different subgroups which had high or low expression and were then used for KEGG analysis. The R software "Limma" package was used to analyse gene expression levels in cancer samples, and the differentially expressed genes were then screened out. Pearson correlation analysis between CRIP1 and differentially expressed genes was carried out using R language, and the differentially related genes were selected with the condition of $P < 0.01$. We conducted KEGG pathway enrichment analysis of these differentially related genes online (http://www.webgestalt.org/).

2.3. Patients and Tissue Samples. Paraffin-embedded tissue samples (cancer tissue and paracancerous tissue) were collected from patients at the Second Affiliated Hospital of Nanchang University, with 50 serous ovarian cancer samples and 25 paracancerous tissue samples. The patients were diagnosed with serous ovarian cancer by surgical pathology. The basic data of patients were collected, including age, lesion size, clinicopathological grading, staging, lymphatic metastases, and preoperative CA125 levels. Patients who received chemotherapy, immunotherapy, or hormone therapy before surgery or those with ovarian cancer combined with other cancers were excluded. Ethical approval was granted by the Ethical Committee of the Second Affiliated Hospital of Nanchang University.

2.4. Cell Lines and Cell Culture. The normal ovarian cell line IOSE80 and human epithelial ovarian cancer cell lines OVCAR3 and A2780 were obtained from Shanghai EK-Bioscience Biotechnology Co., Ltd. A2780 and IOSE80 cell lines were incubated in RPMI-1640 medium containing 10% foetal bovine serum (FBS) and 1% penicillin-streptomycin (PS), while OVCAR3 in RPMI-1640 medium supplemented with 20% FBS, 1% insulin, and 1% PS. Cells were grown in an incubator at 37°C with 5% CO_2. When the cell confluence was about 80-90%, the cells in good condition were collected and digested with trypsin for subculture or frozen for later experiments.

2.5. Immunohistochemistry. All tissue samples were paraffin-embedded and cut into 3-5 mm sections, which were heated in an oven at 72°C for 2 hours, followed by xylene deparaffinization and ethanol gradient rehydration. To block and inactivate endogenous peroxidase, the sections were maintained in 3% H_2O_2 at ambient temperature for 15 minutes, followed by washes in phosphate-buffered saline (PBS). After boiling in citrate buffer and cooling naturally, the sections were again washed with PBS three times for antigen retrieval. Then, the sections were incubated with reagent A (normal goat serum) and anti-CRIP1 rabbit polyclonal antibody (Abcepta, Cat No. AP4707b). The slides were washed with PBS and then incubated with biotin-labelled secondary antigens and rinsed again, followed by streptavidin labelled with horseradish peroxidase for another round of incubation. DAB-H_2O_2 was used as the chromogenic reagent for visualisation, and haematoxylin was added for counterstaining. Then, the software ImageJ was applied to calculate grey values for pathological scoring.

Table 1: The specific primer sequences for qRT-PCR are listed.

Gene symbol	Primer category	Primer sequence(5′ to 3′)
CRIP1 (human)	Forward	CCTGCCTGAAGTGCGAGAAAT
	Reverse	CCTTTAGGCCCAAACATGGC
GAPDH (human)	Forward	TGCACCACCAACTGCTTAGC
	Reverse	GGCATGGACTGTGGTCATGAG

A semiquantitative method was used to detect the expression grade of CRIP1 protein. Percentages of positive cells (0%, 1-25%, 26-50%, 51-75%, and 76-100%) were recorded as 0, 1, 2, 3, and 4 points, respectively. Positive staining intensity was scored as follows: colourless (0 point), pale yellow (1 point), brownish yellow (2 points), and dark brown (3 points). The expression grade was determined by multiplying the two scores: 0-5 represented low expression and 6-12 represented high expression.

2.6. Western Blot. Following the standard procedure, we extracted protein from the OVCAR3, A2780, and IOSE80 cell samples and then measured the protein content with the BCA protein assay kit. After SDS-PAGE electrophoresis, the membrane was transferred and blocked and then incubated with primary and secondary antibodies. The protein content was analysed by X-ray exposure. The antibodies used in this experiment were as follows: β-actin (Cat No. 4970S), β-catenin (Cat No. 8084S), MMP-2 (Cat No. 87809S), and MMP-9 (Cat No. 13667S) were bought from Cell Signaling Technology (Danvers, MA, USA); CRIP1 (Cat No. 15349-1-AP), E-cadherin (Cat No. 20874-1-AP), N-cadherin (Cat No. 22018-1-AP), GSK-3β (Cat No. 22104-1-AP), and p-GSK-3β (Cat No. 14850-1-AP) were purchased from Proteintech (Wuhan, China); vimentin (Cat No. bs-8533R) was obtained from Bioss (Beijing, China).

2.7. Quantitative Real-Time Reverse Transcription PCR. Following the manufacturer's protocol, we isolated total RNA from OVCAR3 cells with TRIzol reagent and reverse-transcribed it into cDNA using a reverse transcription kit (TaKaRa, China). Real-time quantitative PCR was performed on a fluorescent PCR instrument using SYBR Green PCR master mix kits (TaKaRa, China). GAPDH was chosen as the internal control. The relative fold relationship was calculated using fold change = $2^{-\Delta\Delta Ct}$. After repeating the experiments three times, the mean value was calculated. All primers were purchased from General Biol (Anhui, China). Table 1 shows the specific primer sequences.

2.8. siRNA Interference. Three siRNA oligonucleotides targeting the CRIP1 gene, including si-168, si-229, and si-276, were designed and synthesised by General Biosystems (Anhui, China). The three siRNA oligonucleotide sequences are listed as follows: si-168: 5′-GCAACAAGGAGGUGUA CUUTT-3′; si-276: 5′-ACGCUGAGCACGAAGGCAATT-3′; and si-229: 5′-CUGCCUGAAGUGCGAGAAATT-3′. OVCAR3 cells were placed at a density of 1×10^5 cells/ml

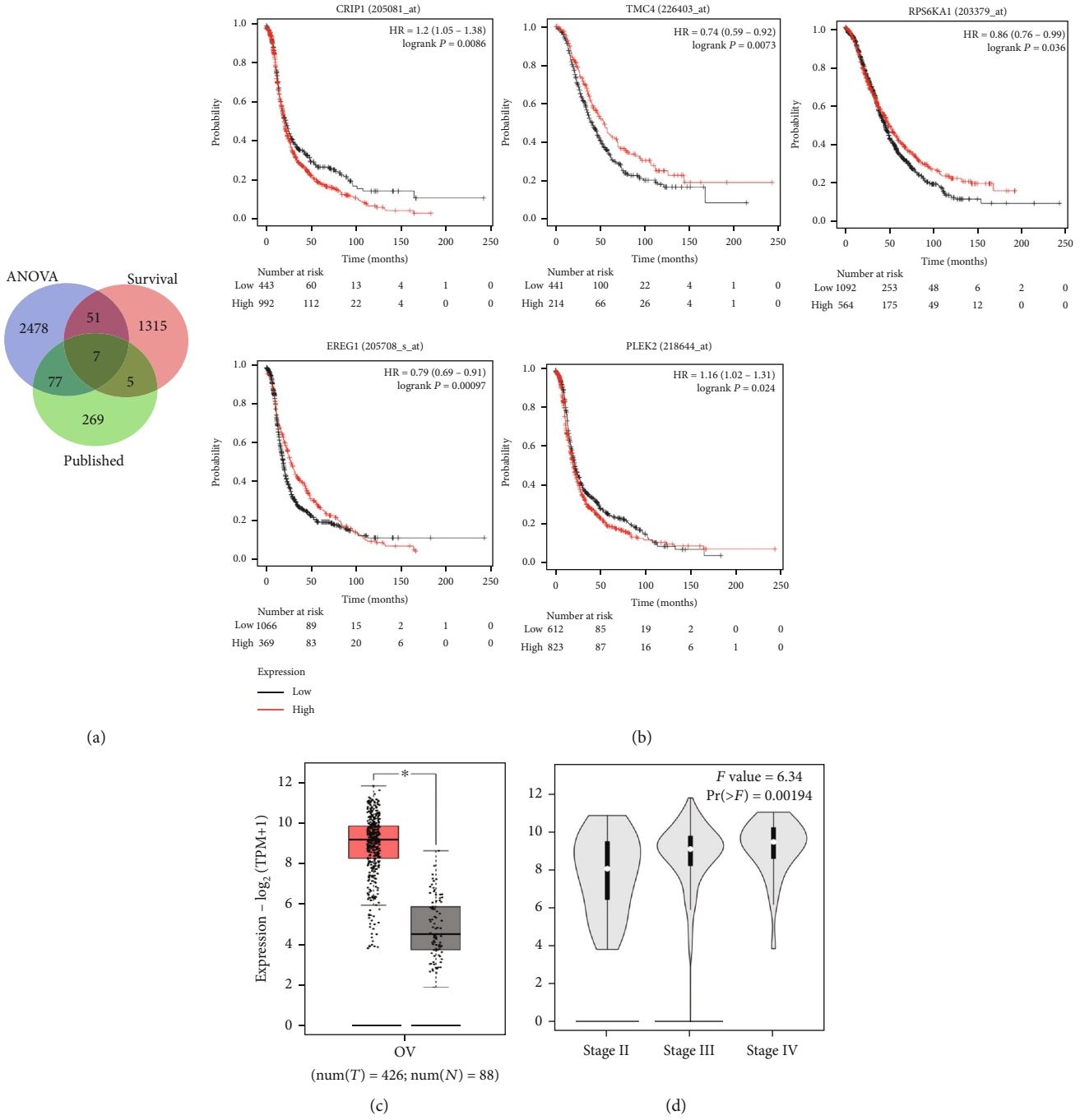

Figure 1: Genetic screening and bioinformatics analysis of cysteine-rich intestinal protein 1 (CRIP1). (a) 2,613 genes were significantly upregulated in ovarian cancer tissues using the online differential gene expression analysis tool, and 1,378 survival significant genes were obtained through survival analysis; 358 genes were excluded for being published on PubMed. After taking the intersection of the three, 51 target genes were obtained in the end. (b) After ranking the 51 target genes by -$\log_{10}$ (P value), the top five genes were obtained, and then, the survival and hazard ratio (HR) analysis of these genes was conducted on the survival analysis website. The survival plots of the top five target genes suggested that only high expression of CRIP1 and PLEK2 could affect prognosis ($P < 0.05$). (c) Box plot showing the significantly upregulated expression of CRIP1 in ovarian cancer tissues (left, red; $n = 426$) compared with nonneoplastic tissues (right, black; $n = 88$) ($P < 0.05$). (d) Violin plot showing a correlation between increased CRIP1 expression and increased pathological grade in ovarian cancer ($P < 0.05$).

into 6-well plates. When the cells were at 30-50% confluent, we conducted transfection. The OVCAR3 cells were transfected with 20 μM small interfering RNA (siRNA) or negative control siRNA (si-NC) (General Biosystems Anhui, China) in reduced serum medium using Lipofectamine™ 3000 Transfection Reagent (Thermo Fisher, USA). After transfecting for 24 to 48 h, the effect of gene knockdown was measured by western blot and qRT-PCR.

2.9. Wound Healing Assay. Cells were seeded on 6-well plates and incubated for 24 hours or longer until cells reached 80-90% confluence, before a scratch wound was created by drawing a straight line with a 10 μl pipette tip. Then, the cells were rinsed with PBS three times and placed in serum-free medium, followed by incubation in an incubator at 37°C with 5% CO_2. Images were taken at 0 and 24 hours. Wound closure was quantified by randomly selecting under the microscope and measuring the remaining unmigrated area using ImageJ in three different fields at each time point. Wound healing percentage (%) = (Area of original wound − Area of actual wound)/Area of original wound × 100%.

2.10. Transwell Assay. After digestion and suspension in serum-free medium, cells were adjusted to a density of 5×10^5/ml. The cell suspension (100 μl) was seeded into the upper Transwell chambers, and the lower chambers were filled with 500 μl of 20% FBS medium. For invasion experiments, the Transwell chambers were Matrigel-coated. Then, the cells were incubated at 37°C for 24 hours in order to assess migration or invasion. After 4% paraformaldehyde fixation and haematoxylin staining of the lower surface, the cells were counted under a microscope.

2.11. 5-Ethynyl-20-Deoxyuridine (EdU) Incorporation Assay. Cell proliferation was evaluated using an EdU Imaging kit (US Everbright Inc., Suzhou, China). Cells were placed into 24-well plates at 5×10^3 cells per well for 24 hours, followed by exposure at 1× EdU (10 μM) at 37°C for 2 hours. The cells were then fixed with 4% paraformaldehyde and permeabilised with 0.5% Triton X-100. After treatment with 100 μl of dyeing reaction cocktail for 30 minutes, the cells were incubated with 300 μl of 1× Hoechst (5 μg/ml) for 20-30 minutes. Finally, EdU-stained cells were visualised under a fluorescence microscope (Olympus). According to the formula (EdU − positive cells/Hoechst − stained cells) × 100%, we calculated the percentage of EdU-positive cells by arbitrarily selecting three fields in each group.

2.12. Cell Counting Kit-8 (CCK8) Assay. We used a Cell Counting Kit-8 (GlpBio, USA) to measure cell viability. OVCAR3 cells were cultured in a 96-well plate with 100 μl culture medium at a concentration of 5×10^3 cells/well, and the dish was then placed into an incubator for preincubation (37°C, 5% CO_2). After 24 hours of incubation, 10 μl of transfected OVCAR3 cells was added to the dish and incubated for 1 to 4 days. Then, 10 μl of CCK8 solution was added to each well, and the dish was placed in the incubator again for 1-4 hours. The solution was mixed gently on the orbital shaker for 1 minute to ensure the colour was distributed evenly. The OD_{450} were measured with a microplate reader.

2.13. Annexin V-FITC/PI Apoptosis Assay. Apoptosis was examined using an Annexin V-FITC Apoptosis Detection kit (Dojindo, Japan) following the manufacturer's instructions and relevant reference [22]. Cells were cultured in 6-well plates overnight. After treating with or without siRNA interference for 24 h, cells were trypsinised with EDTA-free trypsin, followed by three washes with cold PBS. Then, the cells were resuspended in 1× binding buffer to reach a final concentration of 1×10^6 cells/ml. Next, 100 μl of the above cell suspension was collected and mixed with 5 μl of Annexin V-FITC and 5 μl of PI working solution for 15 minutes at room temperature in the dark. Images were then taken using an inverted fluorescence microscope (Olympus).

Table 2: The most important top five genes were displayed through the ranking of 51 target genes by -$\log_{10}$ (P value).

Symbol	Log_2 FC	-Log_{10} (P value)
TMC4	4.567	131.61083390
RPS6KA1	2.369	80.87942607
CRIP1	4.637	60.73754891
TRPM2	2.111	53.67366414
PLEK2	1.842	49.86327943

2.14. Statistical Analysis. All results are presented as the mean ± standard deviation. Student's t-test and one-way ANOVA were used to determine statistical significance, and Pearson's chi-squared (χ^2) test was used to identify the significance of correlations between the expression of CRIP1 and histopathological factors. All data were analysed using GraphPad Prism 7 software, and $P < 0.05$ was considered significant.

3. Results

3.1. Key Genes Identified by Bioinformatics in Ovarian Cancer. To determine the key genes responsible for ovarian cancer, we used the TCGA dataset and online tools. The results show that 2,613 genes were significantly overexpressed in ovarian cancer tissues compared with normal ovarian tissues in the TCGA database and 1,378 survival significant genes were obtained through survival analyses. Meanwhile, 358 genes that were reported in the literature were no longer considered. After taking the intersection of the three, 51 target genes were obtained in the end (Figure 1(a)), which represent not only differential genes but also significant survival genes. To further identify the key genes, we ranked 51 target genes by -$\log_{10}$ (P value). Finally, the top five key genes were found (Table 2). Next, the top five genes were used for the analysis of survival and HR on the survival analysis website to reveal their oncogenic properties. The survival plots suggested that the key genes significantly associated with overall survival and HR > 1 were CRIP1 and PLEK2 (Figure 1(b)). Because CRIP1 was more statistically significant and associated with a higher risk, it was chosen for the following study.

Next, we demonstrated CRIP1 expression in ovarian cancer and its relationship with disease. The box plot shows the significantly upregulated expression of CRIP1 in ovarian cancer tissues compared with adjacent nonneoplastic tissues ($|\log_2 \text{FC}|$ cut-off: 1, P value; cut-off: 0.01, $P < 0.05$) (Figure 1(c)). Interestingly, the violin plot shows that CRIP1 expression increased with an increase in tumour pathological stage, suggesting a close positive correlation between CRIP1 expression and ovarian cancer grade ($F = 6.34$, $P < 0.05$) (Figure 1(d)). These findings indicate that the CRIP1 gene

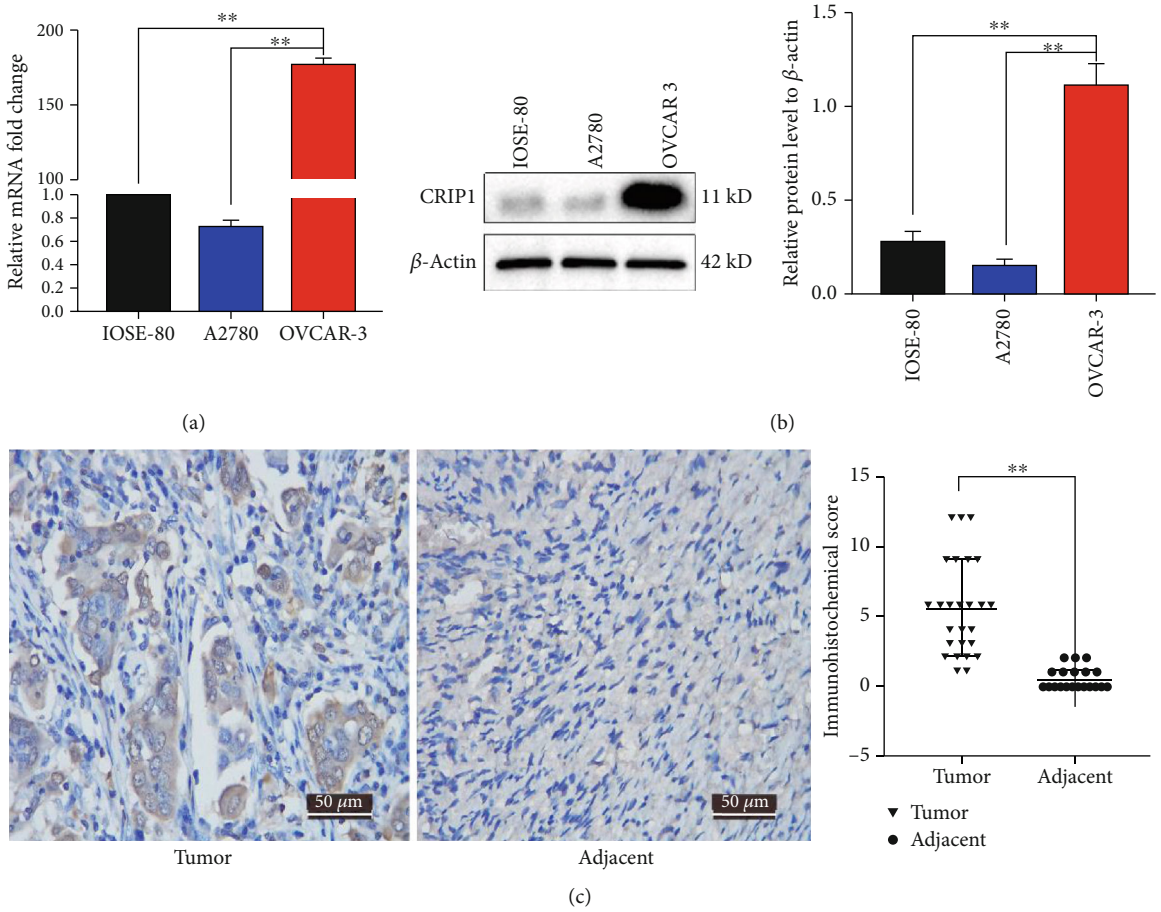

Figure 2: CRIP1 is highly expressed in both ovarian cancer tissue samples and cell lines. (a, b) The mRNA levels (a) and protein levels (b) of CRIP1 in the normal ovarian cell line IOSE-80 and epithelial ovarian cancer cell lines OVCAR3 and A2780 were detected by qRT-PCR and western blot. (c) Immunohistochemical detection of CRIP1 protein levels in tissue samples (cancerous and adjacent tissues) (left). CRIP1 protein is higher in ovarian cancer tissues than tumour-adjacent normal tissues of the same patient (right).

has oncogenic properties, and the high expression of CRIP1 could be a reliable indicator of poor prognosis in ovarian cancer.

3.2. CRIP1 Is Overexpressed in Ovarian Cancer Cell Lines and Cancer Tissues. To verify the expression of CRIP1 in ovarian cancer, we selected two ovarian cancer cell lines (A2780 and OVCAR3) and used the normal ovarian cell line IOSE80 as the control. When compared with IOSE80, the mRNA level of CRIP1 was significantly upregulated in OVCAR3 ($P < 0.01$), whereas CRIP1 expression was relatively unchanged in A2780 ($P = 0.9350$, Figure 2(a)). The western blot also showed the same result at the protein level (Figure 2(b)). Furthermore, the CRIP1 content in ovarian cancer tissues was detected by immunohistochemistry (IHC), including 26 pairs of serous epithelial ovarian cancer tissues with matched adjacent normal tissues. IHC score showed that CRIP1 was highly expressed in cancer tissues, in contrast to no expression in adjacent normal tissues ($P < 0.01$, Figure 2(c)). This result was consistent with the results of the bioinformatics analysis.

In addition, a correlation analysis between the CRIP1 expression and the clinicopathological parameters in 50 cases of serous epithelial ovarian cancer was conducted. Our data showed that high CRIP1 expression was closely related to higher pathological stage, grade, and positive lymphatic metastasis, whereas no relation was detected with age, tumour diameter, or CA125 level (Table 3), indicating that CRIP1 may promote ovarian cancer aggressiveness and distant metastasis. Given the experimental results above, the OVCAR3 cell line was selected for subsequent experiments.

3.3. si-CRIP1 Has No Significant Effect on Cell Proliferation and Apoptosis in OVCAR3 Cells. We confirmed a high level of expression of CRIP1 in OVCAR3 and ovarian cancer tissues. To determine the role of CRIP1 in ovarian cancer, we knocked down CRIP1 in OVCAR3 cells using three different short interfering RNAs (siRNAs), including si-168, si-229, and si-276. Transfection efficiency was verified by qRT-PCR and western blot (Figures 3(a) and 3(b)). Among these three siRNAs, si-229 showed the best silencing effect, so it was chosen for the following experiments.

Next, we evaluated CRIP1 effects on proliferation and apoptosis with or without CRIP1 siRNA. The results from CCK8 assays revealed that CRIP1 silencing did not affect cell viability ($P > 0.05$, Figure 3(c)). Similarly, the EdU assay

Table 3: Correlation analysis between CRIP1 protein level and the clinicopathological parameters in 50 cases of serous epithelial ovarian cancer.

Characteristic	Patients (n)	CRIP1 expression		P value
		High	Low	
Age (years)				0.1452
<50	19	7	12	
≥50	31	18	13	
Tumour diameter				0.6374
<5 cm	5	2	3	
≥5 cm	45	23	22	
Pathological stage				<0.0001
I-II	17	1	16	
III-IV	33	24	9	
Grade				0.0047
G1	10	1	9	
G2-G3	40	24	16	
Lymphatic metastasis				<0.0001
Positive	26	23	3	
Negative	24	2	22	
CA125 (U/ml)				0.3868
<500	30	13	17	
≥500	20	12	8	

suggested that CRIP1 knockdown had no significant effect on cell proliferation ($P = 0.2589$, Figure 3(d)). Furthermore, using the Annexin V-FITC/PI assay to detect apoptosis, we found that there was no difference between si-CRIP1 transfected cells and si-NC transfected cells, suggesting that si-CRIP1 in OVCAR3 cells had no effect on apoptosis ($P = 0.7637$, Figure 3(e)).

3.4. CRIP1 Silencing Abates Migration and Invasion in OVCAR3 Cells. The wound healing assay was conducted to demonstrate whether CRIP1 silencing affects OVCAR3 cell migration. Compared with the si-NC group, the cells with si-CRIP1 showed a more extensive wound closure area (Figure 4(a)), which suggested a significant decrease in migration ability in si-CRIP1 OVCAR3 cells ($P < 0.01$). Similar results were also found in the Transwell assay without Matrigel ($P < 0.01$, Figure 4(b)). These results demonstrate that CRIP1 silencing inhibited cell migration. To understand the role of CRIP1 in cancer cell invasion, we carried out another Transwell assay with Matrigel. As shown in Figure 4(c), when compared with the si-NC group, fewer cells in the si-CRIP1 group entered the lower chamber through the Matrigel-coated membrane ($P < 0.01$). These results revealed that the depletion of CRIP1 suppresses migration and invasion in OVCAR3 cells.

3.5. CRIP1 Induces EMT by the Wnt/β-Catenin Pathway. The above results suggested a clear correlation between CRIP1 expression and cell invasion. As EMT plays a critical role in the process of migration and invasion, it is necessary to further verify the relationship between CRIP1 and EMT. Western blot was carried out to detect the expression of EMT markers, including E-cadherin, N-cadherin, and vimentin. After silencing the CRIP1 gene using CRIP1 siRNA, we observed that the epithelial marker E-cadherin was upregulated, and the mesenchymal markers N-cadherin and vimentin were downregulated (Figure 5(b)). Combined with the results of cell function experiments, we deduced that CRIP1 is involved in the process of cell migration and invasion by regulating EMT in ovarian cancer.

To explore the biological pathways by which CRIP1 is involved in ovarian cancer pathogenesis, we further conducted KEGG pathway enrichment analysis. The results show that the Wnt/β-catenin signaling pathway was significantly enriched (Figure 5(a)). As the Wnt/β-catenin signaling pathway is vital to EMT and cancer metastasis, we selected this pathway for further study and investigated the key proteins of the canonical Wnt/β-catenin pathway by western blot. Our results demonstrate that β-catenin, p-GSK-3β, and downstream genes including matrix metalloproteinase (MMP-2 and MMP-9) were markedly downregulated after CRIP1 silencing, while GSK-3β was unchanged (Figure 5(c)). In general, these results indicate that CRIP1 regulates EMT by modulating the Wnt/β-catenin pathway.

4. Discussion

Ovarian cancer is a gynaecological malignancy, and its high mortality rate has been shown to be largely caused by the metastatic nature of the cancer. Thus, finding a new predictive biomarker for early diagnosis and targeted therapy is of great importance. Although many genetic alterations have been shown to play a part in ovarian cancer metastasis, the potential mechanism is still elusive. Recently, CRIP1, with only one LIM domain, has been studied in several malignancies including colorectal cancer, breast cancer, cervical cancer, and osteosarcoma [20, 21, 23, 24]. It can induce different outcomes in different cancer types, acting as either a tumour-specific suppressor gene or an oncogene [20, 25]. However, its role has not yet been identified in ovarian cancer.

Here, we revealed the function of CRIP1 in ovarian cancer and its underlying mechanism for the first time. Through analysis of the TCGA database, we confirmed that CRIP1 was upregulated in serous ovarian cancer samples and was closely associated with tumour progression. Then, we used tissue samples and cell models to confirm these results. We observed the same trend; i.e., that CRIP1 had a markedly higher expression level in ovarian cancer tissues than in normal samples, suggesting an oncogenic property of CRIP1. However, it is interesting to observe that this result was only seen in the serous ovarian cancer cell line OVCAR3, while CRIP1 expression was relatively unchanged in A2780 cells when compared with normal cells. The reason for this may be that A2780 is a mucinous epithelial ovarian cancer cell line that has a different genetic background, and that CRIP1 expression has a close relationship with tumour type. Further research revealed that elevated CRIP1 was closely correlated with a higher pathological stage, grade, and positive

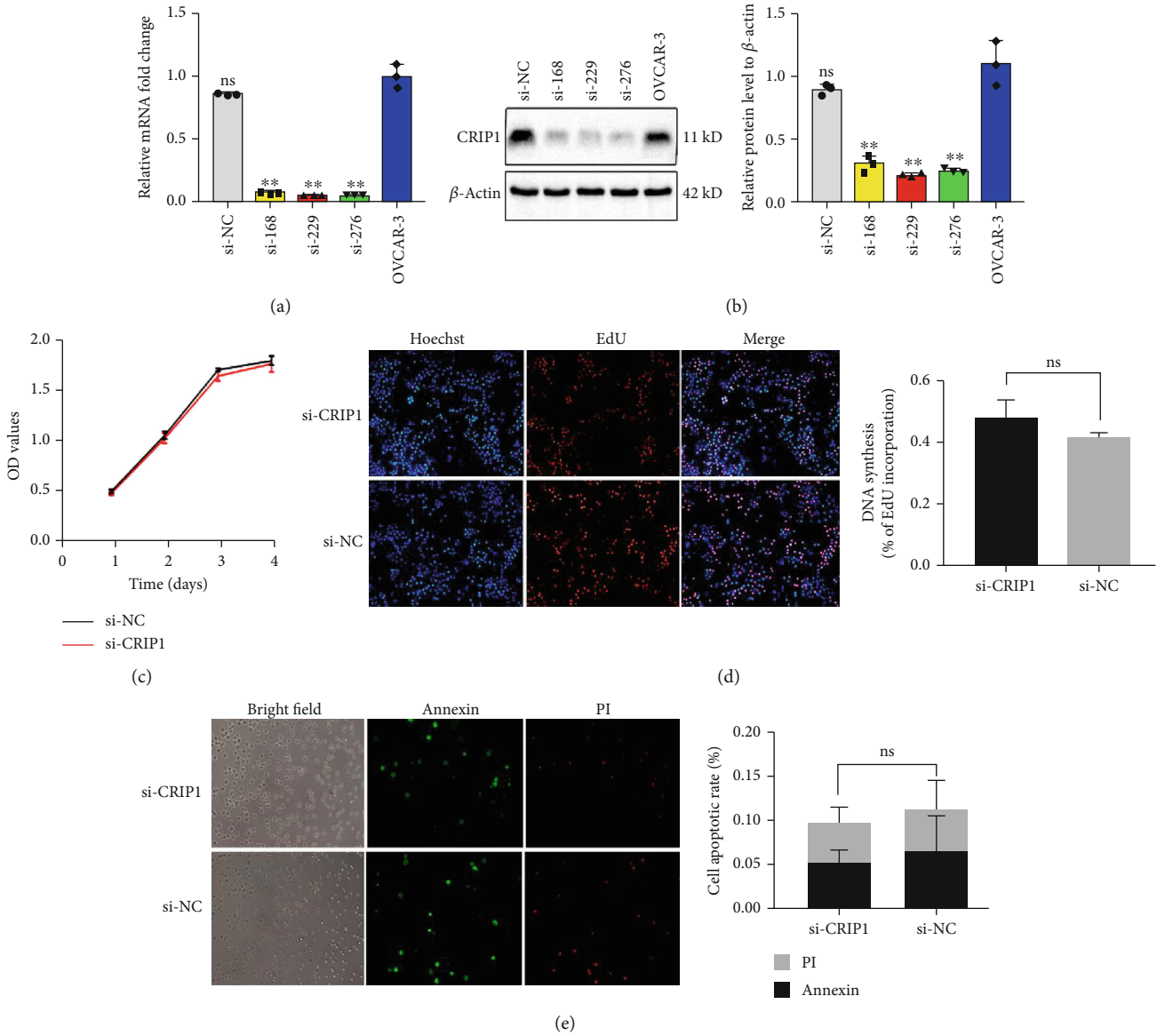

Figure 3: Short interfering RNAs (siRNAs) were used to deplete CRIP1 gene expression *in vitro*. The effect of si-CRIP1 in the OVCAR3 cell line showed no difference in cell proliferation and apoptosis. (a, b) qRT-PCR (a) and western blot (b) were used to detect the gene silencing effect of OVCAR3 cell lines transfected with si-CRIP1 or si-NC. GAPDH and β-actin were used as internal controls. (c) The influence of CRIP1 silencing on cell viability in the OVCAR3 cell line. After transfection with si-CRIP1 or si-NC for 1 day, 2 days, 3 days, and 4 days, cell viability was assessed using CCK8, and OD_{450} was measured. (d, e) The influence of CRIP1 silencing on cell proliferation (d) and apoptosis (e) in the OVCAR3 cell line. After transfection with si-CRIP1 or si-NC, cell proliferation and apoptosis were assessed by the EdU and Annexin V-FITC/PI assays, respectively. Representative graphs are shown on the left. Mean ± SD represents the data of three independent experiments. ns: no statistical significance. $^{*}P < 0.05$ and $^{**}P < 0.01$.

lymphatic metastasis of patients, pointing to a link between increased CRIP1 expression and ovarian cancer aggressiveness. Taken together, these findings show that CRIP1 expression is closely related to tumour type, and that as an oncogene, CRIP1 can serve as a biomarker for a specific diagnosis and as an indicator of early metastasis in serous epithelial ovarian cancer patients.

To date, the role of CRIP1 in tumours has been controversial. To further investigate its oncogenic properties, we silenced the expression of CRIP1 and performed *in vitro* experiments. The results showed no significant change in proliferation and apoptosis in ovarian cancer cells, which was consistent with a recently published study on CRIP1-depleted colorectal cancer cells [16]. However, this result does not agree with a study on breast cancer in which CRIP1 acted as an inhibitor of proliferation and invasion processes [21]. This confirms the previous statement that CRIP1 function may differ depending upon cancer type. Moreover, the wound healing and Transwell assays showed that CRIP1 was mainly involved in the tumour metastasis process.

Next, we explored the mechanism of CRIP1 in regulating tumour metastasis. As EMT is a major driver of cancer

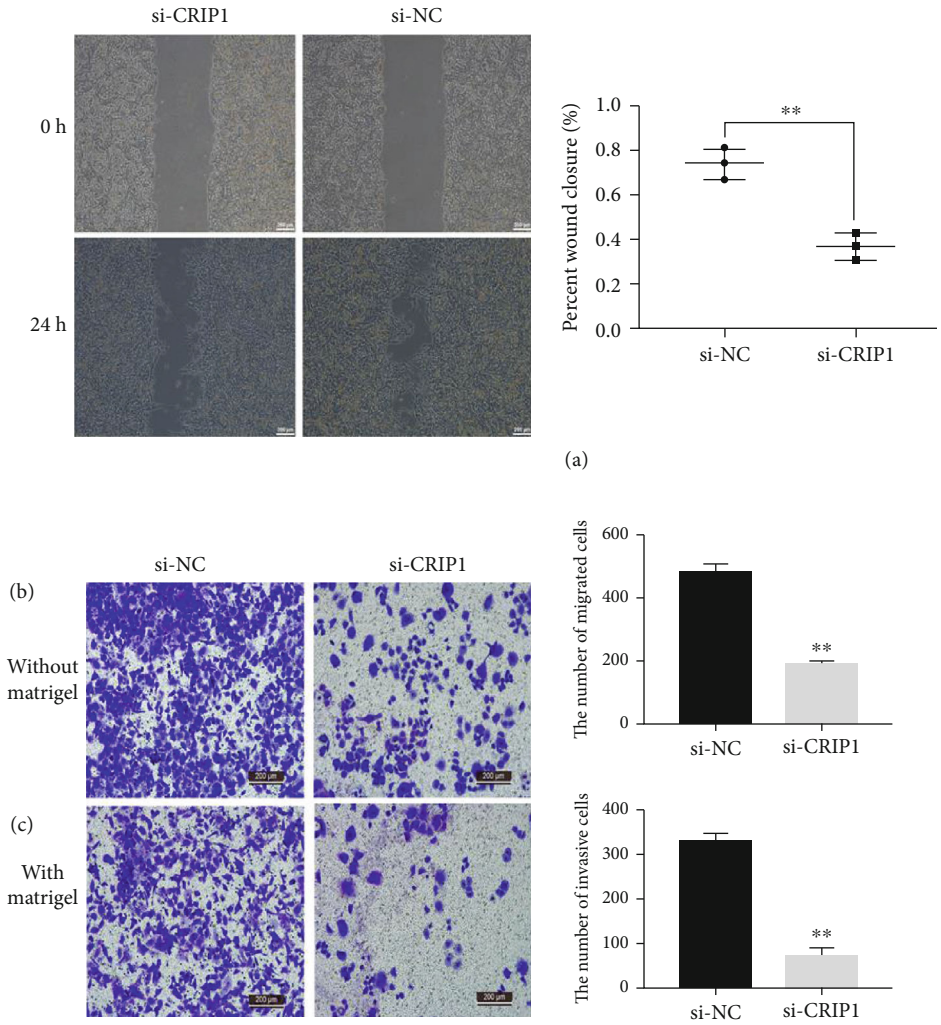

Figure 4: The depletion of the CRIP1 gene inhibited cell migration and invasion in the OVCAR3 cell line. (a) Wound healing assay and (b) Transwell assays without and with (c) Matrigel were used to detect cancer cell migration and invasion abilities, respectively. Representative graphs are shown on the left.

metastasis [26], we further verified the relationship between CRIP1 and EMT. As the results show, CRIP1 knockdown induced the increased expression of the epithelial marker E-cadherin and decreased the expression of the mesenchymal markers N-cadherin and vimentin. E-cadherin is a cell-cell adhesion molecule, able to anchor epithelial cells through the connection of various catenins to the cytoskeleton [27]. Acquiring this epithelial marker allows cancer cells to lose their metastatic ability, presenting a less aggressive phenotype [27]. N-cadherin is also a glycoprotein that mediates cell-cell adhesion, but it is closely linked to activated metastasis and a poor prognosis in many malignancies [28]. Vimentin, a member of the intermediate filament (IF) family, is a potential prognostic factor of EMT-related proteins [29] and is also viewed as a mesenchymal marker [30]. EMT drives the conversion of cells from an epithelial phenotype to a mesenchymal phenotype and could operate in both physiological and pathological processes such as embryogenesis, wound healing, and carcinoma pathogenesis [31]. In cancer pathogenesis, tumour cells gain a higher migration and invasion ability via EMT. Therefore, our findings indicate that EMT may be an indispensable process for CRIP1-mediated ovarian cancer invasion and metastasis.

Up to this stage, the correlation between CRIP1 expression and cancer-related EMT had been confirmed, but how CRIP1 mediated this process remained unclear. Through KEGG pathway enrichment analysis, we discovered that CRIP1 was significantly enriched in the Wnt/β-catenin signaling pathway. This pathway could be stimulated by the binding of the Wnt protein to its receptor called frizzled protein (Frz), which leads to the activation of the downstream cytoplasmic dishevelled protein (Dsh) which blocks the glycogen synthase kinase-3β- (GSK-3β-) mediated phosphorylation/degradation of β-catenin. This allows the accumulation of β-catenin and its further translocation into the nucleus for the binding of transcription factors, leading to the subsequent activation of downstream target genes [32]. In this process, β-catenin is a core component and functions as an important oncogene in many malignant tumours [32, 33]. Our results confirm that β-catenin had relatively high expression in ovarian cancer cells but was downregulated when CRIP1 was knocked down, suggesting that CRIP1

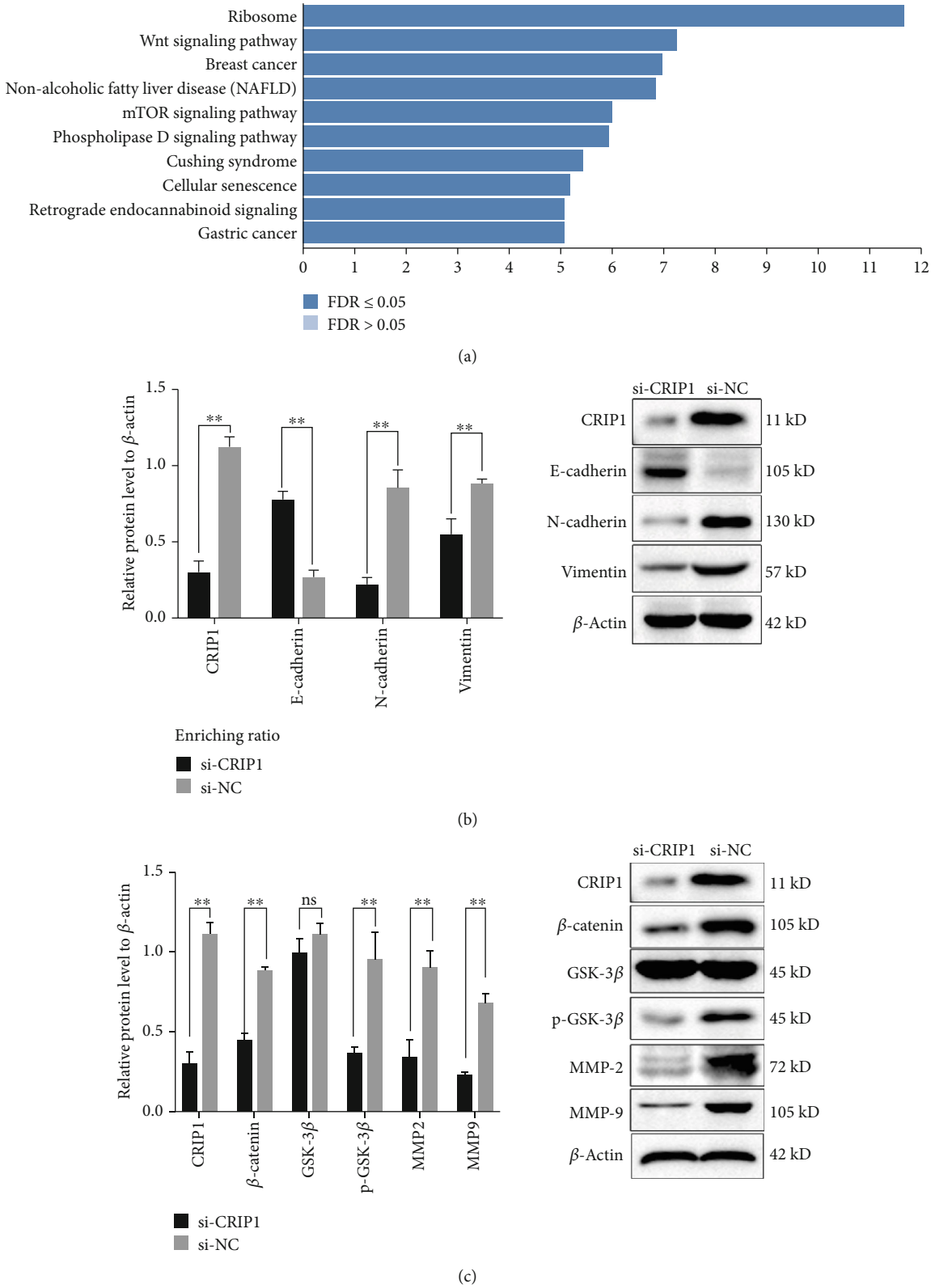

Figure 5: The relationship between CRIP1 and EMT indicates that CRIP1 may function in ovarian cancer development via the Wnt/β-catenin pathway. (a) KEGG pathway enrichment analysis was performed to identify which pathway was significantly enriched in CRIP1-related ovarian cancer progression. (b) The effect of CRIP1 silencing on EMT-related signaling pathways. EMT markers, such as E-cadherin, N-cadherin, and vimentin proteins, were detected by western blot. (c) The effect of CRIP1 silencing on Wnt/β-catenin signaling pathway. The important molecules of this pathway, including β-catenin, GSK-3β, p-GSK-3β, MMP2, and MMP9, were assessed by western blot.

may activate β-catenin. Another key molecule is GSK-3β, which can act as a key negative regulator and promote β-catenin phosphorylation and ubiquitination, leading to subsequent proteasomal degradation. Indeed, in our study, the level of p-GSK-3β, but not total GSK-3β, was downregulated in ovarian cancer when CRIP1 was silenced. The reason for this may be that the activation of Wnt signaling could lead to the phosphorylation and inactivation of GSK-3β, resulting in cytoplasmic GSK-3β pool inactivation without influencing total GSK-3β levels [34].

Matrix metalloproteinases (MMPs) are important downstream target genes of the Wnt/β-catenin signaling pathway [35]. The Wnt/β-catenin/MMPs axis acts as an indispensable component of metastasis and EMT in malignant tumours [36]. It has been reported that MMPs can degrade the extracellular matrix (ECM) and basement membrane, which is the first step in cancer invasion and metastasis. Evidence has shown that MMPs are expressed in various cancer types, and the upregulation of MMPs has been associated with tumour progression and invasiveness [37, 38]. As two crucial members of the MMP family, MMP-2 and MMP-9 have also been found to participate in EMT and cancer metastasis [38]. In our study, when CRIP1 was knocked out in ovarian cells, MMP-2 and MMP-9 were significantly downregulated, together with the downregulation of β-catenin, N-cadherin, and vimentin, while E-cadherin was upregulated. These results suggest that CRIP1 may activate the Wnt/β-catenin signaling pathway, impair cell adhesion, and alter cell migration ability in favour of EMT.

5. Conclusion

The present study first demonstrated that CRIP1 may play an oncogenic role in serous epithelial ovarian cancer development and progression, promoting migration and invasion in the OVCAR3 cell line. In particular, this process may be achieved through the Wnt/β-catenin signaling pathway by inducing EMT, suggesting that CRIP1 may be an important biomarker for ovarian cancer metastasis and prognosis, as well as an important molecular target for ovarian cancer therapy.

However, this study only validated the effect of CRIP1 on the ovarian cancer OVCAR3 cell line at the cellular level. Furthermore, additional ovarian cancer cell lines, overexpression cell models, and animal models (*in vivo*) are required to confirm the links between CRIP1 expression and ovarian cancer progression and prognosis.

Data Availability

The data used to support the findings of this study are included within the article.

Ethical Approval

The study was approved by the Ethics Committee of the Second Affiliated Hospital of Nanchang University.

Consent

Informed consent was obtained from all participants in the study.

Conflicts of Interest

The authors declare that they have no conflicts of interest.

Acknowledgments

This work was supported by the National Natural Science Foundation of China (grant number 81760504). We thank all individuals who participated in this work.

References

[1] M. A. Lisio, L. Fu, A. Goyeneche, Z. H. Gao, and C. Telleria, "High-grade serous ovarian cancer: basic sciences, clinical and therapeutic standpoints," *International Journal of Molecular Sciences*, vol. 20, no. 4, p. 952, 2019.

[2] Y. Zhang, J. Li, X. Dong et al., "PSAT1 regulated oxidation-reduction balance affects the growth and prognosis of epithelial ovarian cancer," *Oncotargets and Therapy*, vol. Volume 13, pp. 5443–5453, 2020.

[3] R. L. Siegel, K. D. Miller, and A. Jemal, "Cancer statistics, 2019," *CA: a Cancer Journal for Clinicians*, vol. 69, no. 1, pp. 7–34, 2019.

[4] K. Brasseur, N. Gévry, and E. Asselin, "Chemoresistance and targeted therapies in ovarian and endometrial cancers," *Oncotarget*, vol. 8, no. 3, pp. 4008–4042, 2017.

[5] L. Zhang, H. R. Yao, S. K. Liu, and L. L. Song, "Long noncoding RNA ROR1-AS1 overexpression predicts poor prognosis and promotes metastasis by activating Wnt/β-catenin/EMT signaling cascade in cervical cancer," *European Review for Medical and Pharmacological Sciences*, vol. 24, no. 6, pp. 2928–2937, 2020.

[6] D. Vergara, B. Merlot, J. P. Lucot et al., "Epithelial-mesenchymal transition in ovarian cancer," *Cancer Letters*, vol. 291, no. 1, pp. 59–66, 2010.

[7] Y. Chen, D. D. Wang, Y. P. Wu et al., "MDM2 promotes epithelial-mesenchymal transition and metastasis of ovarian cancer SKOV3 cells," *British Journal of Cancer*, vol. 117, no. 8, pp. 1192–1201, 2017.

[8] L. Liu, N. Wu, Y. Wang et al., "TRPM7 promotes the epithelial-mesenchymal transition in ovarian cancer through the calcium-related PI3K/AKT oncogenic signaling," *Journal of Experimental & Clinical Cancer Research*, vol. 38, no. 1, p. 106, 2019.

[9] J. Zhu, Y. Zheng, H. Zhang, Y. Liu, H. Sun, and P. Zhang, "Galectin-1 induces metastasis and epithelial-mesenchymal transition (EMT) in human ovarian cancer cells via activation of the MAPK JNK/p38 signalling pathway," *American Journal of Translational Research*, vol. 11, no. 6, pp. 3862–3878, 2019.

[10] J. Zhang, X. J. Tian, and J. Xing, "Signal transduction pathways of EMT induced by TGF-β, SHH, and WNT and their crosstalks," *Journal of Clinical Medicine*, vol. 5, no. 4, p. 41, 2016.

[11] J. Sun, X. Yang, R. Zhang et al., "GOLPH3 induces epithelial–mesenchymal transition via Wnt/β-catenin signaling pathway in epithelial ovarian cancer," *Cancer Medicine*, vol. 6, no. 4, pp. 834–844, 2017.

[12] P. Dong, H. Fu, L. Chen et al., "PCNP promotes ovarian cancer progression by accelerating β-catenin nuclear accumulation and triggering EMT transition," *Journal of Cellular and Molecular Medicine*, vol. 24, no. 14, pp. 8221–8235, 2020.

[13] G. He, H. Zhu, Y. Yao et al., "Cysteine-rich intestinal protein 1 silencing alleviates the migration and invasive capability enhancement induced by excessive zinc supplementation in colorectal cancer cells," *American Journal of Translational Research*, vol. 11, no. 6, pp. 3578–3588, 2019.

[14] P. R. Fernandes, D. A. Samuelson, W. R. Clark, and R. J. Cousins, "Immunohistochemical localization of cysteine-rich intestinal protein in rat small intestine," *The American Journal of Physiology*, vol. 272, 4 Part 1, pp. G751–G759, 1997.

[15] R. J. Cousins and L. Lanningham-Foster, "Regulation of cysteine-rich intestinal protein, a zinc finger protein, by mediators of the immune response," *The Journal of Infectious Diseases*, vol. 182, Suppl 1, pp. S81–S84, 2000.

[16] G. He, L. Zou, L. Zhou, P. Gao, X. Qian, and J. Cui, "Cysteine-rich intestinal protein 1 silencing inhibits migration and invasion in human colorectal cancer," *Cellular Physiology and Biochemistry*, vol. 44, no. 3, pp. 897–906, 2017.

[17] L. Z. Zhang, L. Y. Huang, A. L. Huang, J. X. Liu, and F. Yang, "CRIP1 promotes cell migration, invasion and epithelial-mesenchymal transition of cervical cancer by activating the Wnt/β-catenin signaling pathway," *Life Sciences*, vol. 207, pp. 420–427, 2018.

[18] H. G. Li, L. H. Zhao, Z. H. Zhang et al., "The impact of cysteine-rich intestinal protein 1 (CRIP1) on thyroid carcinoma," *Cellular Physiology and Biochemistry*, vol. 43, no. 5, pp. 2037–2046, 2018.

[19] M. Lambropoulou, T. E. Deftereou, S. Kynigopoulos et al., "Co-expression of galectin-3 and CRIP-1 in endometrial cancer: prognostic value and patient survival," *Medical Oncology*, vol. 33, no. 1, 2016.

[20] D. Baumhoer, M. Elsner, J. Smida et al., "CRIP1 expression is correlated with a favorable outcome and less metastases in osteosarcoma patients," *Oncotarget*, vol. 2, no. 12, pp. 970–975, 2011.

[21] N. Ludyga, S. Englert, K. Pflieger et al., "The impact of cysteine-rich intestinal protein 1 (CRIP1) in human breast cancer," *Molecular Cancer*, vol. 12, no. 1, p. 28, 2013.

[22] C. Qi, X. Wang, Z. Shen et al., "Anti-mitotic chemotherapeutics promote apoptosis through TL1A-activated death receptor 3 in cancer cells," *Cell Research*, vol. 28, no. 5, pp. 544–555, 2018.

[23] T. Gómez del Pulgar, E. Bandrés, C. Espina et al., "Differential expression of Rac1 identifies its target genes and its contribution to progression of colorectal cancer," *The International Journal of Biochemistry & Cell Biology*, vol. 39, no. 12, pp. 2289–2302, 2007.

[24] Y. Chen, C. Miller, R. Mosher et al., "Identification of cervical cancer markers by cDNA and tissue microarrays," *Cancer Research*, vol. 63, no. 8, pp. 1927–1935, 2003.

[25] B. Balluff, S. Rauser, S. Meding et al., "MALDI imaging identifies prognostic seven-protein signature of novel tissue markers in intestinal-type gastric cancer," *The American Journal of Pathology*, vol. 179, no. 6, pp. 2720–2729, 2011.

[26] N. M. Aiello and Y. Kang, "Context-dependent EMT programs in cancer metastasis," *The Journal of Experimental Medicine*, vol. 216, no. 5, pp. 1016–1026, 2019.

[27] A. M. Mendonsa, T. Y. Na, and B. M. Gumbiner, "E-cadherin in contact inhibition and cancer," *Oncogene*, vol. 37, no. 35, pp. 4769–4780, 2018.

[28] Z. Q. Cao, Z. Wang, and P. Leng, "Aberrant N-cadherin expression in cancer," *Biomedicine & Pharmacotherapy*, vol. 118, p. 109320, 2019.

[29] P. F. Liu, B. H. Kang, Y. M. Wu et al., "Vimentin is a potential prognostic factor for tongue squamous cell carcinoma among five epithelial-mesenchymal transition-related proteins," *PLoS One*, vol. 12, no. 6, article e0178581, 2017.

[30] A. M. Richardson, L. S. Havel, A. E. Koyen et al., "Vimentin is required for lung adenocarcinoma metastasis via heterotypic tumor cell-cancer-associated fibroblast interactions during collective invasion," *Clinical Cancer Research*, vol. 24, no. 2, pp. 420–432, 2018.

[31] X. X. Jie, X. Y. Zhang, and C. J. Xu, "Epithelial-to-mesenchymal transition, circulating tumor cells and cancer metastasis: mechanisms and clinical applications," *Oncotarget*, vol. 8, no. 46, pp. 81558–81571, 2017.

[32] Q. Li, M. Sun, M. Wang et al., "Dysregulation of Wnt/β-catenin signaling by protein kinases in hepatocellular carcinoma and its therapeutic application," *Cancer Science*, vol. 112, no. 5, pp. 1695–1706, 2021.

[33] M. J. Hsieh, C. C. Weng, Y. C. Lin, C. C. Wu, L. T. Chen, and K. H. Cheng, "Inhibition of β-catenin activity abolishes LKB1 loss-driven pancreatic cystadenoma in mice," *International Journal of Molecular Sciences*, vol. 22, no. 9, p. 4649, 2021.

[34] M. S. Arrázola, E. Ramos-Fernández, P. Cisternas, D. Ordenes, and N. C. Inestrosa, "Wnt signaling prevents the Aβ oligomer-induced mitochondrial permeability transition pore opening preserving mitochondrial structure in hippocampal neurons," *PLoS One*, vol. 12, no. 1, article e0168840, 2017.

[35] K. Kessenbrock, V. Plaks, and Z. Werb, "Matrix metalloproteinases: regulators of the tumor microenvironment," *Cell*, vol. 141, no. 1, pp. 52–67, 2010.

[36] W. Liu, Y. Chen, H. Xie et al., "TIPE1 suppresses invasion and migration through down-regulating Wnt/β-catenin pathway in gastric cancer," *Journal of Cellular and Molecular Medicine*, vol. 22, no. 2, pp. 1103–1117, 2018.

[37] E. S. Radisky and D. C. Radisky, "Matrix metalloproteinase-induced epithelial-mesenchymal transition in breast cancer," *Journal of Mammary Gland Biology and Neoplasia*, vol. 15, no. 2, pp. 201–212, 2010.

[38] H. Agraval and U. C. S. Yadav, "MMP-2 and MMP-9 mediate cigarette smoke extract-induced epithelial-mesenchymal transition in airway epithelial cells via EGFR/Akt/GSK3β/β-catenin pathway: amelioration by fisetin," *Chemico-Biological Interactions*, vol. 314, p. 108846, 2019.